Stony Brook University

Ratio Method of Measuring the W Boson Mass

A Dissertation Presented

by

Feng Guo

to

The Graduate School

in Partial Fulfillment of the Requirements

for the Degree of

Doctor of Philosophy

in

Physics

Stony Brook University

August 2010

Stony Brook University

The Graduate School

Feng Guo

We, the dissertation committee for the above candidate for the Doctor of Philosophy degree, hereby recommend acceptance of this dissertation.

Michael Rijssenbeek – Dissertation Advisor
Professor, Department of Physics and Astronomy

John Hobbs – Chairperson of Defense
Professor, Department of Physics and Astronomy

Martin Rocek
Professor, Department of Physics and Astronomy

Derek Teaney
Assistant Professor, Department of Physics and Astronomy

Heidi Schellman
Professor, Department of Physics and Astronomy
Northwestern University

This dissertation is accepted by the Graduate School.

Lawrence Martin
Dean of the Graduate School

Abstract of the Dissertation

Ratio Method of Measuring the W Boson Mass

by

Feng Guo

Doctor of Philosophy

in

Physics

Stony Brook University

2010

This dissertation describes an alternative method of measuring the W boson mass in DØ experiment. Instead of extracting M_W from the fitting of $W \to e\nu$ fast Monte Carlo simulations to $W \to e\nu$ data as in the standard method, we make the direct fit of transverse mass between $W \to e\nu$ data and $Z \to ee$ data. One of the two electrons from Z boson is treated as a neutrino in the calculation of transverse mass. In ratio method, the best fitted scale factor corresponds to the ratio of W and Z boson mass (M_W/M_Z). Given the precisely measured Z boson mass, W mass is directly fitted from $W \to e\nu$ and $Z \to ee$ data. This dissertation demonstrates that ratio method is a plausible method of measuring the W boson mass. With the $1\,\mathrm{fb}^{-1}$ DØ Run IIa dataset, ratio method gives $M_W = 80435 \pm 43(\mathrm{stat}) \pm 26(\mathrm{sys})\,\mathrm{MeV}$.

To my parents and my wife.

Contents

List of Figures

List of Tables

Acknowledgements

I am grateful to so many people for their help in my PhD research in DØ experiment at Fermilab. First of all, I would to thank my advisor Prof. Michael Rijssenbeek. The idea of using ratio method to measure the mass of W boson was first proposed and applied the analysis of DØ Run I data by Michael. The essence of the original ratio method is intact in this analysis, although data is 10 times as large. During the two years of my PhD research on ratio method, Michael and I had numerous discussions about the progress and difficulties I encountered in the study. Without the help and guidance from Michael, I would never be able to finish this study.

I also would like to thank Prof. Paul Grannis, Robert McCarthy, John Hobbs and Dean Schamberger in the DØ group of Stony Brook. Their close attention to my research progress is always a valuable encouragement to me. Stony Brook postdoctoral researchers Yuan Hu, Adam Yurkewicz, and especially Junjie Zhu gave me a lot of help on the physics analysis as well as programming skills. I am grateful to the graduate students in the Stony Brook DØ group: Huishi Dong, Jun Guo, Kenneth Herner and Emanuel Strauss. It's a great and memorable experience for me to have my PhD study in the Stony Brook High Energy Physics group.

As a member of the DØ W mass group, I always feel lucky to have the opportunity of collaborating with my colleagues on the W mass measurement of DØ Run IIa data. They are Jan Stark, Pierre Petroff, Heidi Schellman, Tim Andeen, Sahal Yacoob, Sarah Eno, Matt Wetstein, Jyotsna Osta, Alex Melnitchouk, John Hobbs, Bob McCarthy, Junjie Zhu and Jun Guo. Among them, I would like to especially thank Prof. Heidi Schellman. Critical comments and suggestions from her are reflected in many aspects in my dissertation.

Finally, I want to thank my wife Li Wang for the patience, encouragement and love in years of my PhD study.

Chapter 1

Introduction

Particle physics is a branch of modern physics that is dedicated to the understanding of the smallest constituents of matter and the fundamental interaction forces mediating between them. The scale of particle physics is in the range of femtometer (10^{-15}m, the size of the proton) and smaller, where the language of Quantum Mechanics is used. Currently, Quantum Field Theory (QFT) is the theoretical language of choice at the smallest length scales. Over the last several decades, particle physicists have established an elegant theoretical framework which is in excellent agreement with all the current experimental data. This is called the Standard Model of particle physics.

1.1 Standard Model

The Standard Model is a gauge theory of the elementary particles and three of the four known interaction forces. Apart from Gravity, which is described by the theory of general relativity, the Standard Model describes the strong, the electromagnetic, and the weak interaction. In the language of group theory, the strong interaction observes the transformation symmetry of $SU(3)$ while the electroweak interaction observes $SU(2)\otimes U(1)$ gauge transformation symmetry. Together, the three fundamental interactions are described by a gauge theory with $SU(3) \otimes SU(2) \otimes U(1)$ symmetry.

There are two types of elementary particles in the standard model, fermions and bosons, characterized by their half-integer spin and integer spin respectively. Fermions are the constituents of matter, while gauge bosons are responsible for mediating the forces between matters.

Ordinary matter is consisted of only three types of particles, namely electrons, protons and neutrons. Electron is the smallest charged particle with integer charge $-e$, and participates in the electroweak interaction only. In

naturally occurring radioactive decays, neutrons and protons transmute into each other via the weak interaction, which involves the electron and the neutrino. Neutrino is a neutral and near massless particle, it only interacts via weak force. As far as we know, of these four particles only the electron and neutrino are truly fundamental particle; proton and neutron are composites of u and d valence quarks, with gluons which are the gauge bosons of the strong force, binding them together. Quarks have fractional charge, for example u quark has a $+2/3e$ charge, while the d quark has a $-1/3e$ charge. Proton is a uud quark bound state, while the neutron is a udd bound state, and therefore proton has the observed $+e$ charge and neutron is neutral. Quarks participate in both the strong and electroweak interactions. Particles that are immune to strong interaction, such as the electron and neutrino, are called leptons.

The first "generation" particles consisting of neutrino, electron, u and d quarks is not alone. Similar pattern is replicated twice more at higher masses. In the second generation there is the muon(μ^-), first discovered in cosmic rays, 200 times more massive than the electron. In the third generation, there is an even heavier tau(τ^-) lepton. There are 3 generations of neutrinos, of very small but unknown masses.

The first generation quark doublet (u, d) is also replicated twice: the second generation c(charm) and s(strange) quarks, and the third generation t(top), b(bottom) quarks, for a total of six quark "flavors". The strong and electromagnetic interactions are flavor-blind, while the weak interaction allows flavor transitions. As fermions, all quarks have a spin of $(1/2)\hbar$. Up, charm and top quarks (collectively called up-type quarks) have a $+2/3e$ electric charge, while down, strange and bottom (down-type quarks) have a $-1/3e$ electric charge. The third generation top quark, was the last quark to be discovered, at Fermilab Tevatron 15 years ago.

In standard model, the left-handed charged lepton and left-handed neutrino (as well as the left-handed up quark and down quark pair) are treated as a doublet (Eq 1.1) that transforms according to the weak isospin $SU(2)$ symmetry.

$$\begin{pmatrix} e^- \\ \nu_e \end{pmatrix}_L \quad \begin{pmatrix} \mu^- \\ \nu_\mu \end{pmatrix}_L \quad \begin{pmatrix} \tau^- \\ \nu_\tau \end{pmatrix}_L \tag{1.1}$$

$$\begin{pmatrix} e^+ \\ \bar{\nu}_e \end{pmatrix}_R \quad \begin{pmatrix} \mu^+ \\ \bar{\nu}_\mu \end{pmatrix}_R \quad \begin{pmatrix} \tau^+ \\ \bar{\nu}_\tau \end{pmatrix}_R \tag{1.2}$$

Some properties of the leptons are summarized in Table 1.1. In contrast with the strong and electromagnetic interactions, weak force does not preserve parity and indeed violates parity conservation maximally. As a consequence, weak force does act differently with particles of different helicity (the spin

component along the momentum direction), as shown in Figure 1.1. Left-handed and right-handed fermions are identical in strong and electromagnetic interactions, but in weak decays only left-handed fermions are involved. This also explains the fact that the neutrinos we observe are all left-handed.

The lepton doublets in each generation are distinguished by their lepton number. The $(e^-, \nu_e)_L$ doublet has $L_e = 1$, the $(\mu^-, \nu_\mu)_L$ doublet has $L_\mu = 1$ and the $(\mu^-, \nu_\mu)_L$ doublet has $L_\tau = 1$. In all physics experiments, lepton numbers are conserved in weak interaction. Quarks carry zero lepton number, but all have a "baryon-number" equal to 1/3. The "strange" quark carries a strangeness flavor quantum number $S = -1$, likewise other quark flavors have an associated flavor quantum number each of their own.

All particles, leptons and quarks, have their anti-partners, anti-leptons and anti-quarks with exactly the same masses (and spin, lifetime, etc.) but opposite additive quantum numbers such as charge, lepton number, baryon number, strangeness, and so on.

particle(antiparticle)	symbol	charge(e)	spin($\hbar$)	mass(MeV)
electron/positron	e^-/e^+	$-1/+1$	$\frac{1}{2}$	0.511
muon/antimuon	μ^-/μ^+	$-1/+1$	$\frac{1}{2}$	105.658
tau/antitau	τ^-/τ^+	$-1/+1$	$\frac{1}{2}$	1776.84
electron neutrino/antineutrino	$\nu_e/\bar{\nu}_e$	0	$\frac{1}{2}$	$< 2.2 \times 10^{-6}$
muon neutrino/antineutrino	$\nu_\mu/\bar{\nu}_\mu$	0	$\frac{1}{2}$	< 0.17
tau neutrino/antineutrino	$\nu_\tau/\bar{\nu}_\tau$	0	$\frac{1}{2}$	< 15.5

Table 1.1: Three generation of the lepton particles.

Figure 1.1: Left-handed and right-handed helicities.

All quarks carry a three-valued strong charge, the so-called "color"-charge. Similar to the electric charge for the electromagnetic interaction, the color charge determines the strength of the strong interaction between colored particles. An intuitive way is to think of a quark possessing one of the three basic colors "red(R)", "green(G)", or "blue(B)". The theory of the strong interaction, Quatum Chromo-Dynamics (QCD) describes the strong interaction as the color exchange (which is mediated by colored gluons) between quarks,

analogous to the electromagnetic interaction (Quantum Electro-Dynamics - QED) with exchange of (uncharged) photons between charged particles. Table 1.2 list some of the important properties of the six flavors of quarks.

name	symbol	charge	spin	I_3	C	S	T	B	antiparticle
up	u	$+2/3$	$1/2$	$+1/2$	0	0	0	0	$\bar{u}$
down	d	$-1/3$	$1/2$	$-1/2$	0	0	0	0	$\bar{d}$
charm	c	$+2/3$	$1/2$	0	$+1$	0	0	0	$\bar{c}$
strange	s	$-1/3$	$1/2$	0	0	-1	0	0	$\bar{s}$
top	t	$+2/3$	$1/2$	0	0	0	$+1$	0	$\bar{t}$
bottom	b	$-1/3$	$1/2$	0	0	0	0	-1	$\bar{b}$

Table 1.2: Flavor properties of quarks and antiquarks.

Quarks form the constituents of two classes of composite particles, baryons and mesons. Both are hadrons, strongly bound states composed of quarks. A baryon is a bound state of three quarks (or three antiquarks), while a meson is a quark-antiquark composite. Perhaps the best known baryons are the proton (uud) and the neutron (udd). Antiproton and antineutron are of similar constituents, except the consisting particles are antiquark instead of quarks. The exclusiveness of the tree-quark and quark-antiquark bound states is naturally explained from the three-valued "color" quantum number. It is postulated that only "colorless" or white bound states may exist in nature (more precisely: states unchanged under rotations in RGB-color space, i.e. color singlet). Because antiquarks carry anti-colors ($\bar{R}$, $\bar{G}$. $\bar{B}$), the simplest possible colorless configurations are $q_R\bar{q'}_{\bar{R}}$, $q_G\bar{q'}_{\bar{G}}$, and $q_B\bar{q'}_{\bar{B}}$ for mesons, and $q_Rq'_Gq''_B$ for baryons ($\bar{q}_{\bar{R}}\bar{q'}_{\bar{G}}\bar{q''}_{\bar{B}}$ for antibaryons).

Strong interactions are all about the exchange of color. The mediating particle of the strong interactions is the gluon, a vector gauge boson with spin 1. Unlike in QED, where photon is the single carrier of the electromagnetic force, there are 8 gluons. Gluons carry both color and anticolor, a simple example is given in Figure 1.2. Of all 9 possible combinations of 3 colors and 3 anticolors, one is a color singlet and thus does not participate in color exchange.

As mentioned above, quark flavor is preserved in the electromagnetic and strong interactions, while the weak interaction does not. Quarks can change from one flavor to another flavor by emission or absorbtion of a the charged weak vector boson, $W^{\pm}$. The best known example of this kind process is the neutron β decay, in which a valence d quark in the neutron emits a (virtual) W^- boson and changes into a u quark in the process, thereby transforming the neutron into a proton. The virtual W^- boson instantly decays into a pair

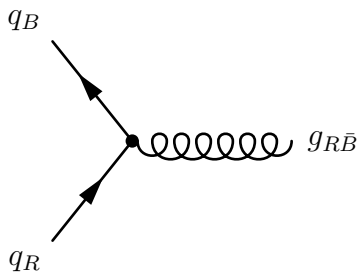

Figure 1.2: The most simple QCD vertex, where a red color quark emit a red-antiblue colored gluon and turns into a blue color quark.

of e^- and $\bar{\nu}_e$ with allowed energies, this process is illustrated in Figure 1.3.

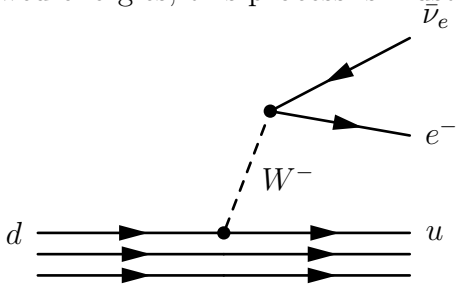

Figure 1.3: β decay of neutron.

The probability of one quark flavor transforming into another flavor is described by the CKM matrix [1]. Technically, the CKM matrix describes the mixing of the eigen states of the strong (and electromagnetic) interaction, with those of the weak interaction. Since the W boson is charged, the transitions only occur between up-type and down-type quarks. Each element of the CKM matrix V_{ij} represents the transition amplitude between a quark of flavor i and of flavor j. V_{ij} is involved in various physical processes and can be determined experimentally. The current value of CKM matrix is shown in Eq 1.3 [1]. It's obvious that quarks tend to transform preferentially within the same generation rather than between generations .

$$\begin{pmatrix} V_{ud} & V_{us} & V_{ub} \\ V_{cd} & V_{cs} & V_{cb} \\ V_{td} & V_{ts} & V_{tb} \end{pmatrix} \simeq \begin{pmatrix} 0.974 & 0.226 & 0.004 \\ 0.226 & 0.973 & 0.041 \\ 0.009 & 0.041 & 0.999 \end{pmatrix} \tag{1.3}$$

Quark mixing through the weak interaction has a direct role in the production of the $W^{\pm}$ in Tevatron experiments. For example, the inverse of neutron β decay is $d + \bar{u} \rightarrow W^-$, which is the dominant process of W^- production in $p\bar{p}$ collisions at the Tevatron. Here, d quark is the valence quark from proton and $\bar{u}$ quark is the valence quark from antiproton.

Since this thesis is mostly concerned with the properties of the $W^{\pm}$ and Z bosons, a more detailed discussion of the theory of weak interaction and WZ boson production at the $p\bar{p}$ collider is given in the next chapter.

1.2 W Mass, Top Mass and the Higgs Boson

The direct experimental discovery of the W and Z bosons in 1983 validated the electroweak theory proposed by theorist. The unification of the electromagnetic and weak interactions in the electroweak gauge theory based on the $U(1)_Y \otimes SU(2)_L$ symmetry broken with the Higgs mechanism (the Glashow-Weinberg-Salam model - GWS) was the major step forward in the 1960's. Together with QCD which is based on the unbroken $SU(3)$ symmetry of color, the electroweak theory forms the bare bone of the Standard Model. The GWS model predicted the existence of a charge neutral Z boson as the massive mixture of the neutral gauge bosons of the $U(1)_Y$ symmetry of weak hypercharge Y and of the $SU(2)_L$ of the left-handed weak interaction symmetry. Mass of Z boson was extremely precisely measured in the LEP experiments. In contrast, measurement of the mass of charged W boson is much more difficult, as explained in the overview of the direct measurement of M_W in section 1.3.

The most important motivation for a very precise measurement of M_W is to confront the Standard Model predictions with experimental results. Because the Standard Model has only on a limited set of a prioriy unknown parameters (9 or 12 lepton and quark masses, 4 CKM mixing parameters, 3 gauge group couplings, and 2 Higgs potential parameters), results from many experiments must show consistency with its predictions. In particular, the bare mass of the W boson receives so-called "radiative" corrections from loop diagrams involving the t and b quarks, and radiative loops involving the putative Higgs boson. A precise measurement of W boson mass acts as a examination of the theory of Standard Model. The loop diagrams that dominate the correction to the W boson mass in Standard Model are shown in Figure 1.4. When loops involving SUSY particles are considered, they contribute further corrections to the boson mass.

In the Standard Model the W boson mass can be written in terms of other fundamental variables as Eq 1.4[8].

$$M_W^2 = \frac{\pi \alpha_{\rm EM}}{\sqrt{2} G_F (1 - M_W^2/M_Z^2)(1 - \Delta r)}. \tag{1.4}$$

M_Z, the mass of the Z boson, is precisely determined by the LEP experiments. G_F is the Fermi constant which is determined extremely precisely by the muon life time. The electromagnetic coupling $\alpha_{\rm EM} = e^2/4\pi$ is extremely well known

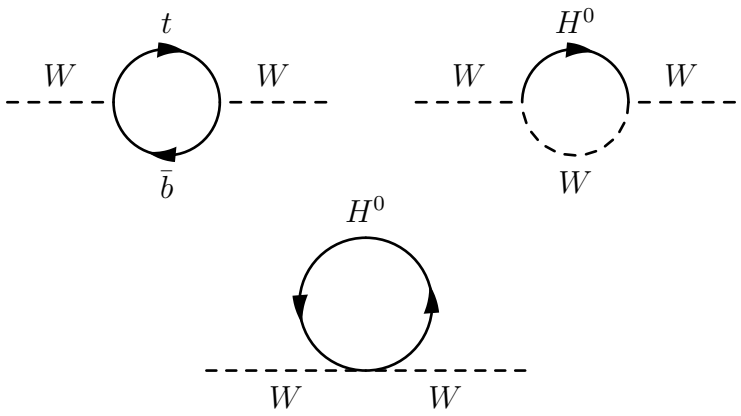

Figure 1.4: The lowest order loop diagram contributing to W boson mass in Standard Model.

and evaluated at $Q^2 = M_Z^2$. The radiative correction term Δr groups all radiative contributions from loops involving the top quark and the Higgs boson. Physics beyond the Standard Model may also enter into Δr. In the Minimal Supersymmetric Standard Model (MSSM), corrections due to SUSY particles can be as large as several hundred MeV[10].

The $t\bar{b}$ loop tends to increase the value of $M_W$by an amount proportional to the square of the top mass M_t^2. The contribution from Higgs loop tends to lower the W mass in proportion to $\ln M_H$. Thus, within the framework of the Standard Model, a precision measurement of M_W and M_t can be converted into a prediction of the mass of the yet-to-be-discovered Higgs boson. A global fit of the parameters is done within the framework of Standard Model [2]. In Figure 1.5 all experimental data (including on M_W and M_Z) except the direct top mass measurements are used to fit the M_t vs. M_H at the 68% confidence level. The direct $M_t$measurement (from the Tevatron experiments) with the $\pm 1\sigma$ uncertainty is also shown for comparison. Figure 1.6 uses all experimentally measured data (now including M_t) except M_W and Γ_W to do the global fit. The fitted M_W vs M_H contour at 68% confidence level is compared with the direct measurement of M_W.

The directly measured M_W and M_t values from LEP-II/Tevatron are compared with the indirectly fitted LEP-I/SLD values in Figure 1.7. Also shown in the same figure is the theoretical M_W vs. M_t value for Higgs masses in the range $114\,\mathrm{GeV} < M_H < 1000\,\mathrm{GeV}$. The uncertainty in the prediction from

the uncertainty of the running of $\alpha_{\rm EM}$ from low energy to the Z mass is indicated. Figure 1.8 shows the relative χ^2 of the fit (from direct or indirect measurements) as function of the Higgs mass.

The confidence level contour of M_W vs. M_t in Figure 1.7 indicates that at present the Higgs mass prediction is limited by the precision of M_W rather than of M_t. With the high integrated luminosity data collected at the Tevatron experiments, CDF and DØ collaborations are working hard to measure the W mass with smallest possible statistical and systematic uncertainties to provide the strongest possible constraints on the Standard Model Higgs mass. Even when the Higgs boson is discovered at the LHC, there is still a strong consistency argument for improving the precision of W mass measurement.

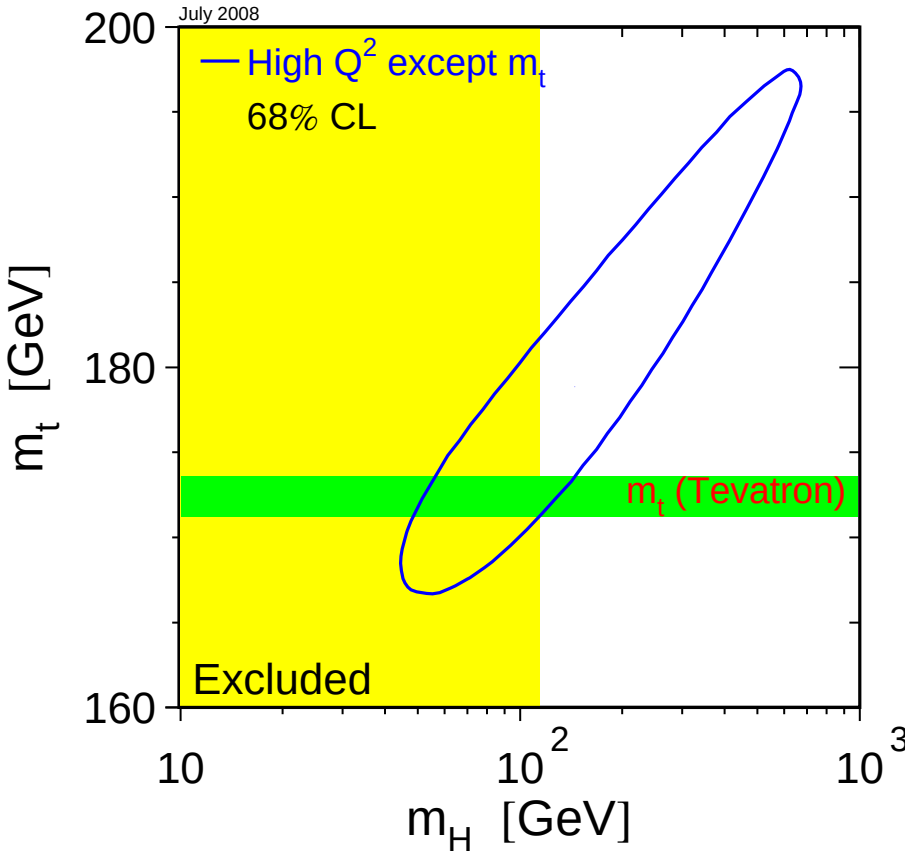

Figure 1.5: Global fit of Standard Model with all data, including M_W, but excluding direct measurements of the top quark mass M_t. The 68% confidence contour of M_t vs. M_H is compared with the directly measured top quark mass M_t which is shown with a $\pm 1\sigma$ band. The yellow band is the 95% CL exclusion region for lower Higgs mass M_H by direct searches. [2]

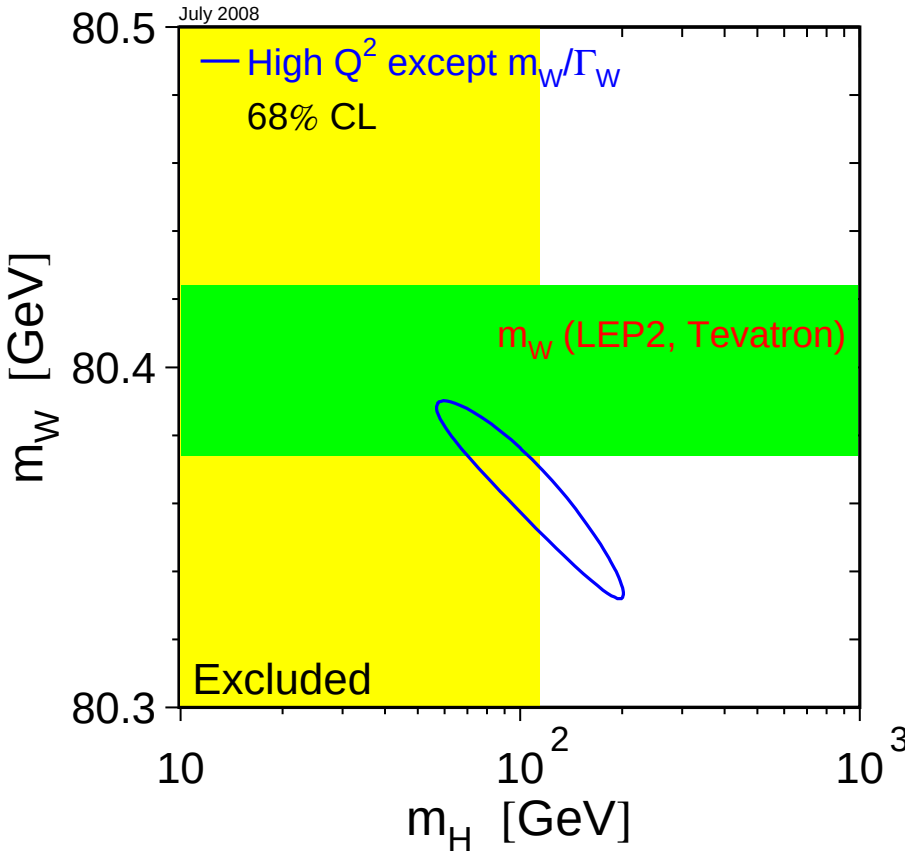

Figure 1.6: Global fit of the Standard Model with all measured data (including M_t) from all experimental data except the direct measuremnts of the W boson mass M_W. The 68% confidence contour of M_W vs. M_H is compared with the directly measured $M_W$which is shown with $\pm 1\sigma$ band. The yellow band is 95% exclusion region at low Higgs mass M_H by direct searches. [2]

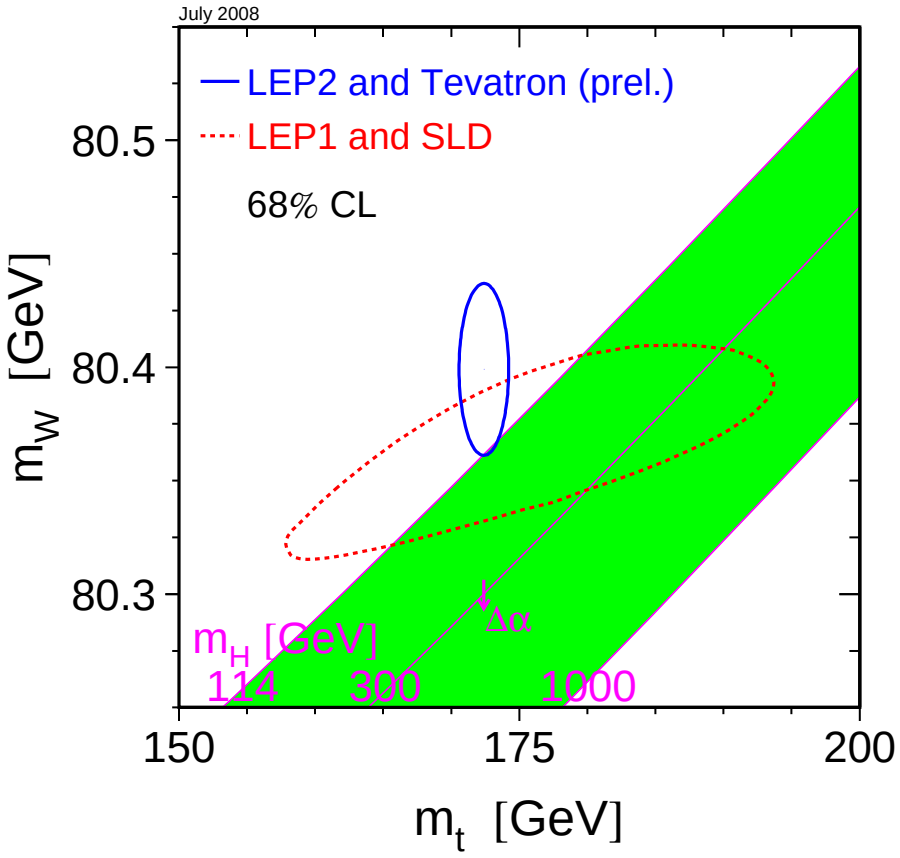

Figure 1.7: The 68% confidence contour of fitted M_W vs. M_t (dashed) from LEP-I/SLD is compared with the directly measured M_W vs. M_t (solid) from LEP-II/Tevatron. The Higgs mass dependence predicted in the Standard Model is also shown. The $\Delta\alpha$ arrow shows the shift in the Higgs mass with a one standard deviation shift of $\alpha_{\rm EM}(m_Z^2)$. [2]

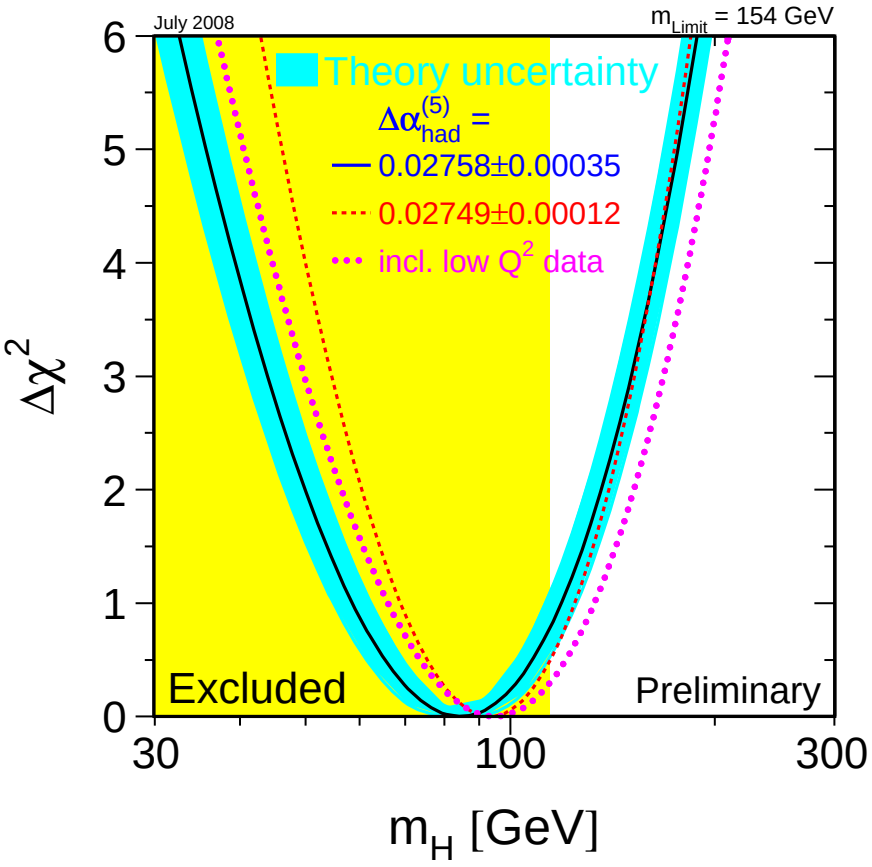

Figure 1.8: $\Delta\chi^2 = \chi^2 - \chi^2_{\text{min}}$ vs $M_H$curve. Band stands for the theoretical uncertainties due to higher order corrections. Dashed line use a different value of strong coupling constant α. The dotted line includes the results from low Q^2 experiments. The left yellow band region is excluded by direct Higgs searches at the 95% confidence level. [2]

1.3 Overview of W Mass Measurement

Since the initial discovery of W and Z bosons by the UA1 [3, 5] and UA2 [3, 5] collaborations in 1983, the study of their properties has never been stopped. As Z bosons can be resonantly produced at e^-e^+ type colliders, the four LEP experiments measured its properties, including its mass, with high precison. The study of W bosons turns out to be much more difficult, as the charged $W^\pm$ can only be produced in a W^+W^- pair at LEP-II, and the most accessible decay modes of the W have neutrinos in the final state, which are invisible to the detectors.

Starting in 1996, the energy of LEP accelerator was increased above the 161 GeV $W^\pm$ pair production threshold. The mass of W boson was measured by the four large LEP collaborations: ALEPH, DELPHI, L3, OPAL. [7]

Two methods were used to extract W mass by the LEP experiments. The first method determines M_W from the onset of the W pair production cross section $\sigma(e^-e^+ \to W^-W^+)$ as function of total energy by comparison with theoretical curves for different M_W. Close to the threshold, the $W^\pm$ pair production cross section is steep and very sensitive to M_W.

The second method used the $W^\pm$ pair data collected by LEP at higher energy, where the energy dependence of the production cross section $\sigma(e^-e^+ \to W^-W^+)$ is rather flat, but where most data are taken. The final states of $q\bar{q}q\bar{q}$ and $q\bar{q}\ell\bar{\nu}_\ell$ are used in the e^-e^+ center of mass frame to compute the invariant mass of the W^-W^+ pair, using the constraint of the well-known overall energy and momentum to reduce the overall uncertainties introduced by the use of jets in the final states.

For the last decade, since the end of LEP-II in 2000, the only place producing large numbers of W bosons is Fermilab Tevatron. The study of this thesis is based on $1\,\mathrm{fb}^{-1}$ Run IIa W and Z data collected at the DØ experiment at the Fermilab Tevatron collider.

At Tevatron, W^- and W^+ bosons are produced in the collisions of gluons and quarks. Both the DØ and CDF collaborations use the $\ell\bar{\nu}_\ell$ lepton final states from the W decays for the W mass analysis. This choice is imposed since $p\bar{p}$ collisons, as collisions of quarks and gluons, are inherently more "dirty"because of the presence of spectator jets than e^-e^+ collisions. Because the initial parton state involved with W production is poorly known, unlike the e^+e^- initial state at LEP, no "beam constraint" is possible and W decays with quark jets in the final state have very high QCD background and are unsuitable for a precision W mass measurement.

Both CDF and DØ published their W mass measurement for Tevatron Run IIa data. The CDF[12] result is based on $200\,\mathrm{pb}^{-1}$ data in $W \to e\nu$ and $W \to \mu\nu$ channels. DØ[11] published its result based on $1\,\mathrm{fb}^{-1}$ $W \to e\nu$ data.

The measuremnt method is similar in both experiments: a precisely tuned, parameterized fast Monte Carlo model is used to produce a fine spectrum of M_W-dependent templates of the lepton p_T, $\not\!\!E_T$ and M_T spectra. The fitted M_W is the mass used in the template that fits the data best, and the uncertainty from the range of templates compatible with the data withing 68% CL. This method is referred to as the "standard method" in the following.

CDF and DØ choose different fast Monte Carlo tuning methods for their W mass analysis, and the choice is closely related to the strengths and weaknesses in performance of their respective detectors. The CDF detector features a strong magnetic tracking system, enabling a precise measurement of a charged particle's momentum. Thus, CDF calibrates its calorimeter energy scale energy with the tracking system, in particular with muons from abundant $J/\psi \to \mu^-\mu^+$ and $\Upsilon \to \mu^-\mu^+$ events. The track momentum calibration is transferred to the electron channel and further calibrates the calorimeter energy by fitting electron's E/p ratio. Tracking and calorimeter calibrations are cross checked with the $Z \to \mu^-\mu^+$ and $Z \to e^-e^+$ events. For $200\,\mathrm{pb}^{-1}$ RunII data, combining the $W \to e\nu$ and $W \to \mu\nu$ channels, CDF published a W mass measurement $M_W = 80.413 \pm 0.048\,\mathrm{GeV}$[12].

DØ's analysis concentrates on the electron channel only. Because the DØ tracker is smaller in radius by 50% and has a half the magnetic field strength of CDF, momentum resolution of W muons is not competitive with the electron calorimeter resolution. The energy of electrons is solely determined by the DØ LAr calorimeter, and the tracker is used only to precisely determine the electron direction. The electron energy and recoil system for $W \to e\nu$ fast Monte Carlo are calibrated by electrons from $Z \to ee$ decays. Because electrons fron the Z largely dominate in the absolute energy scale calibration at high energies, the M_W determined in the standard method is indeed relative to the global the Z boson mass value. For $1\,\mathrm{fb}^{-1}$ RunII data in $W \to e\nu$ channel, the DØ W mass measurement gives $M_W = 80.401 \pm 0.043\,\mathrm{GeV}$[11], a combination of fitting p_T^e, $\not\!\!E_T$ and M_T spectra.

Figure 1.9 [14] shows the updated direct measurements of W mass from LEP and Tevatron. The latest results from CDF [12] and DØ [11] results are also included.

The leading uncertainties quoted in the CDF and DØ W mass analyses are from the following sources: statistical uncertainties of the final templates fitting due to the limited number of W events in the data and the systematic uncertainties of electron energy scale (and tracking momentum scale). The latter is dominated by the statistics of calibration sample (i.e. the number of $Z \to e^-e^+$ events at DØ). Consequently, when larger datasets become available for W mass analyses, both the statistical uncertainty and the energy

(and tracking momentum) scale systematics are expected to improve accordingly. With diminishing experimental uncertainties, the uncertainties in the modeling of the WZ production will become more significant.

This thesis describes an alternative method ("ratio method" vs. the standard method) to measure W boson mass using the $1\,\mathrm{fb}^{-1}$ DØ RunIIa data. A detailed discussion about the differences between the standard method and ratio method will be presented in later Chapters.

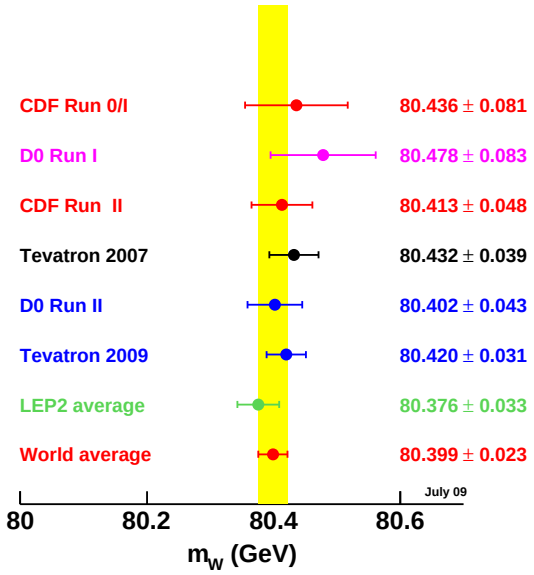

Figure 1.9: Summary of the measurements of the W boson mass and their average as of July 2009. The result from the Tevatron corresponds to the values in Ref. [14]. The LEP II result is from Ref. [15]. An estimate of the world average of the Tevatron and LEP results assuming no correlations between the Tevatron and LEP is included.

Chapter 2

Theory

In this chapter, we first discuss the theoretical framework of electroweak interaction which governs the physics processes like $W \to e\nu$ and $Z \to ee$ through which W mass is measured in this thesis. Then we discuss the production and decay of W and Z boson at Fermilab Tevatron.

2.1 Electroweak Theory

There are many good textbooks on electroweak theory. In this chapter, I mainly follow the treatment in the book by Halzen & Martin [17]. I try to cover the most important and relevant materials in this chapter in a coherent way.

2.1.1 Electromagnetic Current

In the standard model, electromagnetic and weak interaction are two aspects of one unified electroweak interaction. Electromagnetic interaction is mediated by massless photon, while the mediating particles of weak interaction are massive $W^{\pm}$ boson (charged) and Z boson (neutral).

The electroweak theory is easy to explain in term of perturbative theory. A free electron with momentum $\mathbf{p}$ is described by the following wave function

$$\psi = u(\mathbf{p})e^{-ip\cdot x}. \tag{2.1}$$

The electron wave function meets Dirac equation

$$(\gamma_\mu p^\mu - m)\psi = 0. \tag{2.2}$$

In an electromagnetic field described by potential A^μ, the probability T_{fi} for

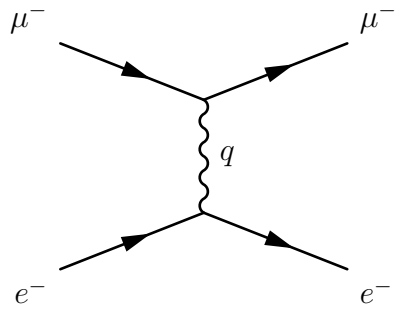

Figure 2.1: Feynmann diagram of $e^-\mu^- \to e^-\mu^-$ scattering. A virtual photon is exchanged between the e^- and μ^- current.

the electron to jump from initial eigenstate i to final eigenstate f can be calculated from first order perturbation Equation 2.3. The interaction potential $V(x)$ is related to A^μ, therefore T_{fi} is related to the electromagnetic current $j_\mu^{fi} \equiv -e\bar{\psi}_f \gamma_\mu \psi_i$ in Equation 2.4.

$$T_{fi} = -i \int \psi_f^\dagger(x) V(x) \psi_i(x) d^4x \tag{2.3}$$

$$= -i \int j_\mu^{fi}(x) A^\mu(x) d^4x \tag{2.4}$$

Ignoring the space dependence, the electromagnetic current j_μ^{fi} can be written in terms of the spinor $u(\mathbf{p})$ (momentum dependent) of the wave function ψ (Equation 2.1).

$$j_\mu^{\text{em}} \equiv j_\mu^{fi} = -e\bar{u}_f \gamma_\mu u_i \tag{2.5}$$

For a simple scattering process $e^-\mu^- \to e^-\mu^-$ shown in Figure 2.1, a virtual photon with 4-momentum q is exchanged between e^- and μ^-. A^μ is related with the electromagnetic current j_{EM}^μ generated with μ^-

$$A^\mu = \frac{1}{q^2} j_{\text{EM}}^\mu \tag{2.6}$$

The invariant magnitude $\mathcal{M}$ is essentially the T_{fi} stripped of the δ function which guarantees the energy conservation between initial and final state. Plugging Equation 2.6 into Equation 2.4, we arrive at an important expression of $\mathcal{M}$ of this process.

$$\mathcal{M} = j_{\text{EM}}^u \frac{1}{q^2} j_u^{\text{EM}} \tag{2.7}$$

The above equation can be rewritten in a more familiar manner: as vertex factor and photon propagator of Feynmann rules.

$$-i\mathcal{M} = \underbrace{(ie\bar{u}\gamma^{\mu}u)}_{e^-\text{current}}\left(\frac{-ig_{\mu\nu}}{q^2}\right)\underbrace{(ie\bar{u}\gamma^{\nu}u)}_{\mu^-\text{current}} \tag{2.8}$$

2.1.2 Weak Current

The invariant amplitude $\mathcal{M}$ for the electromagnetic interactions is expressed in terms of the EM neutral current j_μ which is associated with the exchange of virtual photon. Weak interaction is mediated by the massive $W^{\pm}$ and Z bosons. The charged weak currents j_μ^+ and j_μ^- associated with the $W^{\pm}$ vertices are shown below.

$$\begin{aligned} j_\mu^+ &= \bar{u}_\nu\gamma_\mu\frac{1}{2}(1-\gamma^5)u_e \\ &= \bar{\nu}_L\gamma_\mu e_L \end{aligned} \qquad W^+ \text{ ---▶--- } \begin{matrix}\nu_e \\ e^-\end{matrix} \tag{2.9}$$

$$\begin{aligned} j_\mu^- &= \bar{u}_e\gamma_\mu\frac{1}{2}(1-\gamma^5)u_\nu \\ &= \bar{e}_L\gamma_\mu\nu_L \end{aligned} \qquad W^- \text{ ---▶--- } \begin{matrix}e^- \\ \nu_e\end{matrix}$$

Note the weak current has $\gamma_\mu\frac{1}{2}(1-\gamma^5)$ matrix element, different from γ^μ in electromagnetic current. $\bar{\psi}\gamma^\mu\psi$ and $\bar{\psi}\gamma^\mu\gamma^5\psi$ are vector and axial vector type under the spacetime transformation. This leads to the famous $V-A$ (Vector−Axial Vector) structure observed in weak current.

We all know that weak interaction doesn't observe the symmetry of parity. The mathematical cause of this comes from the $V-A$ structure of weak currents described above. Notice that the spinor u of electron or neutrino can be decomposed of the right-handed u_R and left-handed u_L components, which are called chiral spinors.

$$u = \frac{1}{2}(1+\gamma^5)u + \frac{1}{2}(1-\gamma^5)u \tag{2.10}$$

$$= u_R + u_L \tag{2.11}$$

By writing the weak charged current in terms of the chiral spinors, we

notice that the charged weak current only couples the left-handed neutrinos. As the γ terms can be written in a symmetrical form

$$\gamma_\mu \frac{1}{2}(1-\gamma^5) = \frac{1}{2}(1+\gamma^5)\gamma_\mu \frac{1}{2}(1-\gamma^5) \quad (2.12)$$

$$\bar{u}\gamma_\mu \frac{1}{2}(1-\gamma^5)u = [\bar{u}\frac{1}{2}(1+\gamma^5)]\gamma_\mu[\frac{1}{2}(1-\gamma^5)u] \quad (2.13)$$

Those terms in the [ ] brackets of Equation 2.13 are left-handed chiral spinors $\bar{u}_L$ and u_L. Therefore the weak current can be written as $\bar{u}_L\gamma_\mu u_L$. If the neutrino mass is zero, handness is a Lorentz invariant property of neutrino. The weak current formula $(V-A)$ dictates that only the left-handed neutrino (and left handed antineutrinos) can participate in weak interactions. As weak interaction is the only process through which neutrinos are detected, the right-handed neutrinos thus can never be detected, or simply don't exist. Lastest neutrino experiments prefer a very small neutrino mass $\sim 1\,\mathrm{eV}$ [18]. If neutrinos indeed have non-zero mass, there would be a tiny fraction of right-handed neutrino, although experimental detection of them would be very difficult.

For electrons, handness is not a Lorentz invariant property, because of their non-zero mass. Therefore a e_R can be transformed into e_L by Lorentz transformation. An electromagnetic current can be also shown in chiral spinors, however unlike weak current both the left-hand and right-hand spinors have contributions. Equation 2.5 can be rewritten as Equation 2.14, as the cross terms $\bar{u}_R\gamma u_L$ and $\bar{u}_L\gamma u_R$ vanish.

$$\begin{aligned} j_\mu^{\mathrm{em}} &\equiv \bar{u}\gamma_\mu u = -(\bar{u}_R+\bar{u}_L)\gamma_\mu(u_R+u_L) \\ &= -\bar{u}_R\gamma_\mu u_R - \bar{u}_L\gamma_\mu u_L \end{aligned} \quad (2.14)$$

2.1.3 $SU(2)_L \otimes U(1)_Y$

Weak charged current j^+ and j^- in Equation 2.9 can be written in a unified manner by introducing the following weak isospin doublets for the three generations of leptons:

$$\chi_L = \begin{pmatrix} \nu_e \\ e^- \end{pmatrix}_L, \begin{pmatrix} \nu_\mu \\ \mu^- \end{pmatrix}_L, \begin{pmatrix} \nu_\tau \\ \tau^- \end{pmatrix}_L \quad (2.15)$$

The charged weak currents in Equation 2.9 are thus written in terms of the lepton weak isospin doublets χ_L and the familiar ladder operators $\tau_\pm = \frac{1}{2}(\tau_1 \pm i\tau_2)$ commonly seen in the $SU(2)$ mathematics of spin-$\frac{1}{2}$ system, where τ_i are

the usual Pauli spin matrices.

$$\begin{aligned} j_\mu^+ &= \bar{\chi}_L \gamma_\mu \tau_+ \chi_L \\ j_\mu^- &= \bar{\chi}_L \gamma_\mu \tau_- \chi_L \end{aligned} \tag{2.16}$$

It is natural to generalize the above charged weak current to write the isotriplet weak currents j_μ^i as

$$j_u^i = \bar{\chi}_L \gamma_\mu \frac{1}{2} \tau_i \chi_L \qquad \text{with } i = 1, 2, 3 \tag{2.17}$$

The third component of j_μ^i is a neutral current $j_\mu^3 = \bar{\chi}_L \gamma_\mu \frac{1}{2} \tau_3 \chi_L = \frac{1}{2} \bar{\nu}_L \gamma_\mu \nu_L - \frac{1}{2} \bar{e}_L \gamma_\mu e_L$. The corresponding charges $T^i = \int j_0^i(x) d^3x$ observe the $SU(2)_L$ algebra $[T^i, T^j] = i\epsilon_{ijk} T^k$. The subscript L on $SU(2)$ emphasizes that only the left-handed fermions are coupled to weak currents.

A weak hypercharge current j_μ^Y is defined as

$$j_\mu^{\text{em}} = j_\mu^3 + \frac{1}{2} j_\mu^Y. \tag{2.18}$$

For electron multiplets, the hypercharge current becomes

$$\begin{aligned} j_\mu^Y &= 2j_\mu^{\text{em}} - 2j_\mu^3 \\ &= -2(\bar{e}_R \gamma_\mu e_R + \bar{e}_L \gamma_\mu e_L) - (\bar{\nu}_L \gamma_\mu \nu_L - \bar{e}_L \gamma_\mu e_L) && (2.19) \\ &= -2(\bar{e}_R \gamma_\mu e_R) - (\bar{\chi}_L \gamma_\mu \chi_L) && (2.20) \end{aligned}$$

Weak hypercharge current j_μ^Y incorporates electromagnetic interaction and as a result the hypercharge operator Y generates $U(1)$ algebra. Therefore the combined symmetry of electroweak interaction is $SU(2)_L \otimes U(1)_Y$.

The weak isospin doublet for quarks has the same coupling to the weak current as Equation 2.17. Unlike leptons, where the weak coupling only happens within the same generation, quark weak isospin doublet is mixed, because of the existence of CKM matrix (Eq 1.3). The left-handed quark doublets participating in weak interaction are actually mixed:

$$\chi_L = \begin{pmatrix} u \\ d' \end{pmatrix}_L, \begin{pmatrix} c \\ s' \end{pmatrix}_L, \begin{pmatrix} t \\ b' \end{pmatrix}_L \tag{2.21}$$

Taking the (u, d') weak isospin doublet as an example, and utilizing the CKM values in Eq 1.3, we can estimate that the actual percentages of each process

in the overall process $d' \to u + W^-$.

$d \to u + W^-$ $\quad ((0.974)^2 = 94.8\%)$

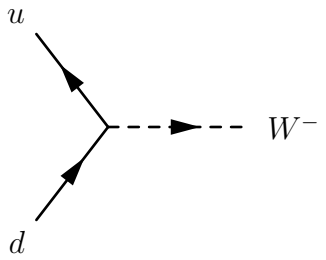

$s \to u + W^-$ $\quad ((0.226)^2 = 5.1\%)$

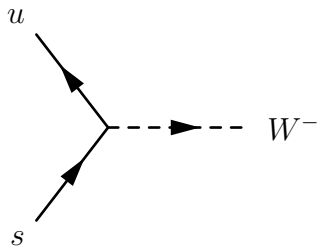

$b \to u + W^-$ $\quad ((0.004)^2 = 1.6 \times 10^{-6})$

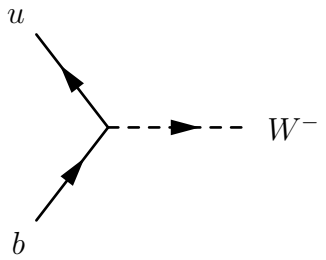

2.1.4 Electro-Weak Mixing

From Eq 2.4, the coupling between electromagnetic current $j_\mu^{\rm em}$ and electromagnetic potential A^μ is

$$\mathscr{L}_{\rm int} = -ie j_\mu^{\rm em} A^\mu. \tag{2.22}$$

In the standard model, the electroweak currents are coupled to vector boson in a similar way. An isotriplet of vector fields W_μ^i are coupled with weak current j_μ^i with strength g. The hypercharge current j_μ^Y is coupled to a singlet vector field B_μ with strength $g'/2$.

$$\mathscr{L}_{\rm EW} = -i\left[g j_\mu^i (W^\mu)_i + \frac{g'}{2} j_\mu^Y B^\mu\right] \tag{2.23}$$

The first term in the above bracket [ ] can be expanded explicitly in terms of the isotriplt weak currents j_μ^i and isotriplet vector fields W_μ^i.

$$j_\mu^i (W^\mu)_i = j_\mu^1 (W^\mu)^1 + j_\mu^2 (W^\mu)^2 + j_\mu^3 (W^\mu)^3 \tag{2.24}$$

Just as $j_\mu^\pm \equiv (1/\sqrt{2})(j_\mu^1 \pm i j_\mu^2)$, the combination of W_μ^1 and W_μ^2 gives the charged $W^\pm$ boson $W_\mu^\pm \equiv (1/\sqrt{2})(W_\mu^1 \mp i W_\mu^2)$. Eq 2.24 can be further written

as the charged current part and the neutral current part.

$$j^i_\mu (W^\mu)_i = j^+_\mu (W^\mu)^+ + j^-_\mu (W^\mu)^- + j^3_\mu (W^\mu)^3 \tag{2.25}$$

The electromagnetic term Eq 2.22 must be incorporated into the neutral current interaction part of Eq 2.23:

$$-i\left[g j^3_\mu (W^\mu)^3 + \frac{g'}{2} j^Y_\mu B^\mu\right] \tag{2.26}$$

To do that, the underlying $SU(2)\otimes U(1)$ symmetry is broken. The two neutral vector field W^3_μ and B_μ in Eq 2.26 are mixed to form a massless neutral field A^μ (photon) and a massive neutral filed Z^μ (Z boson). The linear relation is described by the weak mixing angle θ_W.

$$\begin{pmatrix} A_\mu \\ Z_\mu \end{pmatrix} = \begin{pmatrix} \cos\theta_W & \sin\theta_W \\ -\sin\theta_W & \cos\theta \end{pmatrix} \begin{pmatrix} B_\mu \\ W^3_\mu \end{pmatrix} \tag{2.27}$$

In terms of the physical field A^μ and Z^μ, the electroweak current interaction can be written as

$$\begin{aligned} -i\left[g j^3_\mu (W^\mu)^3 + \frac{g'}{2} j^Y_\mu B^\mu\right] &= -i\left(g\sin\theta_W j^3_\mu + g'\cos\theta_W \frac{j^Y_\mu}{2}\right) A^\mu \\ &\quad -i\left(g\cos\theta_W j^3_\mu - g'\sin\theta_W \frac{j^Y_\mu}{2}\right) Z^\mu \end{aligned} \tag{2.28}$$

The first term in bracket on the right hand side of Eq 2.28 should be a electromagnetic current $e j^{\rm em}_\mu \equiv e(j^3_\mu + \frac{1}{2} j^Y_\mu)$ which is coupled to A^μ. Comparison of the above formulae reveals the relation of coupling strengths.

$$g\sin\theta_W = g'\cos\theta_W = e \tag{2.29}$$

Using the electromagnetic coupling e and weak mixing angle θ_W, we can rewrite the electroweak neutral current as

$$\begin{aligned} -i\left[g j^3_\mu (W^\mu)^3 + \frac{g'}{2} j^Y_\mu B^\mu\right] &= -ie j^{\rm em}_\mu A^\mu \\ &\quad -\frac{ie}{\sin\theta_W\cos\theta_W}\left[j^3_\mu - \sin^2\theta_W j^{\rm em}_\mu\right] Z^\mu \end{aligned} \tag{2.30}$$

The complete electroweak interaction $\mathscr{L}_{\rm EW}$ is thus written in terms of the physical fields $W^\pm$, Z^μ, A^μ, electromagnetic coupling e and the weak mixing

angle θ_W. The obvious deficiency of this unified model is that the masses of the $W^{\pm}$ and Z vector bosons must be zero to keep the apparent gauge symmetry of the electroweak Lagrangian. This difficult can be alleviated by spontaneous symmetry breaking where the gauge symmetry of Lagrangian remains intact but hidden because of the choose of direction in the weak isospin space.

2.1.5 Higgs Mechanism

The gauge invariant Lagrangian for the electron neutrino pair interacting with W_μ^i and B_μ field is

$$\begin{aligned}\mathscr{L}_{\rm EW} &= \bar{\chi}_L\gamma^\mu\left[i\partial_\mu - g\frac{1}{2}\tau_i W_\mu^i - g'(\frac{Y_L}{2})B_\mu\right]\chi_L \\ &\quad +\bar{e}_R\gamma^\mu\left[i\partial_\mu - g'(\frac{Y_R}{2})B_\mu\right]e_R - \frac{1}{4}\mathbf{W}_{\mu\nu}\cdot\mathbf{W}^{\mu\nu} - \frac{1}{4}B_{\mu\nu}B^{\mu\nu} \quad (2.31)\end{aligned}$$

In the above formula, the ordinary partial derivative ∂_μ is replaced by the covariant derivative $D_\mu \equiv \partial_\mu + ig\frac{1}{2}\tau_i W_\mu^i + ig'\frac{1}{2}Y_L B_\mu$ for the left handed weak isospin doublet χ_L. For the right-handed electron singlet e_R, $D_\mu = \partial_\mu + ig'\frac{1}{2}Y_R B_\mu$, as the weak current only has coupling to left-handed fermions. Note the introduced gauge fields $\mathbf{W}_\mu$ and B_μ in the [ ] of Eq 2.31 have exactly the same interaction as Eq 2.23 (except in the form of chiral spinors here). The final two terms are the kinetic energy and self-coupling of the $\mathbf{W}_\mu$ field, the kinetic energy of the B_μ field.

An important property of the Lagrangian $\mathscr{L}_{\rm EW}$ in Eq 2.31 is that a non zero mass term such as $M_W W_\mu^+ W^{-\mu}$ or $M_Z Z_\mu Z^\mu$ can't be added to it without breaking the gauge symmetry. In other words all the vector bosons $\mathbf{W}_\mu$, B_μ, A_μ and Z_μ must be massless according to Eq 2.31. In standard model, the mass of $W^{\pm}$ and Z bosons are generated by the Higgs Mechanism.

The idea is to make the electroweak field be coupled with four real scalar fields ϕ_i which belong to $SU(2)\otimes U(1)$ multiplets. The following $SU(2)\otimes U(1)$ gauge invariant Lagrangian $\mathscr{L}_H$ which describes the interaction between the Higgs field and electroweak field is added to the Lagrangian $\mathscr{L}_{\rm EW}$ in Eq 2.31.

$$\begin{aligned}\mathscr{L}_H &= \left(i\partial_\mu\phi - g\frac{1}{2}\tau_i W_\mu^i\phi - g'(\frac{Y_L}{2})B_\mu\phi\right)^\dagger\left(i\partial^\mu\phi - g\frac{1}{2}\tau_i(W^\mu)^i\phi - g'(\frac{Y_L}{2})B^\mu\phi\right) \\ &\quad -\mu^2\phi^\dagger\phi - \lambda(\phi^\dagger\phi)^2 \quad (2.32)\end{aligned}$$

where ϕ is an $SU(2)$ doublet of complex scalar fields:

$$\phi = \begin{pmatrix} \phi^+ \\ \phi^0 \end{pmatrix} = \frac{1}{\sqrt{2}} \begin{pmatrix} \phi_1 + i\phi_2 \\ \phi_3 + i\phi_4 \end{pmatrix}. \tag{2.33}$$

The last ϕ^4 term indicates the existence of four-particle vertex with coupling λ, in other words ϕ is a self interacting field. For $\mu^2 > 0$, the $-\mu^2\phi^\dagger\phi$ term indicates that the mass of ϕ field is μ. The interesting case is $\mu^2 < 0$ and $\lambda > 0$, with which the Higgs potential $V(\phi) = \mu^2\phi^\dagger\phi + \lambda(\phi^\dagger\phi)^2$ has its minimum at a finite value of $|\phi|$:

$$\phi^\dagger\phi = -\frac{\mu^2}{2\lambda} \tag{2.34}$$

The minimum points occupy a sphere in the $(\phi_1, \phi_2, \phi_3, \phi_4)$ space. One particular choice is

$$\phi_1 = \phi_2 = \phi_4 = 0 \qquad \text{and} \qquad \phi_3^2 = -\frac{\mu^2}{\lambda} \equiv v^2 \tag{2.35}$$

The corresponding point of choice (also called the vacuum expectation value of Higgs field) is

$$\phi_0 = \frac{1}{\sqrt{2}} \begin{pmatrix} 0 \\ v \end{pmatrix} \tag{2.36}$$

Now the $\phi(x)$ field can be expanded around the above vacuum energy point ϕ_0. The original field $\phi(x)$ is substituted with the Higgs field $h(x)$ as shown in Eq 2.37. This is the idea of spontaneous symmetry breaking: after the substitution of $\phi(x)$ with the Higgs field $h(x)$, $\mathscr{L}_H$ will display the mass terms like $-M_W^2 W_\mu^+ W^{-\mu}$ and $-\frac{1}{2}M_Z^2 Z_\mu Z^\mu$. There should be no terms like $-\frac{1}{2}M_A^2 A_\mu^2$, since photons are massless.

$$\phi(x) = \frac{1}{2} \begin{pmatrix} 0 \\ v + h(x) \end{pmatrix} \tag{2.37}$$

Put ϕ_0 into the Lagrangian $\mathscr{L}_H$ of Eq 2.37, the relevant terms to the mass generation of WZ boson are:

$$\begin{aligned} & \left(-g\frac{1}{2}\tau_i W_\mu^i \phi_0 - g'(\frac{Y_L}{2})B_\mu\phi_0\right)^\dagger \left(-g\frac{1}{2}\tau_i (W^\mu)^i \phi_0 - g'(\frac{Y_L}{2})B^\mu\phi_0\right) \\ = & \left(\frac{1}{2}vg\right)^2 W_\mu^+ W^{-\mu} + \frac{1}{8}v^2\left[gW_\mu^3 - g'B_\mu\right]^2 + 0\left[g'W_\mu^3 + gB_\mu\right]^2 \end{aligned} \tag{2.38}$$

The above Lagrangian terms correspond to the following mass terms:

$$M_W^2 W_\mu^+ W^{-\mu} + \frac{1}{2} M_Z^2 Z_\mu^2 + \frac{1}{2} M_A^2 A_\mu^2 \tag{2.39}$$

Comparison between Eq 2.38 and Eq 2.39 gives the mass

$$M_W = \frac{1}{2} v g \tag{2.40}$$

$$M_A = 0 \quad \text{with} \quad A_\mu = \frac{g' W_\mu^3 + g B_\mu}{\sqrt{g^2 + (g')^2}} \tag{2.41}$$

$$M_Z = \frac{1}{2} v \sqrt{g^2 + (g')^2} \quad \text{with} \quad Z_\mu = \frac{g W_\mu^3 - g' B_\mu}{\sqrt{g^2 + (g')^2}} \tag{2.42}$$

The relation of coupling strength and weak mixing angle $g'/g = \tan\theta_W$ from Eq 2.29 makes the A_μ and Z_μ expressions above reproduce the mixing in Eq 2.27. Comparing Eq 2.40 with Eq 2.42, we have the mass ratio of W and Z boson.

$$\frac{M_W}{M_Z} = \cos\theta_W \tag{2.43}$$

2.2 W and Z Boson Production

At Fermilab Tevatron, a $p\bar{p}$ collider with the center of mass energy of $\sqrt{s} = 1.96\,\text{GeV}$, the leading process of W and Z boson production is via the valence quarks from proton and antiproton: $u\bar{d} \to W^+$, $\bar{u}d \to W^-$ and $q\bar{q} \to Z$ where q can be either u or d. Those diagrams are shown in Figure 2.2.

The fraction of the proton momentum x carried by the valence quark of flavor i when probed at the energy scale of Q is called the parton distribution function (PDF) $f_i(x, Q^2)$. The production cross section of W and Z boson can be calculated on the parton level and then convoluted with the PDF. Those partons of the same proton or antiproton that don't participate in the production of W and Z boson are called spectator quarks. The resulting particles come from the spectator quarks usually come with very forward and backward directions and have low E_T. In Monte Carlo simulation, the so called minimum bias (MB) data events are used to estimate their contributions. Those MB data events are triggered when at least one hard collision is recorded.

There are also additional $p\bar{p}$ interactions in the same bunch crossing in which W and Z bosons are produced. These interactions are called pile-ups, as the debris of these interaction usually overlap with the signals from true W and Z events. The so called zero bias (ZB) data events are collected to

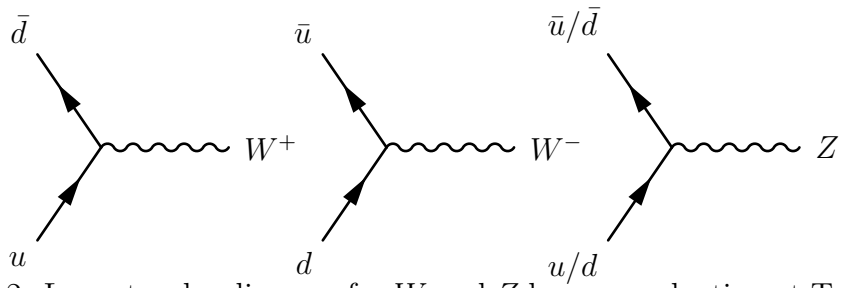

Figure 2.2: Lowest order diagram for W and Z boson production at Tevatron.

simulate their contributions. Those ZB events are taken during the normal running of $p\bar{p}$ collisions, without any trigger requirement. Together MB and ZB events are called the underlying events in the fast Monte Carlo simulation.

2.2.1 Mass Distribution of W and Z Boson

W and Z boson are produced by two spin-$\frac{1}{2}$ quarks according to relativistic Breit-Wigner resonance:

$$\sigma(m) = \frac{m^2\Gamma_W^2/M_W^2}{(m^2 - M_W^2)^2 + (m^2\Gamma_W/M_W)^2} \tag{2.44}$$

where M_W and Γ_W are the pole mass and width of mass resonance. The observed boson mass spectrum should be the Breit-Wigner distribution in Eq 2.44 convoluted with PDF:

$$\sigma(m) = \sum_{i,j} \int f_i(x_A, Q^2) f_j(x_B, Q^2) \hat{\sigma}(ij) dx_A dx_B \tag{2.45}$$

where the index i, j stand for the quark flavors involved in the W boson production from proton and antiproton. $\hat{\sigma}(ij)$ is the W production cross section on parton level. When the momentum transfer equals to the boson mass $Q^2 = m$, Eq 2.45 can be fitted by adding parton luminosity dependence to Breit-Wigner distribution.

$$\sigma(m) = \frac{e^{-\beta m}}{m} \frac{m^2\Gamma_W^2/M_W^2}{(m^2 - M_W^2)^2 + (m^2\Gamma_W/M_W)^2} \tag{2.46}$$

where β is called the parton luminosity slope.

2.2.2 Boson Transverse Momentum and Rapidity

In the lowest order, the transverse momenta of the valence quarks in protons or antiprotons are negligible compared with their longitudinal momentum.

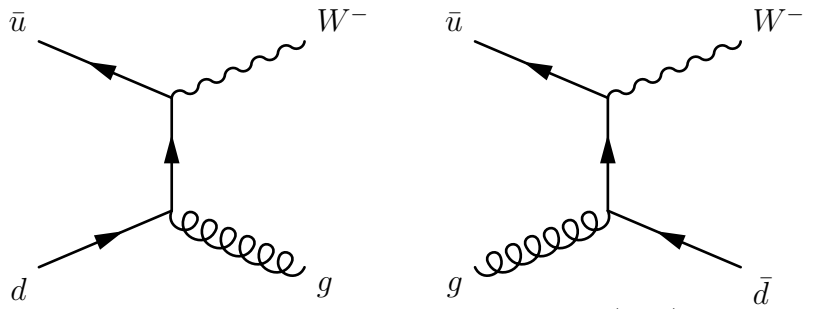

Figure 2.3: A typical initial state radiation of gluon (ISR) in the Drell-Yan production of W^- boson (left). Typical production of W^- via valence quark and sea quark interaction (right). The latter is a much rarer process. Both diagrams contribute to the non zero p_T of W boson.

Therefore the transverse momentum of resulting bosons would have been small on the lowest order, as it is the only product from $q\bar{q}$ interaction. However higher order processes produce recoils against the boson and that makes W and Z bosons have substantial transverse momentum. Among those, the dominant process is the soft gluon radiation by quarks (ISR). Other processes that also contribute to boson p_T include the production of vector bosons from the interaction of valence quarks and sea quarks, although this process is much rare than the Drell-Yan process with ISR.

Straight calculation of boson p_T that takes into account of such diagrams as in Figure 2.3 gives reasonable result for high boson p_T range ($p_T \sim M_W$ or M_Z). However for low boson p_T, the calculation result is divergent. A technique called resummation was proposed to work around this difficulty in calculation [19, 20, 21, 22]. The differential cross section of boson production is

$$\frac{d^2\sigma}{dp_T dy} = \sum_{i,j} \int f_i(x_A, Q^2) f_j(x_B, Q^2) \frac{d^2\hat{\sigma}(ij)}{dp_T dy} dx_A dx_B \tag{2.47}$$

Parton level differential cross section $d^2\hat{\sigma}(ij)/dp_T dy$ can be expanded by a series of strong coupling $\alpha_s \ln(Q^2/p_T^2)$.

$$\frac{d^2\hat{\sigma}}{dp_T dy} \propto \frac{\alpha_s}{p_T^2} \ln\left(\frac{Q^2}{p_T^2}\right) \left[v_1 + v_2 \alpha_s \ln^2\left(\frac{Q^2}{p_T^2}\right) + v_3 \alpha_s^2 \ln^4\left(\frac{Q^2}{p_T^2}\right) + \dots \right] \tag{2.48}$$

The resummation technique rearranges dominant terms of the perturbation series in Eq 2.48 and find the sum of those terms is proportional to an exponential formula. The non-perturbative physics is also taken into account for its importance in the range of $p_T \simeq 0$. The differential cross section in Eq 2.47

is found to be [19]

$$\begin{aligned}\frac{d^2\sigma}{dp_T dy} \propto & \int \frac{d^2b}{(2\pi)^2} e^{i\mathbf{b}\cdot\mathbf{Q}_T} \sum_j \widetilde{W}_j(b_*; Q, x_A, x_B) \\ & \times \exp\left[-\ln\left(\frac{Q}{2Q_0}\right) h_Q(b) - h_{j/A}(x_A, b) - h_{\bar{j}/B}(x_B, b)\right] \\ & + Y(Q_T; Q, x_A, x_B) \end{aligned} \tag{2.49}$$

where b is the the impact parameter in the transverse plane. Small b value corresponds to large p_T and large b value corresponds to small p_T. $\widetilde{W}$ and Y are derived from perturbative calculations. Q_0 is an arbitrary constant. $h_{j/A}$ and $h_{\bar{j}/B}$ are flavor dependent function of momentum fraction x_A and x_B. These two terms describe the nonperturbative behavior at large b, along with function $h_Q(b)$. All these functions are fitted with experimental data. Choice of the $h_Q(b)$, $h_{j/A}$ and $h_{\bar{j}/B}$ function forms must meet the condition that these functions will vanish with $b \to 0$, since non perturbative physics is only important for small p_T (large b value).

One commonly used function form for the non-perturbative physics is [19]:

$$h_Q(b) = g_2 b^2 \qquad h_{j/A}(x_A, b) + h_{\bar{j}/B}(x_B, b) = g_1 b[b + g_3 \ln(100 x_A x_B)], \tag{2.50}$$

where g_1, g_2 and g_3 are phenomenological constants, fitted from data.

2.2.3 W and Z decay

Because of the V-A couplings, at the lowest order W boson is fully polarized along the beam direction. In that case W boson has no transverse momentum and the lepton decaying angle in the W boson rest frame is given by

$$\frac{d\sigma}{d\cos\theta^*} \propto (1 - \lambda q \cos\theta^*)^2 \tag{2.51}$$

where λ is the helicity of the W boson with respect to the proton direction. Most W bosons are produced by the valence-valence quark interaction, in that case $\lambda = -1$. In another extreme case where the incoming quark is from antiproton and the antiquark is from proton, $\lambda = +1$. $q = \pm 1$ is the lepton charge. θ^* is the angle between lepton direction and the proton beam direction in the rest frame of W boson.

When NLO processes are taken into account, W bosons have non zero transverse momentum. θ^* in Eq 2.51 is generalized to θ^* in the Collins-Soper (C-S) frame [24]. C-S frame is the rest frame of the W boson where the z-axis

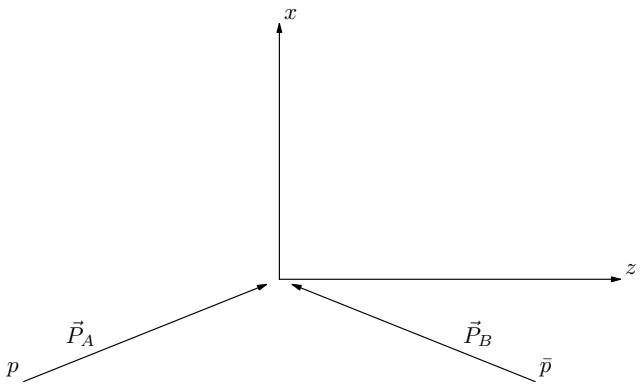

Figure 2.4: Collins-Soper frame. Start with lab frame, boost into the rest frame of the W boson. In that frame the proton momentum $\boldsymbol{P}_A$ is generally not collinear with the antiproton's momentum $\boldsymbol{P}_B$, thus z-axis is defined as the bisector of $\boldsymbol{P}_A$ and $-\boldsymbol{P}_B$. x-axis is defined as the tansverse vector in the plane spanned by $\boldsymbol{P}_A$ and $\boldsymbol{P}_B$.

is defined as the bisector of the proton momentum and the negative of the antiproton momentum with the x-axis along the direction of $\boldsymbol{p}_T^W$ of lab frame.

In the next to leading order QCD calculation, electrons have the polar angle θ^* distribution in the Collins Soper frame as [23]

$$\frac{d\sigma}{d\cos\theta^*} \propto (1 + \alpha_1 \cos\theta^* + \alpha_2 \cos^2\theta^*), \tag{2.52}$$

where the parameters α_1 and α_2 depend on the transverse momentum p_T and rapidity y of W boson.

In the case of $Z \to ee$ events, if we define θ^* as the polar angle of the electron then we have cross section dependence as [25]

$$\frac{d\sigma}{d\cos\theta^*} = C\frac{4}{3}\frac{\pi\alpha^2}{s}R_f[\frac{3}{8}(1 + \cos^2\theta^*) + A_{FB}\cos\theta^*]. \tag{2.53}$$

In the original Collins and Soper's paper [24], $\cos\theta^*$ can be calculated using variables in the proton-antiproton center of mass frame, *i.e.* lab frame. Let $Q(Q_T)$ be the four-momentum (transverse momentum) of the electron and positron pair in $Z \to ee$, P_{e^-} be the four-momentum of the electron and P_{e^+} be the four-momentum of the positron, all measured in the lab frame. Then $\cos\theta^*$ is given by

$$\cos\theta^* = \frac{2}{\sqrt{Q^2(Q^2 + Q_T^2)}}(P_{e^-}^+ P_{e^+}^- - P_{e^-}^- P_{e^+}^+), \tag{2.54}$$

where $P_i^{\pm} = 1/\sqrt{2}(P_i^0 \pm P_i^3)$. P^0 and P^3 represent the energy and z component of four momentum, i stands for either electrons or positrons. In the Collins-Soper frame, electron and posotron are back to back, if electron polar angle is θ^*, then positron would have polar angle as $(\pi + \theta^*)$, and that means positron has opposite $\cos\theta^*$ distribution.

We can modify Eq (2.54) to make it suitable to describe $\cos\theta^*$ for electrons in $W^- \to e^-\bar{\nu}$

$$\cos\theta^* = \frac{2}{\sqrt{Q^2(Q^2+Q_T^2)}}(P_{e^-}^+ P_\nu^- - P_{e^-}^- P_\nu^+). \tag{2.55}$$

Similarly positrons decayed from W^+ have $\cos\theta^*$ as

$$\cos\theta^* = \frac{2}{\sqrt{Q^2(Q^2+Q_T^2)}}(P_{e^+}^+ P_\nu^- - P_{e^+}^- P_\nu^+). \tag{2.56}$$

A detailed derivation of $\cos\theta^*$ Eq 2.54 is given at Appendix A.

2.2.4 Event Generator

Monte Carlo simulations are extensively used in the study of high energy physics. An event generator produces the particles' 4-momentum according the physics distribution. There are two types of Monte Carlo simulations commonly used. One is called fast Monte Carlo, which starts with the physical 4-momentum of particles, then applies energy smearing and other detector effects in explicit function form. The smearing parameters input of fast Monte Carlo are usually obtained from the study of data events. Fast Monte Carlo is very useful in that it provides a parameterized model of the detector effects and physical process, which makes the study of systematic factors much easier.

The other type of Monte Carlo is called full Monte Carlo, which is actually based on the `GEANT` package to simulate the interaction between particles and detector materials. The particle physical 4-momentum are the inputs to the customized `GEANT` package, each particle goes through the complicated particle-material interaction simulation and the output is very much like the real date events.

Two event generators are used in the study of this thesis. The event generator used in the `GEANT` based full Monte Carlo is `PYTHIA`. `RESBOS` is the event generator for the simulation of data, as it uses the resummation technique described in previous section and therefore has better prediction of boson kinematics.

Chapter 3

Experimental Apparatus and Data Acquisition

The data sample of this thesis is collected at the DØ detector of Fermilab Tevatron during its Run IIa period, with integrated luminosity $1\,\mathrm{fb}^{-1}$. DØ has published W mass measurement result using the same dataset [11]. In this chapter, I discuss the major components of DØ detector, especially the calorimeter and tracking subsystems that are used to collect data for the W mass analysis. There are also discussions about the hardware and software of data acquisition (DAQ), trigger system.

3.1 Tevatron

Tevatron is a circular particle accelerator located at Fermilab, in the west suburban of Chicago. Protons and antiprotons are accelerated with center-of-mass energy $\sqrt{s} = 1.98\,\mathrm{GeV}$ in opposite direction along the 6.28 km ring and have collisions at two locations on the ring. Two detectors (DØ and CDF) are built at the collision locations.

A sketch of Tevatron is shown in Figure 3.1. There are several stages before the proton and antiproton are accelerated to the energy of $\sqrt{s} = 1.96\,\mathrm{GeV}$. At the first stage hydrogen gas is ionized at a 750 KeV Cockcroft-Walton pre-accelerator and the negative ions are accelerated by positive voltage. These ions are put into 150 meters long linear accelerator (Linac) and are further accelerated to 400 MeV. At the end of this stage, electrons are removed by the filtering carbon foils and the remaining charged protons are injected in to the Booster.

Booster is a small circular accelerator, where the charged protons continue to be accelerated up to 8 GeV. Protons are then passed to the Main Injector.

The Main Injector serves several purposes, it can further accelerate protons up to 150 GeV before injecting them into Tevatron. Another use of Main Injector is to generate 120 GeV protons which are collided with Nickel target at the antiproton source. A number of particles are produced, including the antiprotons which are kept in the accumulator ring. Antiprotons can be passed back to the Main Injector and then both the protons and antiprotons are injected from Main Injector into the Tevatron ring and are finally accelerated to 980 GeV there.

In March 2001, Tevatron finished upgrading and started Run II. There are 36 bunches of protons and antiprotons along the Tevatron beam line with each bunch spacing of 396 ns. The instantaneous luminosity of RunII on the order of $10^{32}\,\mathrm{cm}^{-2}\mathrm{s}^{-1}$ or more.

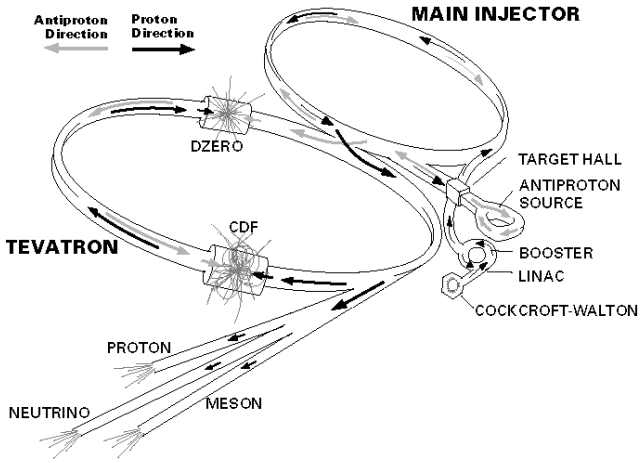

Figure 3.1: Particles in the Fermilab Tevatron. Detailed description can be found in the context.

3.2 DØ Detector

The DØ detector consists of three major subsystems: central tracking detectors, liquid Argon/Uranium calorimeters and a muon spectrometer. There is a significant upgrade of the DØ detector for the Tevatron RunII data taking [16]. Among those major changes, are the addition of magnetic field by solenoid for the tracking and muon subsystems; new tracking systems consisted of the silicon microstrip tracker (SMT) and scintillating-fiber tracker (CFT); new preshower detector added between the tracking system and calorimeter; Muon system updated to provide better radiation resistance and trigger capabilities.

Within the solenoidal magnetic field, the improved tracking system can measure the momentum of charged particles, better muon energy measurement and (E/p) for electrons. SMT also helps in the identification of displaced vertices for b quark tagging. The preshower detector helps to improve the electron identification.

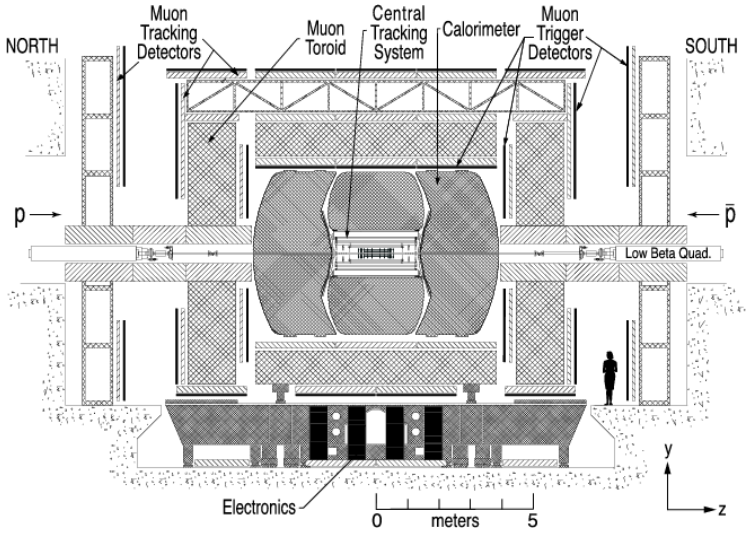

Figure 3.2: The diagram showing DØ detector installed in the collision hall, viewed from inside the Tevatron ring. The central region of the detector is shown in detail in Figure 3.3.

3.2.1 Silicon Microstrip Tracker

Excellent tracking system is essential to the study of electroweak physics. The inner most tracking system of DØ detector is the Silicon Microstrip Tracker (SMT), outer tracking system is the scintillating-fiber tracker (CFT), both of which are surrounded by solenoidal magnet. The combination of SMT and CFT allows the determination the primary interaction vertex with a resolution of 35 μm along the beam line. High precision vertex measurement is necessary for the good measurement of lepton p_T, lepton direction and transverse energy $\not\!\!E_T$.

SMT provides nearly a full $|\eta|$ coverage inside the limited space, due to its hybrid disk/barrel placement of silicon sensors (Figure 3.4). There are 6 barrels in the central region of SMT along the z (beamline) direction, each of them has 4 silicon readout layers. The silicon module installed on each layer is called a "ladder". There are 12 ladders evenly covering ϕ direction for each

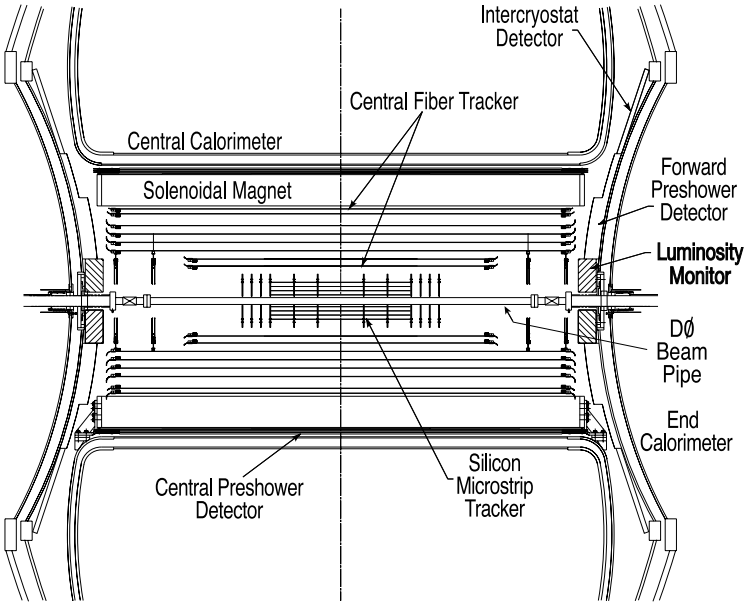

Figure 3.3: Side view of the central tracking system of DØ detector in the x-z plane. Also shown are the preshower detector, central and forward calorimeters.

innermost first and second layer. The number of ladders increases to 24 for the third and fourth layer.

Each barrel is capped at high $|z|$ by a disk with 12 double sided wedge detector, called F-Disk. In the further ends of high z, there are additional 4 H-Disks for large $|\eta|$ coverage. The side view and cross sectional view of the SMT layout are shown in Figure 3.4 and Figure 3.5. Barrel detectors measure the r-ϕ positions and the disk detectors measure the z-r-ϕ positions. For outgoing particles with small $|\eta|$, their tracks are mostly determined by the SMT barrel detectors and the CFT. F-Disks and H-Disks are used in the reconstruction for high $|\eta|$ tracks.

SMT silicon sensors are read out by the 128 channel SVXIIe chip. The chip includes preamp, analog delay, digitization and data specification. Trigger information is received via the serial command link (SLC) by the sequencer crate controller. Sequencer provided by the interface board provides timing and control signals for SVXIIe chips. Upon a Level 1 trigger is accepted, a double correlated sampling is performed and the analog information is converted to digital signal on the SVXIIe chip. Data from the ladder and wedge sensors are sent from sequencers to VME readout buffer (VRB) via optical links. VRBC (VRB controller) receives SCL and use that information to control the operation of VRB. Single Board Computer (SBC) also resides in the

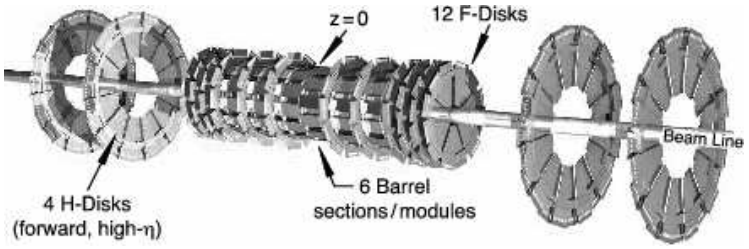

Figure 3.4: The disk/barrel configurations of the SMT sensors.

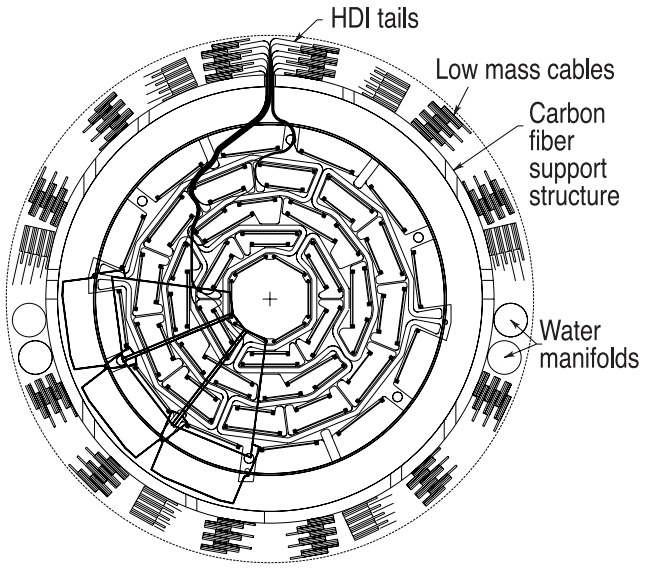

Figure 3.5: Cross sectional view (along the z direction) of the SMT layout. 4 layers of barrel modules and 3 wedges of F-Disk is clearly shown.

same crate of VRB, it collects data from VRB upon the accept of Level 2 trigger and sends to Level 3 readout. The main use of Power PC is data monitoring and calibration. The data flow of SMT operation is briefly described in Figure 3.6.

3.2.2 Central Fiber Tracker

The Central Fiber Tracker (CFT) consists of scintillating fibers mounted on 8 concentric layers. The radial range of the CFT layers is from 20 cm to 52 cm from the center of beam pipe. The inner most two layers of CFT is shorter of 1.66 m length to accommodate the outer SMT H-Disks. The outer 6 layer of CFT are of longer 2.52 m with a coverage of $|\eta| \leq 1.7$. Each layer is actually consisted of three layers of finer fibers, one is oriented along the z direction, and

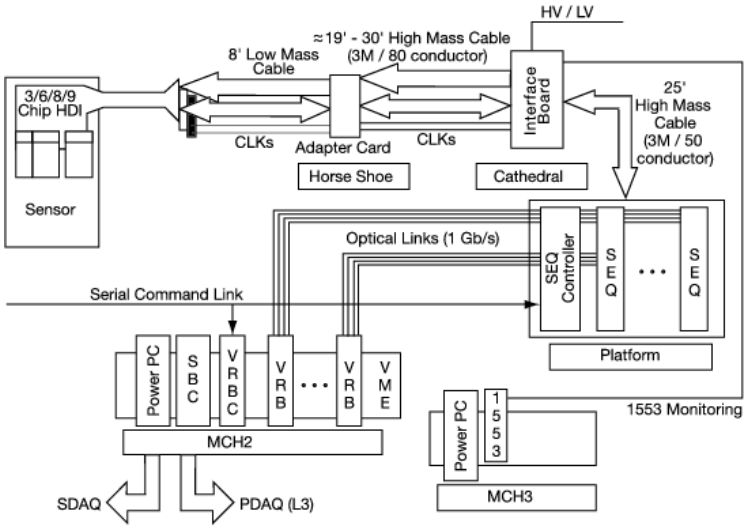

Figure 3.6: Diagram showing the major components of SMT read out system. DAQ will be discussed in section 3.4.

the other is a doublet layer with a slight stereo angle $\phi = +3°$ and $\phi = -3°$. This kind of layout configuration gives better space resolution than the plain all z parallel orientation.

The scintillating fibers are 835 μm in diameter, 1.66 m and 2.52 m in length. Those scintillating fibers are assembled into ribbons consisting of 256 fibers in two layers of 128 each. They are securely fastened into precisely grooved acetal in the supporting cylinder concentric to the beamline.

The scintillating fibers are connected with clear fiber waveguides to transfer the signals to visible light photon counters (VLPC). VLPC is a impurity-bond silicon avalanche photodetector that operates normally at the temperature of 9 K. Their excellent characteristics are suitable to function in an environment with high background noise.

Overall there are about 76800 channels in VLPC read out for CFT. There is an additional 22564 channels of VLPC readout for central and forward preshower detector. Readouts from the doublet layer fibers of CFT are used to form a fast Level 1 hardware trigger based on the number of tracks with minimum p_T threshold. Level 1 track candidates are used in the Level 2 trigger, and the Level 3 trigger uses full CFT information.

3.2.3 Calorimeter

Calorimeter is the major apparatus of DØ detector to measure the energy of electrons, photons and jets, as well as $\not\!\!E_T$ which can be inferred from the

readout of all calorimeter cells. Particles that entering the calorimeter usually initiate showers, the particle's energy is therefore deposited, collected and measured by the calorimeter. Depending on the way energy is measured, most calorimeters are divided into two types: homogeneous and sampling. A homogeneous calorimeter use the same material to produce shower and collect energy. A sampling calorimeter uses two different materials instead. Both the DØ electromagnetic and hadronic calorimeter are of sampling type: dense metal is used for quick shower development while liquid Argon is used to measure the deposited energy. Benefit of a sampling calorimeter is obvious: shower development and energy deposition can take place within different materials, each well-suited to its task. The disadvantage is that some of the shower energy can not be measured directly and thus the overall shower energy has to be estimated.

There are three calorimeters in DØ detector: one center calorimeter covering $|\eta| \leq 1.0$; two end calorimeters ECN (north) and ECS (south), extending coverage to $|\eta| \leq 4$ (Figure 3.7). Each calorimeter contains a inner electromagnetic (EM) section that is close to the interaction point, followed by a fine (FH) and coarse (CH) hadronic section.

The active medium of the calorimeter is liquid Argon, divided into small cells by absorber plates. CC and EC each are contained in its own cryostat which keeps the low temperature at approximately 90 K. Different metals are used as the absorber plates in calorimeters. Thin plates of pure depleted uranium are used in the EM calorimeter. Fine hadronic calorimeter uses the plate made of uranium-niobium alloy, coarse hadronic calorimeter uses relatively thick plate of copper at CC and stainless steel at EC.

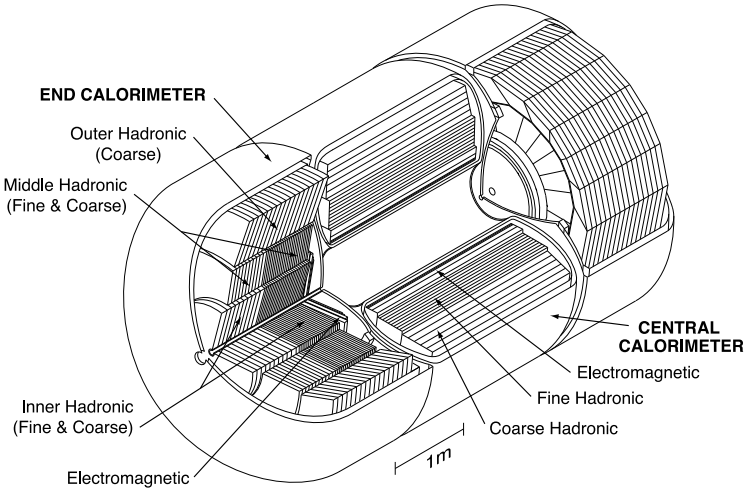

Figure 3.7: Isometric view of the central and two end calorimeters.

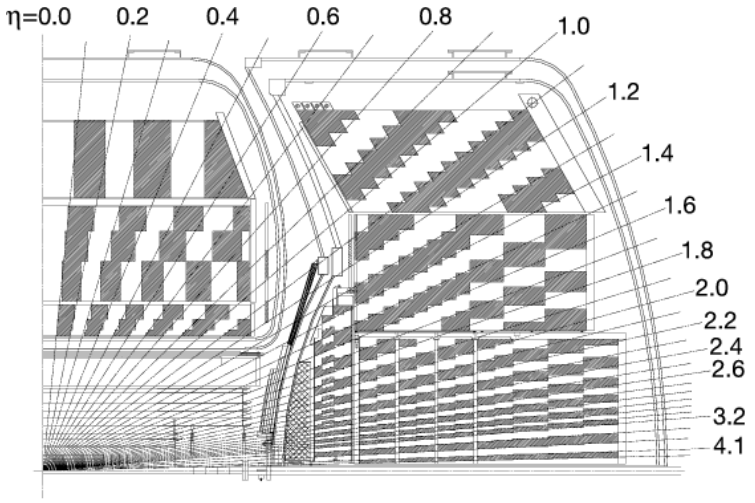

Figure 3.8: Schematic view of a portion of the calorimeters showing the transverse and longitudinal segmentation pattern. The shading pattern indicates groups of cells ganged together for signal readout. The rays indicate pseudorapidity intervals from the center of the detector.

There are 4 separate layers of EM calorimeters in CC and EC. Those layers of EM calorimeters in CC have radiation length 1.4, 2.0, 6.8, $9.8X_0$. For EM calorimeter in EC, the radiation length is 1.6, 2.6, 7.9 and $9.3X_0$. Before entering the calorimeter, electrons and photons have interactions with other materials (SMT, CFT, preshower and cables etc.) and lose some energy in that process. The radiation length of those material is dependent on η of the particle's track. For example, $\eta = 0$ at CC have material of $4X_0$ radiation length before the calorimeter. That value is $4.4X_0$ for $\eta = 2$ in EC.

Calorimeter readout cells layout is shown in Figure 3.8. The transverse size of calorimeter cells is comparable to the transverse width of EM and hadron showers: $1 \sim 2$ cm for EM calorimeter and 10 cm for hadronic calorimeter. Towers in EM and hadronic calorimeter occupy $\Delta\eta \times \Delta\phi = 0.1 \times 0.1$. The third layer of EM calorimeter is segmented twice as fine as the other modules in both η and ϕ, to give better precision of measurement at the location of maximum shower development.

There are 55296 readout channels for the whole calorimeter, among them 47032 channels are actually connected to physical readout module in the cryostat. Each readout channel corresponds to a calorimeter cell. There are three stages for the calorimeter readout. First the signals from the detector is transported to the charge preamplifier located in the cryostat. Then the signals are transported from preamplifier to the analog signal shaping and storage

circuits on the base subtractor boards (BLS). Finally the analog singals from BLS are converted to digital signals via ADC. Those signals entering into Level 3 trigger and stored into tapes.

3.2.4 Muon System

The DØ muon detector consists of a central muon system and a forward muon system. Central muon system ($|\eta| \leq 1.0$ coverage) includes a toroid magnet, the proportional drift chamber (PDT), the cosmic cap and bottom scintillation counters and the $A\phi$ scintillation counter.

There are three layers of PDT, one of them is inside of the toroid magnet and the other two are outside of the toroid magnet. PDT cells are 10.1 cm across, the typical chamber is 24 cells wide with total 72 or 96 cells contained.

The cosmic cap and bottom counters are installed on top, side and bottom of the outer layer of PDT. With the timing information of bunch crossing, it filers the cosmic muon background and provides triggering information for true muon events.

$A\phi$ scintillation counter covers the inner layer PDT. It provides a fast detector for triggering on and identifying muon for rejecting the back scatter from the forward direction.

Forward muon system covers $1.0 < |\eta| < 2.0$ range and consists of four components: end toroid magnets, three layers of MDT for muon tracking reconstruction, three layers of scintillation counter for triggering on events with muon and shielding around the beam pipe.

3.3 Trigger

Trigger system is needed to select interesting events from the vast interaction rate at Tevatron. There are three levels of trigger system examining fewer events with greater details at DØ. The first stage (Level 1 or L1) is based on hardware and the accepting rate is around 2 kHz. The second stage (Level 2 or L2) uses the hardwares and embedded microprocessors of sub-detectors and provide information for a global processor to construct a trigger decision based on individual objects and the correlations between them. Accepting rate for L2 trigger is down to 1 kHz. Trigger information from L1 and L2 are transported to a farm of Lever 3 (L3) microprocessors. Sophisticated algorithms are use in reducing the accepting rate to 50 Hz and these events are recorded in tape for offline reconstruction. An overview of the DØ trigger and data acquisition systems are shown in Figure 3.9. A block diagram showing L1 and L2 trigger is in Figure 3.10.

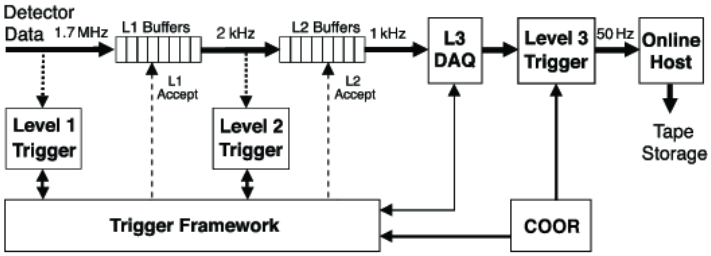

Figure 3.9: Overview of the DØ trigger and data acquisition system.

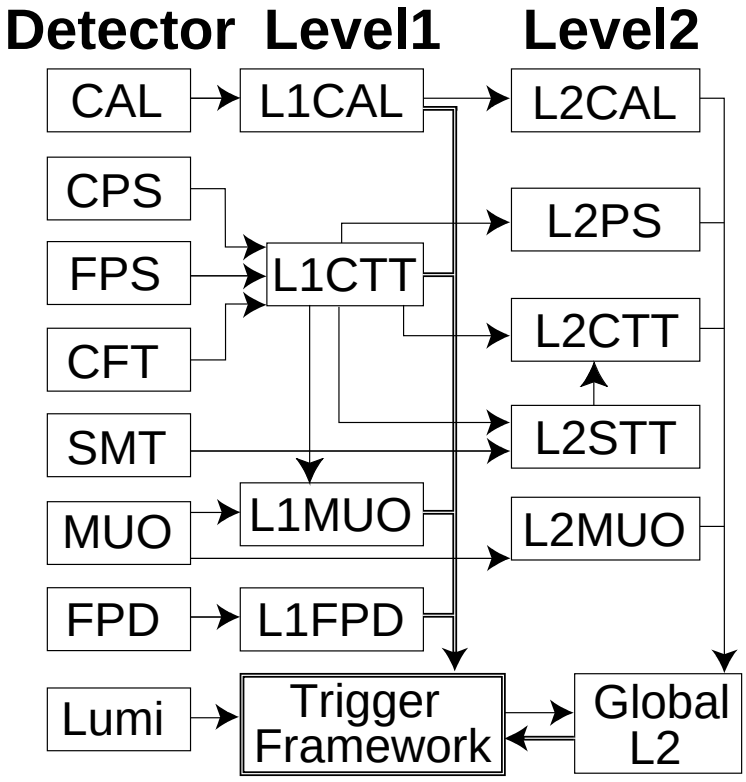

Figure 3.10: Block diagram of DØ L1 and L2 trigger systems. Arrows stand for the flow of trigger related data.

Each event that meets the successive L1 and L2 trigger is fully digitized and sent to a single processor in L3 farm. The buffers of L1 and L2 trigger system reduce the detector dead time while waiting for the L3 trigger decision.

3.3.1 Level 1 Trigger

The Level 1 triggers are implemented in specialized hardware and examine every event for interesting feature. L1Cal uses the calorimeter readout to find the energy deposition exceeding preprogrammed threshold; L1CTT and L1Muon find separate tracks and compare them together to find if they exceed the preset threshold of transverse momentum; the Level 1 forward proton detector trigger (L1FPD) selects diffractive-produced events by triggering protons and antiprotons scattered at small angles.

All L1 trigger information are sent to the trigger framework (TFW). Events are examined at TFW to decide whether a specific event is accepted or not.

For L1Cal, the inputs of trigger include the energy deposition from blocks of calorimeter towers ($\Delta\eta \times \Delta\phi = 0.2 \times 0.2$), extracted from the analog signals in BLS circuits. Energy used in the trigger decision is the sum of E_T of EM calorimeter tower blocks and the total EM plus Hadronic tower blocks.

There are primarily three types of triggers for L1Cal:

- global variables: the sum of all calorimeter towers E_T with 4 thresholds; $\not\!\!E_T$ with 4 thresholds.
- local variables: there is a preset uniform E_T threshold for each of the calorimeter towers, the number of triggered towers can be used in various triggers.
- large tiles: this is mainly for jet triggering, any 4×8 tower in $\eta \times \phi$ above energy threshold are triggered.

L1CTT does hardware based track reconstruction using fast discriminator data from CFT, CPS and FPS. The output of L1CTT is used in overall L1 trigger decision. Although the design of L1CTT is optimized for fast L1 decision, the complete data is stored for latter L2/L3 readout.

L1Muon seeks for patterns that are consistent with muon hits from data of muon drift chamber, scintillating counters and tracks in L1CTT. L1Muon system is divided into central, north and south regions. Data from various front ends arrive at L1Muon asynchronously and must be synchronized before forming a given event for triggering.

3.3.2 Level 2 Trigger

The L2 trigger system collects data from the front-ends and the L1 trigger system to form high quality physics objects and analyze the event-wide correlation across all L2 physics objects. The final decision of L2 trigger is made on the L2Global processor. Events that pass the L2 trigger are fully readout and transported for L3 analysis.

Besides the global processor (L2Global) for the integration of data, there are L2 preprocessors for the following subdetectors: tracking, calorimeter, preshower and muon. The subsystems work in parallel and trigger decisions are made in the L2Global stage based on physics objects reconstructed in the preprocessors.

- **L2Cal**
  L2Cal identifies jets, photons/electrons and calculate event $\not\!\!E_T$ as input for L2Global. Jet algorithm calculates $\sum E_T$ of a 5×5 cluster around seed towers. Seed towers are those with $E_T > 2\,\mathrm{GeV}$. The list of jets is then passed to L2Global which will further apply detailed jets requirements. Photons/electrons algorithms uses a 3×3 cluster around seed towers to calculate an isolation value.

- **L2Muon**
  L2Muon receives the output from L1Muon and front end modules of PDT, MDT and scintillation counters. Quality of muon candidate is further improved in L2Muon.

- **L2PS**
  L2PS has L1CTT as the inputs, which contains the information of both central and forward preshower detectors. Clusters in preshower detectors are combined with the adjacent calorimeter cluster or CFT tracks to give high efficiency electron or photon identification.

- **L2CTT**
  L2CTT receives inputs from L1CTT or L2STT depending on its working mode. Quality of tracks are refined in L2CTT and a final list of tracks sorted in p_T or impact parameters is passed on to L2Global.

- **L2STT**
  L2STT is designed to take inputs from SMT and L1CTT. Starting with the tracks in L1CTT, it utilizes the much fine spaced SMT hits to reconstruct tracks and effectively rejects spurious tracks in L1CTT. Figure 3.11 illustrates the way L2STT works. For each event, L1CTT sends out a list of track candidates. A road is defined around the CFT track,

any SMT hit inside the road is associated with the track. Only the barrel SMT detectors are used in L2STT, where the r-ϕ position is determined. For each successful track fitting, at least 3 of the 4 layer of barrel must have hits; for CFT only the innermost and outermost layer are included in the fit. The result of the fits is sent to L2Global.

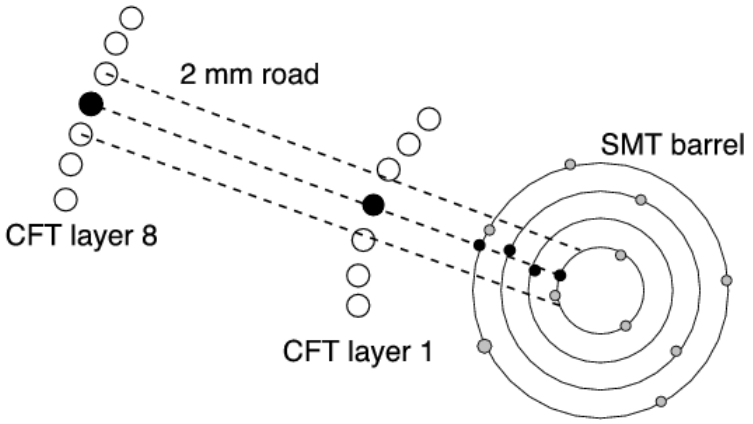

Figure 3.11: Definition of road for L2STT trigger based on L1 tracks and SMT hits.

3.3.3 Level 3 Trigger

L3 trigger is a high level, fully programmable trigger based on software. It does limited event reconstruction, decision is made on not only the individual physical object but also the relationship between them. Interesting variables examined include the longitudinal and azimuthal angle between objects, or invariant mass of them *etc.* Rate of L3 trigger output is 50 Hz, events passing L3 trigger are recorded on tape for offline event reconstruction.

3.4 Data Acquisition

DØ online data acquisition is closely relate to the Level 3 trigger system. Component data of a specific event from VME crates of various subsystems are transported to a node in the L3 farm. Upon accepted by L3 trigger, events are recorded to tape for offline use, hence the name L3DAQ is used. The overall coordination and control of the triggering and acquisition is done by COOR program running on the online host system.

Figure 3.12 shows data flow scheme in L3DAQ. Each event consists of readout information from the 63 VME crates of all subdetector systems. Typical size of the component data for one event is $1 \sim 2\,\mathrm{kB}$. A SBC in each VME is responsible for the readout of VME and send out the data to one or more L3 farm nodes specified by the instructions from Routing Master (RM). An event builder (EVB) process running on the node makes a complete event out of the event fragments. This event is for L3 trigger filter or further permanent storage.

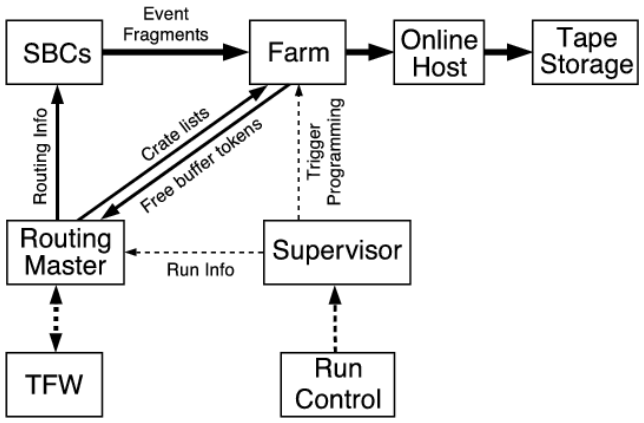

Figure 3.12: Schematic view of the data flow through L3DAQ system.

Communication between L3DAQ and the main DØ run control program (COOR) is through the L3 supervisor process. What it does is to pass the run information (COOR provided) to RM which dictates the collection of event fragment. It also sends the trigger list to the EVB process in relevant L3 farm nodes.

The EVB process on each farm node collates the event fragments received from SBCs into complete events. For each event, the EVB receives an expected-crate list from the RM in order to determine when an event is complete.

Run control and detector configurations are handled by a central coordination program COOR. It receives user setting configurations and send commands such as start and stop run to the detector and the rest of the system.

The online host system receives data from L3 farm node at a rate of 10MB/S (50 Hz with average 200 kB size of each event). Data can be assigned to logging or monitoring streams. Final destination of data is the recoding tape, located at remote Feynmann Computing Center.

Chapter 4

Objects Reconstruction and Events Selection

For the convenience of discussion, let's define the coordinate system used in the DØ experiment. The z-axis is along the proton direction and the y-axis is upward in Figure 3.2, the x-axis is uniquely determined by the right-handed rule. θ and ϕ are the polar and azimuthal angles. The transverse plane is referred as the x-y plane. Pseudorapidity is defined as $\eta = -\ln(\tan\theta/2)$, with $\theta = \pi/2$ corresponding to $\eta = 0$ and $\theta = 0, \pi$ corresponding to $\eta = \pm\infty$. Pseudorapidity equals to the true rapidity $y = 1/2 \ln[(E + p_z c)/(E - p_z c)]$ for limited angles when $mc^2/E \to 0$ for a particle.

The mass of W boson is measured by its decaying particles, in the case of DØ experiment, $W \to e\nu$ is the decay channel of choice. Should the 4-momentum of the electrons and neutrinos are measured, the invariant mass of W boson would have been explicitly calculated. For an electron, its energy and direction can be precisely determined by the calorimeter and tracking system. However the neutrino can only be detected by the in-balance of vector sum of the transverse momentum $\not\!\!E_T$, and no longitudinal information of neutrino can be measured. This make it impossible to directly measure the M_W distribution. An alternative variable M_T called the transverse mass is proposed to substitute the true invariant mass in the measurement [26]. The definition of M_T can be found in Chapter 5. Only the electron transverse momentum p_T^e, $\not\!\!E_T$ and the azimuthal angle ϕ between them are used in the calculation of M_T.

A typical $W \to e\nu$ event features a high p_T electron, large $\not\!\!E_T$ and a hadronic recoil dispersedly against the W boson. $Z \to ee$ data event which usually has two high p_T electrons provides a natural calibration sample, as the invariant Z mass shape can be fully calculated by the 4-momentum of its two decaying electrons. The event display of typical $W \to e\nu$ and $Z \to ee$ events are shown in Figure 4.1.

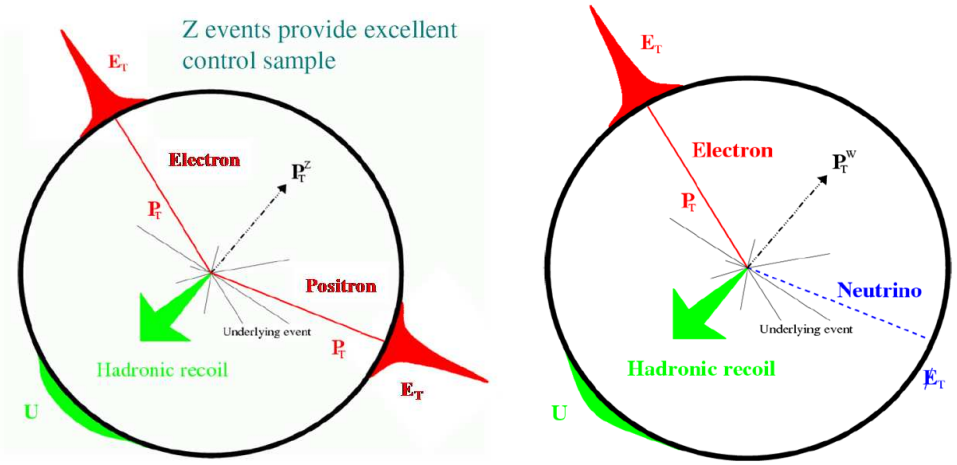

Figure 4.1: The typical event signature of the $Z \to ee$ (left) and $W \to e\nu$ (right) sample on the transverse plane. $Z \to ee$ event features two high p_T electrons, each with large energy deposition in calorimeter. $W \to e\nu$ event has one high p_T electron and large $\not\!\!E_T$. Note the hadronic recoil is against the boson direction. Underlying event has random direction with respect to the physical object.

In the following sections, we will discuss the reconstruction of electron, recoil system and the final event selection of data and full Monte Carlo.

4.1 Electron Reconstruction

Calorimeter is the main apparatus for electron identification and measurement of their energies. The electromagnetic shower of electron are contained within a calorimeter cluster of cone radius $R \equiv \sqrt{(\Delta\eta)^2 + (\Delta\phi)^2} = 0.2$, with the center of cone at the shower peak (Figure 4.2). Energies from cells of EM and FH1 layers within the cone are summed with weights according to the layer location.

Electrons are reconstructed by the `EMReco` package. Depending on the quality of EM showers, different ID numbers are assigned to the reconstructed electrons. The following variables concerning EM shower shape are used in the electron type identification:

- EM isolation f_{iso} is the fraction of energy deposition in the donut region between $0.2 < R < 0.4$ compared with all of the energy within $R < 0.4$.

$$f_{\text{iso}} = \frac{E(R < 0.4) - E(R < 0.2)}{E(R < 0.4)} \tag{4.1}$$

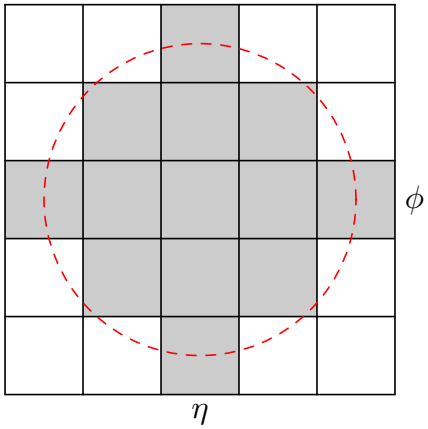

Figure 4.2: The calorimeter cluster within $R \equiv \sqrt{(\Delta\eta)^2 + (\Delta\phi)^2} = 0.2$ for the electron reconstruction. Each small cube in the plot stands for $\Delta\eta \times \Delta\phi = 0.1 \times 0.1$ in calorimeter. Center of the cluster is located at the shower peak.

- EM fraction f_{EM} stands for the EM energy deposition fraction relative to the total energy deposition (EM+FH1 combined).
- HMx7 and HMx8 are the χ^2 variables to describe the shower shape deviation from the standard EM shower shape. HMx7 has better discrimination for electrons in CC and HMx8 is a better variable for electrons in EC.

To determine how close a track is matched to an EM cluster, a track is extrapolated to the EM3 layer of the calorimeter. A match quality χ^2 variable is computed to stand for the distance between the extrapolated track and the calorimeter measured shower center, both in the azimuthal direction Δs and z direction Δz:

$$\delta^2_{\text{trk}} = \left(\frac{\Delta s}{\delta s}\right)^2 + \left(\frac{\Delta z}{\delta z}\right)^2 \tag{4.2}$$

where δs and δz are the spatial resolution of the track. In EC, z is replaced with r, the radial distance from the center of the detector.

If the electron has $E_T > 1.5\,\text{GeV}$ and $f_{\text{EM}} > 0.9$, it is labeled as type ID $= \pm 10$. Depending on whether there is a spatial track associated with this EM cluster, the electron can be further labeled as ID $= \pm 11$. The sign of ID is determined by whether it is an electron or positron.

There are two ways of calculating the direction of electrons. If there is no track associated with the EM cluster, the direction is solely determined by the

central shower position at the finer EM3 layer and the primary vertex.

$$\begin{aligned} \tan\phi(e) &= \frac{y_{\rm cal} - y_{\rm vtx}}{x_{\rm cal} - x_{\rm vtx}} \\ \tan\theta(e) &= \frac{\sqrt{x_{\rm cal}^2 + y_{\rm cal}^2} - \sqrt{x_{\rm vtx}^2 + y_{\rm vtx}^2}}{z_{\rm cal} - z_{\rm vtx}} \end{aligned} \tag{4.3}$$

In the case where a track is associated with the EM cluster, the electron direction is adopted from the track directly, because of the better spatial resolution of the tracking system.

$$\begin{aligned} \phi(e) &= \phi_{\rm trk} \\ \theta(e) &= \theta_{\rm trk} \end{aligned} \tag{4.4}$$

Ignoring the electron mass, the momentum of the electron is given by

$$\overrightarrow{p_e} = E(e) \begin{pmatrix} \sin\theta\cos\phi \\ \sin\theta\sin\phi \\ \cos\theta \end{pmatrix} \tag{4.5}$$

The energy of electron reconstructed in `EMReco` doesn't take into account of the dead materials in front of the calorimeter. This correction is done by studying the single electron events in the full Monte Carlo simulations which contains the right amount dead material as in the real DØ detector. Electron samples with fixed energy from 5 GeV up to 170 GeV are generated and go through the full Monte Carlo simulation. The electron energy obtained from `EMReco` is compared with the input vale, hence the correction factor for dead materials is determined.

The EM correction is obtained as a function of the electron physics η (which is the direct indication of the dead material) and the incident energy. Figure 4.3 shows two of such correction curves in different η range. EM corrections obtained in the above way are incorporated into `EMReco` package and applied to data.

4.2 Recoil System and $\not\!\!E_T$

The raw $\not\!\!E_T^{\rm raw}$ is defined as the vector sum of all the calorimeter cell energy except those in coarse hadronic and ICD region.

$$\overrightarrow{\not\!\!E_T}^{\rm raw} \equiv -\sum_i E_i \sin\theta_i \begin{pmatrix} \cos\phi_i \\ \sin\phi_i \end{pmatrix} \tag{4.6}$$

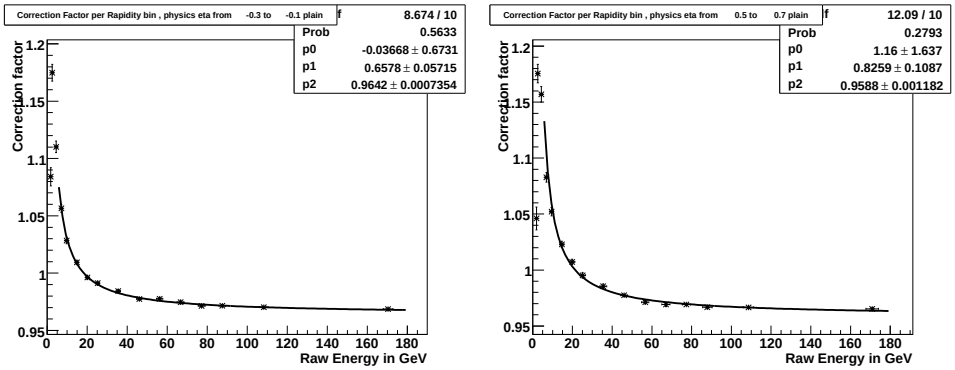

Figure 4.3: Left: Correction factor versus the raw energy as reconstructed in the calorimeter in eta range $-0.3 < \eta < -0.1$. Right: same in eta range $0.5 < \eta < 0.7$ [27].

E_i is the cell energy, θ_i and ϕ_i are the cell direction with respect to the primary vertex. Primary vertex obtained from event reconstruction is replaced with tracking vertex, if the tracking vertex z is more than 2 cm away from the reconstructed vertex. A more meaningful variable is the corrected $\not\!\!E_T$, which has the raw energy of those cells that are belong to quality electron clusters be replaced with object level energy.

The recoil $p_T^{\rm rec}$ (sometimes called u_T) against the W boson is defined as the vector sum of all calorimeter cells (no coarse hadronic and ICD), except for those belong to electron clusters. In Z and W data events, the relation between recoil $p_T^{\rm rec}$ and $\not\!\!E_T$ are thus the following,

$$\overrightarrow{p_T^{\rm rec}}(Z) = -\overrightarrow{p_T^{e_1}} - \overrightarrow{p_T^{e_2}} - \overrightarrow{\not\!\!E_T}(Z) \quad (4.7)$$

$$\overrightarrow{p_T^{\rm rec}}(W) = -\overrightarrow{p_T^{e}} - \overrightarrow{\not\!\!E_T}(W) \quad (4.8)$$

One thing we should be aware of in the above calculation of W and Z recoil is that the underlying event contribution inside the electron window is not taken into account. The more accurate formula of recoil should replace $\overrightarrow{p_T^e}$ with $\overrightarrow{(p_T^e - \Delta u_\parallel)}$ in Eq 4.7 and Eq 4.8. $\Delta u_\parallel$ is the energy flow of underlying event entering the electron cluster. $\Delta u_\parallel$ is dependent on the instantaneous luminosity and $u_\parallel$ which is the projection of recoil p_T on the direction of election p_T.

$$u_\parallel = \overrightarrow{u_T} \cdot \hat{p}_T \quad (4.9)$$

The distribution of $\Delta u_\parallel$ is shown in Fig 4.2 for full Monte Carlo and Fig 4.2 for data [28]. The average $\langle \Delta u_\parallel \rangle = 130$ MeV for electrons in CC.

In the standard method of W mass measurement, energy of underlying

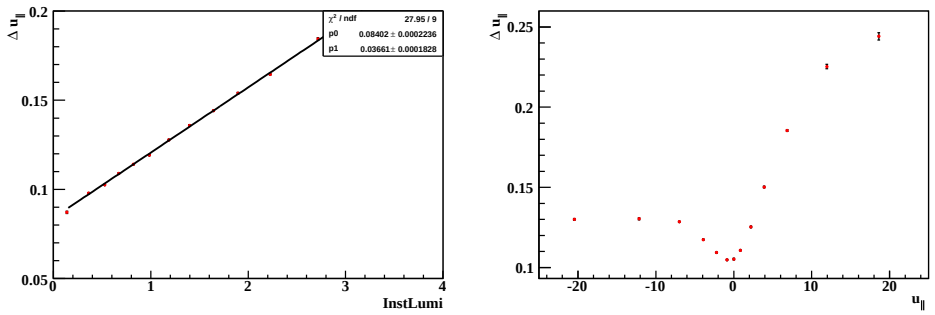

Figure 4.4: Left: Luminosity dependence of $\Delta u_{\parallel}$ correction. Right: $u_{\parallel}$ dependence of $\Delta u_{\parallel}$ correction for GEANT MC events. Unit of $\Delta u_{\parallel}$ is in GeV.

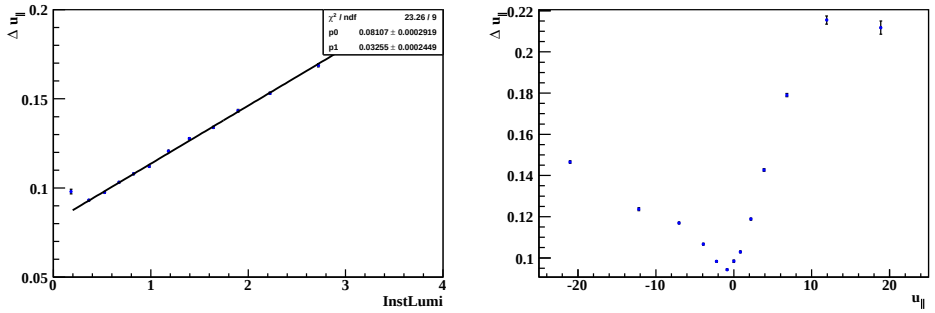

Figure 4.5: Left: Luminosity dependence of $\Delta u_{\parallel}$ correction. Right: $u_{\parallel}$ dependence of $\Delta u_{\parallel}$ correction for real data.

event inside of the electron cluster window is not corrected for data and full Monte Carlo. Instead the $\Delta u_{\parallel}$ correction is applied to fast Monte Carlo.

In data and full Monte Carlo, the measured recoil actually has three contributions of different physics origins (section 2.2).

- The direct recoil against boson is from the initial state radiation (ISR) of incoming quarks. In the fast Monte Carlo simulation, this is called the hard recoil.

- The spectator quark interactions in the same $p\bar{p}$ collision, which is called the soft recoil. Minimum bias (MB) events are used to describe them in the fast Monte Carlo simulations.

- The soft collision from other $p\bar{p}$ in the same bunch crossing. Strictly speaking, this is the true underlying event contribution. In fast Monte Carlo simulations, Zero bias events are used to simulate this process.

Combination of the above contributions in the fast Monte Carlo simulation of underlying events is well calibrated by comparing the relevant physics variables that are sensitive to recoil modelling in $Z \rightarrow ee$ fast Monte Carlo and data events. Detailed discussions about the simulations of electrons and the recoil system in W and Z events will be presented in Chapter 6.

4.3 Event Selections

In ratio method, the electron selection cuts are almost the same as those in the standard method. Two slight different selection cuts in the ratio method are

- One tight and one loose electrons are required for $Z \rightarrow ee$ events in stead of two tight electrons in the standard method. The tight electron is in CC, while the loose electron can be in CC and EC.
- The electron p_T and $\not\!\!E_T$ cuts is set at 30 GeV instead of 25 GeV in the standard method.

The first change in the above has to do with the ratio method itself, the second one is related with the acceptance difference on the M_T of W and Z. Detailed discussion of the choice of cuts will be presented in Chapter 6.

The loose electron selection cuts are the following:

- Electron ID must be ± 10 or ± 11.
- The minimum electron $p_T^e > 15$ GeV.

The tight electron must be loose electron plus the following additional cuts:

- $p_T^e > 30$ GeV.
- EM isolation $f_{\rm iso} < 0.15$ and EM fraction $f_{\rm EM} > 0.90$.
- Electron must be in the η and ϕ fiducial regions of the calorimeter.
- Electron HMx7 < 12 if in CC ($|\eta_{\rm CC}| < 1.05$), or HMx8 < 20 if in EC ($1.5 < |\eta_{\rm CC}| < 2.5$).
- Electrons must have a matched track which has at least one SMT hit and track $p_T > 10$ GeV.

Common selection cuts for both $W \rightarrow e\nu$ and $Z \rightarrow ee$ events are:

- There is at least one primary vertex for each event and $|z_{\text{vtx}}| < 60\,\text{cm}$ for the primary vertex.
- Recoil against W and Z boson in the transverse plane $p_T^{\text{rec}} < 15\,\text{GeV}$.
- $\not\!\!E_T > 30\,\text{GeV}$ for both W and Z events ($\not\!\!E_T$ of Z is after making the loose electron as neutrino and then scaled by (M_W/M_Z).)
- Electron from W is in CC only. Tight electron of Z is in CC and loose electron is in CC or EC.

Chapter 5

Ratio Method Analysis Strategy

The standard method of measuring the W boson mass at DØ and CDF is described in Chapter 1.3. A detailed parameterized fast Monte Carlo simulation of the $W \to e\nu$ events is compared with data. Since the W boson invariant mass can not be explicitly reconstructed, as the z component of neutrino momentum can't be measured, electron p_T^e, $\not\!\!E_T$ and transverse mass M_T spectrum are used in the comparison between fast Monte Carlo and data. Spectrum templates of the above three variables are generated with different M_W and the best matched one corresponds to the M_W in data.

Transverse mass M_T is a variable similar to the M_W, with only the transverse components of 4-momentum involved in the M_T calculation [26]. The invariant mass of W boson is

$$\begin{aligned} M_W^2 &= g_{\mu\nu}(p^\mu(e) + p^\nu(\nu))(p^\mu(e) + p^\nu(\nu)) \\ &= 2(E(e)E(\nu) - p_x(e)p_x(\nu) - p_y(e)p_y(\nu) - p_z(e)p_z(\nu)) \\ &= 2E(e)E(\nu)(1 - \cos\gamma(e,\nu)) \end{aligned} \tag{5.1}$$

where γ is the angle between electron and neutrino direction. Keeping only the transverse components gives the transverse mass:

$$\begin{aligned} M_T^2 &= 2(E_T(e)E_T(\nu) - p_x(e)p_x(\nu) - p_y(e)p_y(\nu)) \\ &= 2E_T(e)E_T(\nu)(1 - \cos\phi(e,\nu)) \end{aligned} \tag{5.2}$$

where $\phi(e,\nu)$ is the azimuthal angle between electron and neutrino. This variable has the advantage that its spectrum is insensitive to the W boson production dynamics. Correction to M_T due to boson dynamics is on the order of $(q_T/M_W)^2$ where q_T is the transverse momentum of W boson. M_T is also not sensitive to selection bias that prefers certain event topologies. M_T variable contains the information of both $\overrightarrow{p_T^e}$ and $\overrightarrow{\not\!\!E_T}$, therefore it is also

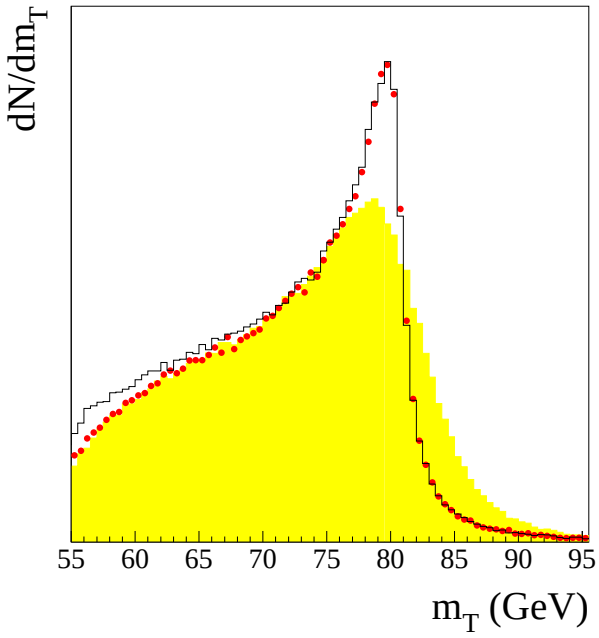

Figure 5.1: M_T spectrum for W bosons with $q_T = 0$ (solid lines), with the correct q_T distribution (•), and with detector resolutions (shaded area) [35].

sensitive to the measurement of electrons as well as the recoil system.

In the rest frame of W boson, electron and neutrino recoils back to back, each carrying energy of $\frac{1}{2}M_W$. The measured spectra of p_T^e and $\not\!\!E_T$ in the lab frame depend on the boost of W boson in the transverse plane. A successful fit of p_T^e and $\not\!\!E_T$ spectrum between fast Monte Carlo and data requires accurate W boson p_T production.

The properties of p_T^e and M_T are illustrated in Fig 5.1 and Fig 5.2, where the effect of W boson p_T and detector simulations on the these variables are shown. W boson p_T has little effect on the shape of M_T, while the effect of detector resolution is much more important. The situation is reversed for p_T^e spectrum, where boson p_T has dominant effect.

5.1 Standard Method of W Mass Measurement

Standard method starts with the 4-momentum of electrons and neutrinos produced by the generator. All the detector effects are put into the fast Monte

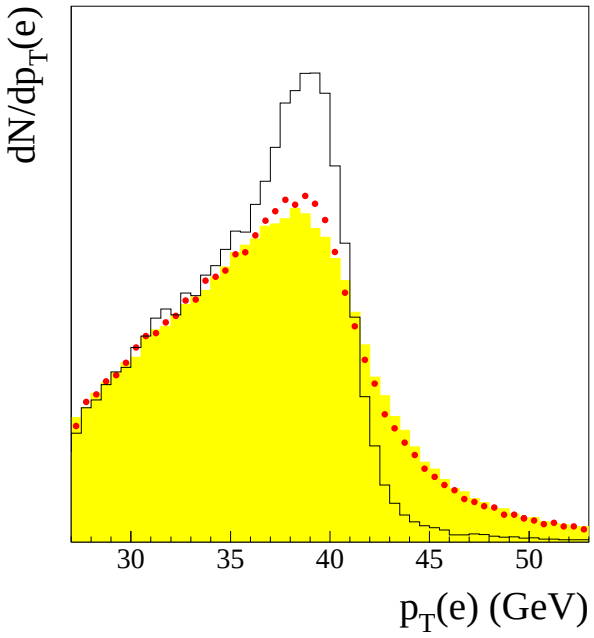

Figure 5.2: Electron p_T^e spectrum for W bosons with $q_T = 0$ (solid line), with the correct q_T distribution (•), and with detector resolutions (shaded area) [35].

Carlo simulations, therefore the resulting $W \to e\nu$ events in fast Monte Carlo is supposed to reproduce every aspect of the $W \to e\nu$ events in data. M_W is fitted for each of the p_T^e, $\not\!\!E_T$ and M_T spectrum, and the three spectra provide a cross-check with complementary systematics.

There are several ways $Z \to ee$ events can be used in the W mass measurement. In the standard method [11], parameterized models are fitted with the $Z \to ee$ sample. The fitted parameters (with fitting uncertainties) are directly or indirectly put into the $W \to e\nu$ fast Monte Carlo simulations. Among those, some of the most important uses of $Z \to ee$ sample include:

- measure the sampling term for electron resolution.
- measure of the EM energy scale and offset for fast Monte Carlo electrons.
- determine hard recoil smearing parameters.
- efficiency measurement, by requiring one tight electron as the tag and measure the efficiency on loose electron.

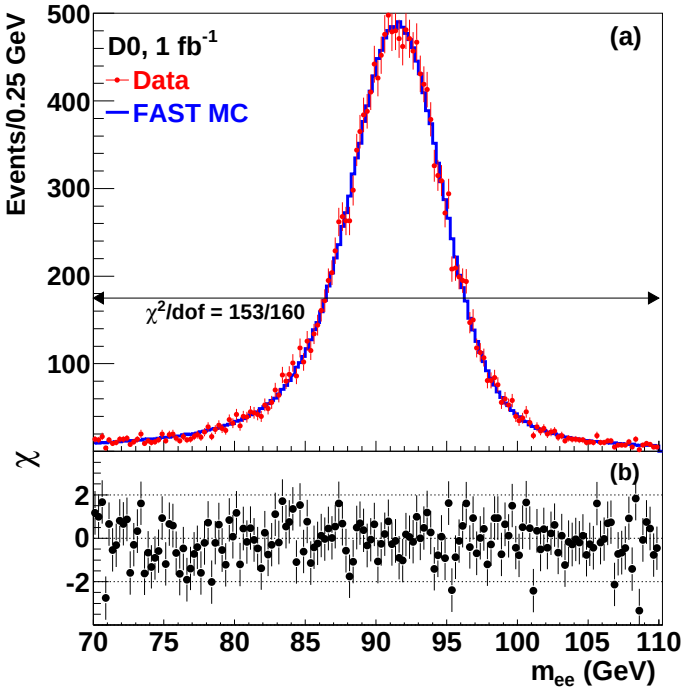

Figure 5.3: The dielectron invariant mass for $Z \to ee$ data and from the fast Monte Carlo simulation [11].

In other words, the calibration of electron energy and recoil system is all done by the $Z \to ee$ sample in the standard method. For example, after the electron calibration, the invariant $Z \to ee$ mass shape are perfectly reproduced in the fast Monte Carlo (Fig 5.3). The measured M_W by fitting fast Monte Carlo simulations and data is actually the W boson mass in scale of the Z mass. Many of the systematic uncertainty in the W fast Monte Carlo model come from the limited $Z \to ee$ statistics in the parameters fitting. Table 5.1 lists the systematic uncertainty from the $1\,\mathrm{fb}^{-1}$ DØ Run IIa measurement. The dominant systematic uncertainty is the electron energy calibration, which measures the energy scale and offset for electrons in the fast Monte Carlo simulation by reproducing the $Z \to ee$ mass peak shape in Fig 5.3.

In standard method, fast Monte Carlo simulation is implemented in a package called `wz_epmcs`. For the $1\,\mathrm{fb}^{-1}$ size data, the simulation of electron and recoil system requires a fairly complicated fast Monte Carlo model that has reasonable agreement with data. With substantial high instantaneous luminosity events recorded in the DØ RunIIa data, the simulation of the recoil system turns out to be especially difficult [30].

For the recoil simulation in fast Monte Carlo, in stead of fitting the com-

Source	σ MeV M_T	p_T^e	$\not\!\!E_T$
Electron energy calibration	34	34	34
Electron resolution model	2	2	3
Electron energy offset	4	6	7
Electron energy loss model	4	4	4
Recoil model	6	12	20
Electron efficiencies	5	6	5
Backgrounds	2	5	4
Experimental Subtotal	35	37	41
PDF	10	11	11
QED	7	7	9
Boson p_T	2	5	2
Production Subtotal	12	14	14
Total	37	40	43

Table 5.1: Systematic uncertainties of the W boson mass measurement [11].

plicated parameterized model with $Z \to ee$ data, one may choose to put the recoil of $Z \to$ data events into the fast Monte Carlo directly, thus omitting the procedure of complex parameterization. This method is called the recoil library method and has been adopted by the DØ Run IIa W width measurement [31]. Recoil library method still uses the templates generated in fast Monte Carlo and extracts M_W and Γ_W by fitting to the $W \to e\nu$ data.

The above "data direct" idea can be pushed even further. For the $W \to e\nu$ simulation, not only the recoil part, but also the electron part is obtained from $Z \to ee$ data directly. In other words the $Z \to ee$ data is compared with $W \to e\nu$ data directly, the best matched $Z \to ee$ gives the measured M_W.

The motivation behind the method of "W and Z data comparison" is to avoid neglecting the correlations inside $W \to e\nu$ and $Z \to ee$ data in the artificially parameterized fast Monte Carlo model. With more W and Z data to be fitted in the standard method, parameterized models of fast Monte Carlo simulation have to be even more complicated to have reasonable agreement with data. High instantaneous luminosity events are likely to have more presence in the recorded data, some correlations will become more important than in those low statistical and low instantaneous luminosity events. In that perspective, data to data comparison will show more attractions than the comparison between fast Monte Carlo and data.

One way to use the $Z \to ee$ data is fully transforming it into $W \to e\nu$ events. In the rest frame of Z, boson mass is changed from M_Z to M_W (with

M_W/M_Z or $(M_W - M_Z)$ as the floating parameters to be fitted). The energy of dileptons are reset from $\frac{1}{2}M_Z$ to $\frac{1}{2}M_W$ while the direction of each lepton is still kept the same. We do know that the $Z \to ee$ and $W \to e\nu$ events have different lepton decaying angles distributions $\cos\theta^*$ in the boson rest frame as shown in both Eq 2.52, Eq 2.53 and Fig 5.5, Fig 5.6 (only polar angle is relevant here, as the azimuthal angle distribution is flat). To really change $Z \to ee$ into $W \to e\nu$, we need to make the lepton $\cos\theta^*$ distribution in Z boson rest frame the same as in $W \to e\nu$ events and that could be done by $\cos\theta^*$ reweighting, which is discussed in Chapter 5.2.1.

In the above $Z \to ee$ to $W \to e\nu$ transformation, one of the two electrons decayed from Z is discarded as the neutrino in $W \to e\nu$ event. Both leptons are then boosted back into lab frame and result in a $W \to e\nu$ event. Since W and Z bosons have different distributions of transverse momentum p_T and rapidity y, a reweighting of both variables is necessary to make sure a perfectly transformed $W \to e\nu$ event in Z boson rest frame is still valid after being boosted back into the lab frame. After these corrections, in lab frame, the transformed $W \to e\nu$ events from $Z \to ee$ should be similar to true $W \to e\nu$ events in every aspect.

In this method (called the transforming method), $(M_W - M_Z)$ or (M_W/M_Z) can be extracted by comparing the p_T^e, $\not\!\!E_T$ and M_T spectra of the transformed W events and the true W events. In the original paper [32], this method is applied up to the generator level $Z \to ee$ and $W \to e\nu$ events with simple Gaussian smearing of the electron and recoil system. The crucial step of how to apply this method to data analysis is not clear.

Another method (called the ratio method) [33, 34] is based on the observation that transverse mass M_T of W and Z boson scales with the boson mass. Here the transverse mass of $Z \to ee$ events is calculated in the same way as $W \to e\nu$: one of Z's two electrons is discarded to be treated as neutrino. If we scale the M_T spectrum of Z, the resulting M_T spectrum would be very similar to the M_T of W events on the condition that the scaling factor is set to M_W/M_Z. For a fixed Z sample, we can generate templates of $M_T^{\rm temp}$ spectrum using the template mass ratio $M_W^{\rm temp}/M_Z$. W mass is then extracted by finding the best matched M_T templates of Z. A fast Monte Carlo simulation of ratio method on M_T spectrum is illustrated in Figure 5.4.

Both the transforming method and the ratio method are applied to the generator level $Z \to ee$ and $W \to e\nu$ events in the following sections. M_T fitting in both methods gives similar measured M_W. Starting from the next chapter of this dissertation, we only discuss ratio method and make W boson mass from data using it. We didn't attempt to make W mass measurement using transformation method.

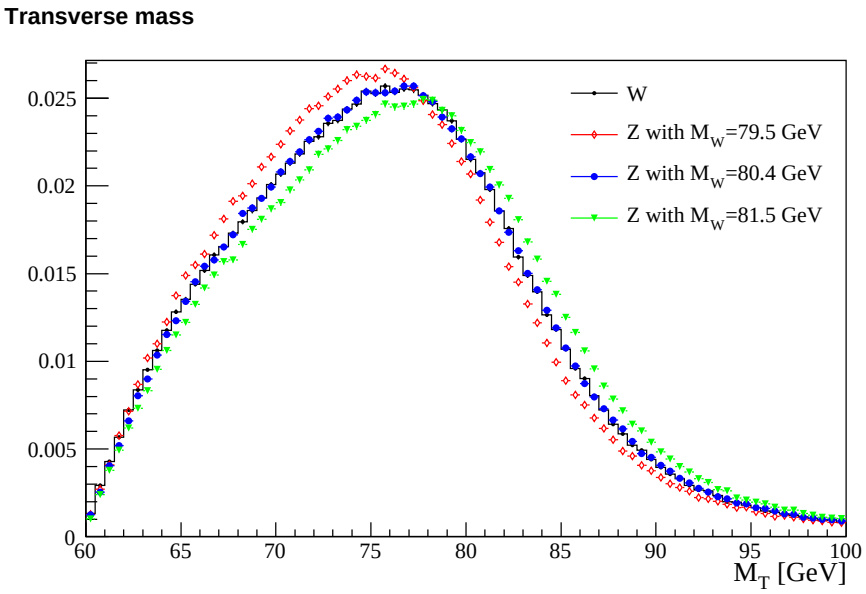

Figure 5.4: Comparison of the M_T spectrum between $W \to e\nu$ and $Z \to ee$ events. M_T of $Z \to ee$ events is scaled with different M_W/M_Z mass ratio. The best matched M_T of $Z \to ee$ events corresponds to the correct W mass (blue points, $M_W = 80.4\,\text{GeV}$). This plot is based on the fast Monte Carlo simulations which have incorporated major physical and detector effects. $2\,\text{fb}^{-1}$ $W \to e\nu$ and $6\,\text{fb}^{-1}$ $Z \to ee$ events.

Extrapolation of the transformation method to data or full Monte Carlo events is not as straightforward as on the generator level. One needs to figure out how to do the physics transformation with the smeared data which are already after acceptance and kinematic cuts. Apart from the above technique difficulty, a more important problem is to justify transforming the $Z \to$ data into $W \to$ data. Physically they have different properties, for data which have undertaken all the detector effects, transforming $Z \to ee$ into $W \to e\nu$ is not easier than the straightforward route of W fast Monte Carlo to W data, which is adopted by the standard method. Transforming $Z \to ee$ to $W \to e\nu$ doesn't offer extra benefit than the standard method.

5.2 Transform $Z \to ee$ to $W \to e\nu$

In this section, a $Z \to ee$ to $W \to e\nu$ transformation is performed on the generator level events. As mentioned in Chapter 2.2.4, `resbos` is used to produce 4-momentum of particles. The analysis procedure is similar to that

described at [32]. The ideas is to make corrections to the physical variables of Z boson (m, p_T, y) and its decayed electrons $(\cos\theta^*)$. The final correction is the product of all separate corrections.

5.2.1 $\cos\theta^*$

Leptons decaying from W and Z boson have different direction distributions (Eq 2.52 and Eq 2.53). Of physics importance is the electron polar angle $\cos\theta^*$ in the Collins-Soper frame (Fig 2.4). The value of $\cos\theta^*$ can be calculated in two ways: one is in terms of the lepton's 4-momentum in the lab frame (Eq 2.55 for W^-); the other is through the `TLorentzVector::Boost()` function in `ROOT` and do the calculation in Collins-Soper frame, according to the definition of $\cos\theta^*$.

The $\cos\theta^*$ distribution of W and Z are shown in Figure 5.5 and Figure 5.6, two calculations coincide with each other. Features such as W boson charge asymmetry and Z boson backward-forward asymmetry are obvious in those plots.

The $\cos\theta^*$ ratio of W over Z for electrons and positrons in Fig 5.7 are treated as event weights in the transformation of Z to W. Due to the symmetry between the electron's and positron's event weight shape, we could envisage that the $\cos\theta^*$ reweighting would be in vain, since the W sample consists of half W^+ events and half W^- events, hence electrons and positrons reweighting would cancel. This is shown in Fig 5.8, there is virtually no difference of $\cos\theta^*$ distribution in Z after applying reweighting. Therefore there is no need to do the $\cos\theta^*$ reweighting if the W sample is inclusive (equal amount of $W^\pm$) and the possibility of electron/positron being chosen to fake neutrino in Z sample is the same.

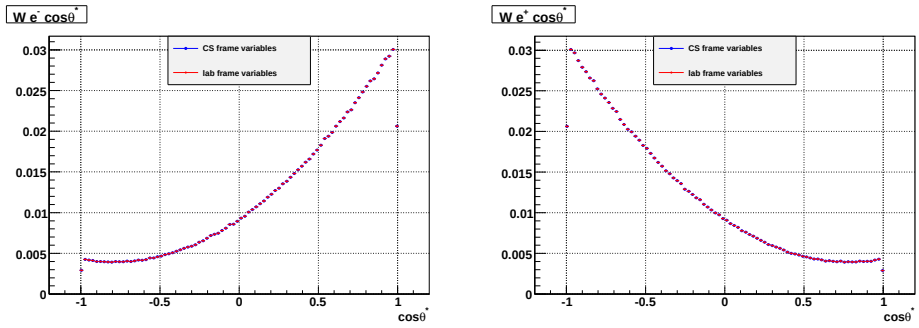

Figure 5.5: Normalized electron $\cos\theta^*$ distribution in $W^- \to e^-\nu$ and positron distribution in $W^+ \to e^+\nu$. Two ways of $\cos\theta^*$ calculation mentioned in the context are shown to be the same.

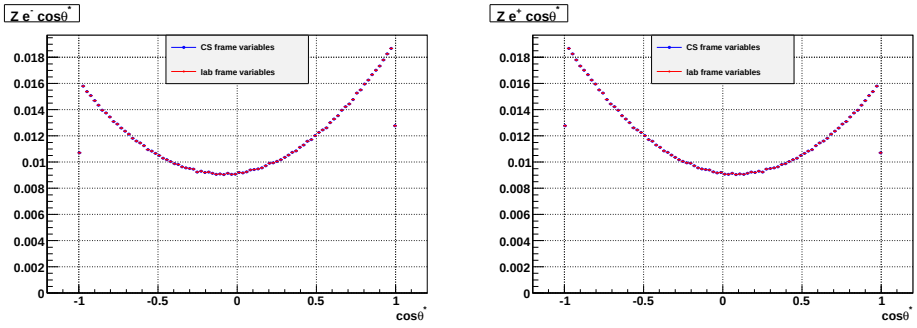

Figure 5.6: Normalized electron and positron $\cos\theta^*$ distribution in $Z \to e^-e^+$.

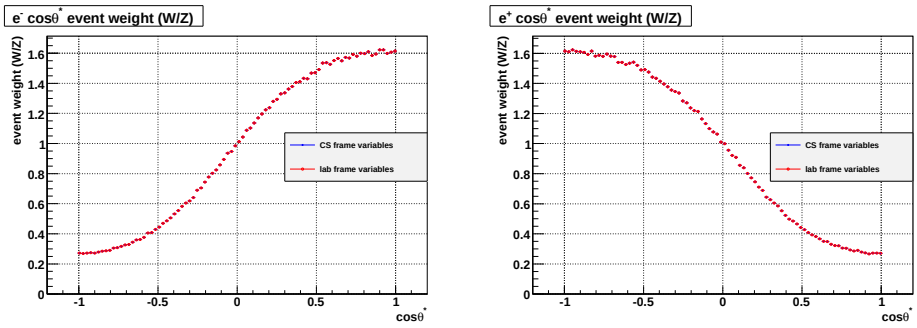

Figure 5.7: $\cos\theta^*$ ratio of W events over Z events, for electrons and positrons.

5.2.2 Boson Mass Shape

The W and Z boson are supposed to follow the Breit-Wigner distribution of mass, with corresponding pole mass M_W, M_Z and width Γ_W, Γ_Z (Eq 2.44). Since we plan to use the mass difference of W and Z as the floating parameter in generating templates, only the width difference of W and Z need to be considered here. The idea is to take each Z event, scale (or shift) its mass m_Z by (M_W/M_Z) or $(M_W - M_Z)$. The resulting W mass m_W is used to calculate an event weight which takes into account of the width difference between Z and W.

For each $Z \to ee$ event with mass m_Z and the transformed (shifted or scaled) m_W, a weight is assigned to the Z event. The event weight is calculated as the ratio of the Breit-Wigner function:

$$\text{weight} = \frac{BW(m_W, M_W, \Gamma_W)}{BW(m_Z, M_Z, \Gamma_Z)} \tag{5.3}$$

However both the `resbos` and `PYTHIA` generator have slightly different boson mass shape with respect to the Breit-Wigner distribution (Eq 2.44) as

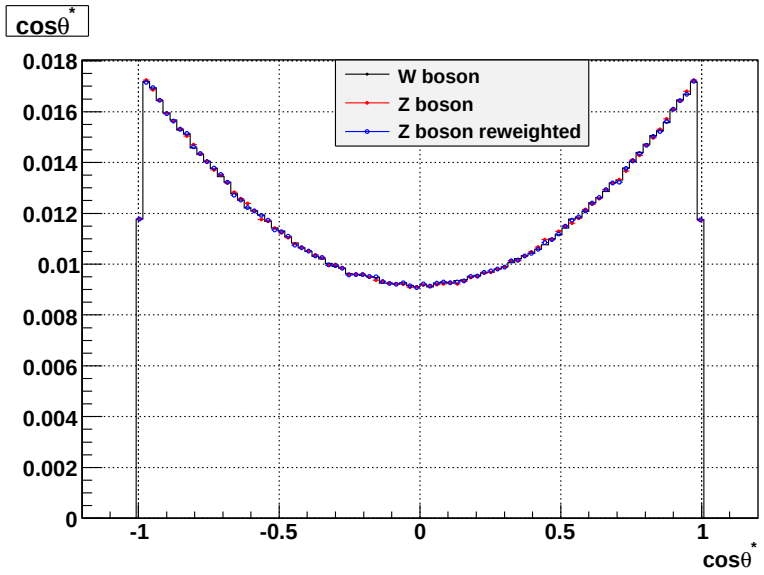

Figure 5.8: $\cos\theta^*$ distribution of leptons in W and Z events. For W events, it's $\cos\theta^*$ of electrons in W^- or positrons in W^+. For Z, we randomly select either electron or positron in each Z event. Therefore half of the leptons in Z are electrons and positrons.

shown in Fig 5.9. To be exact, boson mass should be Breit-Wigner distribution convoluted with the parton luminosity function (Eq 2.46).

A plausible way is to use the normalized W and Z mass shape as the input for mass reweighting, to replace the Breit-Wigner function in Eq 5.3 that fails to describe W and Z's invariant mass shape. Let function $f_W(m_W, M_W, \Gamma_W)$ and $f_Z(m_Z, M_Z, \Gamma_Z)$ be the normalized W and Z mass shape as in Fig 5.10. For each $Z \to ee$ event transformed into $W \to e\nu$ event, the event mass is also changed from m_Z to m_W, by either mass scaling (M_W/M_Z) or mass shifting $(M_W - M_Z)$. The mass reweighting factor is then determined as

$$\text{weight} = \frac{f_W(m_W, M_W, \Gamma_W)}{f_Z(m_Z, M_Z, \Gamma_Z)}. \tag{5.4}$$

Transformed Z mass shape turns out to agree well with the W mass shape after the above reweighting, as shown in Fig 5.11.

5.2.3 Boson Transverse Momentum p_T and Rapidity y

Another important kinematic difference between W and Z boson production is the boson p_T and rapidity y distribution. These two variable are closely

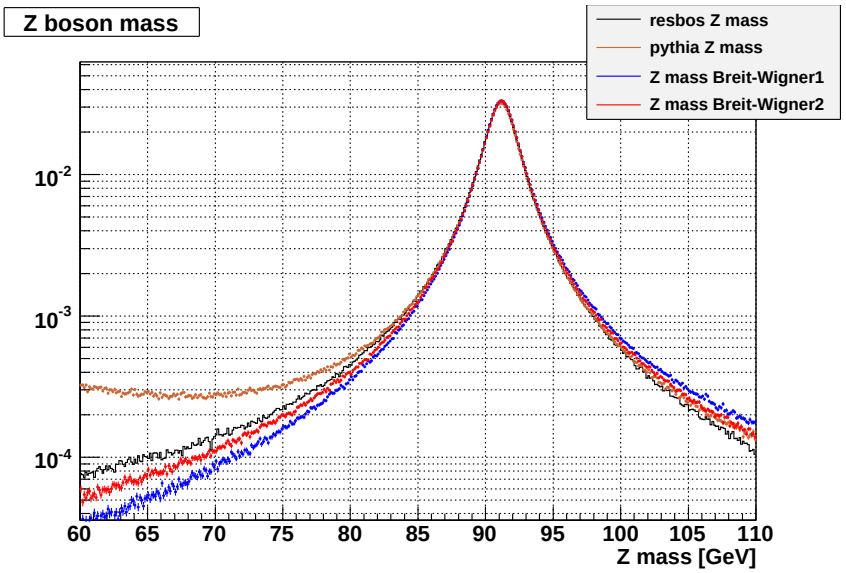

Figure 5.9: Generator level Z boson mass shape from `resbos` and `PYTHIA` is compared with the Breit-Wigner distribution. The `PYTHIA` $Z \rightarrow ee$ sample includes Z/γ^* interference that causes the extra large deviation from Breit-Wigner distribution in low mass region.

correlated as shown in Fig (5.12) and Fig (5.13). To simplify, let's use $f_W^-(p_T, y)$ and $f_W^+(p_T, y)$ denote the p_T v.s. y for W^- and W^+ boson, $f_Z(p_T, y)$ for Z boson. p_T v.s. y 2−D plots are normalized at the same range of p_T and y in both W and Z events.

For each Z events transformed into W event, the rapidity of Z will be kept the same, and the boson p_T will be smaller after the transformation. This is due to the way we do the $Z \rightarrow W$ transformation. In the Z boson's rest frame, the dilepton's direction is kept the same, but the momentum is scaled down by the ratio of M_W/M_Z. The p_T v.s. y reweighting factor is calculated as

$$\text{weight} = \frac{f_W^{\pm}(p_T^W, y)}{f_Z(p_T^Z, y)} \tag{5.5}$$

where $f_W^{\pm}$ denotes whether the specific Z event is transformed to W^- or W^+.

After the two dimensional boson p_T vs y reweighting, Z events are transformed into W with p_T and y distribution similar to that of true W bosons.

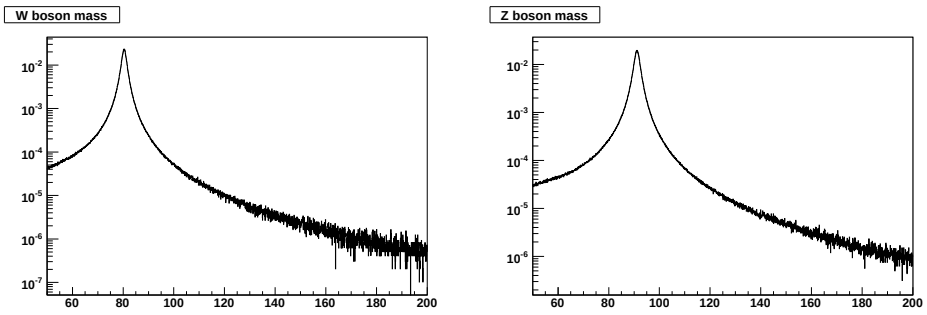

Figure 5.10: Reweighting input W and Z boson mass shape for `resbos` sample. They are both normalized in the $[50\,\text{GeV}, 200\,\text{GeV}]$ range.

5.2.4 Transform $Z \to ee$ to $W \to e\nu$

The procedure to do the transformation of $Z \to ee$ events to $W \to e\nu$ events can be put in the following steps:

- Electrons and positrons in $Z \to ee$ events are boosted into the Z boson rest frame.
- In the Z boson rest frame, we change the Z mass m_Z to W mass m_W by either scaling or shifting the mass.

$$\begin{aligned} m_W &= m_Z \times (M_W/M_Z) \qquad \text{(scaled)}, \\ m_W &= m_Z + (M_W - M_Z) \qquad \text{(shifted)}. \end{aligned} \tag{5.6}$$

- In boson rest frame, lepton has E^0 equals to $m_W/2$. With this relation we can simply rescale the leptop's 4-momentum according to the newly transformed m_W(scaled) or m_W(shifted). In the case of mass scaling, the coefficient $C_1 = M_W/M_Z$. For mass shifting the coefficient $C_2 = m_W/m_Z$. If we define a global mass shift $\Delta M = M_W - M_Z$, we could rewrite $C_2 = 1 + \Delta M/m_Z$. Leptons' 4-momentum are updated as

$$\begin{aligned} p^\mu(\text{scaled}) &= C_1(E^0, p^1, p^2, p^3), \\ p^\mu(\text{shifted}) &= C_2(E^0, p^1, p^2, p^3). \end{aligned} \tag{5.7}$$

- Each Z event randomly fakes either W^- or W^+. $\cos\theta^*$ and boson y reweighting is chosen accordingly. For example, in the case of W^-, electron in Z will be kept as electron in the transformed W^-, and the Z positron will fake neutrino in the transformed W^-, reweighting factor of

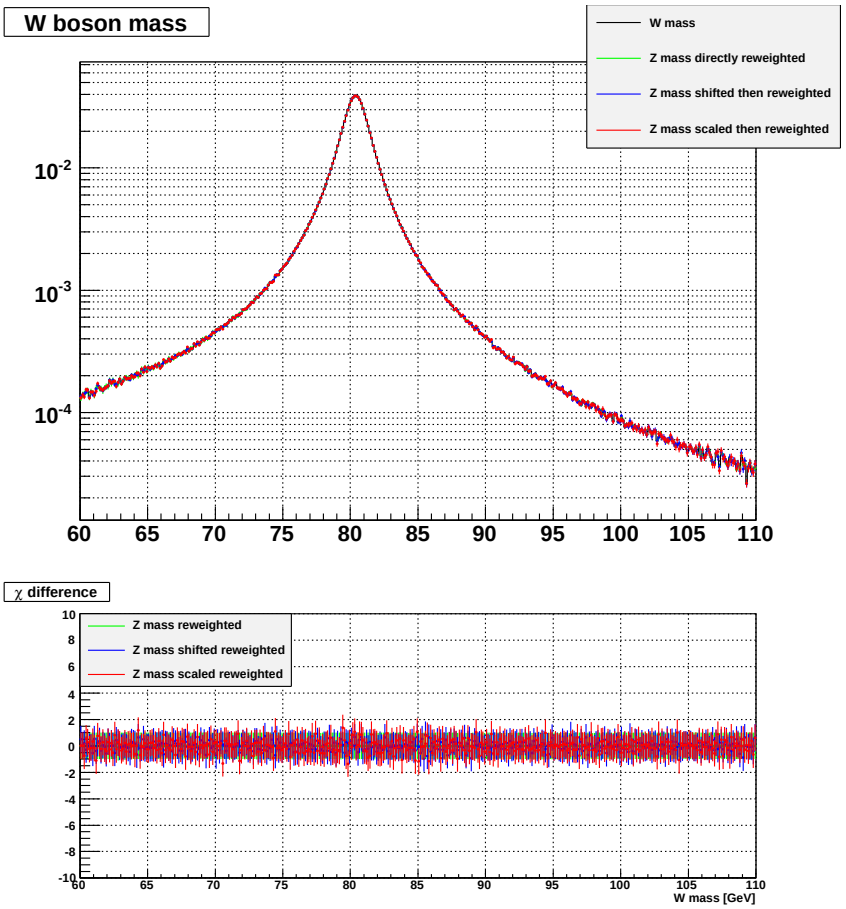

Figure 5.11: Reweighted transformed W events with true W events. Lower χ plot show that the reweighting algorithm works by the definition of closure test.

$\cos\theta^*$ will be read from the left plot in Fig (5.7). p_T and y reweighting will use the left plot in Fig (5.13). As previously mentioned, $\cos\theta^*$ reweighting has no effect here as long as the W sample is inclusive.

- Both leptons are then boost back to the lab frame, the same boost vector are used as before. Electron p_T, $\not\!\!E_T$ and transverse mass M_T are then calculated for the transformed W events, with event weights multiplied from the lepton $\cos\theta^*$ reweighting, boson mass reweighting and p_T vs y reweighting.

- The above procedure is for W and Z's default input values. To extract W mass by template fittings, we let the (M_W/M_Z) or $(M_W - M_Z)$ as a floating parameter around the default vaule and generate a template of

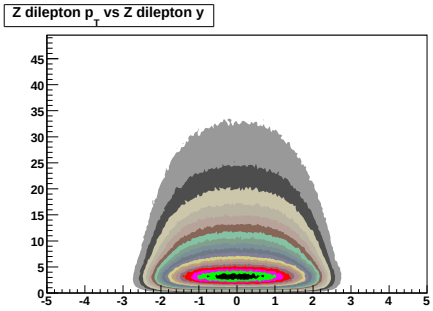

Figure 5.12: Z boson p_T vs rapidity y.

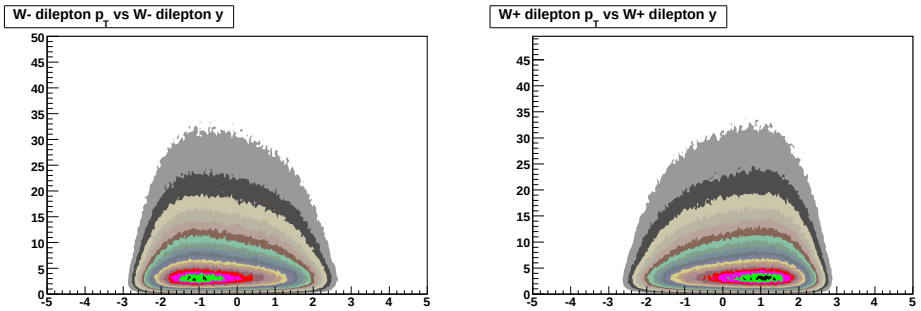

Figure 5.13: W boson p_T vs rapidity y. Note the assymmetry in the rapidity space for W^+ and W^-.

electron p_T, $\not\!\!E_T$ and transverse mass spectra.

`Resbos` has the following input values to generate $W \to e\nu$ and $Z \to ee$ events:

$$\begin{aligned} M_W &= 80423\,\text{MeV} \qquad \Gamma_W = 2048\,\text{MeV} \\ M_Z &= 91188\,\text{MeV} \qquad \Gamma_Z = 2422\,\text{MeV} \end{aligned} \tag{5.8}$$

Fig 5.15 to Fig 5.16 shows the comparison, in which Z sample is transformed with the input M_W of true W events. All three spectra have reasonable agreement.

5.2.5 Templates Fitting

A series of transformed $W \to e\nu$ sample is produced by transforming $Z \to e\nu$ events with the M_W^{temp} templates around the default $M_W = 80423\,\text{MeV}$. To be exact, this means using C^{temp} around the input values of C_1 or C_2 of Eq 5.7 in the transformation. We also apply additional mass reweighting (Eq 5.4) to

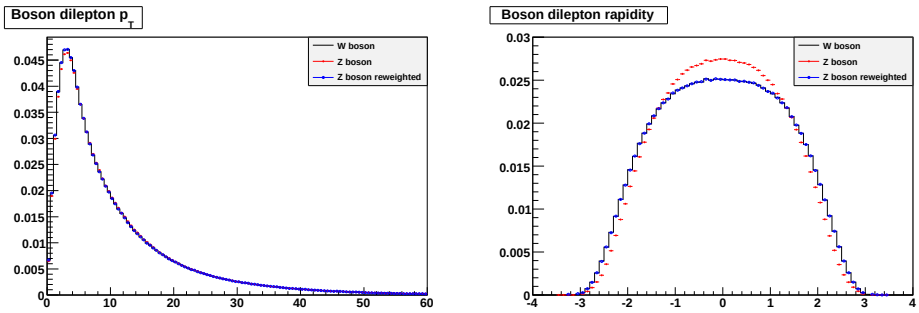

Figure 5.14: p_T and y comparison of the W boson (black), Z boson (red) and the transformed W with two dimensional reweighting (Eq 5.5) applied (blue).

the templates. The remaining $\cos\theta^*$ and boson p_T v.s. y reweightings are the same as default M_W. The step size for mass templates is roughly 5 MeV. M_T histograms are binned with 250 MeV bin width.

The fitting algorithm used here is the method of least squares. A variable called χ^2 is computed for each Monte Carlo M_T histogram (here is the generator level transformed W from Z) and the data M_T histogram (here is the generator level true W).

$$\chi^2 = \sum_i \frac{(y_i^{\rm mc} - y_i^{\rm data})^2}{\sigma_i^2} \tag{5.9}$$

where index i stand for the i bin of both histograms and y_i is the corresponding bin content. Normalization of both histograms need to be equal in the fitting range. χ^2 is plotted against the $M_W^{\rm temp}$ of the Monte Carlo histogram. χ^2 values in this plot usually can be well fitted with a quadratic function of $M_W^{\rm temp}$. Measured M_W corresponds to the minimum χ^2 value. Statistical uncertainty of 1σ is extrapolated to $M_W^{\rm temp}$ with $\chi^2 + 1$.

For the `resbos` generator events, there is one $W \to e\nu$ sample with 5 million events, and two $Z \to ee$ samples, one of 10 million events and one of 0.5 million events. Fitted M_W is reasonably close to the input value $M_W = 80423$ MeV on the M_T spectrum (Fig 5.18). Statistical fluctuation of the template χ^2 distribution is more obvious for the smaller (0.5 million) Z sample. With substantial more Z events, χ^2 distribution is more smooth and the fitted M_W is closer to the input value.

One good quality of M_T spectrum is that it is not sensitive to the kinematics difference between W and Z bosons. We would like to see how good M_T can be fitted, without any reweighting corrections applied. The only thing being changed is the boson mass in the boson rest frame. In this case the fitted

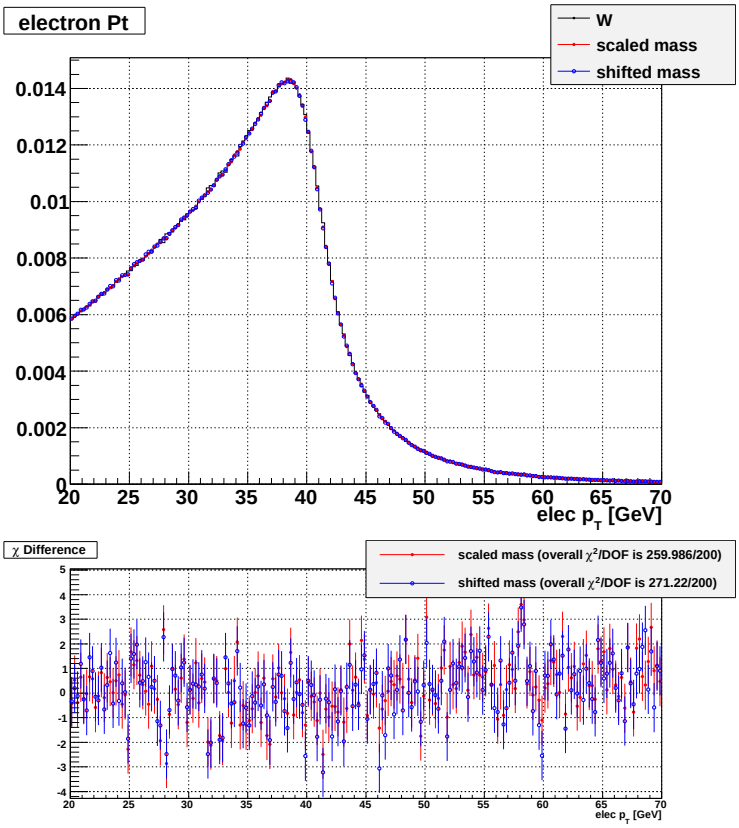

Figure 5.15: Electron p_T comparison between true $W \to e\nu$ and the transformed $W \to e\nu$. Both the shifting and scaling transformed Z are shown here. M_W used in Z transforming is the same as the input M_W of true W sample.

$M_W = 80410 \pm 3\,\text{MeV}$ is pretty close to the input value (fig 5.19). The best fitted M_T has $\chi^2/\text{D.O.F} \simeq 200/80$, much larger than the same comparison with reweighting corrections applied ($\chi^2/\text{D.O.F} \simeq 100/80$ in the left plot of Fig 5.18).

Each W and Z sample is generated with one random seed in `resbos`. Fitting results from the statistical limited one sample doesn't reflect the true distribution of fitting. We can use different random seeds in each of the sample in the Monte Carlo simulation, which is called a pseudo experiment. Fitted result from a series of pseudo experiments are called the pull distribution, which should follow a Gaussian distribution if each pseudo experiment is really statistically independent. In the following context, ensemble test refers to hundreds of pseudo experiments (each with different random seed) that are used in the W mass fitting. Fig 5.20 shows the pull distribution of fitted M_W from 600 pseudo experiment, each is similar to the one in Fig 5.19 (*i.e.* no

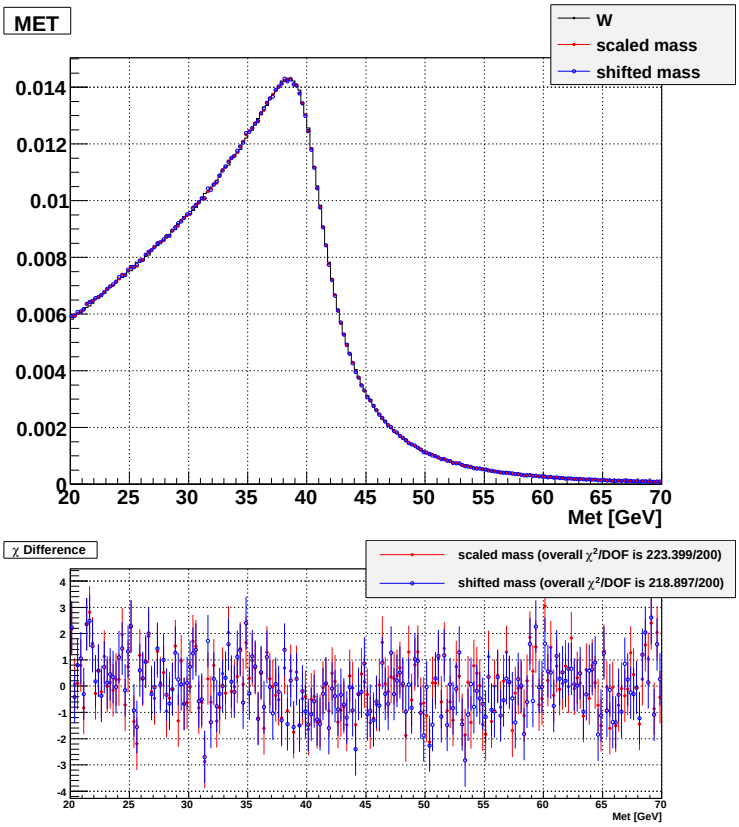

Figure 5.16: $\not\!\!E_T$ (neutrino E_T) comparison.

reweighting corrections).

5.3 Ratio Method of W Mass Measurement

The same `resbos` generator level $W \to e\nu$ and $Z \to ee$ sample is analyzed by ratio method in stead of the transforming method in the previous section. We will show that on the generator level, both method give very close value of measured M_W by fitting on the M_T spectrum.

There is no complicated transforming procedure described in Section 5.2.4. Here for one $Z \to ee$ event, one of the two electrons is discarded to give the right calculation of $\not\!\!E_T$, and then the transverse mass M_T is calculated accordingly. This M_T is timed by the (M_W/M_Z) ratio, on event by event basis and are put into the final M_T histogram to compare with the M_T spectrum of true $W \to e\nu$ events.

The transverse mass M_T of $Z \to ee$ that is scaled with the input M_W/M_Z

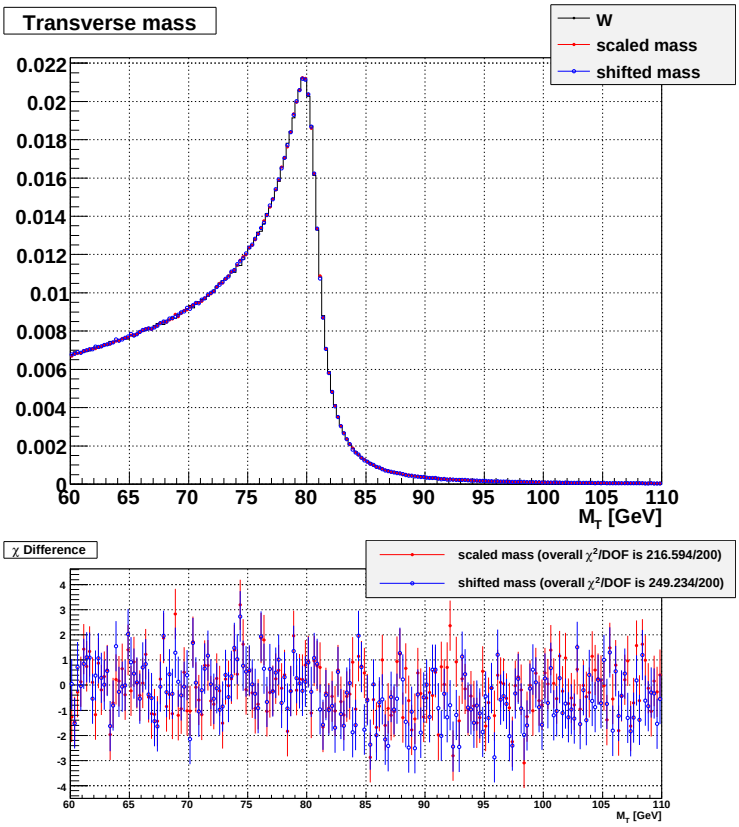

Figure 5.17: M_T comparison.

is compared with the M_T of true $W \to e\nu$ events, reasonable agreement is observed (Fig 5.21).

W mass fitting is performed on one Z sample of 0.5 million events (Fig 5.22) with fitted $M_W = 80418 \pm 9\,\text{MeV}$, consistent with the input $M_W = 80423\,\text{MeV}$. To show the true distribution of fitted M_W due to statistical uncertainty, mass fitting is made on an ensemble test of 600 pseudo experiments. The fitted M_W from ensemble test in ratio method (Fig 5.23) is so identical to that of the transforming method (Fig 5.20), both method is equivalent for extracting W mass using the M_T spectrum on the generator level. Ratio method is more simple and easier to extrapolate to data with realistic smearing and cuts, which will be shown in the next few chapters.

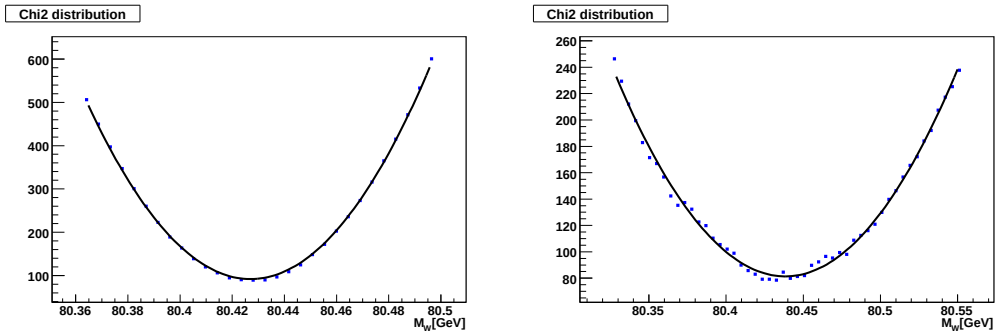

Figure 5.18: Templates χ^2 fitting on the M_T spectrum, with fitting range $70\,\text{GeV} < M_T < 90\,\text{GeV}$. Left plot is for 10 million $Z \to ee$ events (fitted $M_W = 80428 \pm 3\,\text{MeV}$) and the right plot is for 0.5 million $Z \to ee$ events (fitted $M_W = 80438 \pm 11\,\text{MeV}$).

5.4 Effect of Drell-Yan Process

In the studies of the ratio method with the fast Monte Carlo, pure $Z \to ee$ events are used. In contrast, the ee data sample also contains events from the Drell-Yan process ($q\bar{q} \to \gamma^* \to ee$) plus, of course, the contribution of the interference between Drell-Yan and pure $Z \to ee$. Apart from the Breit-Wigner resonance shape of the invariant ee mass distribution, Drell-Yan events have a similar signature to pure $Z \to ee$ events. In the vicinity of Z mass, the interference between Drell-Yan and pure $Z \to ee$ process becomes more important than the pure Drell-Yan contribution. To clarify: for the fast simulation samples we use $Z \to ee$ to denote the pure process and $Z/\gamma^* \to ee$ to denote the sum of the above three processes; for the full Monte Carl and the data, the label $Z \to ee$ denotes both the Drell-Yan and $Z \to ee$ processes together.

It is interesting to study, with the fast simulation, how much the fitted W mass is affected if a $Z/\gamma^* \to ee$ event sample is used instead of a $Z \to ee$ sample in the ratio method. For this we use the event generator `resbos`, with three configuration files: `resbos_z0.in` (pure $Z \to ee$), `resbos_a0.in` (pure Drell-Yan) and `resbos_za.in` (interference). Outputs from these three processes are combined to give the inclusive Z/γ^* sample in `resbos`. The di-electron invariant masses from the pure Z and Z/γ^* samples are compared in Fig 5.24. About $5\,\text{fb}^{-1}$ events are generated for each sample, that is 1.16 million $Z \to ee$ events and 1.36 million $Z/\gamma^* \to ee$ events. Contributions from Drell-Yan and Z/γ^* interference result in an excess in the low and high tails of the Z invariant mass. An identical Z mass shape is observed in the `PYTHIA` sample (Fig 5.9), where inclusive Z/γ^* events are generated by default.

The comparison of the transverse mass spectra of $Z \to ee$ and $Z/\gamma^* \to ee$

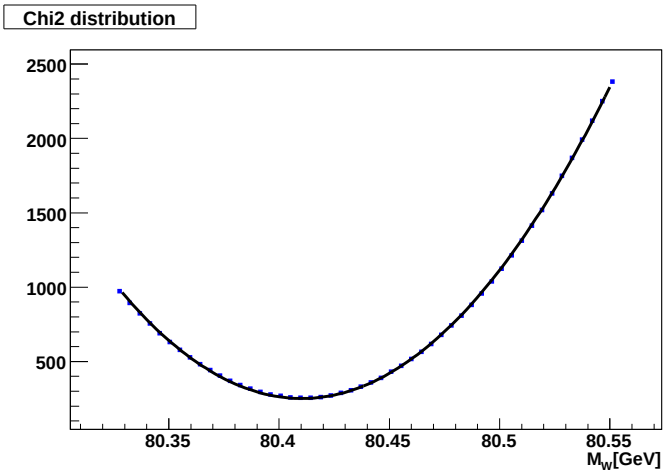

Figure 5.19: Templates χ^2 fitting on the M_T spectrum, with fitting range $70\,\text{GeV} < M_T < 90\,\text{GeV}$ (fitted $M_W = 80410 \pm 3\,\text{MeV}$). No reweighting corrections at all. 10 million $Z \to ee$ events.

is shown in Fig 5.25.

Both the $Z \to ee$ and Z/γ^* samples are compared with a $2\,\text{fb}^{-1}$ $W \to e\nu$ sample (Fig 5.26 and Fig 5.27). Realistic smearing and final selection cuts are applied in these fast Monte Carlo simulation events. With the fitting range of $[66\,\text{GeV}, 96\,\text{GeV}]$, the fitted W mass is $M_W = 80397 \pm 18\,\text{MeV}$ for pure $W \to ee$, and $M_W = 80403 \pm 10\,\text{MeV}$ for inclusive $Z/\gamma^* \to ee$ events.

The proper method to explore a possible shift in the fitted W mass due to the Drell-Yan process and its interference, is an ensemble test. 600 pseudo experiments of $Z \to ee$ and $Z/\gamma^* \to ee$, each with $1\,\text{fb}^{-1}$ events, are generated with different random seeds in `resbos`. After realistic smearing and final selection cuts, W mass fitting is performed for each pseudo experiment. The distributions of the fitted M_W are shown in Fig 5.28. The distributions of the fitted W mass using $Z/\gamma^* \to ee$ or $Z \to ee$ are very similar: when fitted with a Gaussian, the central value for the inclusive $Z/\gamma^* \to ee$ samples is only 4 MeV lower than for the pure $Z \to ee$ samples. The central values in both cases are within 1σ of the input W mass, $M_W = 80423\,\text{MeV}$. Indeed, the statistical uncertainty is indeed a little better at 40 MeV for the $Z/\gamma^* \to ee$ samples.

These results indicate that the use of pure $Z \to ee$ events in the fast Monte Carlo study of the ratio method, instead of $Z/\gamma^* \to ee$, does not change the results obtained earlier. For the statistical uncertainty, we will use 43 MeV obtained with the pure $Z \to ee$ ensemble, thereby erring on the conservative side.

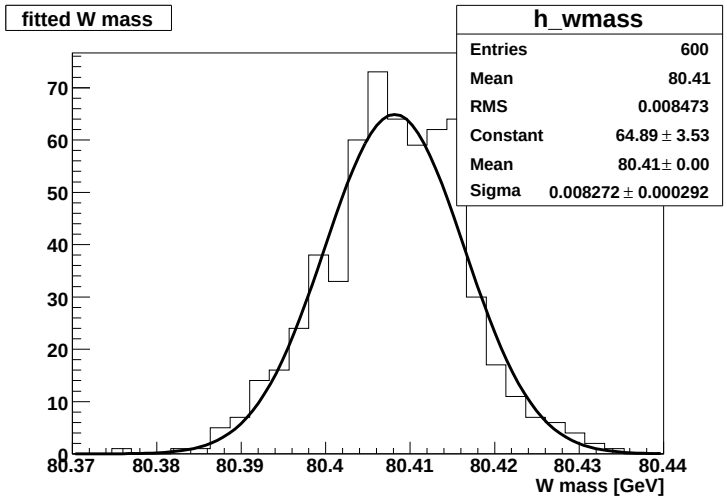

Figure 5.20: Measured M_W pull distribution from the ensemble of 600 pseudo experiments with 0.5 million Z events in each experiment. Fitting is performed on the M_T spectrum with range $60\,\text{GeV} < M_T < 110\,\text{GeV}$ for each of the pseudo experiment. The measured W mass distribution is fitted with a Gaussian function, where the central $M_W = 80407\,\text{MeV}$ and standard deviation $\sigma = 9\,\text{MeV}$. The input $M_W = 80423\,\text{MeV}$.

5.5 Discussion

Ratio method presented in this thesis is based on the Note [33] and the thesis work [34]. M_T spectra of $W \to e\nu$ data and $Z \to ee$ data are compared to extract the boson mass ratio M_W/M_Z. About $100\,\text{pb}^{-1}$ DØ Run I data available in the previous study. Number of $Z \to ee$ events give more stringent statistical limit as their cross section is roughly 1/10 of the $W \to e\nu$. In Run I measurement of ratio method, the direct fit of $Z \to ee$ to $W \to e\nu$ results in a large statistical uncertainty. The same Z statistical limitation translates into the electron energy scale statistical uncertainty in the standard method. That contribution is the largest component of M_W systematic uncertainties, as the fitted M_W has roughly linear dependence on the electron energy scale. Compared with the relevant systematic uncertainty in standard method, the statistical uncertainty in ratio method is considerably larger, that's because the z-component of both Z electrons are not used in the M_T comparison, while the full Z mass peak is used for the determination of electron energy scale in the standard method.

There are about 10 times more data in DØ Run IIa than in DØ Run I. With that many of $Z \to ee$ events, we expect the statistical uncertainty in

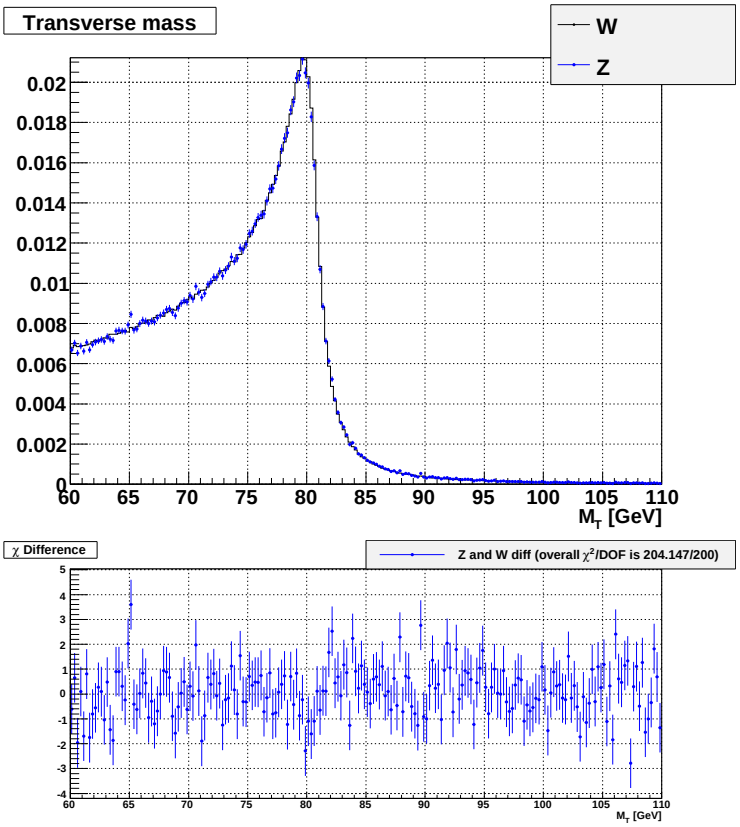

Figure 5.21: M_T comparison on the generator level `resbos` events. Input M_W of the W events are used in the scaling of Z transverse mass.

ratio method will improve significantly, and won't be much larger than the electron energy scale uncertainty in the standard method. In the last Chapter of this thesis, we will have a discussion of this point.

In principle p_T^e and $\not\!\!E_T$ spectra would have been good for ratio method as well, provided W and Z boson have the same p_T distribution. In reality, that doesn't work in a straightforward way because of the difference between W and Z boson p_T distribution, which is especially evident with the $1\,\mathrm{fb}^{-1}$ DØ Run IIa data.

Although in both the transformation method and ratio method, the M_W value is extracted by comparing $Z \to ee$ and $W \to e\nu$ events directly, the way of $Z \to ee$ events being used is quite different. In the original ratio method, $Z \to ee$ events are kept as they are, only the transverse mass M_T is calculated for $Z \to ee$ events and scaled down with (M_W/M_Z). The transformation method attempts to fully transform $Z \to ee$ to $W \to e\nu$ in every aspect. One obvious advantage of the latter is that mass fitting can be performed on all

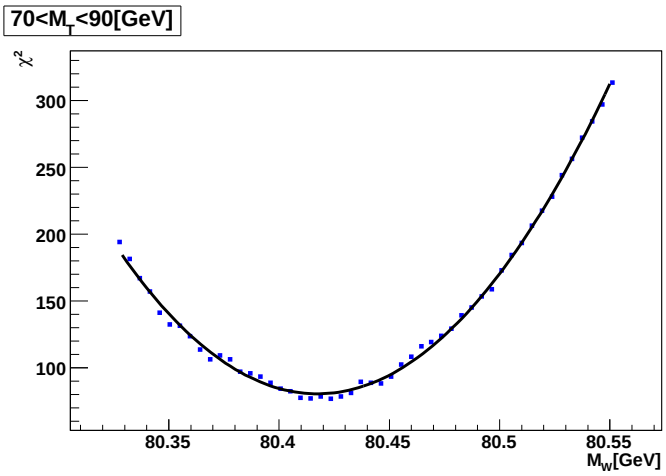

Figure 5.22: Ratio method. Templates χ^2 fitting on the generator level M_T spectrum, with fitting range $70\,\mathrm{GeV} < M_T < 90\,\mathrm{GeV}$ (fitted $M_W = 80418 \pm 9\,\mathrm{MeV}$). 0.5 million $Z \to ee$ events.

the three variables p_T^e, $\not\!\!E_T$ and M_T, just like the standard method.

Inclusion of the discussion about transformation method in this chapter helps to clarify some key difference in ratio method and appreciate the importance of boson kinematics in p_T^e and $\not\!\!E_T$ spectrum. Starting from the next chapter we only discuss ratio method and make our measurement of W boson mass based on it.

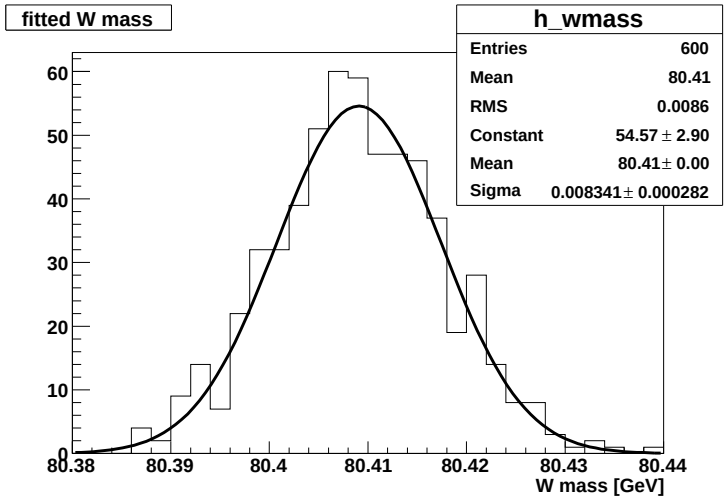

Figure 5.23: Ensemble test of 600 pseudo experiments (generator level `resbos`) in ratio method. Fitting is performed on the M_T spectrum with range $60\,\text{GeV} < M_T < 110\,\text{GeV}$ for each of the pseudo experiment.

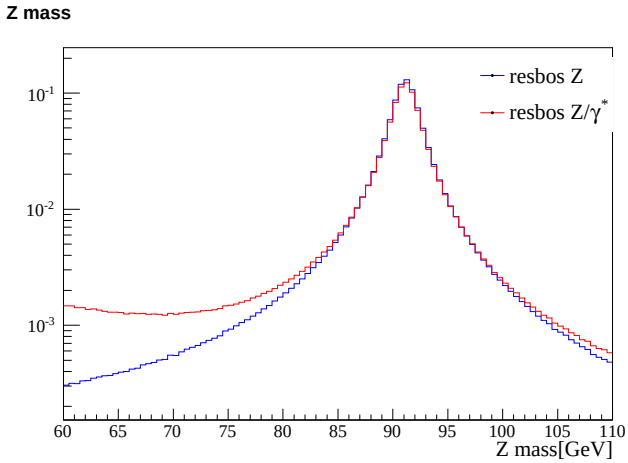

Figure 5.24: The invariant mass distribution of pure $Z \to ee$ and $Z/\gamma^* \to ee$ samples generated by `resbos`. Note the extra tail in both low and high mass region in $Z/\gamma^* \to ee$ sample which is consistent with the shape of Z/γ^* events in `PYTHIA` sample of Fig 5.9.

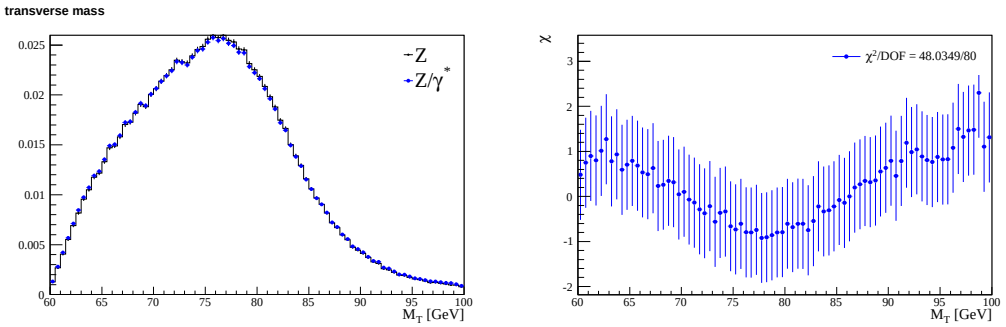

Figure 5.25: Tranverse mass of $Z \to ee$ and $Z/\gamma^* \to ee$ events in `resbos`. They are fast Monte Carlo simulation with realistic smearing after final event selections. $Z \to ee$ events are subset of the $5\,\mathrm{fb}^{-1}$ Z/γ^* sample.

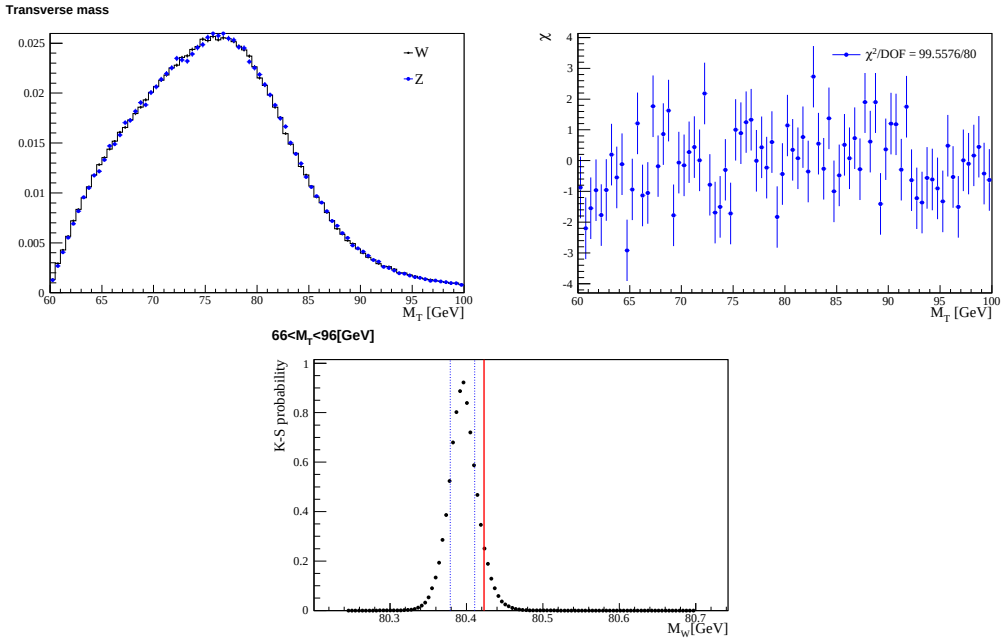

Figure 5.26: M_T comparison between $2\,\mathrm{fb}^{-1}$ $W \to e\nu$ events and $5\,\mathrm{fb}^{-1}$ pure $Z \to ee$ events (scaled with input M_W). Both W and Z samples are fast Monte Carlo with realistic smearing after final event selections. Measured $M_W = 80397 \pm 18\,\mathrm{MeV}$ with fitting range $66\,\mathrm{GeV} < M_T < 96\,\mathrm{GeV}$ for this particular sample.

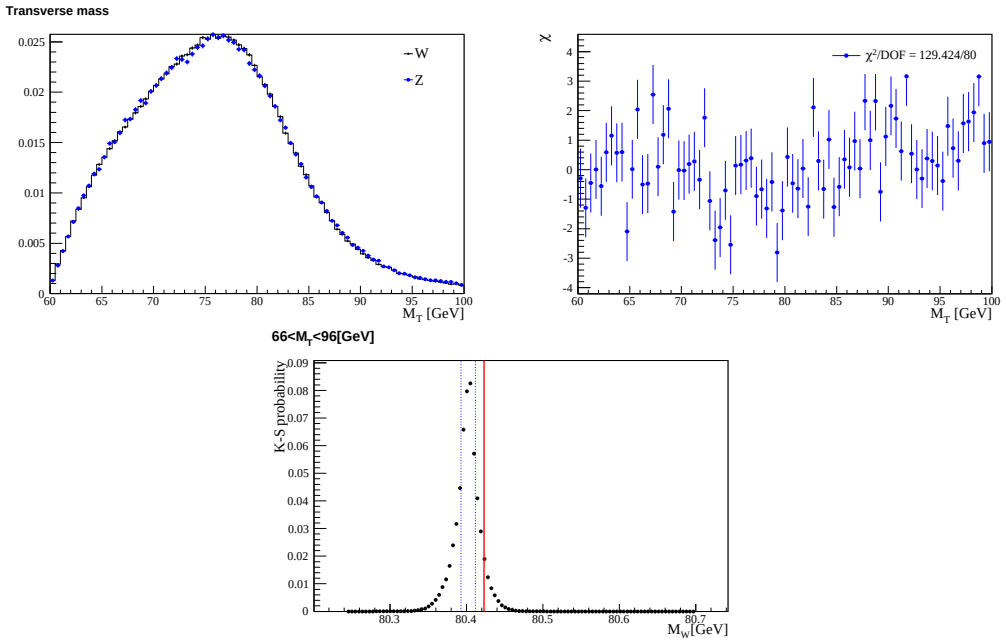

Figure 5.27: M_T comparison between $2\,\mathrm{fb}^{-1}$ $W \to e\nu$ events and $5\,\mathrm{fb}^{-1}$ $Z/\gamma^* \to ee$ events (scaled with input M_W). Both W and Z samples are fast Monte Carlo with realistic smearing after final event selections. Measured $M_W = 80403 \pm 10\,\mathrm{MeV}$ with fitting range $66\,\mathrm{GeV} < M_T < 96\,\mathrm{GeV}$ for this particular sample.

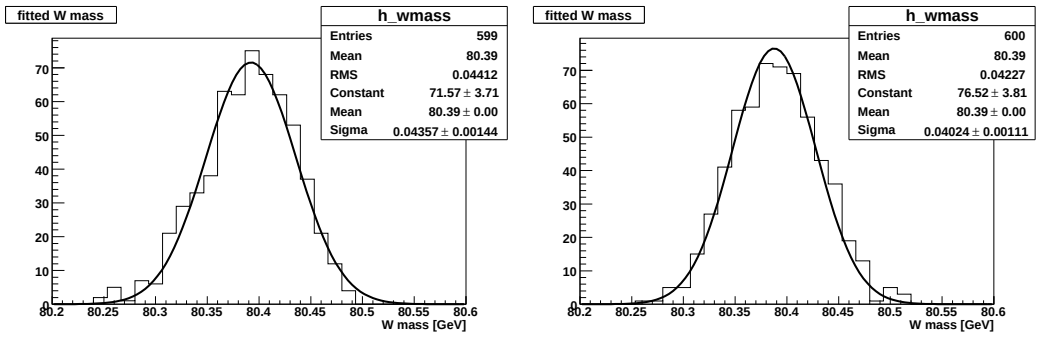

Figure 5.28: Distribution of fitted M_W from 600 ensemble tests of pure $Z \to ee$ (left) and $Z/\gamma^* \to ee$ (right), with fitting range $[66\,\mathrm{GeV}, 96\,\mathrm{GeV}]$. Each pseudo experiment has $1\,\mathrm{fb}^{-1}$ events, with the same smearing and selection as Fig 5.27. Both distributions are fitted by a Gaussian function. Central $M_W = 80392\,\mathrm{MeV}$, and $\sigma = 43\,\mathrm{MeV}$ for the pure $Z \to$ sample. Central $M_W = 80388\,\mathrm{MeV}$ and $\sigma = 40\,\mathrm{MeV}$ for the Z/γ^* sample.

Chapter 6

Ratio Method Validation with Toy Fast Monte Carlo Simulation

Ratio method of W mass measurement relies on the fact that the physics (generator level) M_T scales with the W and Z boson masses. Data $W \to e\nu$ and $Z \to ee$ events already go through detector effects and selection cuts. Among those, the smearing of electron and the recoil system; acceptance cut on the electron; the non trivial energy scale and offset; underlying event contribution *etc.* need to be carefully examined so that the effects of them on the mass-M_T proportionality are well understood. The transverse mass M_T straightly calculated out of W and Z data events doesn't scale with boson.

In this dissertation, we don't attempt to do the unfolding of M_T on the data events, that is for each M_T of data event, a corresponding physics (generator) M_T is obtained. The extraction of M_T out of data reduces to the M_T comparison on the generator level.

Instead, we will make corrections to the calculated M_T of $W \to e\nu$ and $Z \to ee$ data events and compare the corrected M_T of data events to extract the M_W/M_Z ratio. To that end, the understanding of those effects from generator level to data and the bias of them on the M_T scaling with boson mass is crucial for W mass measurement in data using ratio method.

The study of ratio method with fast Monte Carlo simulated events is the most important step towards this goal. A finely tuned fast Monte Carlo simulation `wz_epmcs` used by the DØ experiment has excellent agreement with the Run IIa $W \to e\nu$ and $Z \to ee$ data, and this `wz_epmcs` simulation is essential to the successful measurement of M_W in the standard method.

For ratio method, fast Monte Carlo simulation is ideal for understanding various effects and selection biases, as one can turn on and turn off the simula-

tion of each effect. A simplified toy fast Monte Carlo simulation is developed for ratio method study in a similar manner as the `wz_epmcs` package in the standard method. Major smearing algorithms and selection cuts are implemented in this toy fast Monte Carlo simulation. Corrections that take into account of the difference between $W \to e\nu$ and $Z \to ee$ events are tested on the toy fast Monte Carlo model.

In this chapter, we only consider the simple Gaussian smearings of the electrons and recoil system, as it's simpler to illustrate the idea of extra smearing correction for Gaussian smearing model. In the next chapter, simple Gaussian smearings are replaced with more realistic and complicated smearing algorithms (same as in the tuned `wz_epmcs`) which give much better job of describing data. Fast Monte Carlo model in the next chapter is used to estimate the statistical uncertainty and as a closure test of ratio method. The corresponding extra smearing correction developed for the realistic smearing are applied to the full Monte Carlo and data analysis.

We will discuss some of the most important corrections one by one in the following sections.

6.1 Smearing Resolution

In toy fast Monte Carlo simulation, the Gaussian smearing of electrons is performed as the followings:

- The electron energy scale α and offset β is applied to the truth level electron energy E_{raw},

$$E = \alpha \times E_{\text{raw}} + \beta \tag{6.1}$$

  In the toy fast Monte Carlo simulation, we adopt the values of $\alpha = 1.001514$ and $\beta = -87\,\text{MeV}$. In general, α and β values are anti-correlated to give the same measured energy values for $E = 45\,\text{GeV}$ electrons, as they are determined by fitting Z mass shape.

- Electron energy resolution σ_{EM} is calculated as a function of truth level electron energy E_{raw},

$$\frac{\sigma_{\text{EM}}}{E_{\text{raw}}} = \sqrt{C^2 + \frac{S^2}{E_{\text{raw}}} + \frac{N^2}{E_{\text{raw}}^2}} \tag{6.2}$$

  where C, S and N are called the constant term, sampling term and noise term. Typical values of those terms are used in this study, that is $C = 0$, $S = 30\%\,\text{GeV}^{1/2}$ and $N = 29\%\,\text{GeV}$.

- The smeared energy of electron is

$$E(\text{smeared}) = E + \texttt{Gaussian}(0, 1) \times \sigma_{\text{EM}} \tag{6.3}$$

The smearing of recoil system is similar to the electron smearing. We add the hadronic energy scale to truth level recoil and then apply the hadronic smearing resolution.

- On the generator level, recoil p_T^{rec} is against the boson p_T, with the same magnitude in the opposite direction,

$$p_T^{\text{rec}} = -(p_T^{\text{boson}}(x), p_T^{\text{boson}}(y)) \tag{6.4}$$

- The magnitude of truth recoil is scaled by the hadronic energy scale, which is set at 1.0 in this study.

- ϕ direction of the recoil is smeared by its resolution σ_ϕ. In this chapter σ_ϕ is set to 0, that is recoil ϕ smearing is turned off. We will discuss the non zero σ_ϕ in the next chapter.

The above recoil smearing is only applied to true hard recoil against the boson p_T, that is the first component of recoil which is discussed at the end of Chapter 4.2. The other two contributions of the overall recoil are from the spectator quarks interaction and the soft interaction of other $p\bar{p}$ in the same bunch crossing, which are well modeled by MB and ZB events respectively. The direction of overall contribution from MB and ZB events is randomly distributed with respect to the hard recoil direction. In this chapter, we use a fixed width $\sigma_{\text{UE}} = 3.02\,\text{GeV}$ Gaussian distribution to simulate both x and y component of the combined MB and ZB events. A random number out of the above Gaussian distribution is added to the x and y component of the smeared hard recoil p_T^{rec} to give the final smeared recoil.

$\not\!\!E_T$ is obtained by balancing the smeared electron and recoil p_T. For $W \to e\nu$ event, it is calculated by

$$\overrightarrow{\not\!\!E_T}(W) \equiv -\overrightarrow{E_T^e} - \overrightarrow{E_T^{\text{rec}}}. \tag{6.5}$$

For $Z \to ee$ event, the native $\not\!\!E_T$ is calculated by

$$\overrightarrow{\not\!\!E_T}(Z) \equiv -(\overrightarrow{E_T^{e_1}} + \overrightarrow{E_T^{e_2}}) - \overrightarrow{E_T^{\text{rec}}}. \tag{6.6}$$

One of the two electrons decayed from Z is dropped as a neutrino to calculate the transverse mass M_T. If e_2 is chosen as the neutrino, the proper $\not\!\!E_T$ entering

the M_T calculation of Z is

$$\begin{aligned} \overrightarrow{\not\!\!E_T^{e_2}} &\equiv -\overrightarrow{E_T^{e_1}} - \overrightarrow{E_T^{\rm rec}} \\ &\equiv \overrightarrow{\not\!\!E_T}(Z) + \overrightarrow{E_T^{e_2}} \end{aligned} \tag{6.7}$$

One may ask which Z electron should be treated as the neutrino in the calculation of $\not\!\!E_T$ (hence M_T)? For one $Z \to ee$ event, it is possible to obtain two M_T by choosing e_1 as the neutrino once and choosing e_2 as the neutrino another time. Conceptually this is the right way to do, as there is no reason to prefer one electron over the other one. To be fair to both electrons, each one of them has to take the role of neutrino. In reality this choice also buys us the advantage that more statistics can be put into the M_T spectrum of Z, although the two M_T from one Z event are not statistical independent. A more detailed discussion will be presented in Chapter 6.5.

If we are to do a ratio method W mass measurement straight out of the toy fast Monte simulation and without any cut, two effects will make the mass fitting a failure. First, the non zero electron energy offset causes the calculated M_T no longer scale with the boson mass. Second, the resolution of electrons, recoil systems and the underlying events doesn't scale with boson mass. As Fig 6.1 shows, the M_T spectrum of Z sample which is properly scaled with the input M_W is under smeared, hence has a sharper Jacobian edge than the true W sample.

It is easy to understand the resolution effect on M_T by looking at the electron system. The average electron energy in $Z \to ee$ events is higher than that in the $W \to e\nu$ events due to the higher Z mass. Therefore on average the relative resolution of electron is lower in Z event than in W event, indicated by Eq 6.2. For smeared M_T to scale with boson mass, the relative electron resolution $\sigma/\langle E\rangle$ must be the same in W and Z event. Resolution of the recoil system and the underlying event also cause similar bias on the M_T spectrum of Z. A technique called extra smearing to correct this effect is discussed in Chapter 6.3.

6.2 EM Energy Scale and Offset

To show the effect of non zero electron energy offset on the measured M_T, let's start at the generator level electron energy. We know the average electron energy is proportional to the W and Z boson mass,

$$E^W_{\rm true} = \left(\frac{M_W}{M_Z}\right) E^Z_{\rm true} \tag{6.8}$$

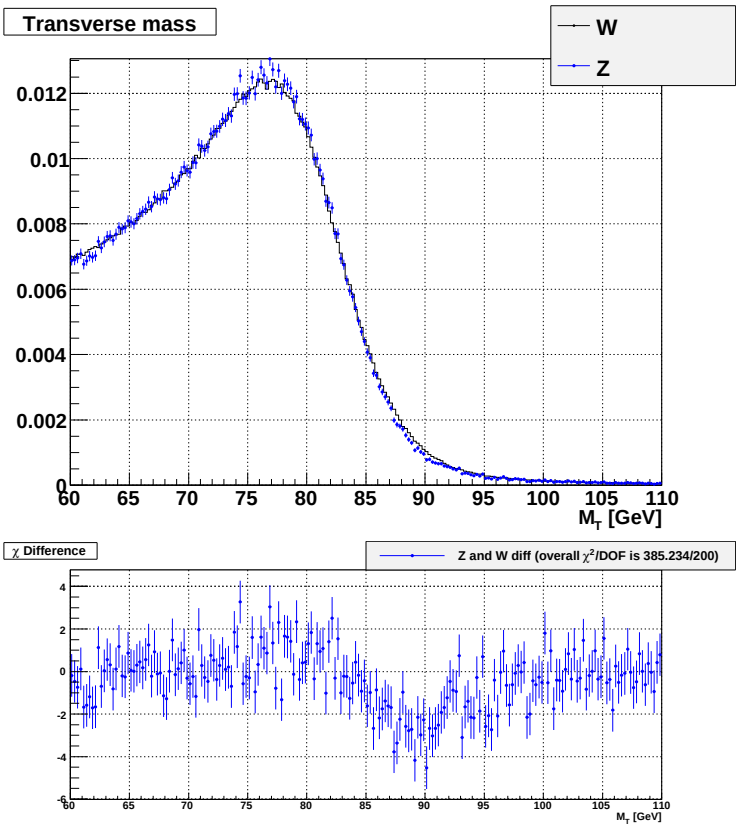

Figure 6.1: The M_T comparison and its χ plot, where M_T of Z events is scaled with input M_W. Electron and the recoil system of both W and Z sample are smeared by simple Gaussian form as described in the context. Notice the M_T of Z sample is less smeared (sharper shape) than W.

This relation is consistent with the M_T scalability with boson mass on the generator level: $M_T^W(\text{true}) = (M_W/M_Z)M_T^Z(\text{true})$. Measured electron energy in W and Z events is related to truth level energy by the energy scale and offset,

$$\begin{aligned} E^W_{\text{mea}} &= \alpha \times E^W_{\text{true}} + \beta \\ E^Z_{\text{mea}} &= \alpha \times E^Z_{\text{true}} + \beta \end{aligned} \tag{6.9}$$

Combining the above equations we can relate the measured electron energy in W and Z events,

$$E^W_{\text{mea}} = \frac{M_W}{M_Z} E^Z_{\text{mea}} + \beta \left(1 - \frac{M_W}{M_Z}\right) \tag{6.10}$$

In the case of $\beta = 0$, measured electron energy would still scale with boson mass. For a non zero β, the measured electron energy is off by $\beta/10$ from the boson mass scaled value. Fitted W mass based on the measured M_T spectrum will also be biased from the input M_W by the order of $\beta/10$. Notice that energy scale α has no effect on the scaling of measured electron energy, as it is cancelled in ratio. For W and Z data, energy offset is estimated to be around $-404\,\mathrm{MeV}$ in the study of standard method. Without correction, fitted M_W will be off from the input value by around $40\,\mathrm{MeV}$.

In order to make the measured M_T scale with the boson mass, one could substitute the electron's energy as $(E_{\mathrm{mea}} - \beta)/\alpha$ in the calculation of M_T for W and Z events.

A series of different α and β values combinations are used in fast Monte Carlo simulations. For each pair of α and β, 600 pesudo experiments (each with different random seed) of fast Monte Carlo $Z \to ee$ sample are produced. Each $Z \to ee$ pseudo experiment has $1\,\mathrm{fb}^{-1}$ events. Another $W \to e\nu$ fast Monte Carlo sample of $1\,\mathrm{fb}^{-1}$ events is produced with input $M_W = 80423\,\mathrm{MeV}$.

Fitted mass from the 600 pseudo experiment is put into a pull histogram, which should have a Gaussian shape distribution if the ensemble of pseudo experiments is truly statistical independent. Mean μ and variance σ of the Gaussian function fitted to pull histogram give the central M_W and the statistical uncertainty.

Table 6.1 shows the fitted M_W out of ensemble test, with different α and β values. The corresponding pull histograms are shown in Fig 6.2 to Fig 6.7. Fitted M_W has no dependence on the energy scale α. For β value to change $400\,\mathrm{MeV}$, fitted M_W value changes about $50\,\mathrm{MeV}$, which is consistent with the estimation of $\beta/10$.

Those W and Z sample in ensemble tests Fig 6.2 to Fig 6.7 are not just applied with electron energy scale and offset. They are the final sample of fast Monte Carlo study in this chapter: they have simple Gaussian smearing, fully acceptance cut, lepton p_T cut and boson p_T cut. For Z sample, the extra smearing correction and acceptance reweighting are also applied. These effects will be discussed in the next few sections.

6.3 Extra Smearing Correction

Without any correction, the scaled M_T of $Z \to$ events is under-smeared (Fig 6.1). This is caused by the smaller smearing resolution (more precisely, the relative resolution σ/E) for electrons and recoil system of Z sample, which on average has higher electron energy and recoil p_T.

To make the mass scaling work on the smeared electron p_T^e, we force the

α	1.001514	1.001514	1.001514	1.0	1.0045	0.9956
β[MeV]	-87	-200	200	0	-200	200
fitted M_W[MeV]	80417	80404	80452	80425	80403	80452

Table 6.1: Central value of fitted M_W from the ensemble test, with different combinations of electron energy scale α and offset β values. Input M_W = 80423 MeV. Because the raw M_T is used here instead of the M_T calculated with $(E - \beta)/\alpha$, only $\beta = 0$ gives the corrected W mass.

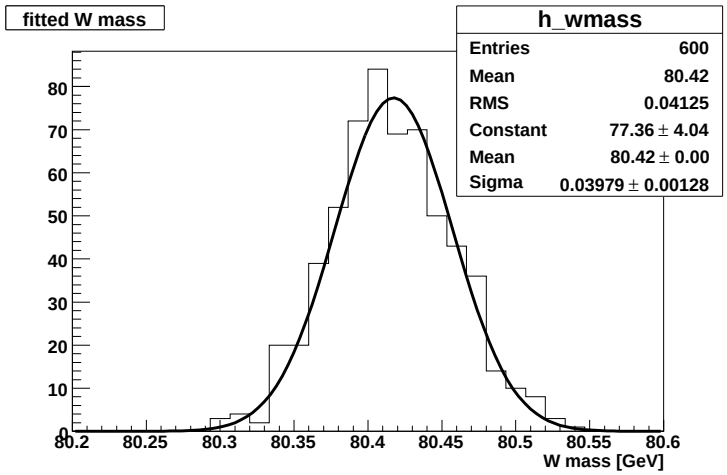

Figure 6.2: $\alpha = 1.001514$ and $\beta = -87$ MeV. Ensemble test give fitted M_W = 80417 MeV and $\sigma(M_W) = 40$ MeV.

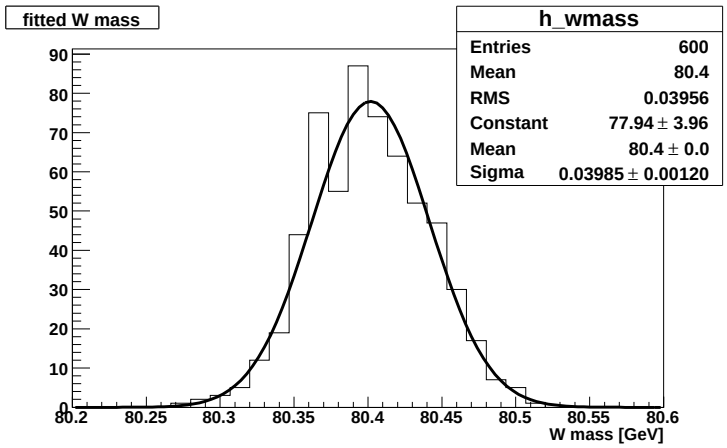

Figure 6.3: $\alpha = 1.001514$ and $\beta = -200$ MeV. Ensemble test give fitted $M_W = 80404$ MeV and $\sigma(M_W) = 40$ MeV.

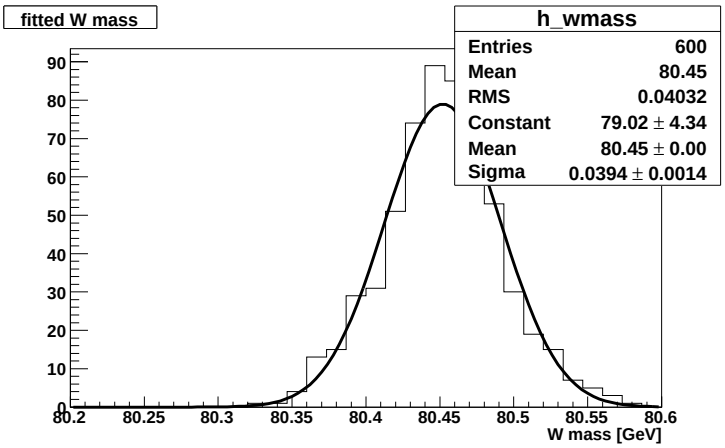

Figure 6.4: $\alpha = 1.001514$ and $\beta = 200\,\text{MeV}$. Ensemble test give fitted $M_W = 80452\,\text{MeV}$ and $\sigma(M_W) = 40\,\text{MeV}$.

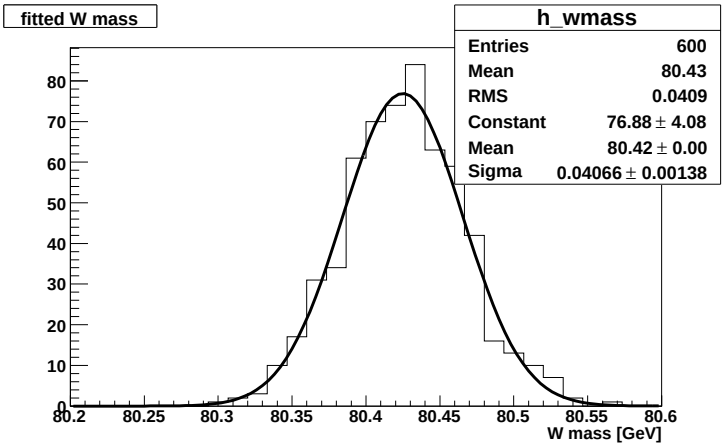

Figure 6.5: $\alpha = 1.0$ and $\beta = 0$. Ensemble test give fitted $M_W = 80425\,\text{MeV}$ and $\sigma(M_W) = 40\,\text{MeV}$.

relative resolution $\sigma/\langle E\rangle$ to be equal for both Z and W by adding extra smearing to Z's electron and recoil system.

$$\left(\frac{\sigma(p_T^e)}{\langle p_T^e\rangle}\right)_Z^2 + \left(\frac{\sigma_{\text{extra}}}{\langle p_T^e\rangle}\right)_Z^2 = \left(\frac{\sigma(p_T^e)}{\langle p_T^e\rangle}\right)_W^2, \tag{6.11}$$

where

$$\langle p_T^e\rangle_W = \frac{M_W}{M_Z}\langle p_T^e\rangle_Z. \tag{6.12}$$

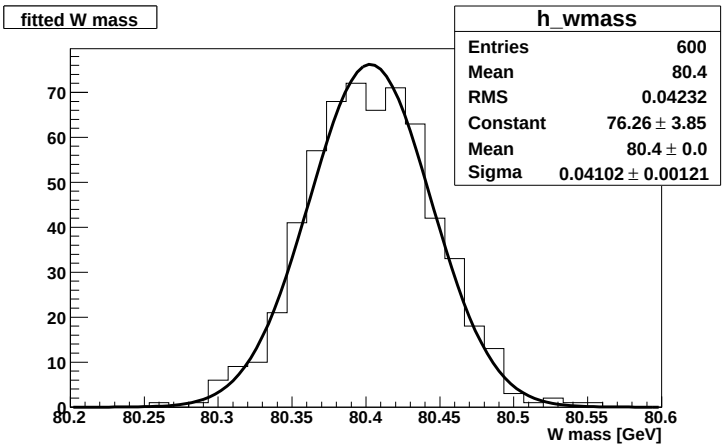

Figure 6.6: $\alpha = 1.0045$ and $\beta = -200\,\text{MeV}$. Ensemble test give fitted $M_W = 80403\,\text{MeV}$ and $\sigma(M_W) = 40\,\text{MeV}$.

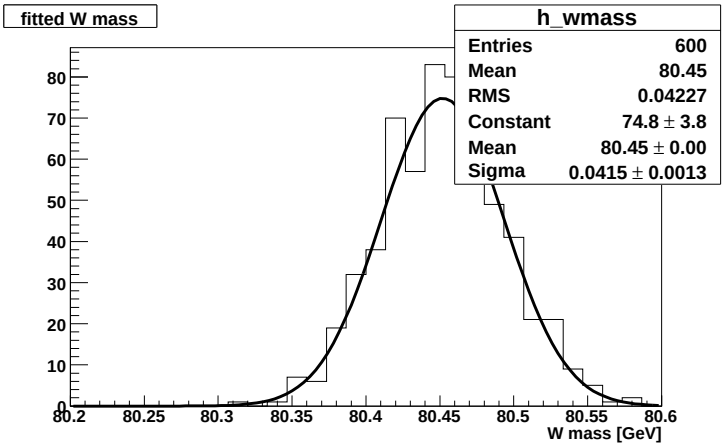

Figure 6.7: $\alpha = 0.9956$ and $\beta = 200\,\text{MeV}$. Ensemble test give fitted $M_W = 80452\,\text{MeV}$ and $\sigma(M_W) = 40\,\text{MeV}$.

The extra smearing resolution of electron is calculated as

$$\sigma^2_{\text{extra}}(\text{EM}) = \left(\frac{M_Z}{M_W}\right)^2 \sigma^2(E)_W - \sigma^2(E)_Z. \tag{6.13}$$

σ_Z is the original resolution of electrons in Z events. σ_W is the hypothetical energy resolution calculated with Z electron energy scaled by M_W/M_Z. For Z electron with energy E, the scaled energy is $E' = (M_W/M_Z)E$. The

hypothetical resolution σ_W is calculated at the energy level of E',

$$\sigma_W = \sqrt{C^2 \times (E')^2 + S^2 \times E' + N^2}. \tag{6.14}$$

For each Z electron with generator level energy E, an additional extra smearing term (with different random seed) is added to the original smearing.

$$E(\text{smeared}) = E + \texttt{Gaussian}(0,1) \times \sigma + \texttt{Gaussian}(0,1) \times \sigma_{\text{extra}} \tag{6.15}$$

A similar equation is derived for the extra smearing of hard recoil which only has $|p_T^{\text{rec}}|$ smearing, no recoil ϕ smearing. The extra smearing resolution applied to hard recoil magnitude is

$$\sigma^2_{\text{extra}}(\text{recoil}) = \left(\frac{M_Z}{M_W}\right)^2 \sigma^2(p_T^{\text{rec}})_W - \sigma^2(p_T^{\text{rec}})_Z \tag{6.16}$$

where for each Z recoil of p_T^{rec}, $\sigma(p_T^{\text{rec}})_W$ is calculated at the scaled energy level of $(M_W/M_Z)p_T^{\text{rec}}$. With the presence of non zero recoil ϕ smearing, extra smearing of hard recoil need to performed in x and y components. Discussion of this will be presented in the next chapter.

The smearing of underlying events uses a fixed $\sigma_{\text{UE}} = 3.02\,\text{GeV}$ Gaussian distribution for the x and y component of recoil. The same σ_{UE} is used for both W and Z events. For each x and y component of the underlying event contribution of the Z event, an extra smearing term is added with the following resolution.

$$\sigma^{\text{UE}}_{\text{extra}} = \left[\left(\frac{M_Z}{M_W}\right)^2 - 1\right]^{\frac{1}{2}} \sigma_{\text{UE}} \tag{6.17}$$

After applying the extra smearing for Z's electron, hard recoil and underlying event, a much better agreement of smeared M_T spectrum is observed between W and Z in Fig 6.8 than the original M_T comparison in Fig 6.1. The direct comparison between W and Z may not be the most straightforward way to show the resolution effect and the need of extra smearing for Z events after scaling.

The most clear way to show the need of extra smearing correction is to compare between Z event and the fake W event. Those fake W events are indeed made from the same Z events, with the energy of both electron being scaled by M_W/M_Z (it is equivalent to say that the mass of Z boson is set to M_W in its own rest frame). One of the two electrons is treated like a neutrino and that results in a fake W sample. It is essentially a $W \to e\nu$ sample with boson mass M_W, but has exactly the same kinematics of $Z \to ee$

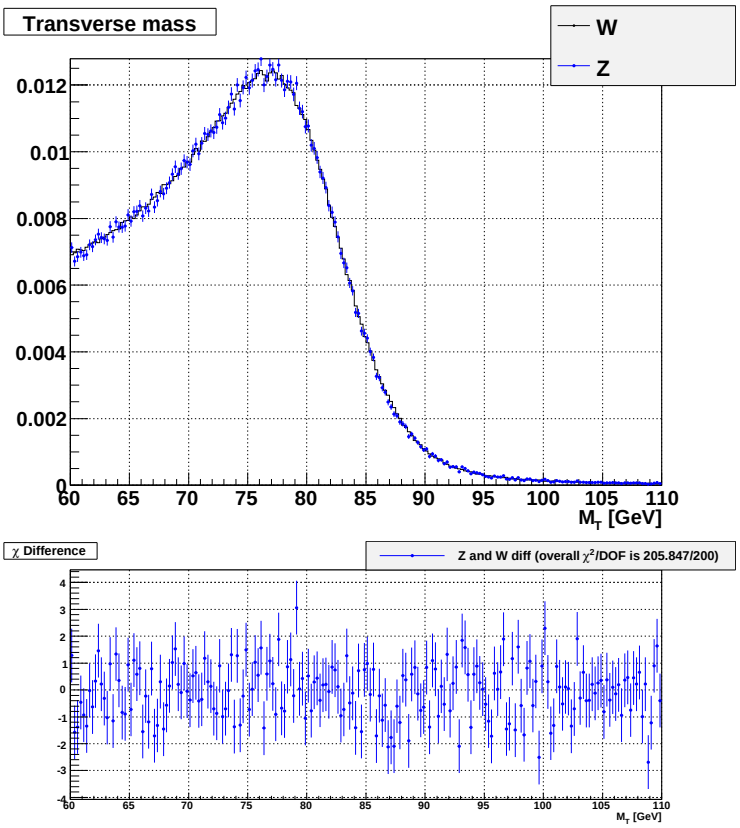

Figure 6.8: The M_T comparison and its χ plot, where M_T of Z events is scaled with input M_W. Extra smearings are applied to $Z \to ee$ events. Compared with Fig 6.1, notice the much better agreement of smeared M_T shape.

events. Smearings of the fake W events are performed at the W level while the original Z events are smeared before the scaling of p_T^e and $\not\!\!E_T$ variables. Direct comparison of these variable between Z and fake W events clearly reveals that M_T, p_T^e and $\not\!\!E_T$ don't scale with boson mass after smearing (Fig 6.9). With the extra smearings applied, smeared p_T^e, $\not\!\!E_T$ and M_T of Z events perfectly scale with boson mass (Fig 6.10).

Since the only difference between fake W events and the original Z sample is due smearing resolution at different energy level, effect of extra smearing correction is shown in Fig 6.9 and Fig 6.10 without any ambiguity.

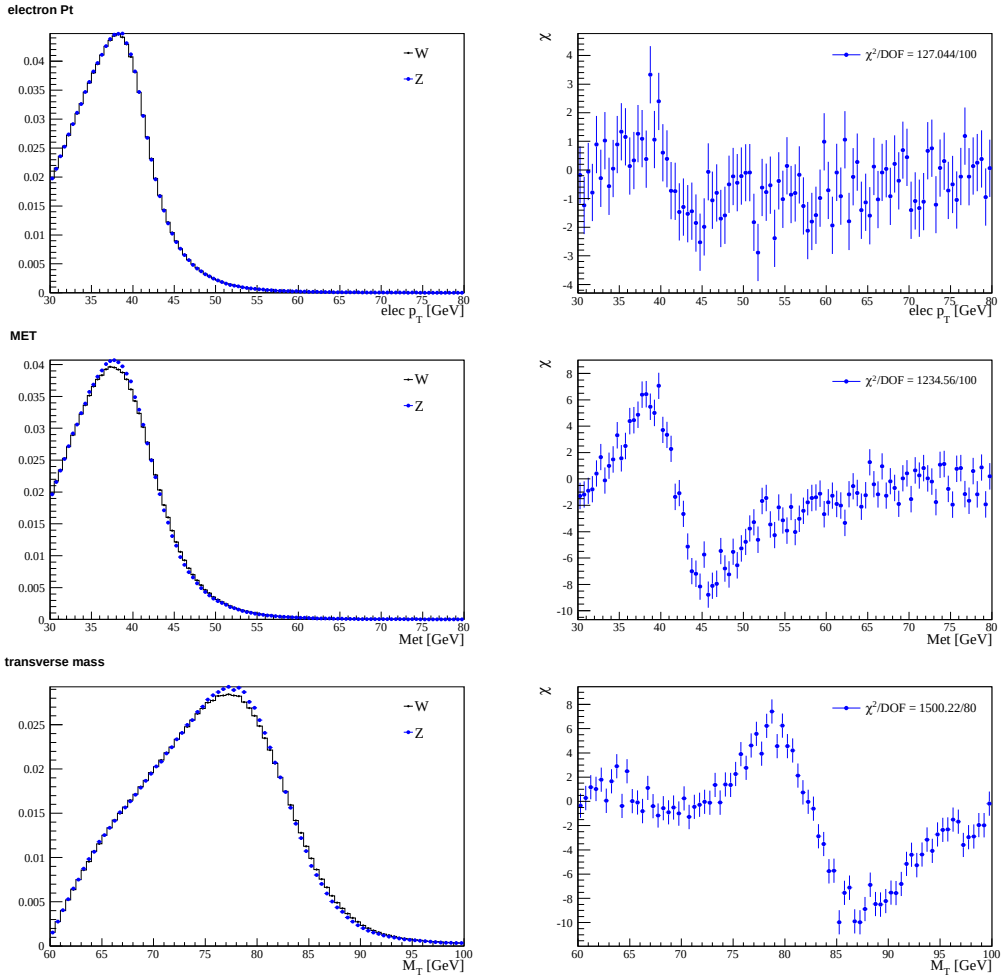

Figure 6.9: Comparison between Z and fake W events. Simple Gaussian smearing , especially no ϕ smearing of electron and hard recoil. There are no extra smearings of EM, recoil and the underlying event.

6.4 Kolmogorov-Smirnov Test

In both the standard method and ratio method, W boson mass is extracted by fitting the M_T spectra templates that are produced with different M_W to the M_T spectrum of W data. M_T templates in the standard method come from fast Monte Carlo simulation, which is statistically unlimited. The main statistical limit there is from the W data sample and it is hardly a limiting factor, as the crossing section of $W \rightarrow e\nu$ events is ten times of $Z \rightarrow ee$ events at Tevatron. To measure the W mass, a likelihood is calculated for between data and each Monte Carlo M_T template, the template with the maximum

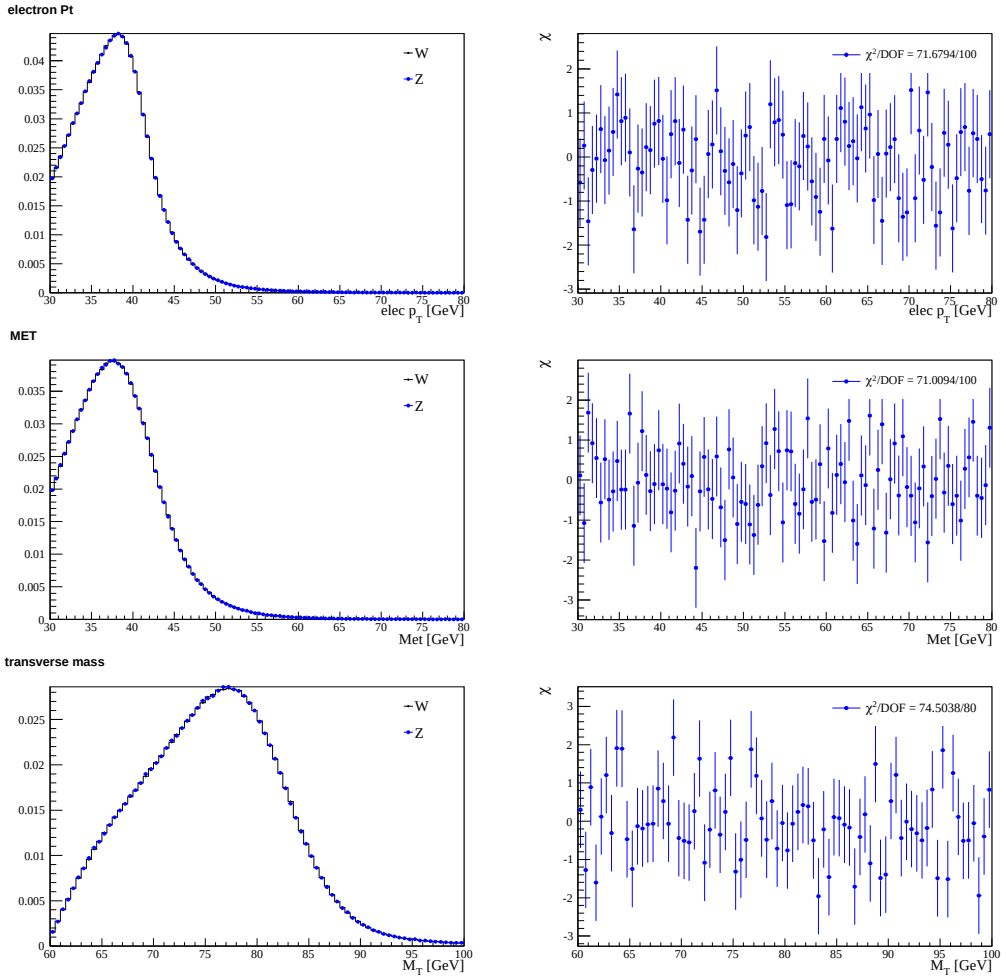

Figure 6.10: Similar comparison as in Fig 6.9, except that extra smearings of EM, recoil and the underlying event are applied to Z events here.

likelihood corresponds to the measured M_W.

In ratio method, the main statistical limit is from the M_T templates made from $Z \rightarrow$ sample. The cross section of $Z \rightarrow ee$ events is about 10 times smaller than $W \rightarrow e\nu$ events in Tevatron. After the acceptance and p_T cut, the final number of $Z \rightarrow ee$ events that entering into M_T spectrum is around 60 thousand (see Chapter 9.1) for the $1\,\mathrm{fb}^{-1}$ integrated luminosity dataset in DØ Run IIa.

Because of the limited statistics from Z, maximum likelihood and χ^2 fitting are not suitable for ratio method. One problem for χ^2 and maximum likelihood fitting is the instability for low statistical sample. For a Z sample of 500 thousand events, χ^2 for mass templates in Fig 5.22 already shows the trend

of instability. By comparison, a similar χ^2 distribution with 5 million events has a much smoother curve in Fig 5.19. In the case of $1\,\mathrm{fb}^{-1}$ Z events in ratio method, the instability of χ^2 and likelihood curve preclude a successful M_W fitting.

This problem is even more severe in the Run I ratio method analysis [33, 34], where only about $100\,\mathrm{pb}^{-1}$ Z events are available for mass fitting. In our analysis we use Kolmogorov-Smirnov (K-S) test to compare the template and data M_T spectrum, which is also used in the Run I ratio method analysis. The M_T template that gives the best fit to data corresponds to the measured M_W.

Kolmogorov Smirnov test is used to check if a statistical sample comes out of a smooth theoretical distribution function [36, 37]. It also can be used to test the compatibility of two statitical sample. In the case of low statistics, χ^2 test may not be suitable and the K-S test is a good alternative here. The original K-S test applies to the unbinned data. As long as the histogram bin width is set small enough compared with any physical quantity we try to measure (such as energy reslution, the step size of mass template *etc*), K-S test can be used to compare such two histograms.

In the W mass measurement, K-S test compares the M_T histogram from data and Monte Carlo. Without loosing generality, both the data and Monte Carlo histograms contain reweighted events. If the original entries are N_{data} and N_{MC} for the unbinned data and Monte Carlo sample, let $x_1 \leqslant x_2 \leqslant \cdots \leqslant x_{N_{\mathrm{data}}}$ be the entries in ascending order for the data histogram, each entry has weight w_i where $i = 1 \cdots N_{\mathrm{data}}$.

Similarly, we can define $x'_1 \leqslant x'_2 \leqslant \cdots \leqslant x'_{N_{\mathrm{MC}}}$ as the Monte Carlo entries in ascending order. The corresponding event weight is w'_j where $j = 1 \cdots N_{MC}$.

The empirical cumulative distribution for data histogram is defined as

$$F_{\mathrm{data}}(x) = \sum_{x_i \leqslant x \leqslant x_{i+1}} P(x_i) \tag{6.18}$$

$$= \frac{\sum_{i=1}^{k} w_i}{\sum_{i=1}^{N_{\mathrm{data}}} w_i} \qquad (x_k \leqslant x \leqslant x_{k+1}). \tag{6.19}$$

The maximum vertical distance D between the data and Monte Carlo cumulative distribution is the varible used to quantify the compatibility of the two histograms in K-S test.

$$D = \max_x |F_{\mathrm{data}}(x) - F_{\mathrm{MC}}(x)| \tag{6.20}$$

K-S test can also calculate the probability of the compatibility between two histograms, given the maximum distance D in the cumulative distribution. Actually the variable entering into the probability calculation in K-S test is the so called effective maximum distance d. If both histograms have no reweighting (*i.e.* $w_i \equiv 1$), the effective maximum distance d is defined as

$$d = \sqrt{\frac{N_{\rm data} N_{\rm MC}}{N_{\rm data} + N_{\rm MC}}} \cdot D \tag{6.21}$$

The probability to get d greater than the observed is given by

$$Q_{\rm KS}(d > \text{observed}) = 2 \sum_{j=1}^{\infty} (-1)^{j-1} \exp(-2j^2 d^2). \tag{6.22}$$

$Q_{\rm KS}$ is the K-S probability we use to in the analysis. Eq 6.22 is far too accurate for any imaginable application. `ROOT` uses a simplified numerical approximation of Equation 6.22 in the calculation of `TMath::KolmogorovProb(d)`.

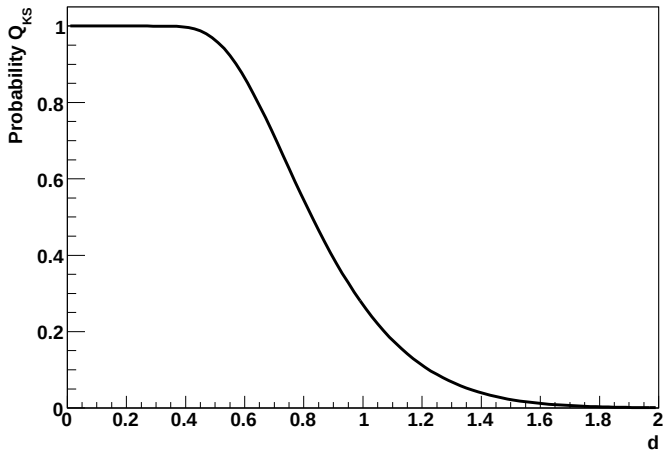

Figure 6.11: The Kolmogorov probability dependence on the effective maximum distance d (defined in Eq 6.21). This is the direct output from the `TMath::KolmogorovProb()` function in `ROOT`.

In the case where the comparing histogram has non trivial weight information (*i.e.* $w_i \neq 1$), $N_{\rm data}$ and $N_{\rm MC}$ need to be replaced with the effective

entries N_e in Eq 6.21 to give the correct d.

$$N_e^{\text{data}} = \frac{(\sum_{i=1}^{N_{\text{data}}} w_i)^2}{\sum_{i=1}^{N_{\text{data}}} w_i^2} \qquad N_e^{\text{MC}} = \frac{(\sum_{i=1}^{N_{\text{MC}}} w_i)^2}{\sum_{i=1}^{N_{\text{MC}}} w_i^2}. \tag{6.23}$$

There are two important observations related to the statistics of the two samples in the calculation of effective distance d. In the ratio method of W mass measurement, W events are put into the data histograms and Z events are put into the Monte Carlo histogram. Because the WZ cross section ratio is roughly 10, which means $N_{\text{data}} \gg N_{\text{MC}}$. The constraint from the statistical part of d is mainly due to limited Z sample, as Eq 6.24 shows.

$$\frac{N_{\text{data}} N_{\text{MC}}}{N_{\text{data}} + N_{\text{MC}}} \approx N_{\text{MC}} \tag{6.24}$$

The other important observation has to do with the event weight. Reweighting is needed at some point as means to make corrections to the W and Z events (for instance, in the acceptance corrections). However event weights greater than 1 tend to diminish the effective entries. This can be illustrated by Table 6.2. Overall larger event weight result in smaller effective entries for the same sample. For the same raw maximum distance D in the cumulative distribution, the effective maximum distance d is smaller for sample with weights > 1 (Eq 6.21).

max weight	events #	`GetEntries`	`Integral`	`GetEffectiveEntries`
$w = 100$	5×10^6	3.16×10^6	2.16×10^6	0.66×10^6
$w = 10$	5×10^6	3.16×10^6	2.10×10^6	1.43×10^6
$w = 7$	5×10^6	3.16×10^6	2.08×10^6	1.53×10^6

Table 6.2: The number of effective entries with different maximum weight allowed. The sample used in this table is based on the W's electron in CC (CC edge is in $\eta < 1.40$). `GetEntries()` include the underflow and overflow of the histogram. `Integral()` doesn't include the underflow and overflow but contains the weight information. `GetEffectiveEntries()` also doesn't include the underflow and overflow.

K-S test is used in ratio method to extract the best matched W mass from the M_T templates. One probability that stands for the data – Monte Carlo compatibility is calculated for each templates. The maximum probability is

from the matched template, and that gives the measured M_W. The statistical uncertainty is defined as such that the K-S probability drops to $e^{-1/2}$ of its maximum value. However the statistical uncertainty calculated in this way is not valid because of the two M_T calculated from one Z event is correlated to some extent (see the next section). The correct statistical uncertainty comes from ensemble test.

6.5 Electrons Selection Bias

Ratio method assumes one of the $Z \to ee$ electrons to fake a neutrino from W and the M_T is calculated accordingly. There is a question about how to choose the Z's two electrons to fake neutrino. For each Z event, we can either randomly select one of the electrons or we can use both of the two electrons, calculating two M_T by making each of them to fake neutrino. From the following, we use the term "$1Z1W$" to stand for the former and "$1Z2W$" for the latter.

On the generator level, it can be shown that one W and two Ws are fully correlated. The two M_T calculated from one Z event are actually the same, since the E_T^e and $\not\!\!E_T$ are symmetrical in Eq 6.25. This is illustrated in Fig 6.12, where M_T spectra calculated from this two methods are compared.

$$M_T = \sqrt{2E_T^e \not\!\!E_T (1 - \cos\phi)} \tag{6.25}$$

An ensemble test with 600 pseudo experiments is used to study the true statistical uncertainty of the fitted M_W. Each pseudo experiment is generated with distinct random seed. $1Z2W$ (Fig 6.13) has the same statistical uncertainty of fitted M_W as $1Z1W$ (Fig 6.14). For the M_T histogram of $1Z2W$, the error bar of each bin that calculated in the standard way is not correct, as the number of entries is twice as large as the actual entries of independent M_T. Statistical uncertainty calculation of $1Z2W$ based on the raw entries of histograms is thus not accurate. The standard deviation of the fitted M_W pull distribution from ensemble test is the correct value of statistical uncertainty.

In other words, using the same Z events to make two Ws doesn't improve the statistical power of the ratio method. The two M_T calculated from one Z event is fully correlated on the generator level.

After the smearing of the electron and recoil system, the two M_T calculated from the same $Z \to ee$ event become only partially correlated (instead of fully correlated as in generator level). Each electron has its own smearing (uncorrelated) while the recoil system is commonly shared (fully correlated) in the calculations of the two M_T. Putting both M_T into the histogram does

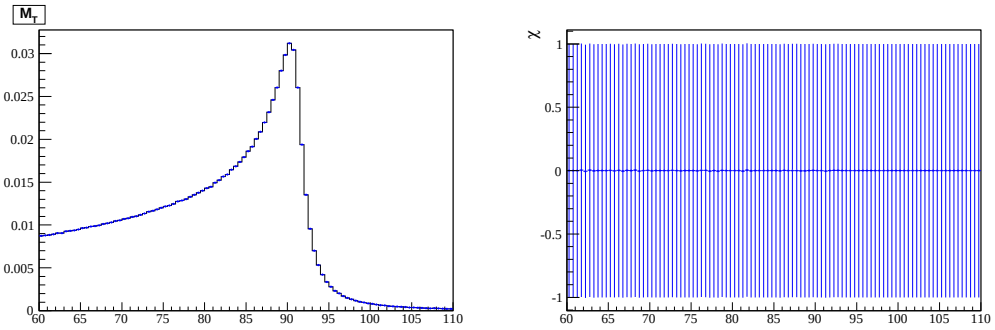

Figure 6.12: Overlay of generator level (no cuts) M_T from Z events (before mass scaling). Each Z make one W (blue) or two W (black), from the same Z sample. Right plot shows the χ difference between the two M_T.

offer the benefit of additional statistics. Fig 6.15 and Fig 6.16 show that after smearing without any cut, $1Z1W$ and $1Z2W$ give very similar M_T spectrum.

What's really interesting for the study of electron selection bias is to observe what will happen after applying the additional acceptance cut. A detailed discussion on the effect of acceptance will be presented in Chapter 6.6. There the acceptance cut for Z is one electron e_1 in CC (Central Cal) and the other electron e_2 is in either CC or EC (End Cal). If Z pass this acceptance cut, the M_T calculated with $\overrightarrow{E_T^{e_1}}$ and $\overrightarrow{\not\!\!E_T^{e_2}}$(Eq 6.7) will entering the histogram. The other partially correlated M_T by switching e_1 and e_2 will also enter the histogram if e_2 is in CC and e_1 is in either CC or EC.

Acceptance cut for the $1Z1W$ sample requires the randomly selected electron to be in CC and the other electron (fake neutrino) in EC. With other selection cuts and relevant corrections applied, the fitted M_W distribution of ensemble test for $1Z1W$ and $1Z2W$ is shown in Fig 6.17 and Fig 6.18. $1Z2W$ does provide better statistical uncertainty, without introducing noticeable bias of the central M_W when compared with $1Z1W$.

6.6 Acceptance

As shown in Fig 3.8, the DØ calorimeter provides coverage up to $|\eta| < 1.1$ by CC and $1.5 < |\eta| < 4.1$ by EC. There is a gap of $1.1 < |\eta| < 1.5$ between CC and EC η coverage. For CC, ϕ coverage is not complete either, there are small gaps for the placement of data cables between the adjacent modules of the total 32 CC modules which spans over the ϕ space of 2π. Electrons that hit in the calorimeter region far away from the η or ϕ edge are well measured, hence

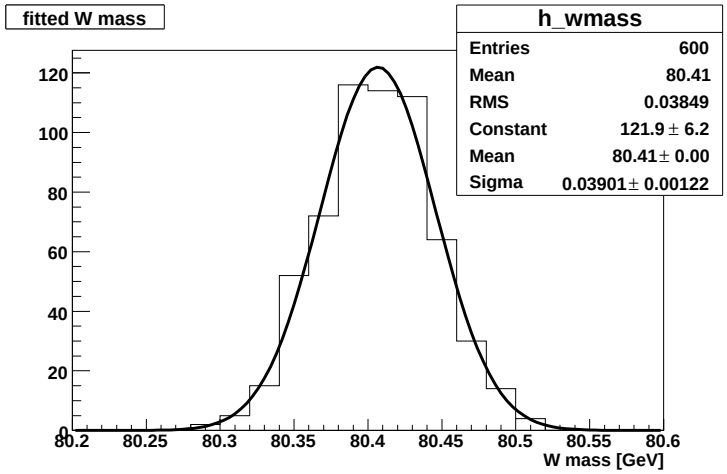

Figure 6.13: $1Z1W$. Fitted M_W of the 600 ensemble tests (each of $1\,\mathrm{fb}^{-1}$ events) on the generator level, no cuts. $\sigma(M_W) = 39\,\mathrm{MeV}$ is the true statistical uncertainty.

these regions are called the fiducial area. The standard choice for W mass measurement is that the η fiducial area covers $|\eta| < 1.05$ and the ϕ fiducial area covers the central 10% to 90% region of each ϕ module. The EC coverage for Z electrons is chosen as $1.5 < |\eta| < 2.5$. There is no structure of ϕ modules in EC.

Because electrons in CC are very well studied, the standard method of W mass measurement selects only the CC fiducial electrons in their final event selection. In ratio method, we adopt the same selection cut of CC electrons for the $W \to e\nu$ sample (Chapter 4.3). There is no way to constrain the neutrino acceptance in $W \to e\nu$ events, which means neutrinos have full acceptance.

In ratio method, to make the M_T of $Z \to ee$ event scale with boson mass, one would like to make $Z \to ee$ event have the similar acceptance cut as $W \to e\nu$. The tight electron of Z (which is the equivalent of W electron) should be in CC fiducial only. The loose electron of Z in principle should have the full acceptance, just like a neutrino, but in reality the best we can do is to require it in either CC or EC.

There are a few problems concerning the slight difference of lepton acceptance in $W \to e\nu$ and $Z \to ee$ events.

- The upper limit of EC η coverage is $|\eta| = 2.5$, which means the very forward and backward neutrinos are very difficult to be simulated by the loose electron of Z.
- The CC/EC gap ($1.1 < |\eta| < 1.5$) for the loose electron of Z.

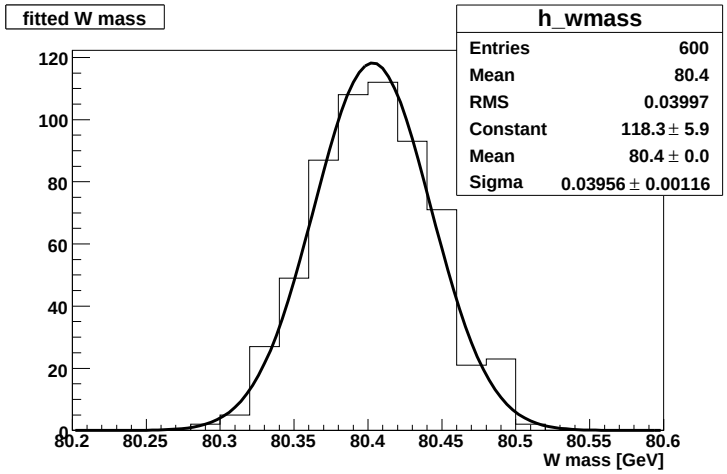

Figure 6.14: $1Z2W$. Fitted M_W of the 600 ensemble tests (each of $1\,\mathrm{fb}^{-1}$ events) on the generator level, no cuts. $\sigma(M_W) = 39\,\mathrm{MeV}$.

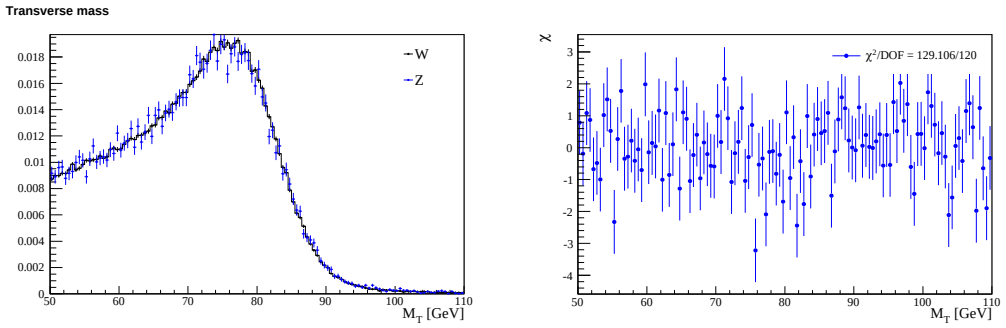

Figure 6.15: Comparison of M_T on the fully smear level, $1\,\mathrm{fb}^{-1}$, no cuts applied. $1Z1W$.

- What's the effect on M_T spectrum by selecting the tight electron in CC only for both W and Z events? Assume the loose electron of Z is assumed to have the same full acceptance as neutrino.

6.6.1 Neutrinos with $|\eta| > 2.5$

The upper limit of EC acceptance $|\eta| < 2.5$ is on the detector η of electrons. Without vertex smearing, detector η is the same as physics η. In this case, the loose electrons of Z are not able to cover the phase space beyond $|\eta| > 2.5$. One way to observe this bias on M_T spectrum is to apply the η cut on the generator level neutrino η. As shown by Fig 6.19, those W events with high $|\eta|$ loose electrons that fail the acceptance cut mostly reside in the lower range

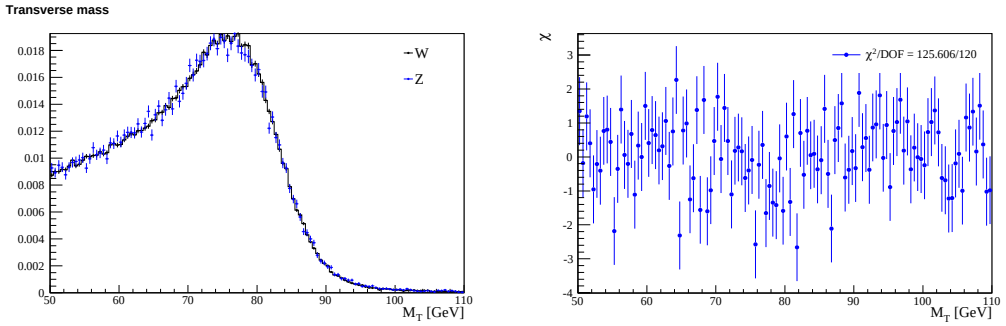

Figure 6.16: Comparison of M_T on the fully smear level, $1\,\mathrm{fb}^{-1}$, no cuts applied. $1Z2W$.

of M_T, roughly $M_T < 82\,\mathrm{GeV}$.

In reality this bias is less severe than in the generator level, due to the vertex smearing along z direction. Detector η cut at 2.5 still allows some loose electrons with physics $|\eta| > 2.5$ to be detected in EC. The wide the vertex smearing resolution σ_z is, the higher the probability is for loose electron with large pesudo rapidity to be detected in EC. From this perspective, ratio method prefers to have minimal vertex z cut in the event selection. Fig 6.20 gives the bias of missing large pesudo rapidity electron on the smeared M_T spectrum. The influence is mostly in the lower range (below 75 GeV) of the M_T spectrum. The overall bias of this cut and other acceptance cuts will be discussed in the following sections.

6.6.2 Bias of M_T by Tight Electron in CC

The acceptance cut for the tight electrons of Z is the same as the W electrons: in CC fiducial region. This cut itself actually introduces substantial bias on the M_T spectrum in ratio method. As mentioned earlier, the CC η fiducial cut requires the electron to have detector $\eta < 1.05$ and the CC ϕ fiducial cut requires the electron hit must be away from the edges of those 32 modules. The ϕ fiducial bias is somewhat easy to understand. Both electrons decayed from Z boson have high tendency of being back to back in the transverse plane because of the boson p_T is small compared with its invariant mass. If one of the electrons hit the edge of CC ϕ module, the other electron also tends to be close to the edge of the opposite module. The same event selection preference can't be applied to W events, as the neutrino is not directly measured by calorimeter. However the effect on M_T spectrum due to this bias is minimal compared with the η fiducial cut.

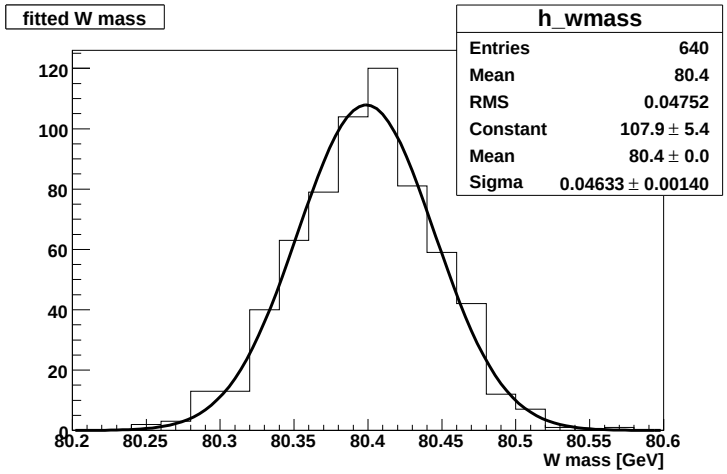

Figure 6.17: $1Z1W$. Fitted M_W of the 600 ensemble tests (each of $10\,\text{fb}^{-1}$ events) on the smeared level, after acceptance cuts and other cuts. $\sigma(M_W) = 48\,\text{MeV}$ is the true statistical uncertainty.

Toy Calorimeter Without CC/EC Gap

The bias of M_T spectrum due to CC η fiducial cut is not straightforward at first glance, as the same cut is applied to both the W and Z electrons. A toy calorimeter model is used in the fast Monte Carlo study to preclude bias by other cuts other than the CC η fiducial cut. In this toy calorimeter model, Central Calorimeter covers pseudo rapidity range up to $|\eta| < 1.2$ and the End Calorimeter covers the $1.2 < |\eta| < 100$ range. In other words, CC and EC have continuous η coverage with no gap between them. Also the EC η coverage now extends to the extremely forward and backward direction.

With the same standard η acceptance selection in the ratio method (first bullet in Chapter 4.3), the loose electron of Z now has full η acceptance, same as the W neutrino. It's interesting to observe the effect of the η acceptance cut of Z's tight electron on the M_T spectrum.

To that end, the M_T spectrum comparisons of W and Z events are divided into categories according to acceptance cut of tight electron. Lepton p_T cut is also varied to show that higher cuts can alleviate the bias caused by acceptance cut.

- No lepton p_T cuts for Fig 6.21 to Fig 6.23.
- $p_T^e > 25\,\text{GeV}$ and $\not\!\!E_T > 25\,\text{GeV}$ for Fig 6.24 to Fig 6.26.
- $p_T^e > 30\,\text{GeV}$ and $\not\!\!E_T > 30\,\text{GeV}$ for Fig 6.27 to Fig 6.29.

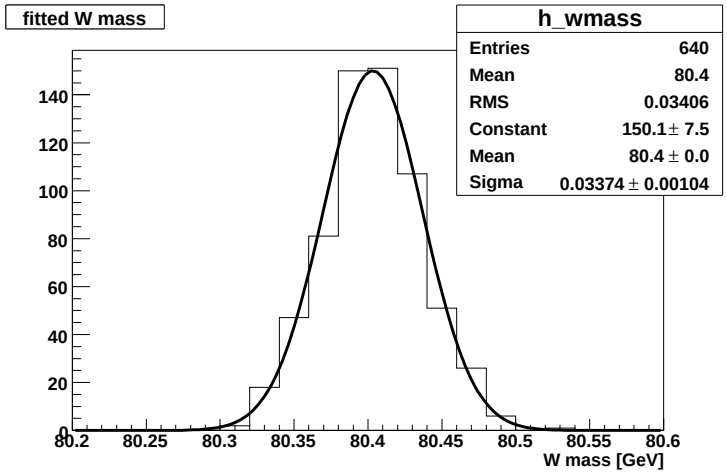

Figure 6.18: $1Z2W$.Fitted M_W of the 600 ensemble tests (each of $10\,\mathrm{fb}^{-1}$ events) on the smeared level, after acceptance cuts and other cuts. $\sigma(M_W) = 34\,\mathrm{MeV}$.

Each of the above category contains the M_T comparison Figures based on the acceptance cut of the tight electron.

- The tight electrons of Z and the W electrons are in CC.
- The tight electrons of Z and the W electrons are in EC.
- The tight electrons of Z and the W electrons are in either CC or EC (full acceptance).

Guassian smearing are applied to both the W and Z events. For Z sample, the relevant extra smearing corrections are also applied. Therefore the corrected M_T spectrum of Z sample is essentially the same as that of fake W events (Chapter 6.3). Without lepton p_T cuts, good agreement of M_T spectrum is observed when the tight electron of Z and the W electron has full acceptance (Fig 6.23), which is essentially the same plot in Fig 6.8. Significant difference is observed when the tight electron is restricted to partial acceptance, as shown in Fig 6.21 (CC) and Fig 6.22 (EC).

It is believed that the difference of boson p_T and lepton decaying angle $\cos\theta^*$ between $W \to e\nu$ and $Z \to ee$ events causes the failure of M_T scaling with W and Z boson mass. As shown in the next section, by forcing the boson p_T and $\cos\theta^*$ distribution to agree (approximately, by first order reweighting), we could obtain the M_T spectrum to scale with W and Z boson mass when the tight electron is required to be in CC. This study is performed on the generator level events only for illustration, which will be discussed shortly. No

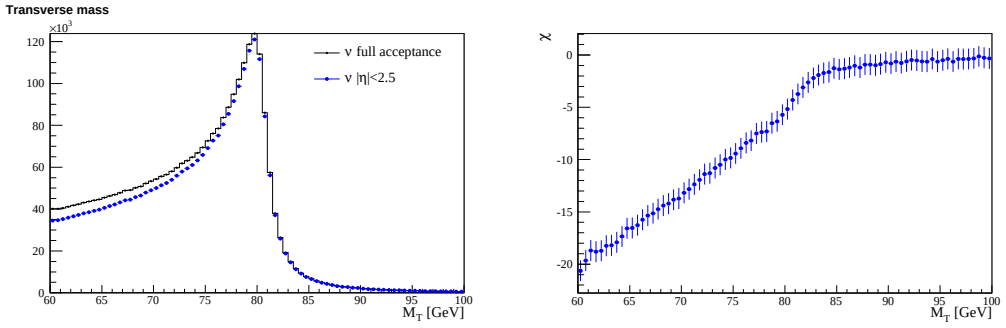

Figure 6.19: Comparison of the generator level M_T of $W \to e\nu$ events. One sample is with full acceptance, the other requires neutrino $|\eta| < 2.5$. Both histograms are not normalized.

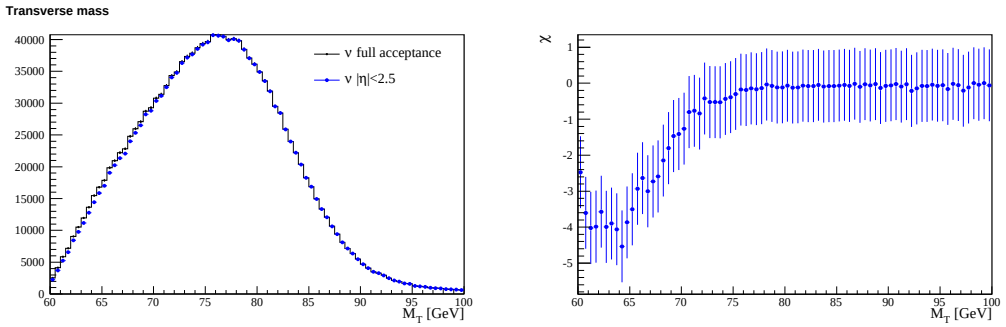

Figure 6.20: Comparison of the smeared level M_T of $W \to e\nu$ events. The primary vertex of both sample are smeared with Guassian function along the beam direction with resolution $\sigma_z = 25\,\text{cm}$. One sample is with full acceptance, the other requires neutrino to have detector $|\eta| < 2.5$. Both histograms are not normalized.

such kinematic reweighting corrections are applied to smeared Monte Carlo events or data.

The most interesting plot is Fig 6.21 (tight electron in CC), as it has the official acceptance cut. Without any corrections, it is impossible to extract W mass when such a large discrepancy of M_T spectrum is observed. After applying the lepton p_T cut of 25 GeV (Fig 6.24) and 30 GeV (Fig 6.27), better agreement is observed in the Jacobian edge of M_T spectrum (75 GeV to 90 GeV). In the final events selection (Chapter 4.3), lepton p_T cut is chosen at 30 GeV instead of 25 GeV (which is used in the standard method), as the agreement of M_T Jacobian edge is better in the case of 30 GeV cut. When the fitting range is careful chosen to avoid the lower M_T range (Fig 6.27), it is possible to make a successful fit of M_W that is close to the input W mass.

Bias due to acceptance cut on tight electron is among the most prominent effects in ratio method. The cause of this bias comes from the different kinematic distributions of leptons in the rest frame of W and Z boson (see the lepton $\cos\theta^*$ distributions of W and Z events Fig 5.5 and Fig 5.6). This is further complicated by different boost of W and Z boson. It's not totally a surprise that a big difference of M_T spectrum is observed after the same η cut on the electrons of W and Z.

The above argument is corroborated by a test on generator events (kinematic reweighting) that is described in the next section. For the final W mass fitting, we don't apply corrections to the acceptance cut of tight electrons. Instead, we use the range of Jacobian edge (for example, the range of 70 GeV to 90 GeV) for the fitting, which is relatively less affected by this bias. Together with other cuts, a systematic bias is obtained in the ensemble test of fast Monte Carlo simulations. This bias is added to the M_W out of data fitting to give the final fitted value.

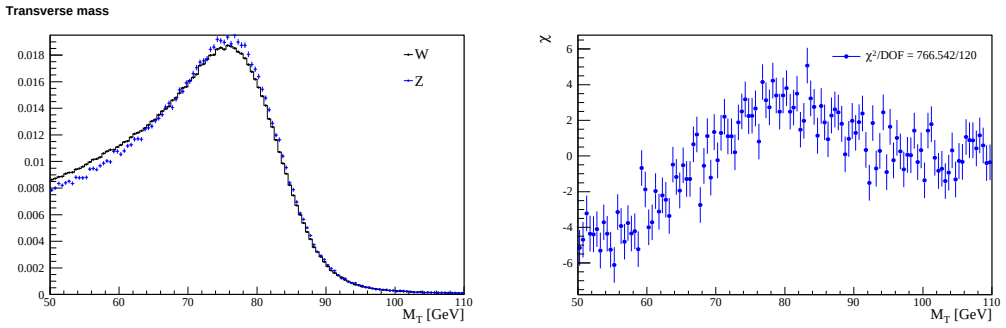

Figure 6.21: M_T comparison of W and Z. No lepton p_T cut, tight electron in CC, loose electron in CC or EC (full acceptance).

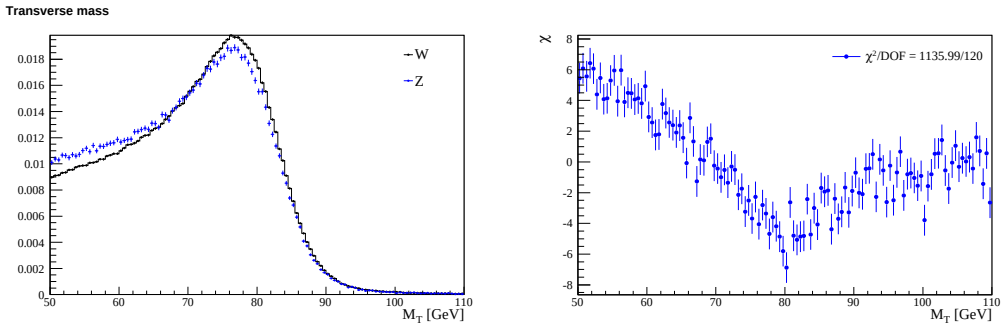

Figure 6.22: M_T comparison of W and Z. No lepton p_T cut, tight electron in EC, loose electron in CC or EC (full acceptance).

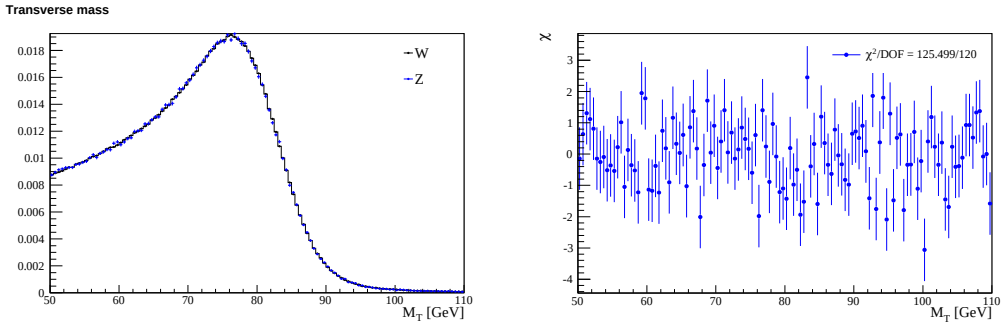

Figure 6.23: M_T comparison of W and Z. No lepton p_T cut, tight electron in CC or EC (full acceptance), loose electron in CC or EC (full acceptance).

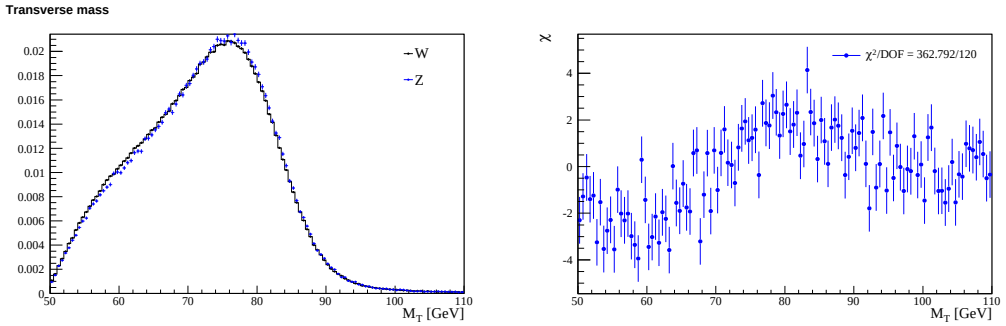

Figure 6.24: M_T comparison of W and Z. $p_T^e > 25\,\text{GeV}$ and $\not\!\!E_T > 25GeV$, tight electron in CC, loose electron in CC or EC (full acceptance).

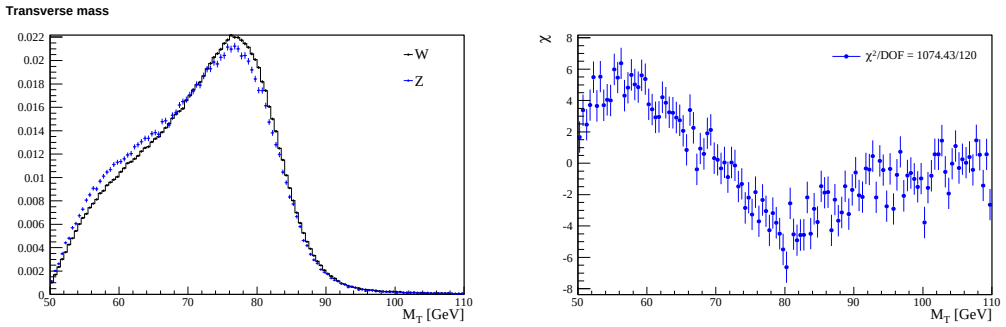

Figure 6.25: M_T comparison of W and Z. $p_T^e > 25\,\text{GeV}$ and $\not\!\!E_T > 25GeV$, tight electron in EC, loose electron in CC or EC (full acceptance).

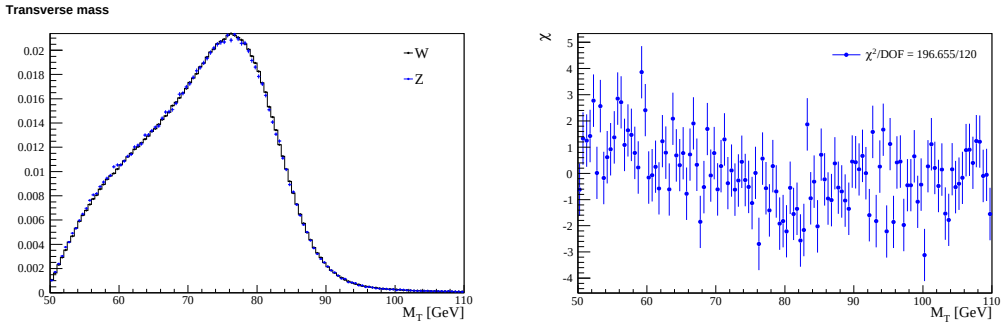

Figure 6.26: M_T comparison of W and Z. $p_T^e > 25\,\text{GeV}$ and $\not\!\!E_T > 25GeV$, tight electron in CC or EC (full acceptance), loose electron in CC or EC (full acceptance).

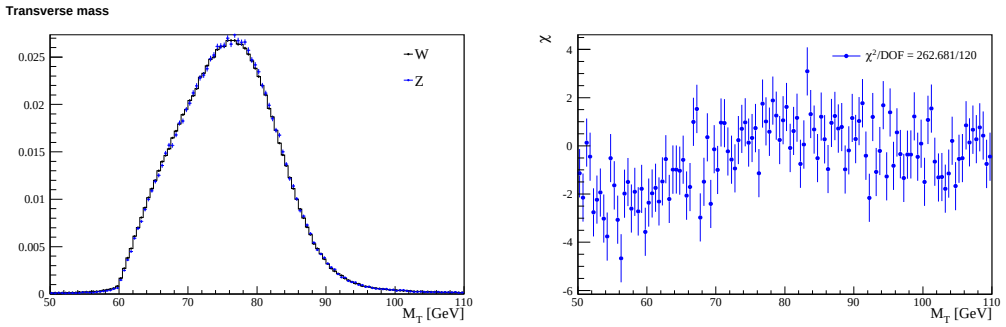

Figure 6.27: M_T comparison of W and Z. $p_T^e > 30\,\text{GeV}$ and $\not\!\!E_T > 30GeV$, tight electron in CC, loose electron in CC or EC (full acceptance).

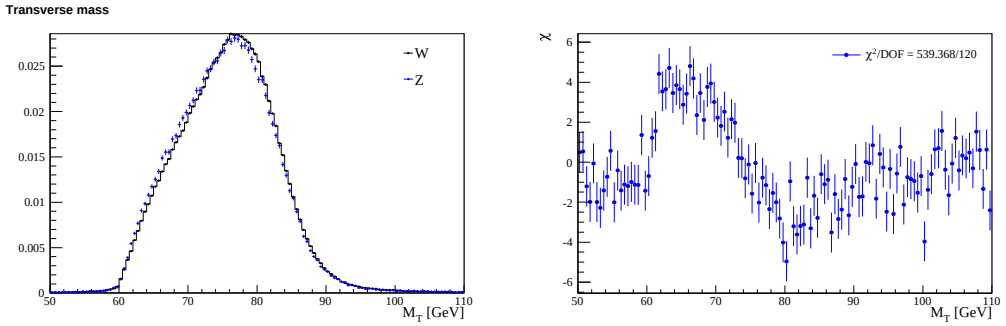

Figure 6.28: M_T comparison of W and Z. $p_T^e > 30\,\text{GeV}$ and $\not\!\!E_T > 30GeV$, tight electron in EC, loose electron in CC or EC (full acceptance).

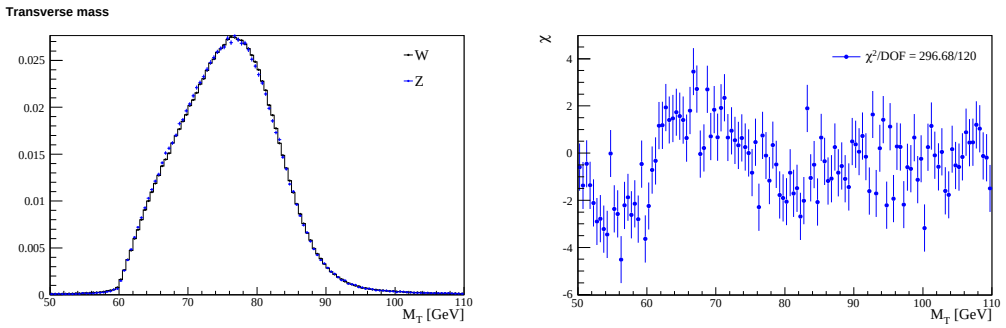

Figure 6.29: M_T comparison of W and Z. $p_T^e > 30\,\text{GeV}$ and $\not\!\!E_T > 30GeV$, tight electron in CC or EC (full acceptance), loose electron in CC or EC (full acceptance).

Kinematics Reweighting

Similar discrepancy of M_T caused by requiring tight electron in CC for the smeared Monte Carlo events (Fig 6.21) is observed on the generator level events. When the tight electron is required to have physics $|\eta| < 1.05$, substantial disagreement is observed in the lower range of M_T spectrum (Fig 6.30). This is caused by the different distribution of boson p_T and the lepton decaying angle θ^*. For instance in Fig 6.31, the physics η distribution of electrons is different in W and Z events. Electrons decayed from Z tend to be more forward than those from W. As expected, a fixed acceptance cut at $|\eta| = 1.05$ causes selection bias which is reflected in the comparison plot of M_T spectrum.

To test this assumption, we make a series of corrections to the Z events and make the boson and lepton kinematics to be identical to those in W events. Then the M_T spectra is compared again with the acceptance on tight electrons.

The corrections are identical to those described in Chapter 5.2. The procedure consists of reweighting lepton $\cos\theta^*$, boson p_T and y distribution of $Z \to ee$ events. In particular, to simplify, we didn't use a two dimensional boson p_T versus y, but doing the iterative one dimensional reweighting of p_T and y. After the reweighting corrections, the electron η distribution of Z events is much similar to the one in W events (right plot in Fig 6.31). Because the reweighting corrections don't treat the correlation of boson p_T and y properly, there is still small difference remaining in the electron η distribution after correction.

After the above reweighting corrections to $Z \to ee$ events, the updated M_T spectrum has reasonable agreement over the range of 60 GeV to 110 GeV (Fig 6.32).

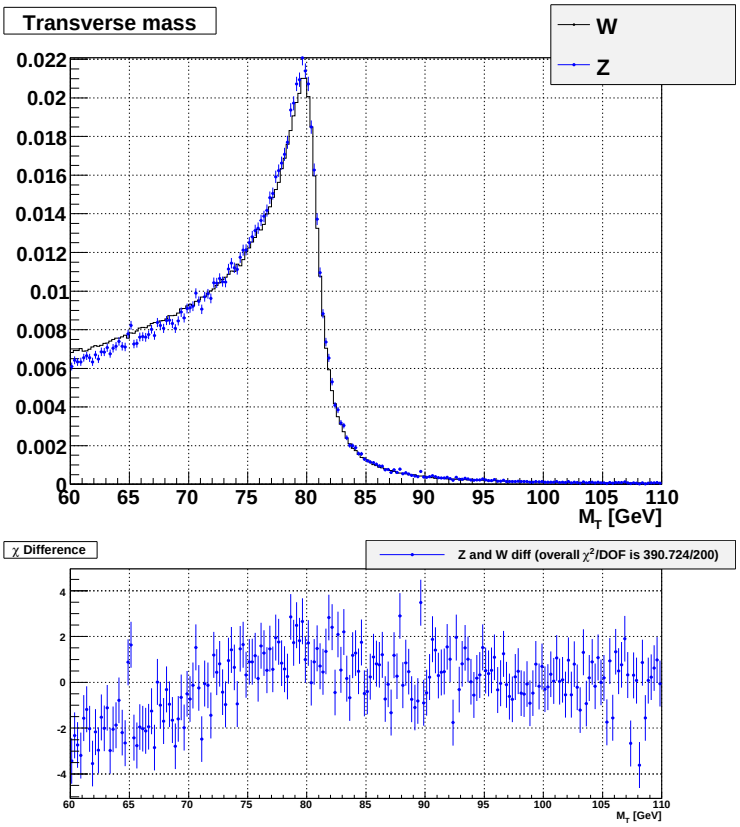

Figure 6.30: Generator level M_T comparison. Both the W electron and the tight electron of Z are required to have physics $|\eta| < 1.05$.

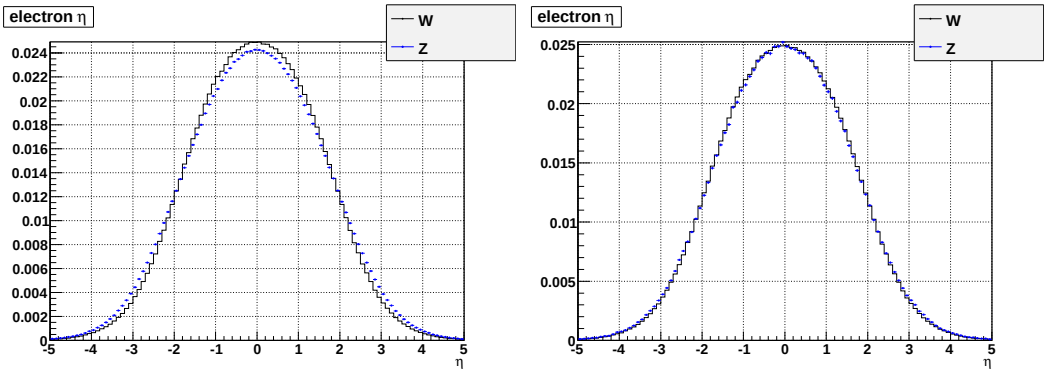

Figure 6.31: Generator level electron η distribution in W and Z sample. Left plot is before any correction, the right one is after kinematics reweighting corrections.

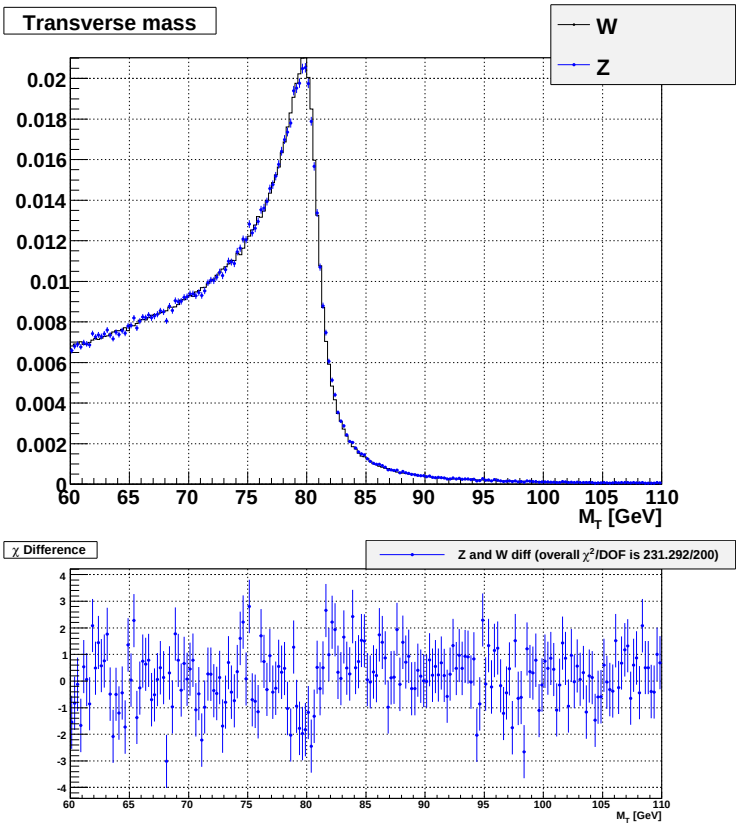

Figure 6.32: Same M_T comparison plot as in Fig 6.30, but after the reweighting correction.

6.6.3 Reweighting Correction of Loose Electron for the CC/EC Gap

Without the smearing of primary vertex along the z axis, CC/EC gap of $1.05 < \eta_{\text{det}} < 1.5$ makes those loose electrons of Z with physics η in the same range of η_{det} fail to pass the event selection cut. The DØ Run IIa W and Z data in this analysis are known to have smearing of primary vertex z with resolution $\sigma \simeq 25\,\text{cm}$. In this case, some Z's loose electrons with $1.05 < \eta_{\text{phys}} < 1.5$ pass the event selection cut. With known vertex smearing shape and the dimensions of the CC/EC edge, the probability for a specific electron to enter the CC or EC depends on the physics η of that electron.

Let f_z be the distribution of the primary vertex z_{vtx}. The probability for electron with physics η (or equivalently θ) to reach the CC or EC is the integral of the normalized vertex distribution between the point of $z_1(\theta)$ and $z_2(\theta)$, which are the projections of CC/EC edges along angle θ of electron(s).

Eq 6.26 is the mathematical definition of probability calculation.

$$p = \bigcap_{i=1(,2)} \sum_{CC,EC} \int_{z_1(\theta_i)}^{z_2(\theta_i)} f(z)dz, \tag{6.26}$$

A sketch diagram is helpful to the understand of the above procedure. In Fig 6.33 the vertex distribution is of Gaussian shape. The shaded area of the normalized Gaussian distribution stands for the probability for the electron to reach CC or EC. The integral of a normalized Gaussian function

$$\varphi_{\mu,\sigma}(z) = \frac{1}{\sigma\sqrt{2\pi}} e^{-\frac{(z-\mu)^2}{2\sigma^2}}, \tag{6.27}$$

is actually an error function

$$\begin{aligned} \Phi_{\mu,\sigma}(z) &= \int_{-\infty}^{z} \varphi_{\mu,\sigma}(t)dt \\ &= \frac{1}{2}\left[1 + \mathrm{erf}(\frac{z-\mu}{\sqrt{2}\sigma})\right]. \end{aligned} \tag{6.28}$$

Error function can be evaluated analytically using the `TMath::Erf` method in `ROOT`. In the case of non Gaussian form z_{vtx} smearing in data, the integral can be evaluated numerically. The left plot in Fig 6.34 shows the probability for one electron to hit CC or EC as a function of its physics η, given the $\sigma = 25\,\mathrm{cm}$ Gaussian smearing of z_{vtx} and the calorimeter CC/EC geometry. The probability drop near physics $|\eta| \simeq 1.35$ is caused by the CC/EC gap while the sharp drop after physics $|\eta| \simeq 2.5$ reflects the upper limit of EC detector η coverage. The probability for two electrons to be in CC/EC is shown in the right plot of Fig 6.34. For official acceptance cut, the probability of W and Z events is shown in Fig 6.35.

The corrections we would like to apply is to make those Z's loose electrons in CC or EC have the same physics η as W's neutrino (full acceptance). One way to accomplish this is to assign higher event weights to those loose electrons that are less likely to reach CC or EC, due to the CC/EC gap. Missing loose electrons due to no EC coverage beyond $|\eta| > 2.5$ have no big effect in ratio method, as discussed in Chapter 6.6.1. The event weight is chosen as the reciprocal of the probability for an electron with physics η to reach CC/EC (Fig 6.35). For electrons with very small probability, event weights are quite large. Without cutting on the upper limit of event weight, spikes are observed in M_T spectrum and the number of effective entries of M_T spectrum for template fitting in the K-S test are also reduced. Therefore a maximum

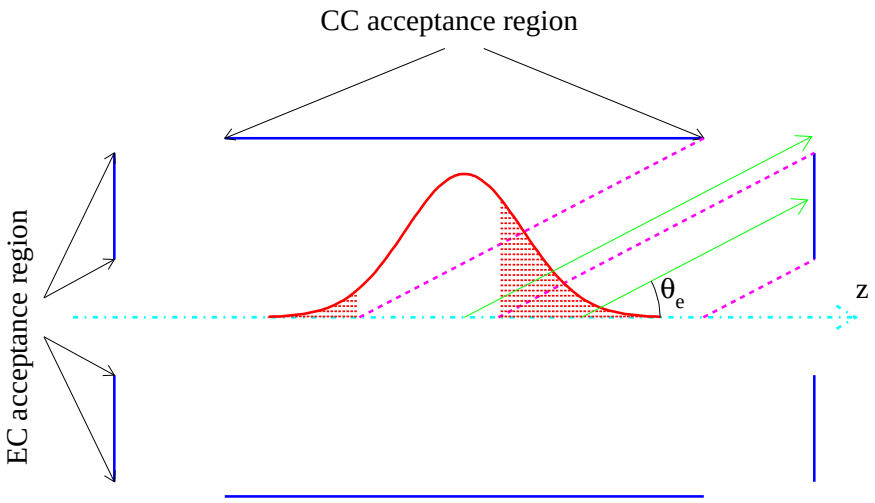

Figure 6.33: With Gaussian vertex smearing and the dimension of calorimeter acceptance shown (not in scale), the probability of an electron with incoming polar angle θ to reach either CC or EC is the red shadow area (normalized) of the gaussian function.[34]

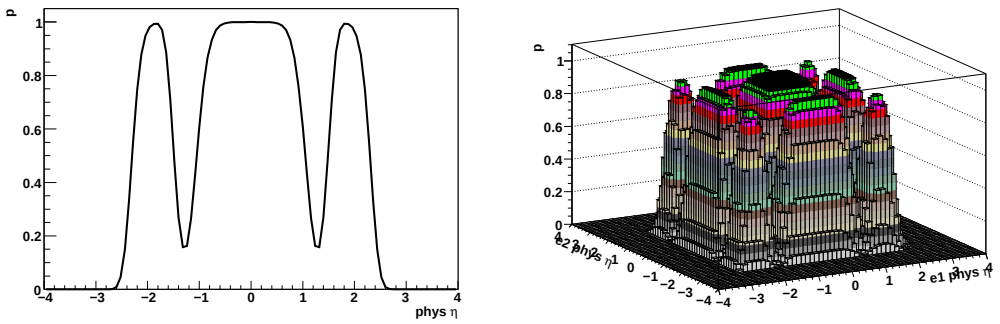

Figure 6.34: The probability for one electron to reach in the CC or EC η fiducial region (left). The right plot is for two electrons either in CC or EC.

value of 10 is set for large event weights. Typical probability distributions for tight and loose electrons are shown in Fig 6.36.

The original physics η distribution of Z's loose electron that is in CC or EC is shown in the left plot of Fig 6.37. The impact of CC/EC gap is evident on the drop of events around physics $\eta = \pm 1.3$. After the acceptance reweighting correction, those drops of physics η around ± 1.3 are largely recovered. The overall physics η distribution of loose electrons is more smooth, close to

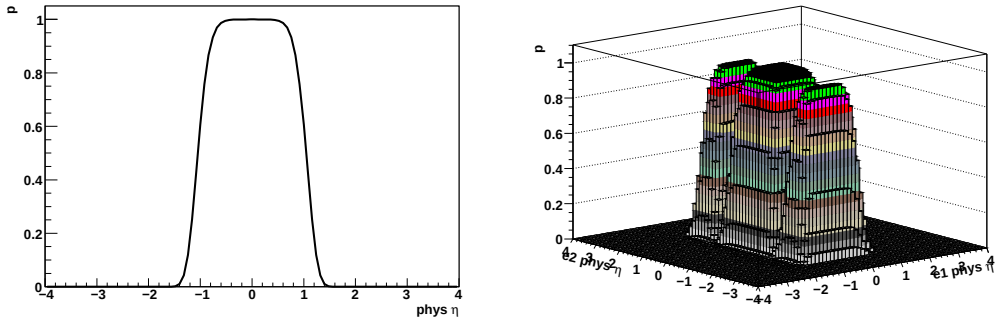

Figure 6.35: The probability of official events selection. The left plot is for the W event, electron in CC. The right plot is for Z, the tight electron in CC and the loose electron in either CC or EC.

(but not exactly the same as) the case where the loose electron of Z has full acceptance.

One way to appreciate the reweighting correction is to compare the transverse mass distribution before (Fig 6.38) and after (Fig 6.39) the reweighting correction. The M_T spectrum of Z events has much better agreement with that of the W sample after the CC/EC gap effect is corrected. The other two acceptance biases (of the three listed at page 96) are not corrected and the M_T spectrum in Fig 6.39 still has disagreement that is consistent with Fig 6.20 and Fig 6.21.

With additional lepton p_T cuts at 30 GeV, the acceptance bias will be further mitigated (similar to the change from Fig 6.21 to Fig 6.27). The fitted M_W central value from the ensemble test in the fast Monte Carlo simulation that has all the major factors included should give the overall bias of the ratio method. This will be done in the next Chapter where the simple Gaussian smearings used in this Chapter will be replaced with more complicated `wz_epmcs` smearing. The complicated smearing algorithms developed in `wz_epmcs` have reasonable agreement with the $1\,\mathrm{fb}^{-1}$ DØ Run IIa data, and that is crucial to the measurement of M_W in the standard method [11].

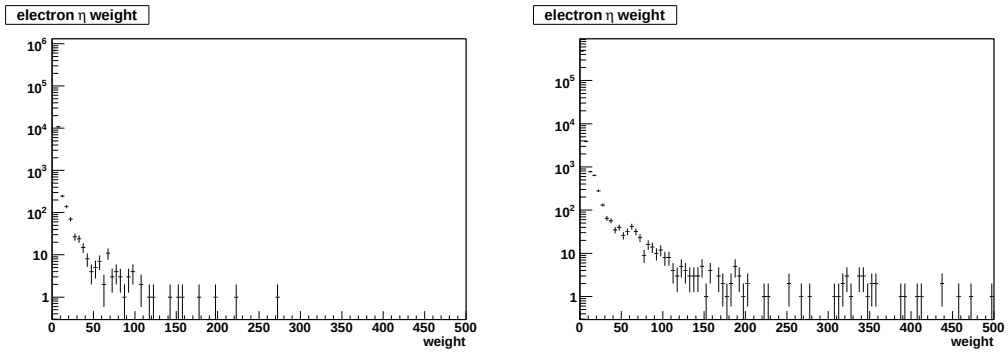

Figure 6.36: The event weight for W electron in CCEC (left) or in CC only (right). The event weight is calculated as the reciprocal of the probability in the left plots of Fig 6.34 and Fig 6.35. Very few events have high weights, since there are not many events in the lower probability physics η range. The maximum reweighting factor allowed is set to 10 in the correction.

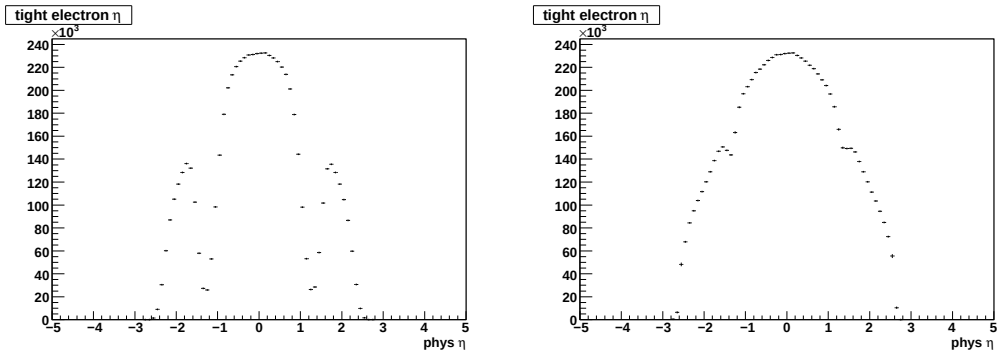

Figure 6.37: Physics η distribution of Z's loose electrons that are in CC or EC (the histogram title is not labelled correctly). There is not acceptance cut on the tight electron of Z. The left plot is without the reweighting, the right plot has the reweighting applied (reciprocal of the left plot in Figure 6.34). The maximum reweghting factor allowed is 10.

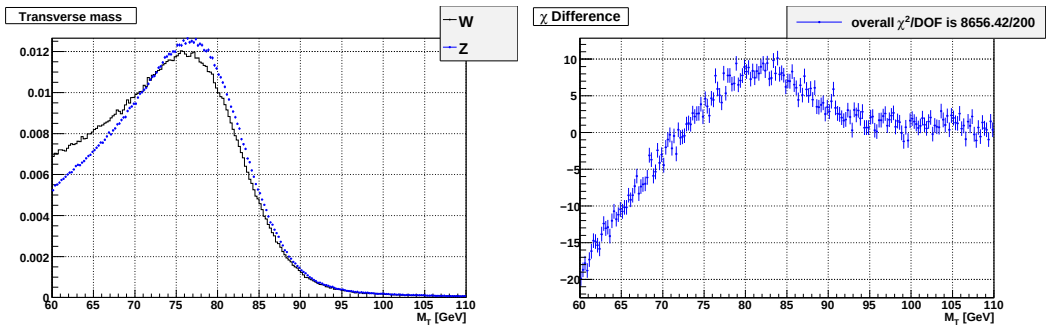

Figure 6.38: M_T comparison with official acceptance cut, no lepton p_T cut and no reweighting correction. The W electron and Z's tight electron is in CC, Z's loose electron is in either CC or EC. There are no lepton p_T cuts. Large difference here is caused by the combination of the three acceptance cuts in page 96.

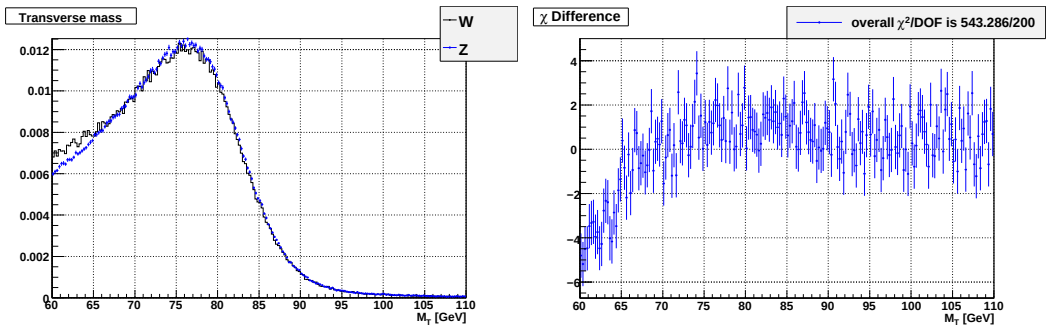

Figure 6.39: The same M_T comparison after reweighting corrections. Among the three acceptance biases, only the CC/EC gap for loose electron acceptance is taken care of. Biases due to CC cut on the tight electrons and the upper limit of EC detector η_{det} at 2.5 are obvious in the lower M_T region.

Chapter 7

Fast Monte Carlo Simulation with Realistic Smearing

In the previous chapter, we used a toy fast Monte Carlo simulation that has simple Gaussian smearings to study various effects and corrections. In particular, the illustration of the extra smearing correction is more clear and straightforward using the Gaussian smearing. However we can't use it to estimate the bias of the measured M_W in fast Monte Carlo simulation. In the development of fast Monte Carlo model for the standard method, it is found out that the simple Gaussian smearing model is inadequate of describing the $1\,\mathrm{fb}^{-1}$ DØ Run IIa data. Complicated smearing models (no simple Gaussian form) are developed from the study of W and Z data and are put into the official `wz_epmcs` package that is used to measure M_W in the standard method.

In this chapter, we first introduce the basics of non Gaussian smearing used in the `wz_epmcs` package. Then we put the non Gaussian smearing into our the fast Monte Carlo simulation and discuss the extra smearing correction for non Gaussian smearing model. In the end, we apply the major selection cuts to the updated fast Monte Carlo simulation that is smeared by non Gaussian models of `wz_epmcs` and measure M_W in ratio method. The difference between measured M_W (central value of ensemble test) and the input value is quoted as the systematic bias. With the final fitting range of $66\,\mathrm{GeV} < M_T < 96\,\mathrm{GeV}$ used in data, this bias is found to be within the statistical uncertainty 43 MeV, which is the width of the fitted M_T distribution in ensemble test.

7.1 Non Gaussian Smearings from `wz_epmcs`

The realistic smearings used in the `wz_epmcs` package of standard method are discussed briefly for the electron, recoil and the underlying events system in

the following sections. Details about the recoil simulation in `wz_epmcs` can be found in [39].

7.1.1 Electron Smearing

The main change from the normal electron smearing Eq 6.2 is that the sampling term $S_{\rm EM}$ is no longer a constant number in `wz_epmcs`. Instead the new sampling term is dependent on the electron energy and its angle. The dependence reflects the effect of the radiation length of calorimeter material on the energy loss of electrons.

$$S_{\rm EM} = (S_1 + \frac{S_2}{E}) \times \frac{e^{S_{\rm exp}} \sin\theta}{e^{S_{\rm exp}}}, \tag{7.1}$$

where the exponential term

$$S_{\rm exp} = S_3 - S_4/E - S_5^2/E^2. \tag{7.2}$$

The determination of $S_{\rm EM}$ form in Eq 7.1 and the associated parameters S_i where $i = 1 \cdots 5$ are all based full Monte Carlo $Z \rightarrow ee$ events. For the extra smearing correction of electrons, this new smearing algorithm has small influence on the value of fitted W mass compared with the simple Gaussian based extra smearing correction.

7.1.2 Recoil Smearing

Among the three components that contribute to the recoil system of W and Z events (see Chapter 4.2 in page 48), the hard recoil against the boson is modeled by a bifurcated function while the soft recoil and underlying event contribution is picked up from a library of MB and ZB events.

Bifurcated Model of Hard Recoil

To understand the calorimeter response to the hard recoil against boson, full Monte Carlo $Z \rightarrow \nu\nu$ events are used to find the relation between true $p_T^{\rm rec}$ and the smeared $p_T^{\rm rec}$. These special $Z \rightarrow \nu\nu$ events are generated by `PYTHIA` in which only the hard collision parton level processes are kept, the interactions from spectator quarks and additional $p\bar{p}$ are turned off. Since the final product of neutrinos are undetected in full Monte Carlo, the calorimeter response are left with contribution from hard recoil only. These generator level $Z \rightarrow \nu\nu$ events go through `D0Reco` package and are reconstructed in the same manner as data events. There is no underlying event overlaying on this special $W \rightarrow \nu\nu$

full Monte Carlo sample, only the hard recoil component is what we want to keep.

Two parameters that characterize the hard recoil smearing are the recoil p_T resolution R and ϕ angle resolution $\Delta\phi$. They are defined as

$$R = \frac{u_T - q_T}{q_T} \qquad (R < 1) \tag{7.3}$$

$$\Delta\phi = \phi(\boldsymbol{u}_T) - \phi(\boldsymbol{q}_T) \qquad (|\Delta\phi| < \pi), \tag{7.4}$$

where q_T and u_T are the true hard recoil ($-p_T^Z$) and the reconstructed hard recoil. The $Z \to \nu\nu$ events are divided into 32 subsamples from $q_T = 0$ up to $q_T = 100\,\mathrm{GeV}$. For each subsample, a two dimensional histogram is made to show the joint distribution of smearing resolution R and $\Delta\phi$. An empirical parameterization is fitted to each of the subsamples,

$$f(x,y) = p_0 \exp\left[-\frac{1}{2}\left(\frac{x-\mu(y)}{\sigma_x(x,y)}\right)^2\right] \exp\left[-\frac{1}{2}\left(\frac{y}{\sigma_y(y)}\right)^2\right]. \tag{7.5}$$

In the above formula (called bifurcated function), $x \equiv R$, $y = \Delta\phi$, $\mu = p_1 + p_2 y$ and

$$\sigma_x(x,y) = \begin{cases} p_3 & \text{when } x < \mu(y) \\ p_4 & \text{when } x > \mu(y) \end{cases}$$

$$\sigma_y(y) = p_5 + p_2 y.$$

p_i where $i = 0 \cdots 5$ are the parameters to fit. Of these, p_0 is a normalization constant, the other 5 parameters are put into the smearing function $f(\boldsymbol{q}_T)$ in `wz_epmcs`. Typical two dimensional distribution (of different q_T range) and the comparison with the bifurcated function fit are shown in Fig 7.1 and Fig 7.2.

Hard recoil smearing procedure takes the true recoil $\boldsymbol{q}_T$ as an input and apply the corresponding parameterized bifurcated function to give the smeared $\boldsymbol{u}_T$ as the output. The correlation of the recoil ϕ smearing and recoil p_T smearing is included in the bifurcated function. This bifurcated function is also used in the calculation of extra smearing correction in ratio method.

Spectator Quarks and Additional $p\bar{p}$ Interactions

Interactions from spectator quarks in the same $p\bar{p}$ collision that produces the W and Z boson are called the soft recoil. The additional $p\bar{p}$ interactions in the same bunch crossing are the true underlying events. Usually they are modeled by the MB (minimum bias) and zero bias (ZB) events respectively. Because both MB and ZB events have diffusive energy deposition in calorimeter and

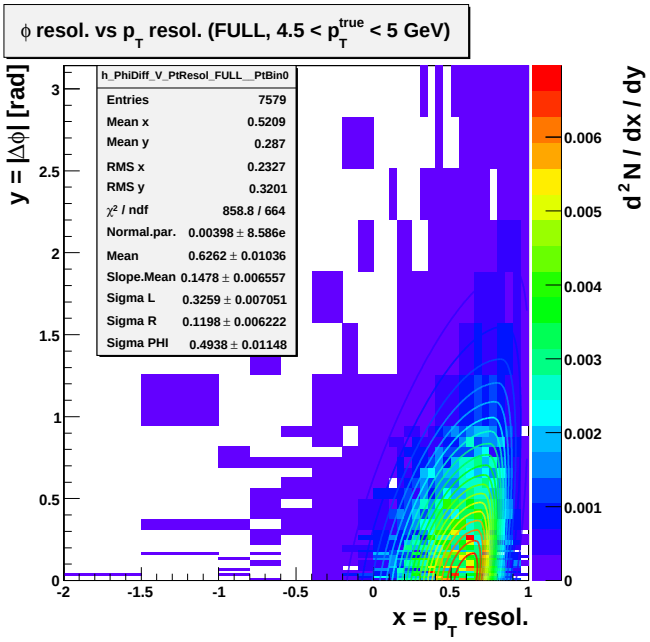

Figure 7.1: Two dimensional distribution of recoil p_T and ϕ resolution for the truth recoil p_T between 4.5 GeV and 5 GeV. Box is full Monte Carlo, contour is fit of Eq 7.5. [39]

the vector sum of calorimeter response is randomly distributed on the transverse plane, MB and ZB events usually are referred together as the underlying events. In the toy fast Monte Carlo of previous chapter, a simple Gaussian smearing with $\sigma = 3.02$ GeV is added to the overall recoil to represent the combined contribution from MB and ZB events. In that case, the corresponding extra smearing correction is as simple as Eq 6.17 shows.

In reality, the simple Gaussian smearing is a very coarse approximation and doesn't have good agreement with the 1 fb^{-1} DØ Run IIa data. To have better description of data, fast Monte Carlo simulation of standard method `wz_epmcs` reads the MB and ZB contribution for each simulated event from the prepared libraries that are reweighted to have the same instantaneous luminosity and scalar E_T of full Monte Carlo or data W and Z events. We also use the corresponding MBZB libraries (two sets, one for full Monte Carlo and one for data) in the correction of extra smearing.

7.2 Extra Smearing

The extra smearing corrections of $Z \to ee$ events need to be updated accordingly from the simple Gaussian smearing model in Chapter 6 when the realis-

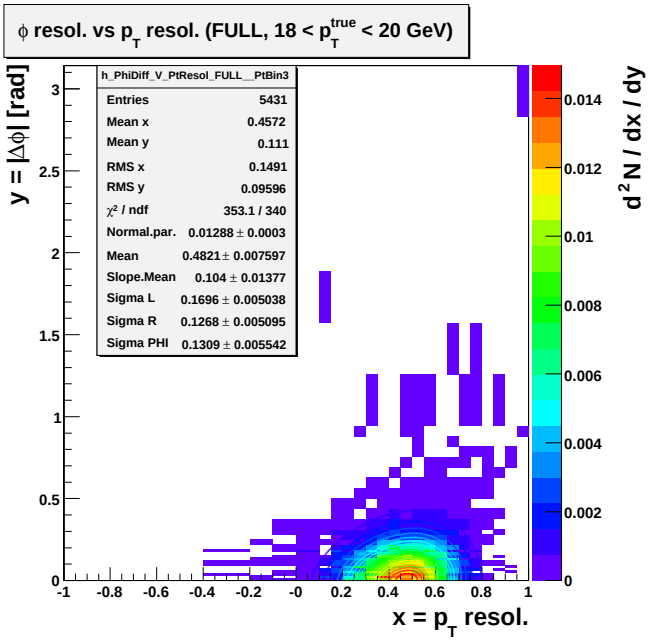

Figure 7.2: Two dimensional distribution of recoil p_T and ϕ resolution for the truth recoil p_T between 18 GeV and 20 GeV. Box is full Monte Carlo, contour is fit of Eq 7.5. [39]

tic `wz_epmcs` smearings are used in the fast Monte Carlo simulation. Change of extra smearing for the electron system is minimal. EM smear resolution (Eq 6.14) is calculated with the new sampling term (Eq 7.1) to give the extra smearing correction.

7.2.1 Extra Smearing of Hard Recoil

Extra smearing for the hard recoil is not as simple as the electron system. Both the recoil magnitude and ϕ direction of hard recoil are smeared at the same time. It's natural to apply extra smearing to both the x and y components of the smeared recoil in this case. This algorithm actually works pretty well in the test of extra smearing between Z and fake W events. However the right amount of extra smearing is not suitable for the comparison between Z and true W events. In the case where hard recoil is smeared by the bifurcated function, there is substantial difference of M_T spectrum between fake W events and true W events (Fig 7.4). The same comparison shows good agreement if hard recoil is smeared by simple Gaussian form (Fig 7.3). The exact cause of the bias of extra smearing of hard recoil for bifurcated smearing observed in Fig 7.4 is not clear. Correlation between ϕ and $|p_T|$ can be excluded, since

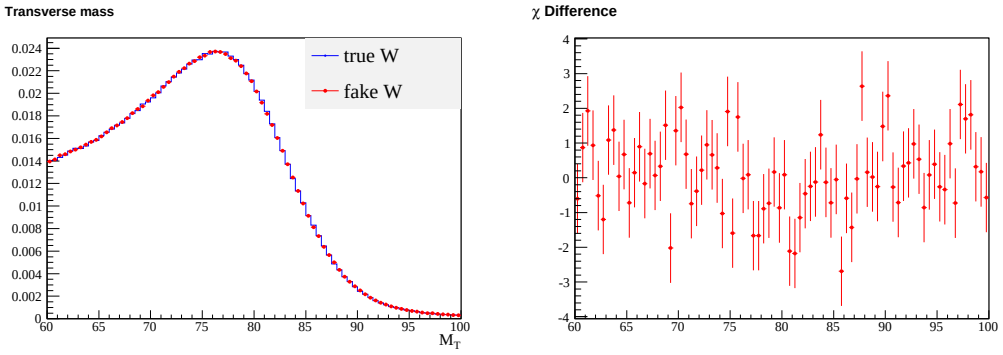

Figure 7.3: Comparison between true W and fake W events. All smearings are simple Gaussian based. No cuts. Both samples have 5.2 million events.

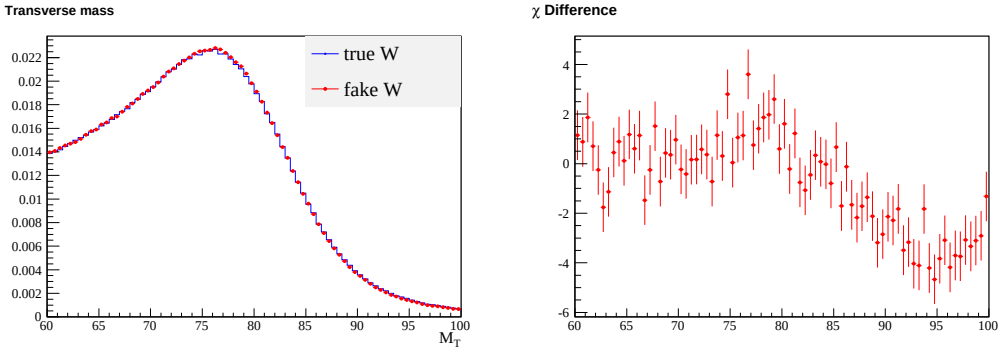

Figure 7.4: Comparison between true W and fake W events. EM and soft recoil smearings are simple Gaussian based, hard recoil smearing uses the `wz_epmcs` smearing. No cuts. Both samples have 5.2 million events.

even after ϕ smearing is turned off for hard recoil, identical discrepancy of M_T spectrum is still present.

Through the bifurcated smearing function $f(q_T, \phi)$ Eq 7.5, a pair of input recoil of Z event $(p_T(Z), \phi(Z))$ (true) has the corresponding smeared value $(p_T(Z), \phi(Z))$ (smeared). The same pair of input (p_T, ϕ) is scaled to the W level, where $p_T^{\rm rec}(W) = (M_W/M_Z)p_T^{\rm rec}(Z)$ and $\phi(W) = \phi(Z)$.

The $p_T^{\rm rec}$ difference in the x and y component is calculated for the original $p_T^{\rm rec}(Z)$ and the scaled $p_T^{\rm rec}(W)$.

$$\begin{aligned}
\Delta p_x^{\rm rec}(W) &= p_T^{\rm rec}({\rm smear})\cos\phi({\rm smear}) - p_T^{\rm rec}({\rm true})\cos\phi({\rm true}) \\
\Delta p_y^{\rm rec}(W) &= p_T^{\rm rec}({\rm smear})\sin\phi({\rm smear}) - p_T^{\rm rec}({\rm true})\sin\phi({\rm true}) \\
\Delta p_x^{\rm rec}(Z) &= p_T^{\rm rec}({\rm smear})\cos\phi({\rm smear}) - p_T^{\rm rec}({\rm true})\cos\phi({\rm true}) \\
\Delta p_y^{\rm rec}(Z) &= p_T^{\rm rec}({\rm smear})\sin\phi({\rm smear}) - p_T^{\rm rec}({\rm true})\sin\phi({\rm true}) \qquad (7.6)
\end{aligned}$$

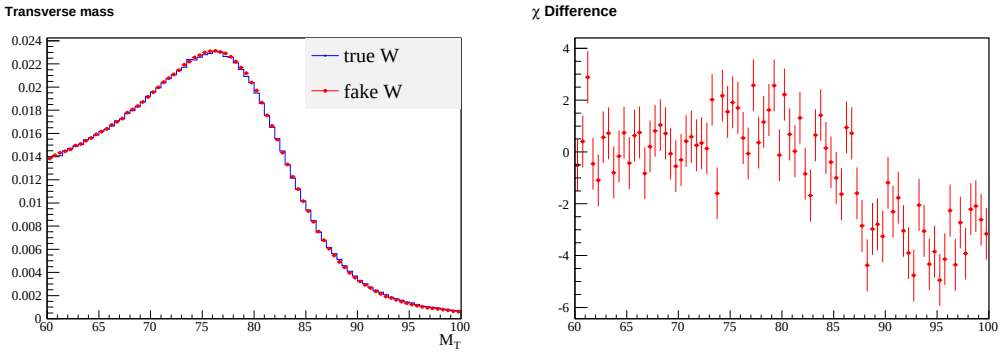

Figure 7.5: Identical comparison as in Fig 7.4, except that there is no ϕ smearing of hard recoil.

The extra smearings for the x and y component of recoil p_T are calculated as the following,

$$\begin{aligned} \Delta p_x^{\rm rec}({\rm extra}) &= \left(\frac{M_Z}{M_W}\right)\Delta p_x^{\rm rec}(W) - \Delta p_x^{\rm rec}(Z) \\ \Delta p_y^{\rm rec}({\rm extra}) &= \left(\frac{M_Z}{M_W}\right)\Delta p_y^{\rm rec}(W) - \Delta p_y^{\rm rec}(Z) \end{aligned} \tag{7.7}$$

The above extra smearing correction for hard recoil gives reasonable agreement for the M_T comparison between Z and fake W events (Fig 7.6). This indicates that Eq 7.7 is the right extra smearing correction for bifurcated smearing of hard recoil in `wz_epmcs`. Because of the M_T difference between fake W and true W events (Fig 7.4), it's not a surprise that the same comparison fails on the true W events (Fig 7.7). After the extra smearing of Eq 7.7, M_T of Z events seems to be slightly under-smeared compared with that of the true W events.

To have a successful fit of W mass, we use the following *ad hoc* extra smearing for hard recoil smeared by bifurcated function. Compared with the proper extra smearing of Eq 7.7, the *ad hoc* extra smearings are added in the $p_T^{\rm rec}$ and $\phi^{\rm rec}$ terms in stead of $p_T(x)$ and $p_T(y)$ components. Assuming $\Delta p_T^{\rm rec}({\rm random})$ and $\phi^{\rm rec}({\rm random})$ are randomly drawn from two separate histograms where $p_T^{\rm rec}({\rm smeared}) - p_T({\rm true})$ and $\phi^{\rm rec}({\rm smeared}) - \phi({\rm true})$ of bifurcated smearing information are stored, the following extra smearings are added to $p_T^{\rm rec}({\rm smeared})$

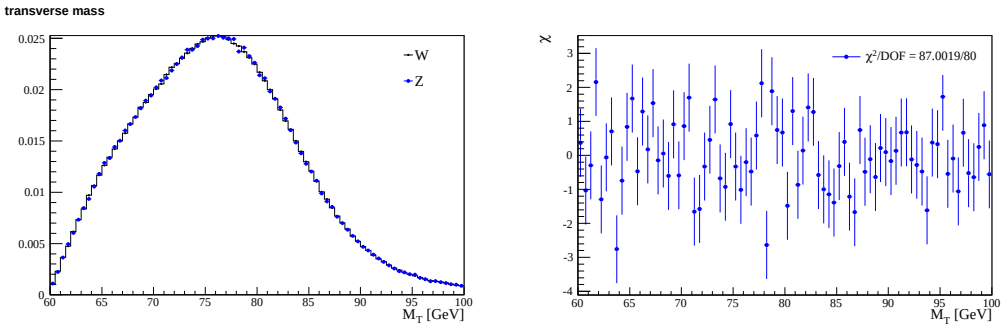

Figure 7.6: Comparison between Z and fake W events. Simple Gaussian smearing of EM and soft recoil. Hard recoil smearing uses the bifurcated model (smear both p_T and ϕ, same as in the official `wz_epmcs`). Extra smearing of EM and soft recoil is also of the corresponding Gaussian form. Extra smearing of the hard recoil is applied in the x and y component as shown in the formula of Eq 7.7.

and $\phi^{\rm rec}$(smeared).

$$\begin{aligned} \Delta p_T^{\rm rec}({\rm extra}) &= \left(\frac{M_Z}{M_W} - 1\right) \Delta p_T^{\rm rec}({\rm random}) \\ \Delta \phi^{\rm rec}({\rm extra}) &= \left(\frac{M_Z}{M_W} - 1\right) \Delta \phi^{\rm rec}({\rm random}) \end{aligned} \tag{7.8}$$

As Fig 7.8 shows, the *ad hoc* correction *per se* is not the right extra smearing correction. It causes the M_T spectrum of Z to be somewhat over smeared. Considering that M_T of the true W events is slightly wider than fake W events (Fig 7.4), the *ad hoc* extra smearing correction is actually ideal for the comparison with true W events. This is confirmed by Fig 7.9, where reasonable agreement is observed.

7.2.2 Extra Smearing of Soft Recoil and Underlying Event

In `wz_epmcs` simulation, soft recoil and the underlying event contribution is randomly picked up from libraries that are made of minimum bias (MB) and zero bias (ZB) events. The MBZB libraries are made to have the same scalar E_T and instantaneous luminosity as full Monte Carlo or data W and Z events.

Extra smearing correction of the soft recoil and underlying event is similar to the case of simple Gaussian smearing. In this case, the extra smearing term is no longer from Gaussian distribution but drawn from the MBZB libraries

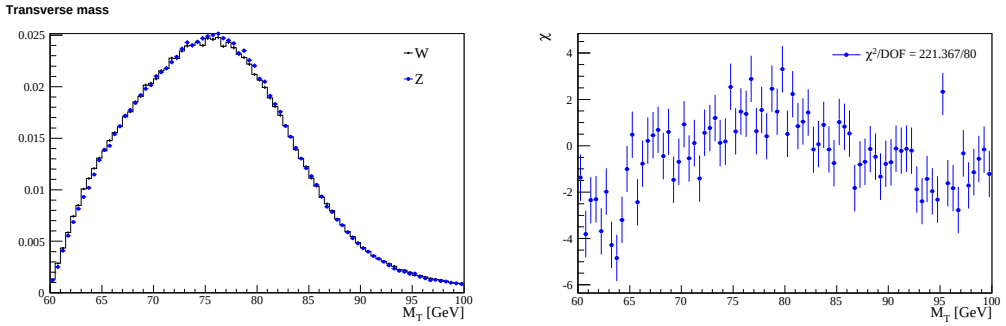

Figure 7.7: Identical comparison as in Fig 7.6, except that the comparison is between Z and true W events. Notice the proper extra smearing of hard recoil of Z events in Fig 7.6 appears to be slightly under-smeared, with respect to the true W events.

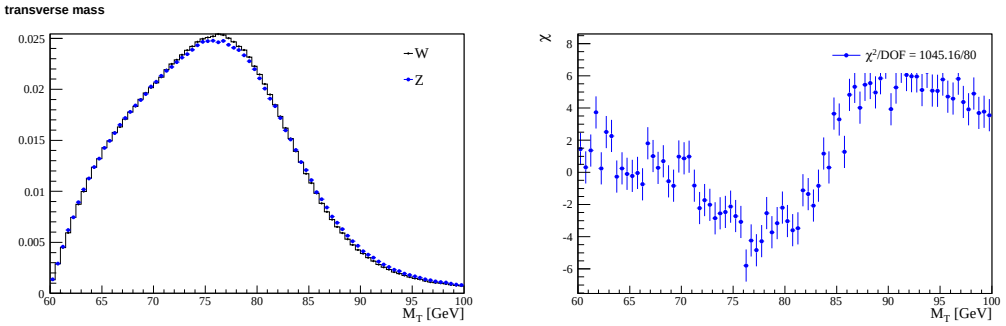

Figure 7.8: Identical comparison as in Fig 7.6, except that the extra smearing correction to the hard recoil of Z is the *ad hoc* form in Eq 7.8. This causes M_T of Z slightly over smeared. This feature is needed to make it close to M_T of true W events.

instead. For each Z event, a pair of $\not\!\!E_T(x)$ and $\not\!\!E_T(y)$ is randomly drawn from MB and ZB library events separately. Overall $\not\!\!E_T(x)$ and $\not\!\!E_T(y)$ are the sum of MB and ZB contributions. The extra smearing correction on the x and y components are the overall $\not\!\!E_T(x,y)$ times a small coefficient that is the same as in Eq 6.17.

$$\begin{aligned} \not\!\!E_T^{\text{extra}}(x) &= \left[\left(\frac{M_Z}{M_W}\right)^2 - 1\right]^{\frac{1}{2}} \not\!\!E_T(x) \\ \not\!\!E_T^{\text{extra}}(y) &= \left[\left(\frac{M_Z}{M_W}\right)^2 - 1\right]^{\frac{1}{2}} \not\!\!E_T(y) \end{aligned} \tag{7.9}$$

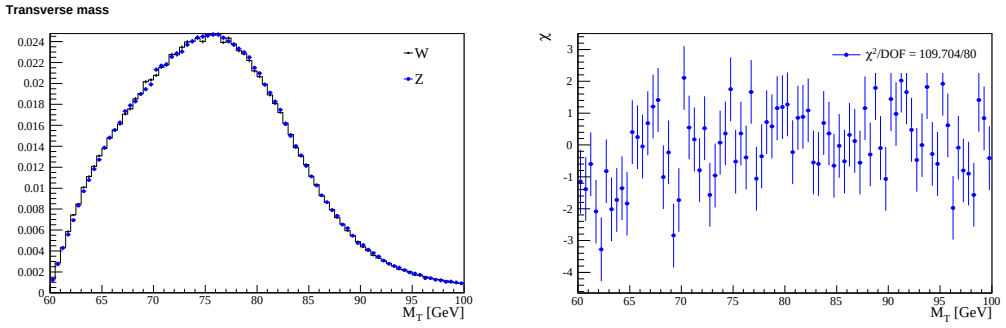

Figure 7.9: Identical comparison with the true W events as Fig 7.7. *ad hoc* extra smearing correction (Eq 7.8) is used on the hard recoil of Z.

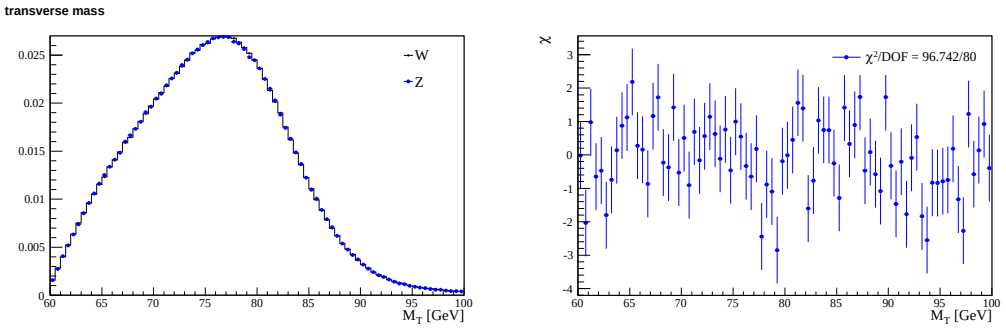

Figure 7.10: Comparison between Z and fake W events. EM and hard recoil are smeared by simple Gaussian, and both are proper corrected. Soft recoil and underlying event are smeared by the MBZB library. The extra smearing correction is Eq 7.9.

Again, the above extra smearing algorithm is tested on the fake W events. Both EM and hard recoil have simple Gaussian smearing and are properly corrected. Extra smearing of Eq 7.9 on the soft recoil and underlying event gives good agreement (Fig 7.10).

7.3 Fast Monte Carlo Closure Test

The toy fast Monte Carlo simulation for ratio method study resembles a full fledged `wz_epmcs` package. Major effects that have influences on ratio method are simulated:

- Complicated realistic smearing algorithms that have very good agreement with data are implemented for electron, recoil and underlying event.

- Proper extra smearing corrections are obtained for all of the realistic smearings.
- Acceptance cut for the electrons of W and Z events: W electron (Z's loose electron) is in CC, Z's loose electron is in CC or EC.
- Reweighting correction for the CC/EC gap on the acceptance of Z's loose electron is applied.
- Lepton p_T cuts: $p_T^e > 30\,\text{GeV}$ and $\not\!\!E_T > 30\,\text{GeV}$.
- Boson p_T cut: $p_T^W < 15\,\text{GeV}$ and $p_T^Z < 15\,\text{GeV}$.

A closure test of M_W measurement on such a toy fast Monte Carlo simulation is useful to estimate the systematic bias of M_W measured in ratio method. The M_T spectrum of Z events that are scaled with the input M_W is compared with that of the true W events. Good agreement is observed in the Jacobian edge of M_T spectrum (top two plots in Fig 7.11). K-S probability of M_T templates is shown as the lower left plot in Fig 7.11, where $68\,\text{GeV} < M_T < 96\,\text{GeV}$ is chosen as the fitting range for this particular fitting. The distribution of fitted M_W due to statistical fluctuation is shown in the plot of ensemble test in Fig 7.11. This distribution can be well fitted by a Gaussian function, which indicates good statistical fluctuation of each pseudo experiment in the ensemble test. For the particular fitting range of $68\,\text{GeV}, M_T < 96\,\text{GeV}$, the Gaussian mean value of fitted M_W is 80402 MeV, that's about 21 MeV lower than the input M_W. The Gaussian standard deviation of fitted M_W in ensemble test is 43 MeV. This is the true statistical uncertainty of the fitted W mass.

Table 7.2 shows the central fitted W mass and its statistical uncertainty for different fitting ranges. The corresponding distributions are shown in Fig 7.14 and Fig 7.15. Input M_W value is covered by the fitted W mass within the statistical uncertainty for various fitting ranges.

The Jacobian edge (roughly $75\,\text{GeV} < M_T < 90\,\text{GeV}$) of the M_T spectrum is most sensitive to W boson mass and usually chosen to be included in the fitting range. Inclusion of the range lower than 75 GeV or higher than 90 GeV in mass fitting gives better statistical uncertainty. In ratio method, various selection cuts and corrections have notable bias on the M_T spectrum. Fitted central values of M_W in ensemble test usually have dependence on the choice of fitting range.

Choice of the lower end of fitting range is constrained by the acceptance cut. One needs to have the fitting range away from the lower M_T region to have a successful W mass fit. To show this effect, we make W mass fitting on high statistical $W \to e\nu$ ($2\,\text{fb}^{-1}$) sample and $Z \to ee$ ($6\,\text{fb}^{-1}$) sample. M_T

comparison of such W and Z samples is shown in Fig 7.11, where the K-S fitting probability of mass templates over a specific range $68 < M_T < 96\,\text{GeV}$ is also shown. Fitted M_W over various fitting ranges are shown in Table 7.1 and the corresponding K-S probability distributions are shown in Fig 7.12 and Fig 7.13. In Table 7.1, a significant bias of fitted W mass is observed when the lower limit of fitting range extends beyond 66 GeV. There is no obvious dependence on the choice of upper limit. Considering the region of high M_T values are also affected by effects such as boson width, we choose the upper limit of fitting range at 96 GeV.

Therefore, $66\,\text{GeV} < M_T < 96\,\text{GeV}$ is chosen as the official range for W mass fitting of full Monte Carlo and data. From Table 7.2, we can find the statistical uncertainty is 43 MeV.

range[GeV]	$60 < M_T < 96$	$62 < M_T < 96$	$64 < M_T < 96$	$66 < M_T < 96$
fitted M_W[MeV]	80346 ± 8	80355 ± 12	80374 ± 18	80403 ± 15
	$68 < M_T < 96$	$70 < M_T < 96$		
	80407 ± 15	80407 ± 14		
range[GeV]	$66 < M_T < 90$	$66 < M_T < 92$	$66 < M_T < 94$	$66 < M_T < 96$
fitted M_W[MeV]	80394 ± 14	80394 ± 14	80400 ± 15	80403 ± 15
	$66 < M_T < 98$	$66 < M_T < 100$		
	80402 ± 14	80404 ± 15		

Table 7.1: Fitted W mass and statistical uncertainty for different fitting ranges. $W \to e\nu$ sample has $2\,\text{fb}^{-1}$ events and $Z \to ee$ sample has $6\,\text{fb}^{-1}$ events. As mentioned earlier, the statistical uncertainty quoted here is not accurate. Top row shows the case where the upper limit is fixed at 96 GeV and the lower limit is scanned from 60 GeV to 70 GeV. In the lower row, the upper limit is scanned from 90 GeV to 100 GeV with the lower limit fixed at 66 GeV. The corresponding K-S probability distributions are shown in Fig 7.12 and Fig 7.13. Notice the input M_W is 80423 MeV.

range[GeV]	$66 < M_T < 96$	$68 < M_T < 96$	$70 < M_T < 96$	$72 < M_T < 96$
fitted M_W[MeV]	80392 ± 43	80402 ± 43	80406 ± 48	80417 ± 47
	$74 < M_T < 96$	$76 < M_T < 96$		
	80380 ± 54	80383 ± 69		
range[GeV]	$70 < M_T < 90$	$70 < M_T < 92$	$70 < M_T < 94$	$70 < M_T < 96$
fitted M_W[MeV]	80400 ± 49	80400 ± 47	80402 ± 46	80406 ± 48
	$70 < M_T < 98$	$70 < M_T < 100$		
	80411 ± 46	80416 ± 45		

Table 7.2: Central value of fitted M_W and its statistical uncertainty in ensemble test for different fitting ranges. This is the official fast Monte Carlo simulation with realistic cuts, smearing and the appropriate corrections. The upper limit of fitting range is fixed at 96 GeV and the lower limits of fitting range are selected from 66 GeV to 76 GeV. Similar study is done for fixed lower limit at 70 GeV and the upper limit varies from 90 GeV to 100 GeV. The corresponding distributions are shown in Fig 7.14 and Fig 7.15. Notice the input M_W is 80423 MeV.

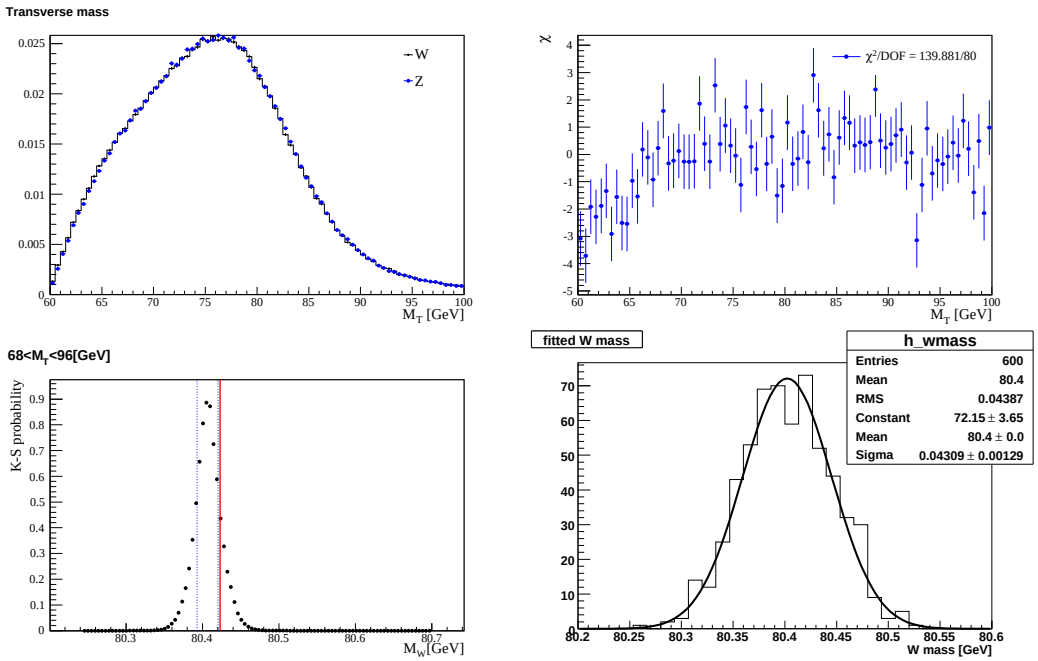

Figure 7.11: $2\,\mathrm{fb}^{-1}$ W events and $6\,\mathrm{fb}^{-1}$ Z events. M_T comparison of toy fast Monte Carlo simulation with realistic `wz_epmcs` smearing and other major selection cuts. Corrections described before are properly applied. Input M_W are used in the comparison of top two plots. Lower left shows the K-S probability distribution between the M_T of W and Z templates, fitting range is $68 < M_T < 96\,\mathrm{GeV}$. The maximum probability corresponds to fitted W boson mass. Red line is the input M_W, blue lines stand for the statistical uncertainty (wrong) calculated without considering the correlation of two M_T from one Z event. Fitted $M_W = 80407 \pm 15\,\mathrm{MeV}$. Similar distributions for different fitting ranges are shown in Fig 7.12 and Fig 7.13. The lower right plot shows the distribution of fitted M_W from 600 pseudo experiments (ensemble test), each with $1\,\mathrm{fb}^{-1}$ events and fitting range is also $68\,\mathrm{GeV} < M_T < 96\,\mathrm{GeV}$. This distribution should be well described by a Gaussian function if the two histograms being compared are statistical independent. Mean value of the Gaussian fitting function is the final measured $M_W = 80402\,\mathrm{MeV}$. The standard deviation $\sigma = 43\,\mathrm{MeV}$ is the statistical uncertainty.

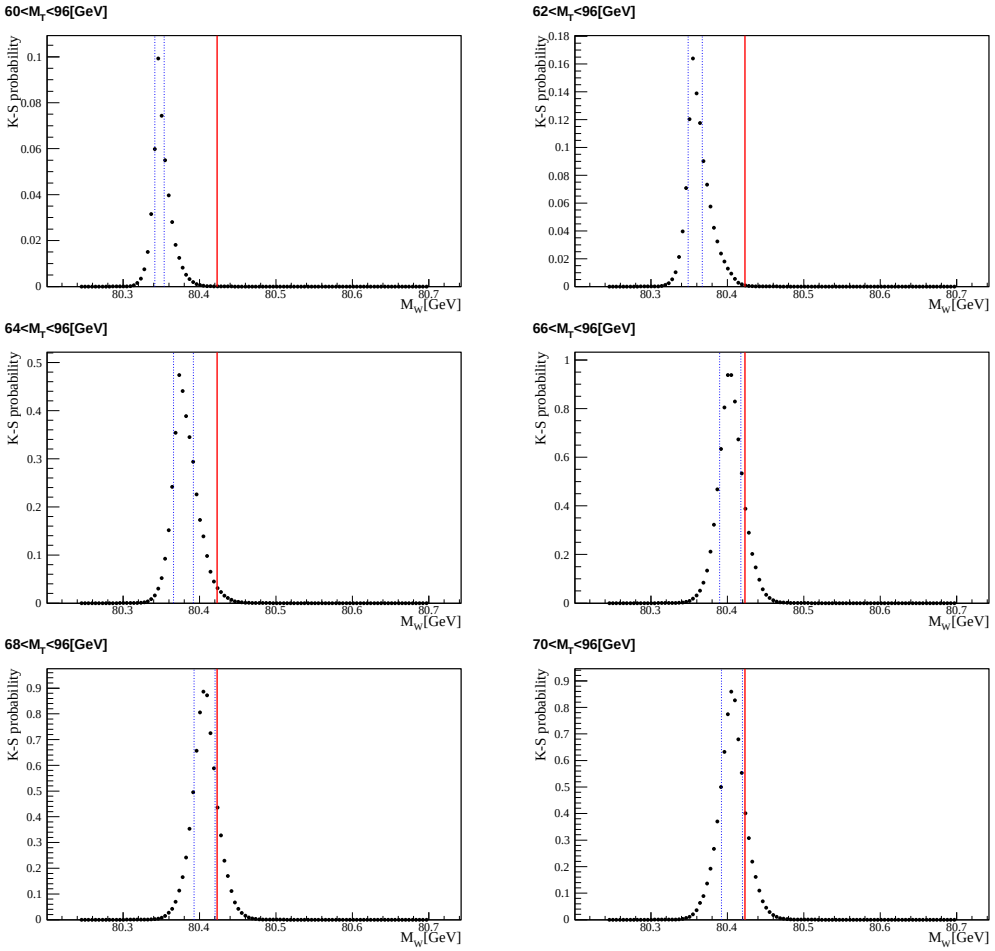

Figure 7.12: K-S probability distribution of W mass templates. $2\,\mathrm{fb}^{-1}$ $W \to e\nu$ sample and $6\,\mathrm{fb}^{-1}$ $Z \to e\nu$ events. Upper limit of the fitting range is fixed at 96 GeV, lower limit is chosen to be $60, 62, 64, 66, 68$ and 70 GeV. Red line stands for the input W mass, and the blue dots line stand for the (inaccurate) statistical uncertainty. Best fitted results are shown in Fig 7.1.

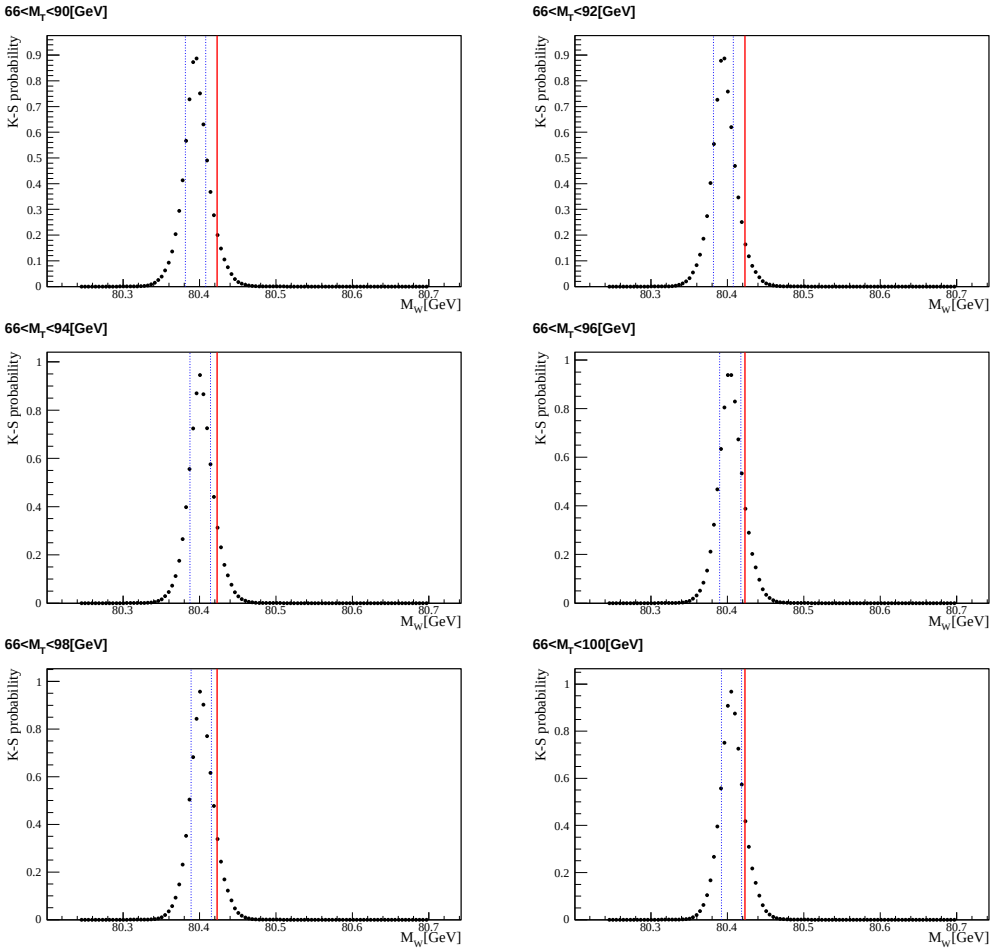

Figure 7.13: K-S probability distribution of W mass templates. $2\,\mathrm{fb}^{-1}$ $W \to e\nu$ sample and $6\,\mathrm{fb}^{-1}$ $Z \to e\nu$ events. Lower limit of the fitting range is fixed at 66 GeV, upper limit is chosen to be $90, 92, 94, 96, 98$ and 100 GeV. Red line stands for the input W mass, and the blue dots line stand for the (inaccurate) statistical uncertainty. Best fitted results are shown in Fig 7.1.

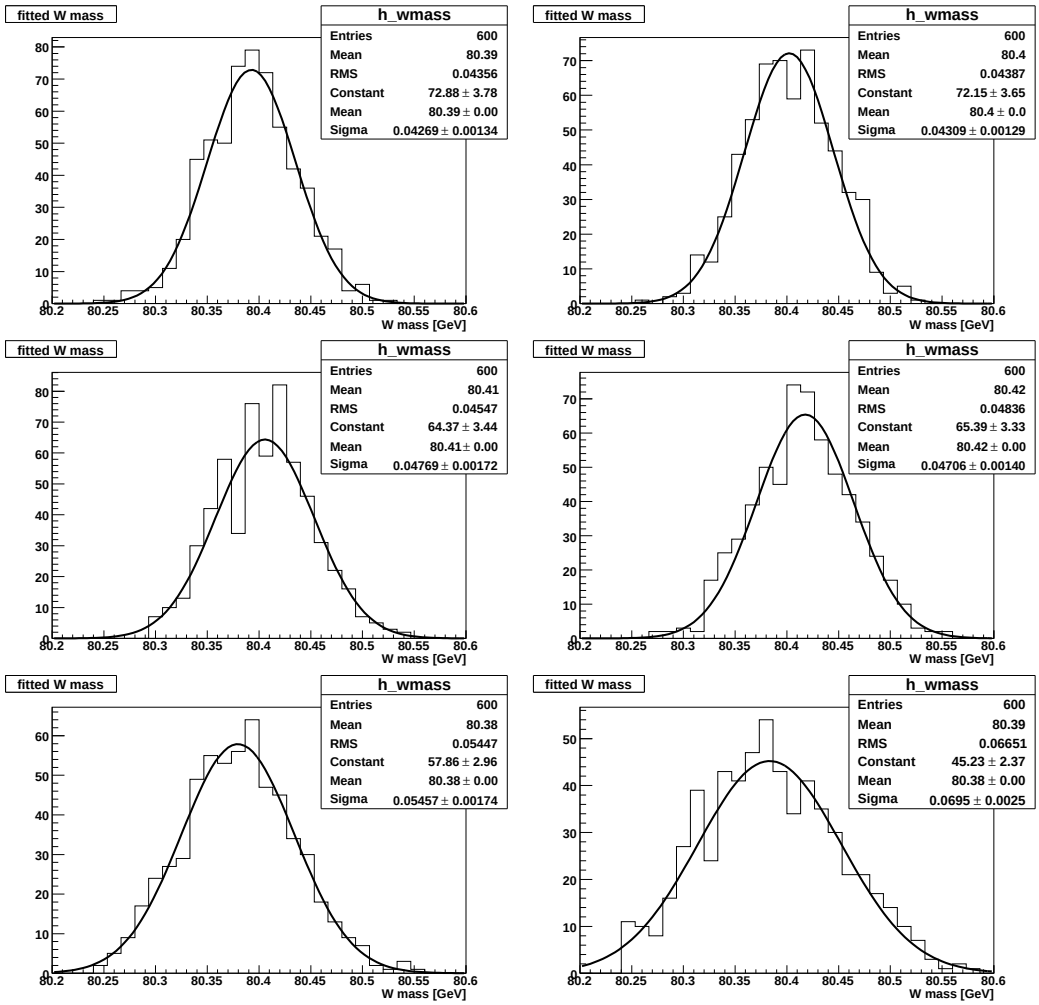

Figure 7.14: Distribution of fitted M_W from ensemble test of fast Monte Carlo simulation. Upper fitting range is fixed at 96 GeV, the lower range is set at $66, 68, 70, 72, 74, 76$ GeV from top left to lower right. Central value of fitted M_W and the corresponding standard deviation are shown in the upper block of Table 7.2.

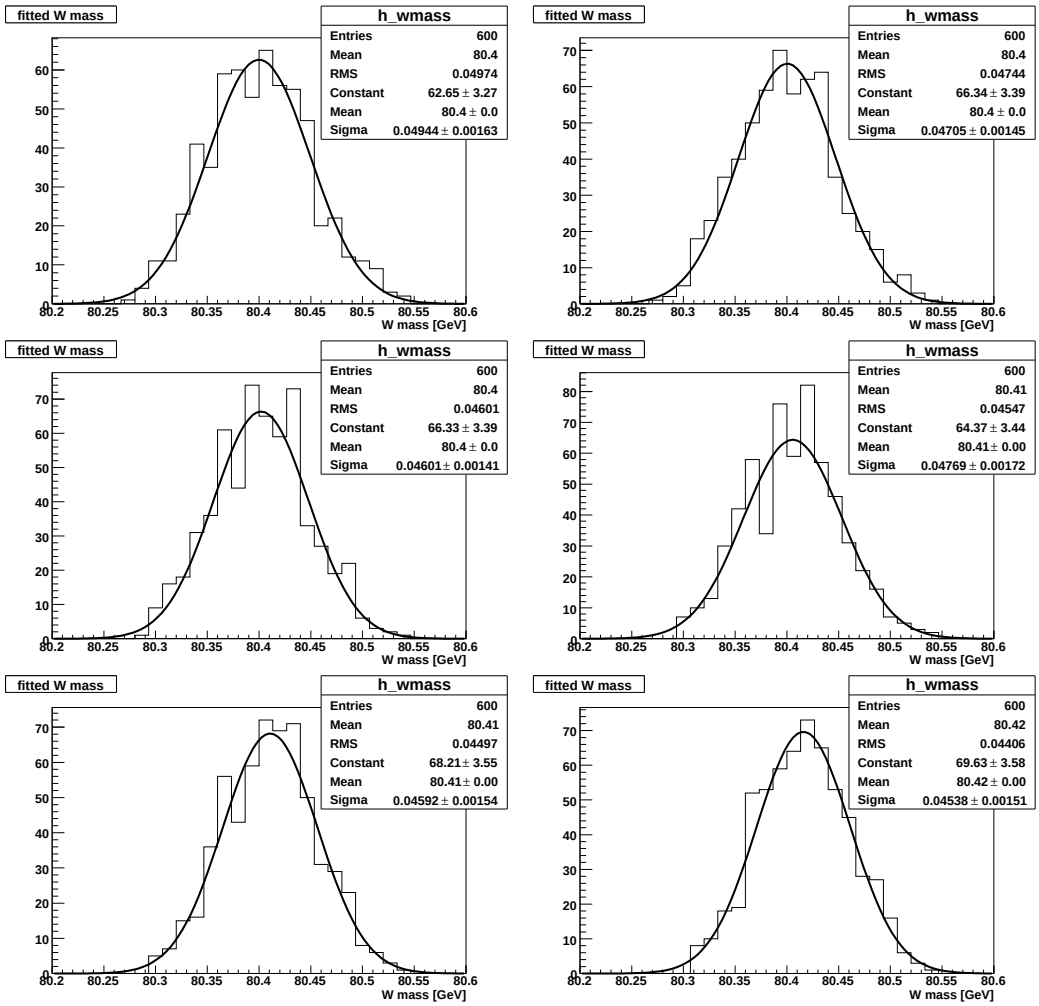

Figure 7.15: Same as Fig 7.14. Lower fitting range is fixed at 70 GeV, the upper range is set at $90, 92, 94, 96, 98, 100$ GeV from top left to lower right. Central value of fitted M_W and the corresponding standard deviation are shown in the lower block of Table 7.2.

Chapter 8

Full Monte Carlo Simulation

Ratio method of measuring the W mass works pretty well in the fast Monte Carlo simulations. Before applying the ratio method to data events, we can test the corrections developed in the fast Monte Carlo on the `GEANT` based full Monte Carlo events. $W \to e\nu$ and $Z \to ee$ events are generated by `PYTHIA` with known input W and Z boson mass. These events go through the full `GEANT` simulation that has the same configurations of material and geometry as the physical DØ detector. Output events are digitized and reconstructed in the same way as data events. Comparison of measured W mass and the input M_W provides a valuable check for the ratio method.

Although full Monte Carlo events are very close to data, there are several differences between data and full Monte Carlo.

There is no underlying event process on the generator level event production from `PYTHIA`. Zero bias events recorded during normal data taking are overlaid with the signal events in the digitization process. Instantaneous luminosity and scalar E_T distribution of the overlaying ZB events are reweighted to be the same as those of data $W \to e\nu$ and $Z \to ee$ events.

Trigger and background events are not simulated in full Monte Carlo. However trigger is hardly a problem in ratio method, with electrons p_T^e cut set to 30 GeV in data, electrons are almost 100% triggered. Contributions of background events to M_T spectrum are subtracted in data before mass fitting is performed.

The SAM dataset definition used for the full Monte Carlo closure test is

- `wzcross-wenu-fsr-nosup-05all-MC-caf`
  5.8 million ($2\,\text{fb}^{-1}$) $W \to e\nu$ events, generated with $M_W = 80.450\,\text{GeV}$. This corresponds to roughly $2\,\text{fb}^{-1}$ W events.

- `wzcross-zee-nosup01all-MC-caf`
  1.8 million ($6\,\text{fb}^{-1}$) $Z \to ee$ events, generated with $M_Z = 91.188\,\text{GeV}$.

This dataset is evenly divided into 6 sub samples, each contains roughly $1\,\mathrm{fb}^{-1}$ events.

Event selection of the full Monte Carlo sample is described in Chapter 4.3. Extra smearing and the acceptance reweighting of CC/EC gap is the same as in the realistic fast Monte Carlo simulation (Chapter 7).

One correction that is not included in the study of fast Monte Carlo simulation is underlying energy inside the loose electron window. When the loose electron of Z event is treated like a neutrino, calorimeter is left with an empty hole at the location of loose electron. Energy flow of Underlying event should be put back into that location. This energy flow of underlying event depends on the instantaneous luminosity and projection of recoil on the direction of loose electron $u_{\parallel}$ (on transverse plane). In our ratio method, we take an average value of $U_{\mathrm{UE}} = 130\,\mathrm{MeV}$, which is measured in the study of standard method [28].

The above consideration means that the proper $\overrightarrow{\not\!\!E_T^{e_2}}$ that entering the M_T calculation of Z events needs to be modified from Eq 6.7 to

$$\begin{aligned} \overrightarrow{\not\!\!E_T^{e_2}} &\equiv -\overrightarrow{E_T^{e_1}} - \overrightarrow{E_T^{\mathrm{rec}}}, \\ &\equiv \overrightarrow{\not\!\!E_T}(Z) + \overrightarrow{(E_T^{e_2} - U_{\mathrm{UE}})}. \end{aligned} \tag{8.1}$$

First we compare the M_T spectrum of Z which is scaled with the input $M_W = 80450\,\mathrm{MeV}$ (Fig 8.1) using the inclusive samples of $2\,\mathrm{fb}^{-1}$ W events and $6\,\mathrm{fb}^{-1}$ Z events. Reasonable agreement is observed for the Z M_T spectrum scaled with input W mass. W mass is fitted in the range of $70\,\mathrm{GeV} < M_T < 96\,\mathrm{GeV}$ and the corresponding K-S fitting probability of mass templates is shown in the lower plot of Fig 8.1. Fitted M_W gives the input W boson mass, using this specific fitting range.

In order to observe the statistical fluctuation of mass fitting, the $2\,\mathrm{fb}^{-1}$ $W \to e\nu$ sample is divided into 2 sub-samples $\mathcal{A}, \mathcal{B}$, each with roughly $1\,\mathrm{fb}^{-1}$ events. The $6\,\mathrm{fb}^{-1}$ $Z \to ee$ sample is divided into 6 sub samples $\mathcal{A}, \mathcal{B}, \mathcal{C}, \mathcal{D}, \mathcal{E}, \mathcal{F}$, each with roughly $1\,\mathrm{fb}^{-1}$ events.

There are 12 statistically independent combinations out of the above samples. Various fitting ranges are used for each of the 12 sub samples and the fitting results is shown in Table 8.1 and Table 8.2. The statistical uncertainty of fitted M_W quoted in the table is based on one specific sample, not from ensemble test. Therefore it is not the right statistical uncertainty.

The lower fitting range and the upper fitting range are changed separately, one of them is fixed while the other is varied. Table 8.1 shows the fitted M_W with various lower fitting range from 66 GeV to 76 GeV while the upper fitting

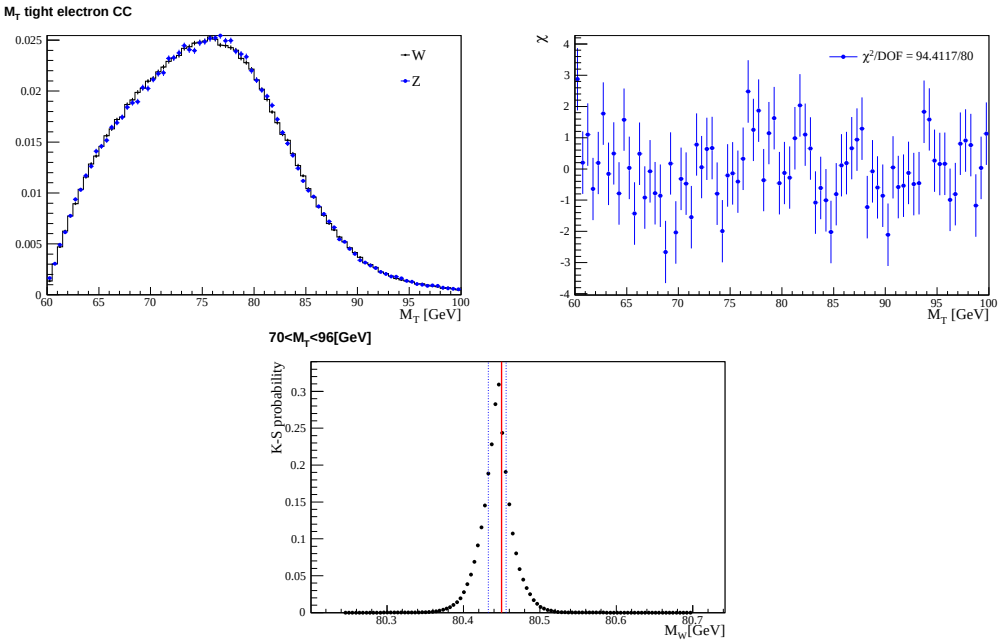

Figure 8.1: Full Monte Carlo $2\,\mathrm{fb}^{-1}$ W events and $6\,\mathrm{fb}^{-1}$ Z events. M_T comparison between W and Z scaled with input $M_W = 80450\,\mathrm{MeV}$. With fitting range $70\,\mathrm{GeV} < M_T < 96\,\mathrm{GeV}$, fitted $M_W = 80445 \pm 13\,\mathrm{MeV}$, where the statistical uncertainty of 13 MeV is not accurate.

range is fixed at 96 GeV. Table 8.2 shows the results with various upper fitting range from 90 GeV to 100 GeV and the lower fitting range is fixed at 70 GeV.

The value of fitted M_W has a systematic dependence on the lower limit of fitting range, which is obvious in the inclusive sample of Table 8.1. For the various upper limits, there is no significant effect on the fitted M_W. With the final fitting range of $66\,\mathrm{GeV} < M_T < 96GeV$, for the 12 subsamples of $1\,\mathrm{fb}^{-1}$ W and Z events, 5 subsamples have fitted M_W lower than input value (80450 MeV) and the other 7 subsamples have fitted M_W higher than the input M_W. For the combined $2\,\mathrm{fb}^{-1}$ W events and $6\,\mathrm{fb}^{-1}$ Z events, fitted $M_W = 80412\,\mathrm{MeV}$, which is 38 MeV lower than the input value. True statistical uncertainty for the combined sample is not clear in this case (which should be obtained from the ensemble test). If 30 MeV is a reasonable estimation of the statistical uncertainty, that means our fitted M_W is more than 1σ away from the input W mass.

Z	$\mathcal{A}$	$\mathcal{B}$	$\mathcal{C}$	$\mathcal{D}$	$\mathcal{E}$	$\mathcal{F}$
W $\mathcal{A}$	80358 ± 28	80460 ± 36	80340 ± 35	$80245 \pm$ NA	80475 ± 42	80309 ± 44
W $\mathcal{B}$	80454 ± 42	80523 ± 42	80413 ± 26	80284 ± 28	80555 ± 37	80408 ± 40
all	80412 ± 13 $(66\,\text{GeV} < M_T < 96\,\text{GeV})$					
Z	$\mathcal{A}$	$\mathcal{B}$	$\mathcal{C}$	$\mathcal{D}$	$\mathcal{E}$	$\mathcal{F}$
W $\mathcal{A}$	80427 ± 59	80429 ± 48	80343 ± 46	$80239 \pm$ NA	80476 ± 39	80318 ± 64
W $\mathcal{B}$	80497 ± 32	80481 ± 67	80405 ± 30	$80261 \pm$ NA	80556 ± 42	80398 ± 34
all	80415 ± 11 $(68\,\text{GeV} < M_T < 96\,\text{GeV})$					
Z	$\mathcal{A}$	$\mathcal{B}$	$\mathcal{C}$	$\mathcal{D}$	$\mathcal{E}$	$\mathcal{F}$
W $\mathcal{A}$	80480 ± 77	80395 ± 64	80391 ± 33	$80265 \pm$ NA	80491 ± 37	80391 ± 99
W $\mathcal{B}$	80521 ± 36	80463 ± 63	80458 ± 35	80319 ± 65	80579 ± 34	80421 ± 33
all	80445 ± 13 $(70\,\text{GeV} < M_T < 96\,\text{GeV})$					
Z	$\mathcal{A}$	$\mathcal{B}$	$\mathcal{C}$	$\mathcal{D}$	$\mathcal{E}$	$\mathcal{F}$
W $\mathcal{A}$	80495 ± 71	80357 ± 62	80410 ± 38	80340 ± 76	80508 ± 37	80387 ± 84
W $\mathcal{B}$	80561 ± 53	80427 ± 58	80498 ± 30	80416 ± 92	80606 ± 32	80482 ± 64
all	80462 ± 16 $(72\,\text{GeV} < M_T < 96\,\text{GeV})$					
Z	$\mathcal{A}$	$\mathcal{B}$	$\mathcal{C}$	$\mathcal{D}$	$\mathcal{E}$	$\mathcal{F}$
W $\mathcal{A}$	80500 ± 76	80321 ± 64	80426 ± 39	80336 ± 71	80508 ± 35	80380 ± 70
W $\mathcal{B}$	$80625 \pm$ NA	80448 ± 49	80551 ± 30	80426 ± 90	80641 ± 30	80512 ± 66
all	80491 ± 21 $(74\,\text{GeV} < M_T < 96\,\text{GeV})$					
Z	$\mathcal{A}$	$\mathcal{B}$	$\mathcal{C}$	$\mathcal{D}$	$\mathcal{E}$	$\mathcal{F}$
$W\mathcal{A}$	80498 ± 70	80387 ± 78	80487 ± 45	80322 ± 91	80487 ± 42	80403 ± 95
$W\mathcal{B}$	80623 ± 81	80510 ± 70	80595 ± 65	80421 ± 90	$80660 \pm$ NA	80542 ± 98
all	80514 ± 19 $(76\,\text{GeV} < M_T < 96\,\text{GeV})$					

Table 8.1: Fitted W mass for the 12 combinations of $1\,\text{fb}^{-1}$ $W \to e\nu$ and $Z \to ee$ events. The upper fitting range is fixed at 96 GeV, the lower fitting range is set at different values from 66 GeV to 76 GeV. The statistical uncertainty is base on one sample, therefore the correlation of two M_T from Z is not taken in to account. The fitting for all samples is performed on the combined $2\,\text{fb}^{-1}$ W events and $6\,\text{fb}^{-1}$ Z events.

Z	$\mathcal{A}$	$\mathcal{B}$	$\mathcal{C}$	$\mathcal{D}$	$\mathcal{E}$	$\mathcal{F}$
W $\mathcal{A}$	80480 ± 88	80390 ± 76	80363 ± 40	$80256 \pm$ NA	80487 ± 39	80390 ± 90
W $\mathcal{B}$	80536 ± 37	80434 ± 58	80413 ± 37	80295 ± 68	80572 ± 40	80442 ± 53
all	80435 ± 16 $(70\,\text{GeV} < M_T < 90\,\text{GeV})$					
Z	$\mathcal{A}$	$\mathcal{B}$	$\mathcal{C}$	$\mathcal{D}$	$\mathcal{E}$	$\mathcal{F}$
W $\mathcal{A}$	80480 ± 85	80394 ± 72	80385 ± 35	$80261 \pm$ NA	80500 ± 37	80390 ± 87
W $\mathcal{B}$	80530 ± 39	80448 ± 61	80443 ± 32	80303 ± 76	80575 ± 31	80422 ± 33
all	80441 ± 12 $(70\,\text{GeV} < M_T < 92\,\text{GeV})$					
Z	$\mathcal{A}$	$\mathcal{B}$	$\mathcal{C}$	$\mathcal{D}$	$\mathcal{E}$	$\mathcal{F}$
W $\mathcal{A}$	80480 ± 81	80393 ± 72	80380 ± 36	$80267 \pm$ NA	80490 ± 37	80391 ± 92
W $\mathcal{B}$	80533 ± 32	80452 ± 59	80448 ± 38	80319 ± 68	80580 ± 30	80423 ± 32
all	80441 ± 12 $(70\,\text{GeV} < M_T < 94\,\text{GeV})$					
Z	$\mathcal{A}$	$\mathcal{B}$	$\mathcal{C}$	$\mathcal{D}$	$\mathcal{E}$	$\mathcal{F}$
W $\mathcal{A}$	80480 ± 82	80390 ± 76	80428 ± 54	$80272 \pm$ NA	80506 ± 36	80390 ± 75
W $\mathcal{B}$	80507 ± 41	80435 ± 57	80468 ± 30	80320 ± 67	80579 ± 27	80425 ± 32
all	80444 ± 14 $(70\,\text{GeV} < M_T < 98\,\text{GeV})$					
Z	$\mathcal{A}$	$\mathcal{B}$	$\mathcal{C}$	$\mathcal{D}$	$\mathcal{E}$	$\mathcal{F}$
W $\mathcal{A}$	80433 ± 115	80381 ± 70	80428 ± 52	$80272 \pm$ NA	80498 ± 37	80398 ± 70
W $\mathcal{B}$	80503 ± 42	80417 ± 54	80469 ± 30	80320 ± 66	80571 ± 30	80435 ± 30
all	80439 ± 13 $(70\,\text{GeV} < M_T < 100\,\text{GeV})$					

Table 8.2: Fitted W mass for the 12 combinations of $1\,\text{fb}^{-1}$ $W \to e\nu$ and $Z \to ee$ events. The lower fitting range is fixed at 70 GeV, the upper fitting range is set at different values from 90 GeV to 100 GeV. The statistical uncertainty is base on one sample, therefore the correlation of two M_T from Z is not taken in to account. The fitting for all sample is performed on the combined $2\,\text{fb}^{-1}$ W events and $6\,\text{fb}^{-1}$ Z events.

Chapter 9

Measure Data W Mass and Systematic Uncertainties

9.1 Data

The same CAF package for the analysis of full Monte Carlo events is applied to the analysis of data. Configuration file is switched to the one that is tuned by data. Event selection cuts are the same as in the full Monte Carlo simulation and are described in Chapter 4.3. Since the electron p_T cut is set to 30 GeV, trigger rate for EM objects is almost 100% for CC and EC electrons in W and Z events. In the study of ratio method for data, trigger efficiency is not taken into account.

Another major difference between full Monte Carlo and data is the background subtraction for the M_T histograms of W and Z data events. By construction, only the signal M_T distribution scales with the W and Z boson mass. For data M_T spectrum, the background distributions need to be removed before the mass fitting is performed in ratio method. There are three major backgrounds for $W \to e\nu$ sample: QCD, $Z \to ee$ and $W \to \tau\nu \to e\bar{\nu}\nu\nu$. For $Z \to ee$ sample, QCD is the only major background that needs to be considered.

A QCD event can fake a $W \to e\nu$ event if a high p_T jet passes the electron selection cuts and there is significant $\not\!\!E_T$ measured in the event. The most effective cut to differentiate electron from jet is whether there is a track associated with the EM cluster of electron. This track matching requirement is included in the electron selection cuts, therefore the QCD background can be estimated by the well established matrix method.

To measure the QCD background shape in matrix method, two variables known as the track matching efficiency ϵ_{trk} and fake rate f_{QCD} are known

beforehand. $\epsilon_{\rm trk}$ stands for the efficiency of real electrons to pass the track matching cut. Fake rate $f_{\rm QCD}$ stands for the fraction of true QCD events that pass the track matching cuts, that is the probability of a jet to fake an electron.

All the other standard selection cuts are applied to $W \to e\nu$ events, with and without the track match requirement. The total number of $W \to e\nu$ events before and after the track matching cut can be related with the number of signal and QCD background event as the following two equations:

$$\begin{aligned} N &= N_W + N_{\rm QCD} \\ N_{\rm trk} &= \epsilon_{\rm trk} N_W + f_{\rm QCD} N_{\rm QCD} \end{aligned} \tag{9.1}$$

N, $N_{\rm trk}$ are the number of events before and after tracking matching cut, they can be read directly from histograms. $\epsilon_{\rm trk}$ and $f_{\rm QCD}$ values are predetermined (will be discussed below). It is easy to solve the above equations to get the number of signal event N_W and background event number $N_{\rm QCD}$. In the M_T spectrum, matrix method calculation is performed bin by bin to give the overall signal and background M_T shape.

$\epsilon_{\rm trk}$ is usually measured by the "tag and probe" method applied to $Z \to ee$ data. The idea is that the $Z \to ee$ sample is almost solely consisted of two high p_T electrons and contains a very small fraction of background events. For each candidate data $Z \to ee$ event, one tight electron that passes standard cuts, especially the track matching cut is required to make sure the event is of $Z \to ee$ type. A second probe electron with loose cuts (same as tight cuts without track matching requirement) is used to measure the efficiency of passing track matching cut $\epsilon_{\rm trk}$.

QCD fake rate $f_{\rm QCD}$ is estimated by applying track matching cut to the QCD enriched data sample. Standard method determines $\epsilon_{\rm trk} = 0.778$ and $f_{\rm QCD} = 0.022$, those values are also used in the computation of QCD background distribution of ratio method.

In terms of event signature, $W \to \tau\nu \to e\bar{\nu}\nu\nu$ event is indistinguishable from the $W \to e\nu$ signal event. As a result of lepton universality, W boson has the same branching ratio of decaying through the $e\nu$ and $\tau\nu$ channels. Compared with the signal events, electrons and neutrinos decayed from τ has much lower transverse momentum on average, therefore it is very hard for the $W \to \tau\nu$ background events to pass the lepton p_T cut. The shape and normalization of $W \to \tau\nu$ background are estimated by applying the standard $W \to e\nu$ selection to full Monte Carlo $W \to \tau\nu \to e\bar{\nu}\nu\nu$ events. This background accounts for 1.6% of the final $W \to e\nu$ sample.

$Z \to ee$ event could fake a $W \to e\nu$ signal event when one of the Z's electron hits the non fiducial region of the calorimeter and a substantial $\not\!\!E_T$ is observed. Its background shape and normalization are estimated by applying

the $Z \to ee$ event selection cuts on the $W \to e\nu$ data events. This background accounts for 0.6% of the final $W \to e\nu$ sample. M_T shapes of all the above three backgrounds are shown in Figure 9.1.

QCD event is the major background of $Z \to ee$ sample. The probability for two jets to successfully fake electrons are quite low. In ratio method, since we only require one tight and one loose quality electron, the background fraction is higher than that in the standard method where both electrons are required pass tight quality cuts. QCD background shape is estimated by running the same $Z \to ee$ event selection cuts on data, with the H-Matrix cut inverted and the track matching requirement being dropped. The obtained QCD background shape of $Z \to ee$ sample is shown in Figure 9.2.

To determine the normalization of QCD background, we sum the invariant mass of QCD background and fast Monte Carlo $Z \to ee$ events. The resulting mass spectrum is compared with data $Z \to ee$ event. Fraction of QCD background is kept as a floating parameter and determined by the best fitted invariant mass of $Z \to ee$ sample. In ratio method, the measured QCD background fraction is 0.6%.

After the final selection cuts, there are 379402 $W \to e\nu$ data events left. For $Z \to ee$, there are about 61116 events left after the final selection cuts. Among them, 23843 events are eligible for $1Z2W$ and 37273 events are able to make $1Z1W$. The final number events entering into the M_T spectrum from $Z \to ee$ is 84959.

Decomposition of the backgrounds and signal M_T distribution is shown at fixed $M_W = 80400\,\text{MeV}$ in Figure 9.3. Mass fitting is performed on the M_T spectrum after background subtraction. Final fitting range is chosen to be $66\,\text{GeV} < M_T < 96\,\text{GeV}$, the fitting probability is shown in Figure 9.4. Fitted $M_W = 80.435\,\text{GeV}$. The statistical uncertainty 43 MeV is quoted from ensemble test of fast Monte Carlo.

9.2 Systematic Uncertainty

Some of the systematic uncertainties of ratio method are similar to those in the standard method, while the others are unique to each method. Table 5.1 lists major systematic uncertainties in the standard method. The leading contribution of the systematic uncertainty is from the electron energy calibration. In standard method, the electron energy scale and offset is calibrated by fitting the invariant mass shape of $Z \to ee$ events. Therefore the electron calibration uncertainty is actually constrained by the statistics of $Z \to ee$ sample.

In ratio method, $Z \to ee$ events are used directly in the mass fitting. The statistical uncertainty of standard method in final mass fitting and the leading

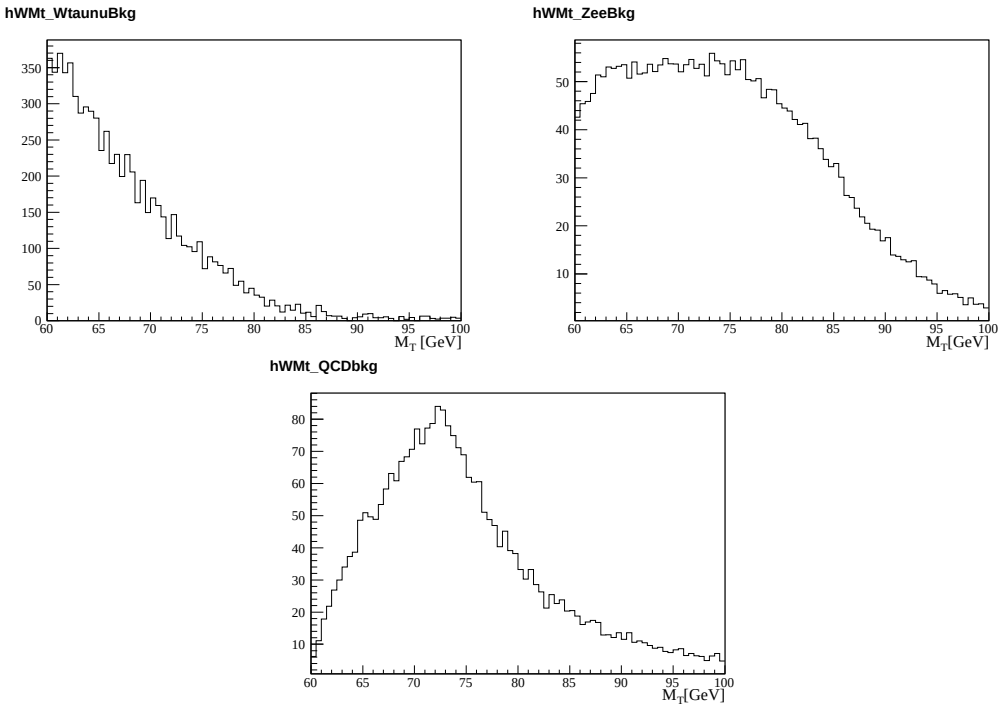

Figure 9.1: Shape of $W \to \tau\nu$ background, $Z \to ee$ background and QCD background. All three background distributions are properly normalized to W data histogram and ready to be subtracted from the M_T histogram of data $W \to e\nu$ sample.

systematic uncertainty of electron calibration are replaced by the statistical uncertainty in ratio method. The above statement is only an approximation, as the fitting ranges, event selection cuts are slightly different in these two methods. The lower end of M_T fitting range is less extended in ratio method to avoid the bias of acceptance cuts. The electron p_T and $\not\!\!E_T$ cuts are raised from 25 GeV to 30 GeV in ratio method. As a result, there is slightly less events in the final sample of ratio method and the statistical uncertainty is also worse.

From the physics point of view, in ratio method the longitudinal component of electrons momentum is discarded in the M_T calculation for $Z \to ee$ events, whereas the full 4-momentum is used in the Z invariant mass calculation. The above two effects result in the statistical uncertainty of ratio method (43 GeV) being larger than the combination of statistical uncertainty (21 MeV) and the systematic uncertainty (34 GeV) of electron energy calibration in standard method.

Many of the other systematic uncertainties in ratio method are identical to

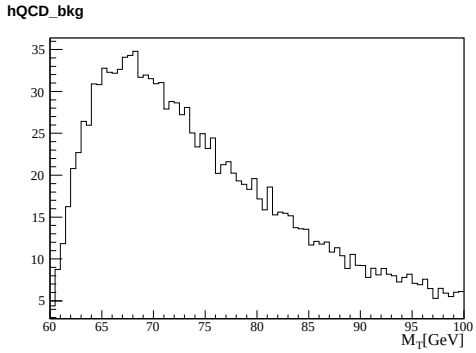

Figure 9.2: M_T spectrum of QCD background for $Z \rightarrow ee$ events. Shown distribution is normalized to Z data histogram.

those in standard method, for example the backgrounds, parton distribution function. These systematic uncertainties are quoted the same as in Table 5.1. Discussions of other parameters relevant to ratio method are presented below. The overall systematic uncertainties of ratio method are shown in Table 9.1. Combining those uncertainties in Table 9.1, we obtain the overall systematic uncertainty of measure M_W in ratio method: 26 MeV.

Electron Resolution

Knowledge of electron resolution is used in the calculation of extra smearing of electrons. To estimate this effect on the fitted W mass value, we use two different electron energy smearing algorithms in the fast Monte Carlo closure test. One of the smearing algorithm is the usual simple Gaussian smearing, the other algorithm uses a variable sampling term (dependent on electron energy and direction Eq 7.1). The difference of fitted M_W in ensemble tests between these two smearing algorithms is 2 MeV. This is quoted as the systematic uncertainty due to electron resolution model.

Electron Energy Scale and Offset

Unlike in the standard method, electron energy scale α is effectively cancelled in the ratio of M_W/M_Z. On the other hand, without non zero electron energy scale β, the fitted M_W is shifted away from the input value by $\beta/10$ (Chapter 6.2). The uncertainty of electron energy scale in data is measured to be 210 MeV [40]. This indicates the systematic uncertainty of M_W due to electron energy offset is 21 MeV.

Recoil Model

Extra smearing correction of the recoil system in data depends on its smearing model. The realistic smearing model (Non Gaussian in Chapter 7) used in our extra smearing correction of data is known to be a good description of the $1\,\mathrm{fb}^{-1}$ DØRun IIa data. To estimate the systematic uncertainty of measured M_W due to the extra smearing model of hard recoil, we make ensembles test with two different recoil smearing models (and the correspond extra smearing): simple Gaussian and the realistic `wz_epmcs` smearing. The central value difference of fitted M_W in ensemble test is 5 MeV. This is quoted as the systematic uncertainty due to hard extra smearing correction.

Underlying Event

Similar to the extra smearing correction of hard recoil system, extra smearing correction to the underlying event in data is based on the realistic `wz_epmcs` model. Correction terms of the soft recoil and underlying event are randomly picked up from a MBZB library that is tuned to W and Z data events. Detailed description of this correction is given in Chapter 7.2.2. To estimate the systematic uncertainty of underlying event smearing, another simple extra smearing model is used in the fast Monte Carlo simulation, where the correction terms are drawn from the a Gaussian distribution with $\sigma = 2.4\,\mathrm{GeV}$ (Eq 6.17) width. The difference of fitted M_W from ensemble test between these two correction is 7 MeV, which is quoted as the systematic uncertainty.

Background

Background contribution to the M_T spectrum is identical to that in the standard method. In both methods, the percentage of background events normalization is varied around the measured value and W mass fitting using high statistical W and Z sample are performed at those varied pints. Difference of fitted mass at the varied points is quoted as the systematic uncertainty. The background shape and normalization in ratio method are not exactly the same as in the standard method, because of the slight different event selection cuts. Considering that the overall systematics due to background is a small value, the 2 MeV (Table 5.1) systematic uncertainty from standard method is still a good estimation for ratio method.

Production Model (PDF , ISR and FSR)

The generator events used in the validation of ratio method are produced by `resbos` with a specific set of Parton Distribution Function (PDF), CTEQ6M.

Parameters used in each CTEQ version comes from a global fit of results from various experiments. The choice of parameter values in CTEQ has effects on the shape of M_T spectrum of W and Z sample. Therefore the measured W mass also depends on the PDF parameters used in fast Monte Carlo simulation. Our current knowledge of PDF parameters is limited by the available experimental results. To estimate the systematic shift of measured W mass due to the uncertainty of PDF parameters, one needs to vary the PDF parameters in the `resbos` event generations and perform the mass fitting. The variance of fitted W mass stands for different PDF sets stands for the systematic uncertainty.

Study of above effect for the standard method is described in [41]. A large number of W and Z events are generated by `resbos` with a central PDF set. For each varied PDF set, the events in the central PDF sample are reweighted accordingly to reflect the varied PDF parameter. Mass fitting using M_T spectrum are performed between the central PDF set and varied PDF set. In this way, the difference of measured M_W is free of statistical fluctuation, and reflects the contribution from PDF only. In ratio method, for each varied PDF set, mass fitting should be done to the PDF reweighted W and Z sample. Difference with the fitted M_W from W and Z generated by central PDF set should be the correct systematic uncertainty. We didn't make such a study and quote the 10 MeV (Table 5.1) from standard method as a reasonable estimation of the PDF uncertainty in ratio method.

The initial state radiation (ISR) of gluons by boson have direct influence on the boson p_T distribution. Events generated by `resbos` have reasonably good description of the ISR processes. Compared with ISR, the final state radiation (FSR) from the electrons of W and Z bosons is more dominant. Photons radiated from electrons carry away energy that make the invariant mass (or M_T) of the dilepton pair smaller than the original value. Those radiated photons tend to be colinear with the electrons and that makes the electron energy reconstructed by calorimeter towers be able to recover most of the energy carried away by FSR photons. In the study of standard method, the number of FSR photons as well as its lower energy threshold are varied in the fast Monte Carlo simulation. Both W and Z events are affected by FSR in a similar way, albeit in different scale, as two electrons decay from each Z boson in contrast of only one electron from W boson. In both method, only the relative change of W mass with respect to Z mass is meaningful. Systematic uncertainty due to ISR and FSR is 7 MeV, quoted from the result of standard method.

sources	systematic uncertainty σM_W [MeV]
Electron resolution	2
Electron energy offset	21
Hard recoil model	5
Underlying event	7
Backgrounds	2
PDF	10
QED	7
Combined	26

Table 9.1: List of systematic uncertainties of ratio method.

9.3 Conclusion and Discussion

The measured W boson mass in ratio method using the $1\,\mathrm{fb}^{-1}$ DØ Run IIa data in electron channel is $M_W = 80435 \pm 43(\mathrm{stat}) \pm 26(\mathrm{sys})\,\mathrm{MeV}$. This result is consistent with the current world average value of W boson mass $M_W = 80399 \pm 23\,\mathrm{MeV}$.

It's interesting to compare the above result with that from the standard method [11], as both method measure W mass on the same $1\,\mathrm{fb}^{-1}$ DØ RunIIa data. The measured W mass in standard method is $M_W = 80401 \pm 21(\mathrm{stat}) \pm 38(\mathrm{sys})\,\mathrm{MeV}$. Compared with the standard method, M_W measured in ratio method has larger statistical uncertainty and smaller systematic uncertainty. That's what we expected as a consequence of the direct M_T comparison of Z and W in the mass fitting of ratio method. Limitation of Z statistics is reflected in the final statistical uncertainty. The same Z statistical limitation in standard method takes the form of uncertainty of the electron energy scale and offset parameters which is determined by the invariant mass of Z data.

Calculation of transverse mass M_T only involves the transverse momentum of electrons from Z, information of the z component of electron's momentum is discarded. As a result, the overall uncertainty of ratio method should be worse than its standard method counterpart. The advantage of ratio method relies on the direct calculation of M_T from $Z \to ee$ data. By skipping the construction of a full fledged, complicated fast Monte Carlo model (which starts from the physical 4 momentum of particles) of $W \to ee$ and $Z \to ee$ events, ratio method is considered to be a easy and fast alternative way of measuring the W boson mass. Corrections needed to apply to $Z \to ee$ events are less complicated than the full construction of fast Monte Carlo model. Therefore the systematic uncertainty is expected to be less in the ratio method.

However this convenience doesn't come without price. In addition to the

inherent worse uncertainty, ratio method (used in this analysis) is only applicable to M_T spectrum, unlike in the standard method where p_T^e and $\not\!\!E_T$ spectra can be used in mass fitting as well. In this particular analysis, the acceptance cut that requires tight electron to be in CC causes substantial bias in the lower M_T range. Lepton p_T cut is raised from 25 GeV to 30 GeV and the fitting range is chosen to be outside of the bias region in order to have a successful mass fit. More events could have been included (hence better statistical uncertainty) in the final fitting if the tight electrons in EC are also included in the event selection, not just because of the added events, but also because of the relaxed lepton p_T cut and fitting range in this case (Fig 6.21 to Fig 6.23). Lack of knowledge for EC electrons prevents its inclusion in this analysis.

Larger dataset (up to 10 fb^{-1}) of DØ and CDF Run IIb will be used in the future W mass measurement. Statistical uncertainty as well as the electron calibration uncertainty will be significantly lowered. Indirect constraints on the mass of Higgs boson will be even more stringent. The complexity of fast Monte Carlo simulation of those high luminosity events is a big challenge for standard method. If we could understand the smearing algorithms of electron and recoil system for those high luminosity events, reasonable extra smearing correction is plausible to implement accordingly and that will make ratio method a worthy alternative way of measuring W boson mass.

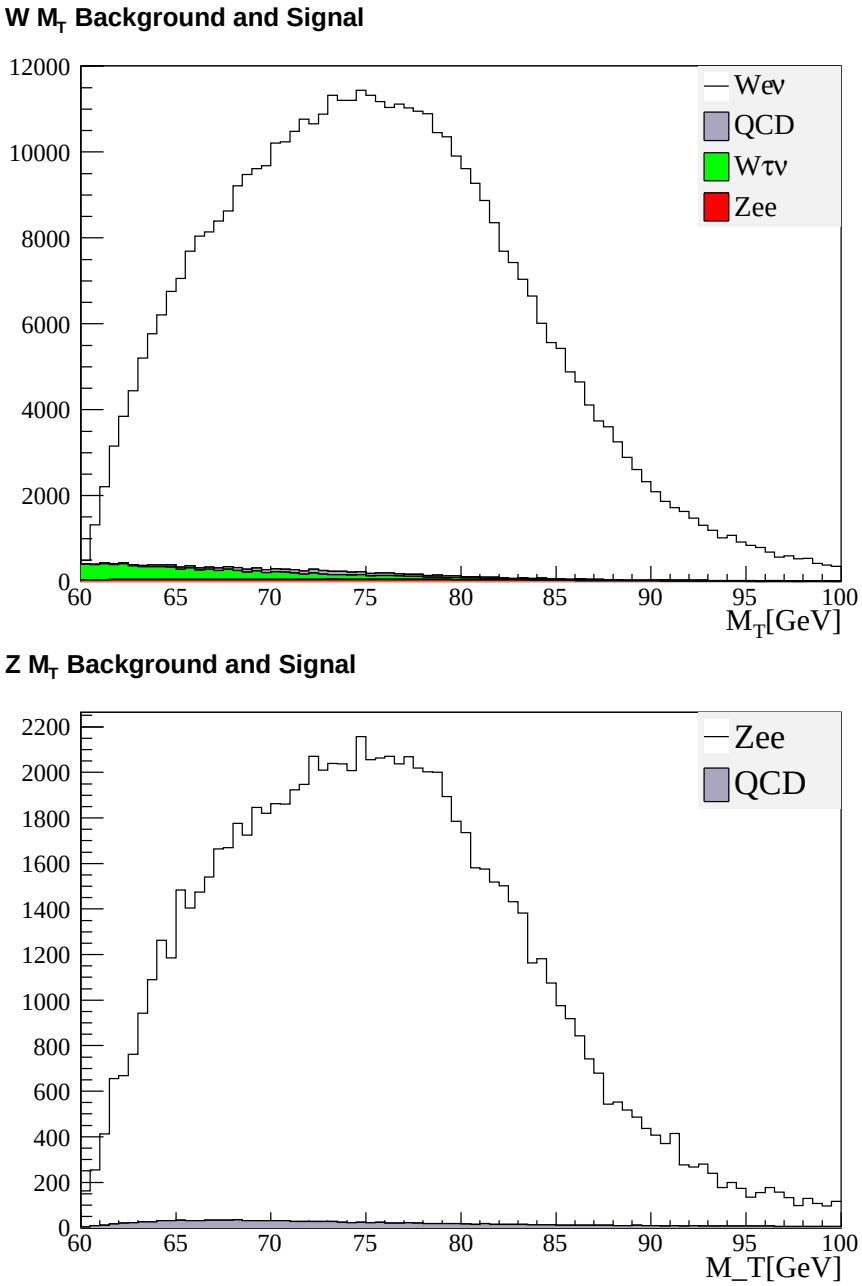

Figure 9.3: Comparison of $Z \to ee$ backgrounds and signal. The M_T of QCD background is calculated at fixed $M_W = 80.40\,\text{GeV}$.

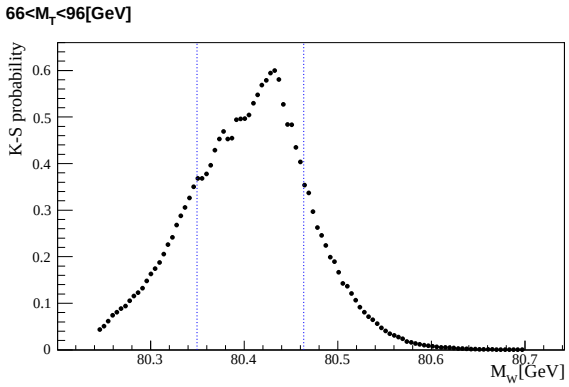

Figure 9.4: K-S probability for the M_T fitting of data template. Fitted $M_W = 80435\,\text{MeV}$. Fitting range is $66\,\text{GeV} < M_T < 96\,\text{GeV}$. Blue dotted lines stand for the statistical uncertainty from the fit. The true statistical uncertainty of 43 GeV is from ensemble test of fast Monte Carlo.

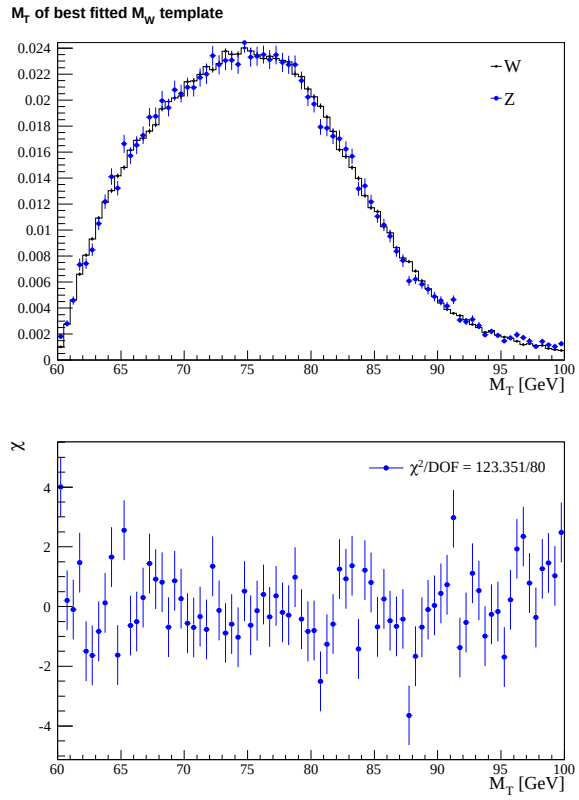

Figure 9.5: Comparison between M_T of W data and the best fitted M_T template from Z data, which is 80435 MeV. Range between 66 GeV and 96 GeV is used in the mass fitting.

Bibliography

[1] C. Amsler *et al.* "Review of Particles Physics: The CKM Quark-Mixing Matrix", Phys. Lett. B **667**, 145 (2008).

[2] The LEP Electroweak Working Group, CERN-PH-EP/2008-20, arXiv:0811.4682 [hep-ex] (2008).

[3] UA1 Collaboration, G. Arnison *et al.*, Phys. Lett. B **122**, 103 (1983).

[4] UA2 Collaboration, M. Banner *et al.*, Phys. Lett. B **122**, 476 (1983).

[5] UA1 Collaboration, G. Arnison *et al.*, Phys. Lett. B **126**, 398 (1983).

[6] UA2 Collaboration, M. Bagnaia *et al.*, Phys. Lett. B **129**, 130 (1983).

[7] The LEP Collaborations: ALEPH, DELPHI, L3, OPAL and the LEP Electroweak Working Group, and the SLD Heavy Flavor Group, CERN-EP-2002-091, hep-ex/0212036.

[8] A. Sirlin, Phys. Rev. D **22**, 971 (1980).

[9] D. C. Kennedy *et al.*, Nucl. Phys. B **322**, 1 (1989).

[10] S. Heinemeyer *et al.*, J. High Energy Phys. 08 (2006) 052.

[11] V. Abazov *et al.*, Phys. Rev. Lett. **103**, 141801 (2009).

[12] T. Aaltonen *et al.*, Phys. Rev. Lett. **99**, 151801 (2007). Phys. Rev. D **77**, 112001 (2008).

[13] C. Balazs and C.P. Yuan, Phys. Rev. D **56**, 5558 (1997).

[14] Tevatron Electroweak Working Group, arXiv:0908.1374v1 [hep-ex] (2009).

[15] The LEP Collaborations, arXiv:0612034 [hep-ex] (2006).

[16] DØ Collaboration, Nucl. Instrum. Methods in Phys. Res. A **565**, 463 (2006).

[17] F. Halzen and A. D. Martin, "Quarks & Leptons: An Introductory Course in Modern Particle Physics", published by John Wiley & Sons (1984).

[18] G. Karagiorgi *et al.*, Phys. Rev. D **75**, 013011 (2007).

[19] G. A. Ladinsky and C.P. Yuan, Phys. Rev. D **50**, 4239 (1994).

[20] C. Balazs and C.P. Yuan, Phys. Lett. B **355**, 548 (1995).

[21] J. Collins, D. Soper and G. Sterman, Nucl. Phys. B **250**, 199 (1985).

[22] P. B. Arnold and R. P. Kauffaman, Nucl. Phys. B **349**, 381 (1991).

[23] E. Mirkes, Nucl. Phys. B **387**, 3 (1992).

[24] J. Collins and D. Soper, Phys. Rev. D **16**, 2219 (1977).

[25] CDF Collaboration, Phys. Rev. D **71**, 052002 (2005).

[26] J. Smith, W. L. van Neerven and J. A. M. Vermaseren, Phys. Rev. Lett. **50**, 1738 (1983).

[27] DØ W mass group, DØ Note 5659.

[28] J. Zhu and F. Guo, DØ Note 5661.

[29] DØ Collaboration, "A Novel Method for Modeling the Recoil in W Boson Events at Hadron Colliders", [arXiv:hep-ex/09073713].

[30] T. Andeen *et.al*, DØ Note 5668.

[31] DØ Collaboration, Phys. Rev. Lett., **103**, 231802 (2009).

[32] Alexander Schmidt, Diplomarbeit, University of Karlsruhe, Germany (2004).

[33] S. Rajagopalan and M. Rijssenbeek, DØ Note 3000 (1996).

[34] Dennis L. Shpakov, PhD Thesis, Stony Brook University (2000).

[35] DØ Collaboration, Phys. Rev. D **58**, 092003 (1998).

[36] Leopold Schmetterer, "Introduction to Mathematical Statistics", published by Springer-Verlag (1974).

[37] Edward J. Dudewicz and Satya N. Mishra, "Modern Mathematical Statistics", published by John Wiley & Sons (1988).

[38] William H. Press *et.al*, "Numerical Recipes - The Art of Scientific Computing" published by Cambridge University Press (2007).

[39] T. Andeen *et al.*, DØ Note 5668 (2008).

[40] T. Andeen and Alex Melnitchouk, DØ Note 5662 (2008).

[41] J. Guo *et.al*, "PDF Uncertainty of the W Mass Measurement", DØ Note xxxx (2007).

Appendix A

Derivation of $\cos\theta^*$ in the Collins Soper Frame

In the lab frame, the cartesian 4-vector of the protons and antiprotons are $p^\mu_{h_1,h_2} = \sqrt{S}/2(1,0,0,\pm 1)$, where $\sqrt{S} = 1.98\,TeV$, h_1 stands for proton and h_2 for antiproton. Because of the symmetry in the ϕ direction of Z boson, without losing generality, we consider Z boson only has transverse momentum in x-axis. The 4-momentum of Z boson is $q^\mu = (q^0, Q_T, 0, q^3)$ in the lab frame. If we denote the lab frame as O and the Z boson rest frame is O', then we have relation $p'^\mu(\text{rest}) = \Lambda^\mu_\nu(\text{lab} \to \text{rest})p^\nu(\text{lab})$. Collins-Soper frame is essentially the Z boson rest frame, with axis rotated to make z-axis bisect the angle between proton monmentum p_{h_1} and negative antiproton momentum $-p_{h_2}$ in the Z boson rest frame.

By definition, the boost matrix from lab frame O to the Z boson rest frame O' is

$$\Lambda^\mu_\nu(\text{lab}\to\text{rest}) = \begin{pmatrix} \gamma & -\gamma\beta_1 & -\gamma\beta_2 & -\gamma\beta_3 \\ -\gamma\beta_1 & 1+\dfrac{(\gamma-1)\beta_1^2}{\beta^2} & \dfrac{(\gamma-1)\beta_1\beta_2}{\beta^2} & \dfrac{(\gamma-1)\beta_1\beta_3}{\beta^2} \\ -\gamma\beta_2 & \dfrac{(\gamma-1)\beta_1\beta_2}{\beta^2} & 1+\dfrac{(\gamma-1)\beta_2^2}{\beta^2} & \dfrac{(\gamma-1)\beta_2\beta_3}{\beta^2} \\ -\gamma\beta_3 & \dfrac{(\gamma-1)\beta_1\beta_3}{\beta^2} & \dfrac{(\gamma-1)\beta_2\beta_3}{\beta^2} & 1+\dfrac{(\gamma-1)\beta_3^2}{\beta^2} \end{pmatrix}. \tag{A.1}$$

Boost from lab frame O to boson rest frame O' is $\boldsymbol{\beta} = \boldsymbol{q}(\text{lab})/q^0 = (Q_T/q^0, 0, q^3/q^0)$.

It is easy to show

$$\gamma = \frac{1}{\sqrt{1-\beta^2}} = \frac{q^0}{Q} \tag{A.2}$$

$$-\gamma\beta_1 = -\frac{q^0}{Q}\frac{Q_T}{q^0} = -\frac{Q_T}{Q} \tag{A.3}$$

$$-\gamma\beta_2 = 0 \tag{A.4}$$

$$-\gamma\beta_3 = -\frac{q^0}{Q}\frac{q^3}{q^0} = -\frac{q^3}{Q} \tag{A.5}$$

$$1+\frac{(\gamma-1)\beta_1^2}{\beta^2} = 1+\frac{(\gamma-1)(Q_T/q^0)^2}{[Q_T^2+(q^3)^2]/(q^0)^2} = 1+\frac{[(q^0/Q)-1]Q_T^2}{Q_T^2+(q^3)^2} = 1+\frac{1}{Q}\frac{(q^0-Q)Q_T^2}{(q^0-Q)(q^0+Q)}$$

$$= 1+\frac{1}{Q}\frac{Q_T^2}{q^0+Q} \tag{A.6}$$

$$(\gamma-1)\frac{\beta_1\beta_2}{\beta^2} = 0 \tag{A.7}$$

$$(\gamma-1)\frac{\beta_1\beta_3}{\beta^2} = (\gamma-1)\frac{(Q_T/q^0)(q^3/q^0)}{1-1/\gamma^2} = \frac{Q_T q^3}{(q^0)^2}\frac{\gamma^2}{\gamma+1} = \frac{Q_T q^3}{Q(q^0+Q)} \tag{A.8}$$

$$1+\frac{(\gamma-1)\beta_2^2}{\beta^2} = 1 \tag{A.9}$$

$$\frac{(\gamma-1)\beta_2\beta_3}{\beta^2} = 0 \tag{A.10}$$

$$1+\frac{(\gamma-1)\beta_3^2}{\beta^2} = 1+\frac{(\gamma-1)(q^3/q^0)^2}{1-1/\gamma^2} = 1+(\frac{q^3}{q^0})^2\frac{\gamma^2}{\gamma+1} = 1+\frac{(q^3)^2}{Q(q^0+Q)} \tag{A.11}$$

With the above relations, we can rewrite Eq (A.1) as

$$\Lambda^\mu_\nu(\text{lab}\rightarrow\text{rest}) = \frac{1}{Q}\begin{pmatrix} q^0 & -Q_T & 0 & -q^3 \\ -Q_T & Q+\dfrac{Q_T^2}{q^0+Q} & 0 & \dfrac{Q_T q^3}{q^0+Q} \\ 0 & 0 & Q & 0 \\ -q^3 & \dfrac{Q_T q^3}{q^0+Q} & 0 & Q+\dfrac{(q^3)^2}{q^0+Q} \end{pmatrix}. \tag{A.12}$$

$Q = \sqrt{(q^0)^2-Q_T^2-(q^3)^2}$ is the Z boson invariant mass and the transverse mass is defined as $M_T = \sqrt{Q^2+Q_T^2}$. Now we can write the proton and antiproton's 4-momentum in the Z boson rest frame $p'^\mu_{h_1,h_2}(\text{rest}) = \Lambda^\mu_\nu(\text{lab}\rightarrow$

rest)$p^{\nu}_{h_1,h_2}$(lab).

$$
\begin{aligned}
p'^{\mu}_{h_1}(\text{rest}) &= \frac{\sqrt{S}}{2}(\frac{q^0-q^3}{Q}, -\frac{Q_T}{Q}\frac{q^0+Q-q^3}{q^0+Q}, 0, \frac{(Q-q^3)(q^0+Q)+(q^3)^2}{Q(q^0+Q)}) \\
-p'^{\mu}_{h_2}(\text{rest}) &= \frac{\sqrt{S}}{2}(-\frac{q^0+q^3}{Q}, \frac{Q_T}{Q}\frac{q^0+Q+q^3}{q^0+Q}, 0, \frac{(Q+q^3)(q^0+Q)+(q^3)^2}{Q(q^0+Q)})
\end{aligned}
$$

It's obvious that the proton and antiproton's momentum generally would not be collinear any more in the Z boson rest frame. We can determine the new z-axis as the bisector of proton and antiproton's momentum in the Z rest frame. For simplicity, we rewrite the spatial components of Eq (A.13) and Eq (18) by taking out proportionality.

$$
\begin{aligned}
\boldsymbol{p}_{h_1}(\text{rest}) &= (-Q_T(q^0+Q-q^3), 0, (Q-q^3)(q^0+Q)+(q^3)^2) \quad \text{(A.13)} \\
-\boldsymbol{p}_{h_2}(\text{rest}) &= (-Q_T(q^0+Q+q^3), 0, (Q+q^3)(q^0+Q)+(q^3)^2) \quad \text{(A.14)}
\end{aligned}
$$

The length of $\boldsymbol{p}_{h_1}$ is

$$
\begin{aligned}
|\boldsymbol{p}|^2_{h_1} &= Q_T^2(q^0+Q-q^3)^2 + [(Q-q^3)(q^0+Q)+(q^3)^2]^2 \\
&= (q^0)^2Q_T^2 + 2q^0QQ_T^2 + Q^2Q_T^2 - 2q^0q^3Q_T^2 - 2QQ_T^2q^3 + Q_T^2(q^3)^2 \\
&\quad +[Q^2(q^0)^2 + 2q^0Q^3 + Q^4 - 2Qq^3(q^0)^2 - 4q^0q^3Q^2 - 2q^3Q^3 + (q^0)^2(q^3)^2 \\
&\quad +2q^0(q^3)^2Q + (q^3)^2Q^2] \\
&\quad +2Qq^0(q^3)^2 + 2(q^3)^2Q^2 - 2q^0(q^3)^3 - 2Q(q^3)^3 + (q^3)^4 \\
&= (q^0)^2M_T^2 + 2q^0QM_T^2 + Q^2M_T^2 - 2q^0q^3M_T^2 - 4Qq^3(q^0)^2 + (q^3)^2M_T^2 - 2q^0q^3Q^2 \\
&\quad +(q^0)^2(q^3)^2 + 4Qq^0(q^3)^2 + 2(q^3)^2Q^2 - 2q^0(q^3)^3 + (q^3)^4 \\
&= (q^0)^2[(q^0)^2 - 2q^0q^3 + (q^3)^2] + Q^2[(q^0)^2 - 2q^0q^3 + (q^3)^2] \\
&\quad +2Q(q^0)[(q^0)^2 - 2q^0q^3 + (q^3)^2] \\
&= (q^0+Q)^2(q^0-q^3)^2. \quad \text{(A.15)}
\end{aligned}
$$

Flipping q^3 with $-q^3$ in Eq (A.15), we can get

$$
|\boldsymbol{p}|^2_{h_2} = (q^0+Q)^2(q^0+q^3)^2. \quad \text{(A.16)}
$$

Now we are ready to normalize the proton and negative antiproton vector

$\boldsymbol{p}_{h_1}$ and $-\boldsymbol{p}_{h_2}$,

$$\hat{\boldsymbol{p}}_{h_1}(\text{rest}) = \left(\frac{-Q_T(q^0+Q-q^3)}{(q^0+Q)(q^0-q^3)}, 0, \frac{(Q-q^3)(q^0+Q)+(q^3)^2}{(q^0+Q)(q^0-q^3)}\right) \quad \text{(A.17)}$$

$$-\hat{\boldsymbol{p}}_{h_2}(\text{rest}) = \left(\frac{-Q_T(q^0+Q+q^3)}{(q^0+Q)(q^0+q^3)}, 0, \frac{(Q+q^3)(q^0+Q)+(q^3)^2}{(q^0+Q)(q^0+q^3)}\right) \quad \text{(A.18)}$$

In the Z boson rest frame, we can write the z-axis of Collins-Soper frame as bisector of $\hat{\boldsymbol{p}}_{h_1}$ and $-\hat{\boldsymbol{p}}_{h_2}$

$$\boldsymbol{z}(\text{CS}) = \hat{\boldsymbol{p}}_{h_1} - \hat{\boldsymbol{p}}_{h_2}. \quad \text{(A.19)}$$

It's easy to show that

$$\begin{aligned}
\frac{-Q_T(q^0+Q-q^3)}{(q^0+Q)(q^0-q^3)} + \frac{-Q_T(q^0+Q+q^3)}{(q^0+Q)(q^0+q^3)} &= -\frac{2QQ_Tq^3}{(q^0+Q)M_T^2}, \\
\frac{(Q-q^3)(q^0+Q)+(q^3)^2}{(q^0+Q)(q^0-q^3)} + \frac{(Q+q^3)(q^0+Q)+(q^3)^2}{(q^0+Q)(q^0+q^3)} &= \frac{2(QM_T^2+Q^2q^0)}{(q^0+Q)M_T^2}.
\end{aligned}$$

So the Collins-Soper z-axis would then be

$$\boldsymbol{z}(\text{CS}) = \frac{2Q}{(q^0+Q)M_T^2}(-Q_Tq^3, 0, M_T^2+Qq^0). \quad \text{(A.20)}$$

We can easily calculate that

$$(-Q_Tq^3)^2 + (M_T^2+Qq^0)^2 = M_T^2(Q+q^0)^2, \quad \text{(A.21)}$$

therefore the vector length of $\boldsymbol{z}(\text{CS})$ is $2Q/M_T$ and the unit z-axis of Collins-Soper frame is

$$\hat{\boldsymbol{z}}(\text{CS}) = \frac{1}{(q^0+Q)M_T}(-Q_Tq^3, 0, M_T^2+Qq^0). \quad \text{(A.22)}$$

Simple geomeometrical relations of the Collins-Soper frame is shown in Fig A.1. Half of the opening angle between proton momentum and negative momemtum of antiproton is $\alpha/2 = \arctan(Q_T/Q)$. Collins-Soper frame is rotated by an angle $\omega = \arctan((-Q_Tq^3)/(M_T^2+Qq^0))$ in the x-z plane.

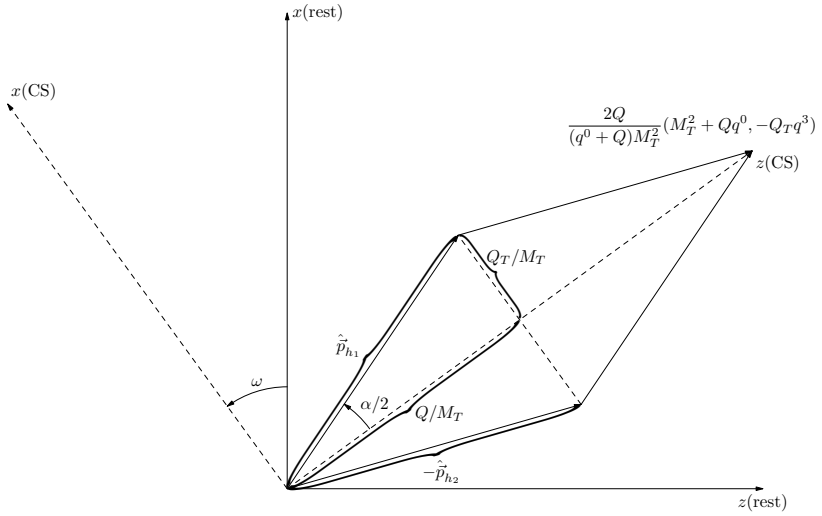

Figure A.1: Geometrical illustration of the Collins-Soper frame. Without loosing generality the y-axis is suppressed in both the lab frame and the Z boson rest frame. The Collins-Soper is just the Z boson rest frame rotated by ω angle in the x-z plane.

Electrons in the Z boson rest frame have 4-momentum

$$p_e'^{\mu}(\text{rest}) = \Lambda^{\mu}_{\nu}(\text{lab}\to\text{rest})p_e^{\nu} = \frac{1}{Q}\begin{pmatrix} q^0p_e^0 - Q_Tp_e^1 - q^3p_e^3 \\ -Q_Tp_e^0 + (Q+\dfrac{Q_T^2}{q^0+Q})p_e^1 + (\dfrac{Q_Tq^3}{q^0+Q})p_e^3 \\ p_e^2Q \\ -q^3p_e^0 + (\dfrac{Q_Tq^3}{q^0+Q})p_e^1 + (Q+\dfrac{(q^3)^2}{q^0+Q})p_e^3 \end{pmatrix}. \tag{A.23}$$

We know in the Z boson rest frame, the magnitude of electron momentum should be exactly half of Z boson mass $|\boldsymbol{p}_e|(\text{rest}) = Q/2$. The polar angle θ^* of electron in the Collins-Soper frame is determined by

$$\begin{aligned}\cos\theta^* &= \frac{\boldsymbol{p}_e(\text{rest})}{|\boldsymbol{p}_e|(\text{rest})}\cdot\hat{\boldsymbol{z}}(\text{CS}) \\ &= \frac{2}{Q}\frac{1}{Q}\frac{1}{M_T(q^0+Q)}[Q_T^2q^3p_e^0 - (Q+\frac{Q_T^2}{q^0+Q})Q_Tq^3p_e^1 - \frac{(Q_Tq^3)^2}{q^0+Q}p_e^3 \\ &\quad -(M_T^2+Qq^0)q^3p_e^0 + (\frac{Q_Tq^3}{q^0+Q})(M_T^2+Qq^0)p_e^1 + (Q+\frac{(q^3)^2}{q^0+Q})(M_T^2+Qq^0)p_e^3].\end{aligned}$$

Expand all the terms with q^0+Q as denominators in the r.h.s. of the above

equation, we can easily check the following relations hold

$$\begin{aligned} -\frac{Q_T^3 q^3 p_e^1}{q^0+Q} + \frac{Q_T M_T^2 q^3 p_e^1}{q^0+Q} + \frac{Q_T Q q^0 q^3 p_e^1}{q^0+Q} &= Q Q_T q^3 p_e^1, \\ -\frac{Q_T^2 (q^3)^2 p_e^3}{q^0+Q} + \frac{(q^3)^2 M_T^2 p_e^3}{q^0+Q} + \frac{(q^3)^2 Q q^0 p_e^3}{q^0+Q} &= Q (q^3)^2 p_e^3. \end{aligned} \tag{A.24}$$

Then we can rewrite Eq (A.24) simply as

$$\begin{aligned} \cos\theta^* &= \frac{2}{Q^2 M_T (q^0+Q)}[-Q^2 q^3 p_e^0 - Q q^0 q^3 p_e^0 - Q Q_T q^3 p_e^1 + Q (q^3)^2 p_e^3 \\ &\quad + Q Q_T q^3 p_e^1 + Q M_T^2 p_e^3 + Q^2 q^0 p_e^3] \\ &= \frac{2}{Q^2 M_T (q^0+Q)}[-Q^2 q^3 p_e^0 - Q q^0 q^3 p_e^0 + Q (q^0)^2 p_e^3 + Q^2 q^0 p_e^3] \\ &= \frac{2}{Q M_T}(q^0 p_e^3 - q^3 p_e^0). \end{aligned} \tag{A.25}$$

Now we substitute p_e^μ with $p_{e^-}^\mu$ to make it more cleat that $\cos\theta^*$ we calculated is for electron. We also use $p_{e^+}^\mu$ to stand for the 4-momentum of positron. Since we know both the electron and positron decay from the Z boson, we have $q^\mu = p_{e^-}^\mu + p_{e^+}^\mu$. Equipped with this equation, we can further rewrite Eq (A.25)

$$\begin{aligned} q^0 p_{e^-}^3 - q^3 p_{e^-}^0 &= (p_{e^-}^0 + p_{e^+}^0) p_{e^-}^3 - (p_{e^-}^3 + p_{e^+}^3) p_{e^-}^0 \\ &= \frac{1}{2}(p_{e^-}^3 p_{e^+}^0 + p_{e^-}^3 p_{e^+}^0 - p_{e^-}^0 p_{e^+}^3 - p_{e^-}^0 p_{e^+}^3) \\ &= \frac{1}{2}(p_{e^-}^0 p_{e^+}^0 - p_{e^-}^0 p_{e^+}^3 + p_{e^-}^3 p_{e^+}^0 - p_{e^-}^3 p_{e^+}^3 \\ &\quad - p_{e^-}^0 p_{e^+}^0 - p_{e^-}^0 p_{e^+}^3 + p_{e^-}^3 p_{e^+}^0 + p_{e^-}^3 p_{e^+}^3) \\ &= \frac{1}{2}[(p_{e^-}^0 + p_{e^-}^3)(p_{e^+}^0 - p_{e^+}^3) - (p_{e^-}^0 - p_{e^-}^3)(p_{e^+}^0 + p_{e^+}^3)] \\ &= \frac{1}{\sqrt{2}}(p_{e^-}^0 + p_{e^-}^3)\frac{1}{\sqrt{2}}(p_{e^+}^0 - p_{e^+}^3) - \frac{1}{\sqrt{2}}(p_{e^-}^0 - p_{e^-}^3)\frac{1}{\sqrt{2}}(p_{e^+}^0 + p_{e^+}^3) \\ &= P_{e^-}^+ P_{e^+}^- - P_{e^-}^- P_{e^+}^+. \end{aligned} \tag{A.26}$$

Putting Eq (A.26) into Eq (A.25), we get the exact result as Eq (2.54)

$$\cos\theta^* = \frac{2}{Q M_T}(P_{e^-}^+ P_{e^+}^- - P_{e^-}^- P_{e^+}^+) = \frac{2}{\sqrt{Q^2(Q^2+Q_T^2)}}(P_{e^-}^+ P_{e^+}^- - P_{e^-}^- P_{e^+}^+). \tag{A.27}$$

A.0.1 Redo the C-S frame calculation in 3 dimension

We have previously shown the analytical calculation of $\cos\theta^*$ by taking an assumption that the W/Z boson transverse momentum is aligned along the x-axis. Although this assumption doesn't alter the calculation of any physical variable, I still would like to give the complete $\cos\theta^*$ calculation in the situation where the boson p_T has both x and y component, as it proves to be useful when I painstakingly debug the `C++` code with the analytical calculation as a crosscheck.

If the 4-momentum of Z boson in the lab frame is $q^\mu = (q^0, q^1, q^2, q^3)$, the general boost matrix is

$$\Lambda^\mu_\nu(\text{lab}\to\text{rest}) = \frac{1}{Q}\begin{pmatrix} q^0 & -q^1 & -q^2 & -q^3 \\ -q^1 & Q+\dfrac{(q^1)^2}{q^0+Q} & \dfrac{q^1q^2}{q^0+Q} & \dfrac{q^1q^3}{q^0+Q} \\ -q^2 & \dfrac{q^1q^2}{q^0+Q} & Q+\dfrac{(q^2)^2}{q^0+Q} & \dfrac{q^2q^3}{q^0+Q} \\ -q^3 & \dfrac{q^1q^3}{q^0+Q} & \dfrac{q^2q^3}{q^0+Q} & Q+\dfrac{(q^3)^2}{q^0+Q} \end{pmatrix}. \tag{A.28}$$

The spatial component of the proton and antiproton momentum is then

$$\begin{aligned} \boldsymbol{p}_{h_1}(\text{rest}) &= (-q^1(q^0+Q)+q^1q^3, -q^2(q^0+Q)+q^2q^3, (-q^3+Q)(q^0+Q)+(q^3)^2), \\ \boldsymbol{p}_{h_2}(\text{rest}) &= (-q^1(q^0+Q)-q^1q^3, -q^2(q^0+Q)-q^2q^3, (-q^3-Q)(q^0+Q)-(q^3)^2). \end{aligned}$$

The length of $\boldsymbol{p}_{h_1}$ and $\boldsymbol{p}_{h_2}$ is

$$|\boldsymbol{p}|^2_{h_1} = (q^0+Q)^2(q^0-q^3)^2, \tag{A.29}$$

$$|\boldsymbol{p}|^2_{h_2} = (q^0+Q)^2(q^0+q^3)^2. \tag{A.30}$$

Now we can rewrite the normalized vector of $\boldsymbol{p}_{h_1}$ and $-\boldsymbol{p}_{h_2}$ as

$$\begin{aligned} \hat{\boldsymbol{p}}_{h_1} &= \left(\frac{-q^1(q^0+Q)+q^1q^3}{(q^0+Q)(q^0-q^3)}, \frac{-q^2(q^0+Q)+q^2q^3}{(q^0+Q)(q^0-q^3)}, \frac{(-q^3+Q)(q^0+Q)+(q^3)^2}{(q^0+Q)(q^0-q^3)}\right), \\ -\hat{\boldsymbol{p}}_{h_2} &= \left(\frac{q^1(q^0+Q)+q^1q^3}{(q^0+Q)(q^0+q^3)}, \frac{q^2(q^0+Q)+q^2q^3}{(q^0+Q)(q^0+q^3)}, \frac{(q^3+Q)(q^0+Q)+(q^3)^2}{(q^0+Q)(q^0+q^3)}\right). \end{aligned}$$

The z-axis of Collins-Soper frame is then

$$\boldsymbol{z}(\text{CS}) = \hat{\boldsymbol{p}}_{h_1} - \hat{\boldsymbol{p}}_{h_1} = \frac{2Q}{(q^0+Q)M_T^2}(-q^1q^3, -q^2q^3, M_T^2+q^0Q). \tag{A.31}$$

Unit z-axis vector is

$$\hat{\boldsymbol{z}}(\mathrm{CS}) = \frac{1}{(q^0+Q)M_T}(-q^1q^3, -q^2q^3, M_T^2 + q^0Q). \tag{A.32}$$

Electron 4-momentum in the boson rest frame is

$$p_e'^{\mu}(\mathrm{rest}) = \frac{1}{Q}\begin{pmatrix} q^0p_e^0 - q^1p_e^1 - q^2p_e^2 - q^3p_e^3 \\ -q^1p_e^0 + (Q + \dfrac{(q^1)^2}{q^0+Q})p_e^1 + \dfrac{q^1q^2}{q^0+Q}p_e^2 + \dfrac{q^1q^3}{q^0+Q}p_e^3 \\ -q^2p_e^0 + \dfrac{q^1q^2}{q^0+Q}p_e^1 + (Q + \dfrac{(q^2)^2}{q^0+Q})p_e^2 + \dfrac{q^2q^3}{q^0+Q}p_e^3 \\ -q^3p_e^0 + \dfrac{q^1q^3}{q^0+Q}p_e^1 + \dfrac{q^2q^3}{q^0+Q}p_e^2 + (Q + \dfrac{(q^3)^2}{q^0+Q})p_e^3 \end{pmatrix}. \tag{A.33}$$